Galactic Archaeology with *Gaia*

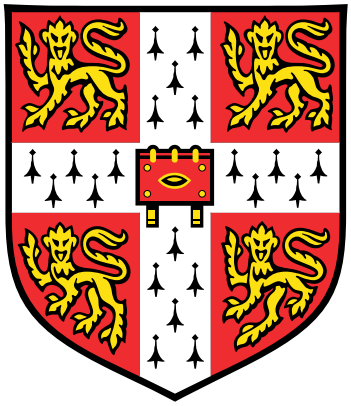

GyuChul Myeong

Institute of Astronomy

University of Cambridge

This dissertation is submitted for the degree of

Doctor of Philosophy

Pembroke College July 2019

Declaration

I hereby declare that except where specific reference is made to the work of others, the contents of this dissertation are original and have not been submitted in whole or in part for consideration for any other degree or qualification at the University of Cambridge, or any other University. This dissertation is the result of my own work and includes nothing which is the outcome of work done in collaboration, except where specifically indicated. This dissertation contains less than 60,000 words including abstract, appendices, footnotes, tables and equations and has less than 150 figures.

GyuChul Myeong
July 2019

Abstract

GyuChul Myeong: Galactic Archaeology with *Gaia*

The halo of our Galaxy is believed to be mainly formed by the materials accreted/merged in the past, and so has "extragalactic" origin. Such formation process will leave dynamical traces imprinted in the halo, like stellar substructures, distinguishable from the in-situ halo component. Studying the present-day structure and substructures of the Milky Way halo is one of the most direct ways of understanding the formation and the evolutionary history of the Galaxy, as well as investigating the ΛCDM model on the galaxy scale which has not yet been tested thoroughly. It has been a challenge to obtain a sufficiently large sample of halo stars for such study due to the sparse density of the halo. The recent *Gaia* mission can open a new era for the study of Galactic Archaeology as it provides quality data for ~ 1.3 billion stars across the Milky Way which had remained uncharted so far.

In Chapter 1, I describe a history of study on the Milky Way halo so far, and present algorithms that are developed to investigate the substructures of the halo with various aspects.

Chapter 2 is a morphological study of the Milky Way halo based on the chemo-dynamical information. It reveals various interesting aspects of the halo and its origin, such as the chemodynamical duality (evidence of a past major merger – the *"Gaia Sausage"*), traces of a past retrograde accretion (clues as to the origin of the retrograde halo component), and the resonant feature (evidence of dynamical influence of the Milky Way bar).

Chapter 3, 4 and 5 are examples of a more focused study on the halo substructures with various new methods that differ from the conventional studies. In addition to the discovery of new stellar streams, I investigate the properties of the potential progenitors (past accreted dwarf galaxies) of these substructures, and also the potential association with ω Centauri.

Chapter 6 is a study investigating the potential extragalactic origin of the Milky Way globular clusters based on their dynamics and various other information such as age, metallicity, horizontal branch index. It reveals a collection of globular clusters with extragalactic origin, originating from the *"Gaia Sausage"*.

Chapter 7 is a chemo-dynamical study showing the evidence for another early accretion event – the *"Sequoia"*. From multiple tracers in the Milky Way halo, including the stellar streams and globular clusters, I investigate the dynamical and the chemical signature of the *"Sequoia"* progenitor and its present-day remnants.

To my loving family

Acknowledgements

I wish to express my most sincere thanks to my supervisors, Prof. N. Wyn Evans and Prof. Vasily Belokurov, for their continuous support and guidance throughout my study and research. Their immense knowledge and wisdom coupled with their warm encouragement have been a great help to me throughout my entire Ph. D. years. I am profoundly grateful to have been under their supervision and the past three years could not have been more fun.

My sincere thanks also go to Dr. Jason Sanders, Dr. Eugene Vasiliev, Prof. Sergey Koposov, Dr. Denis Erkal, Dr. David Aguado, Dr. Nicola Amorisco and every member of the Cambridge Streams research group for sharing their knowledge and experience with me and for numerous helpful discussions.

My heartfelt thanks go to Prof. Ken Freeman and Prof. Rosemary Wyse for their invaluable supports and encouragements. I cannot express my appreciation enough for the amazing opportunities that they have created for me.

A special gratitude goes out to Mr. Fadi Boustany for his warm supports throughout my study and for providing me with an internship opportunity in Monaco. I wish to thank the Boustany Foundation, especially Ms. Alison Pitt, the Isaac Newton Studentship and Cambridge Trust for supporting my study.

I would like to thank the staffs at the Institute of Astronomy and Pembroke College, especially Prof. Paul Hewett and Ms. Debbie Peterson, for their precise and effective supports. I also wish to thank Ms. Margaret de Vaux for her kind and thoughtful supervisions which have been very helpful.

Dr. Giuliano Iorio always has been a great colleague and a thoughtful friend. I would also like to thank my fellow students, especially James Grady, Peter McGill, Daniel Muthukrishna and Luis Welbanks for being amazing friends and for making good memories.

Above all, I wish to send my deepest thanks to my family, especially to my parents, RohSun Myeong and JiEon Lim, and my sister, GyuRi Myeong, for their endless love and support. I am truly grateful for their unceasing encouragement.

Table of contents

List of figures

List of tables

Chapter 1

Introduction

1.1 Milky Way Halo and Galactic evolution

It has been widely accepted that large galaxies such as the Milky Way have been formed through accretion and merger events of a large number of protogalactic fragments (Blumenthal et al., 1984; Searle and Zinn, 1978). This hierarchical scenario also has been supported by observational evidence such as the detection of the ongoing disruption process of the Sagittarius satellite galaxy (e.g. Ibata et al., 1994) as well as by numerical simulations (e.g. Abadi et al., 2006).

The Milky Way has a sparse, large "halo" surrounding the main body (e.g., the bulge, discs) of the Galaxy. Unlike other components, the halo is believed to be mainly formed by materials that are not from the Milky Way, but instead, by materials accreted/merged in the past – and so have an "extragalactic" origin. The stellar halo of the Milky Way was initially believed to be a smooth spheroidal distribution of stars, typically composed of an old, metal-poor population. This view was developed by Eggen et al. (1962) based on their study on the orbital eccentricity and the metallicity of stars, and the authors found that the older stars possess more eccentric orbits. To explain such correlations,Eggen et al. (1962) suggested that the dissipation played the major role in the halo formation during the rapid collapse of the gas towards the galactic centre and to the plane. Later, a new view on the stellar halo was suggested by Searle and Zinn (1978) in their attempt to explain the origin of the halo globular clusters. Searle and Zinn (1978) showed that the metal abundance of outer halo globular clusters appears to be independent of their Galactocentric distance, and suggested that the halo globular clusters and the outer halo of the Milky Way have been formed from the accretion or merger events of extragalactic fragments.

The currently favoured cosmological model, the Λ Cold Dark Matter (ΛCDM) theory, has long been considered as a "standard model" as it provides a reasonably good account

of the various properties of the cosmos by postulating concepts such as dark matter. The simulations based on the ΛCDM model suggest that a large galaxy, such as the Milky Way, is formed through the hierarchical accretion and merger of numerous low mass fragments (e.g., dwarf galaxies). Interestingly, the simulations also show that the halo of such large galaxy is also formed as the result of these accretion processes (Abadi et al., 2006; Font et al., 2006) – similar to what Searle and Zinn (1978) suggested from their study on the halo globular clusters of the Milky Way.

When a satellite galaxy is accreted to the Milky Way, it undergoes tidal disruption as a result of dynamical interaction with the Milky Way. The disintegrated materials from the satellite are spread along its orbit, populating the halo of the Milky Way. The accretion/merger processes will also leave dynamical traces imprinted in the halo structure as this process can form substructures like stellar streams or shells along the orbital paths of the dissolving satellite. Over recent years, various large area sky surveys have been conducted and have provided us with valuable data ranging from astrometry (e.g., Hipparcos, *Gaia*) to photometry (e.g., SDSS, DES, Pan-STARRS, ATLAS) and to spectroscopy (e.g., APOGEE, SEGUE, RAVE, LAMOST, GALAH). This allowed us to map the Milky Way in greater detail compared to the past, and indeed, a significant number of stellar streams has been discovered in the halo of the Milky Way (e.g., Belokurov et al., 2007a, 2006a,b; Grillmair, 2006; Grillmair and Dionatos, 2006b; Ibata et al., 2001; Ivezić et al., 2000; Yanny et al., 2000), suggesting that a large fraction of the halo population exists as a form of substructure, not only as a smooth distribution. Such substructures will have unique dynamical properties which differ from the *in-situ* halo component (see also, Chapter 3, 4, 5). Since the timescale for the dynamical relaxation is much longer in this region of the Galaxy, these tracers can preserve their dynamical signatures for a very long time, and their current-day dynamics reflect the initial state at the time of accretion.

It is now widely believed that a significant portion of the halo stellar population and dwarf satellite galaxies are the depopulated remains from numerous destructive events such as tidal disruption during the hierarchical accretions and mergers (Font et al., 2011; Ibata et al., 1994). The significance of such processes in Galaxy formation/evolution is of great interest, especially since the *in-situ* star formation appears to be limited due to lack of gas content in the halo region (Helmi, 2008). Studying the internal dynamics and the morphology of the halo can shed light on this question, as they are closely related to the formation/evolution mechanism of the halo (see also, Chapter 2).

1.1.1 Milky Way Globular clusters

One interesting point is that some of the accreted dwarf galaxies contain globular clusters. Due to their high stellar density, these globular clusters can survive the accretion process even after their parent dwarf galaxies are dissolved under the tidal disruptions (Peñarrubia et al., 2009). Mackey and Gilmore (2004) suggested that a noticeable number of Milky Way globular clusters originated from such accretion events, and a significant portion of the current halo stellar mass has been donated by their host dwarf galaxies. In this case, these surviving globular clusters have kinematics that reflects their parent galaxy so we can infer the properties of this past merger, as well as some initial conditions of this infall.

Indeed, the globular clusters observed across the Milky Way don't appear to be a monolithic group. Zinn (1993) introduced a classification for these Milky Way globular clusters, in which the clusters are divided into bulge/disc, old halo and young halo clusters based on the metallicity and the horizontal-branch morphology (colour) of each cluster (see also, Mackey and Gilmore, 2004; Mackey and van den Bergh, 2005). Forbes and Bridges (2010) also noticed that there exist two distinct branches in the age–metallicity relation for the Milky Way's globular clusters. There is broad swathe of bulge/disc and old halo globular clusters with a near constant age of ~ 12.8 Gyr which comprises the bulk of the Milky Way globular cluster set. On the other hand, a separate track that branches to younger ages can be found with a combination of old and young halo globular clusters and globular clusters associated with the Sagittarius dwarf galaxy. Such differences in the horizontal-branch morphology and the age–metallicity relation are the result of the mass and the star formation history of the progenitor galaxy, as this is closely related to the iron enrichment process for the interstellar medium by the Type Ia supernova and the gas in/outflow (Forbes and Bridges, 2010). Therefore, the age–metallicity relation observed in the present-day Milky Way globular clusters can provide us with some clues about the evolutionary history of the Milky Way as well as about the initial properties of the Milky Way and the past accreted satellite galaxies. For example, by comparing the age–metallicity distribution observed from a set of cosmological zoom-in simulations and from the Milky Way globular clusters, Kruijssen et al. (2019) studied the number of potential past merger events as a function of satellite mass ratio and redshift.

The combined chrono-chemo-dynamical information of these Milky Way globular clusters can provide a multi-perspective view for understanding the complex nature of the Milky Way's halo. In addition, a large number of globular clusters and dwarf satellite galaxies around the Milky Way has been found to be tidally disrupted, providing observational evidence of the hierarchical Galaxy formation scenario and the view of Searle and Zinn (1978) on the stellar halo. Based on the age, chemical and dynamical information, we can also

look for possible links between the halo globular clusters and potential *ex-situ* halo stellar components that may have the same (extragalactic) origin (see also, Chapter 6 and 7).

1.1.2 Halo Substructure

During the accretion process, accreted materials such as dwarf galaxies are torn and disrupted such that their debris forms into stellar substructures, typically into large tidal streams. It has been suggested that some of the Milky Way globular clusters are found associated with stellar streams today as they were originally the members of captured dwarf galaxies (Freeman and Bland-Hawthorn, 2002; Lynden-Bell, 1982). They were torn away from their parent dwarf galaxies and embedded in the streams of debris from their parent. It has been observed from the halo of M31 (e.g., Mackey et al., 2010) and from the disruption process of the Sagittarius that its stellar contents appear to be stretched into stream-like features along its orbit (Ibata et al., 1994; Mateo et al., 1998), while a number of globular clusters including M54, Terzan 7, Terzan 8, Arp 2 and Palomar 12 (Da Costa and Armandroff, 1995; Dinescu et al., 2000; Sbordone et al., 2005) appear to be co-moving with the Sagittarius at a similar distance (e.g., Geisler et al., 2007; Sohn et al., 2018). This is further direct observational evidence supporting the idea that the accretion of dwarf satellite galaxies is a major contributor to the Milk Way's stellar halo and globular cluster populations (Forbes and Bridges, 2010; Martínez Delgado et al., 2004). NGC 1851 is another example of a cluster surrounded by substructures with might be the result of tidal influences on the dwarf spheroidal galaxy (Olszewski et al., 2009).

Stellar streams emerge as the result of the dynamical evolution of the satellite body orbiting the host. Such evolution is driven by both internal (e.g., the 2-body relaxation and stellar evolution inside of the globular cluster) and external (the consequence of the tidal forces exerted by the gravitational potential of the host galaxy) effects. For a satellite embedded in an external gravitational field, the field injects kinetic energy and modifies the outermost regions of the satellite. This allows those satellite stars to cross the equipotential surface and become unbound (escape) from the satellite, causing mass loss (or evaporation) of the satellite. In this rotating 2-body system, two Lagrange points L_1 and L_2 included in the Roche surface (the zero-velocity surface) are the main gateway for those escaping stars (see Fig. 1.1). This is because any weak perturbation, such as disc shocks, bulge shocks, or tidal shocks at the pericentre, can easily elevate the star's energy to exceed the effective potential, $\Phi_{\rm eff}$, around two Lagrange points (Klement, 2010). For a satellite on some circular orbit (for simplicity) around a parent galaxy, the Jacobi energy can be defined as, $E_J = 1/2v^2 + \Phi_{\rm eff}$, for a co-rotating frame, with a time-independent $\Phi_{\rm eff}$ (Johnston, 2016). Regarding the saddle points in $\Phi_{\rm eff}$, the limiting boundary (tidal radius, r_t) of the satellite in the gravitational

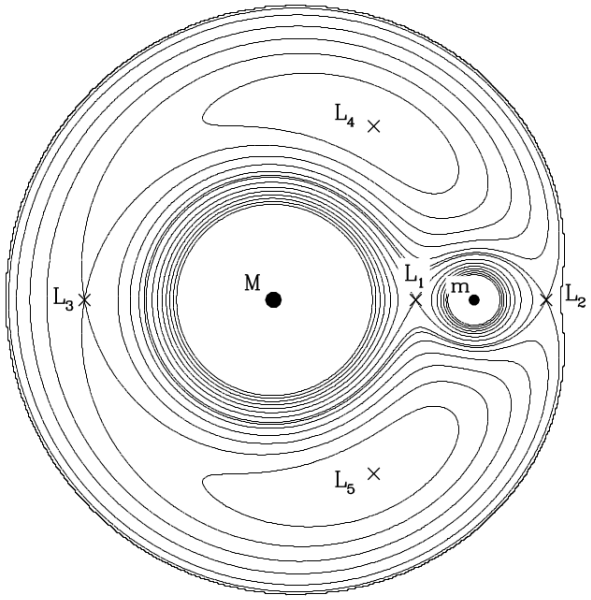

Fig. 1.1 Contours of effective equipotential $\Phi_{\rm eff}$ for two point masses with a mass ratio of $m/M = 1/9$ in a circular orbit (see Chapter 8.3 of Binney and Tremaine, 2008, and also, Eq. 1.1). The Lagrange points are marked as $L_{1,2,3,4,5}$. Two unstable Lagrange points, L_1 and L_2, are the main gateways for escaping stars. [Image Credit: Binney and Tremaine (2008)]

potential of the parent can be estimated as,

$$r_t = \left(\frac{m_s}{3M_R}\right)^{\frac{1}{3}} R \tag{1.1}$$

where m_s is the mass of the satellite, M_R is the enclosed mass of the parent within R, and R is the orbital radius (Binney and Tremaine, 2008; Johnston, 2016). Or course, this tidal radius does not necessarily define a solid boundary around the satellite that separates the unbound stars and the bound ones. It also depends on the kinematics of the star (Klement, 2010). Besides, most satellites are likely to be on non-circular orbits and it is impossible to define a definite tidal radius or a Jacobi energy (non-static combined gravitational potential) (Johnston, 2016). Note that a scale of, $r/R \sim (m_s/M_R)^{1/3}$, appears to depict the dynamical spread of the tidal debris from the satellite (Binney and Tremaine, 2008) which also have been noticed from numerical simulations with various masses and orbits (see e.g., Eyre and Binney, 2011; Johnston, 2016; Johnston et al., 1999; Küpper et al., 2012).

The stars leaving the satellite through two Lagrange points then form a leading and a trailing tails. The stars leaving through the outer point have higher energy with relatively longer orbital period so will form a trailing tail, while the stars leaving through the inner

point have lower energy with relatively shorter orbital period and so will form a leading tail. The tails are approximately projected along the orbital path of the satellite and so can provide some idea about its orbit, but this does not necessarily reveal the exact trajectory of the satellite (Sanders and Binney, 2013). The Sagittarius dwarf satellite (Ibata et al., 1994; Mateo et al., 1998) and the disrupting globular clusters Palomar 5 (Odenkirchen et al., 2001) and NGC 5466 (Belokurov et al., 2006a) are good examples of the stellar stream with distinct tidal tails (see also, Myeong et al., 2017b, for more recent examples with Palomar 15, and Eridanus). Interestingly, Choi et al. (2007) suggested that stars in the leading tail would sink towards the host galaxy (e.g., the inner part of the halo) due to the gravitational pulling and deceleration by the satellite, while the parent satellite remains in its orbit in the outer part of the halo.

As we see the thin disc as the dominant component of the Milky Way, Freeman and Bland-Hawthorn (2002) suggested that the most of the accretion events that contributed to the current stellar halo occurred before disc formation, as such infall would have heated the early stellar disc and formed the galactic thick disc. Quinn et al. (1993) suggested that even a single relatively low mass merger with its mass equivalent to a few percent of the disc can cause a considerable disruption on the disc. The stellar substructure resulted from the tidal disruption and the mass loss of the Milky Way satellites can be used to trace the accretion and merger events in the past, and allows us to unveil the formation and the evolutionary history of the Galaxy.

There has been a number of studies suggesting the dichotomy of the stellar halo. Chiba and Beers (2000) suggested the existence of two halo components with different morphology (flatter inner halo, and more spherical outer halo), while Carollo et al. (2010) suggested a prograde inner halo and a retrograde outer halo. While these two studies claim a radius dependent dual-halo, there are also studies suggesting the metallicity dependent halo duality. Deason et al. (2011b) suggested a prograde metal-rich halo and a retrograde metal-poor halo. Belokurov et al. (2018) and Myeong et al. (2018c) recently showed evidence of a flatter metal-rich halo and a isotropic metal-poor halo based on the velocity dispersion of the halo stars. Such a change in the halo's morphology is difficult to explain with a pure hierarchical view of Searle and Zinn (1978) involving numerous random mergers (although a single massive infall – or a group infall along the same direction at similar epoch can create a halo component with a specific morphology). It appears that a view which can encompass both hierarchical and dissipation scenario might be necessary. In this regard, it is important to identify the smooth (presumably with no connection to the accretion and merger events) and the non-smooth (as the result of such events) components of the stellar halo, as their characteristics may shed light on the physical mechanism and the stages of the halo

formation (Fermani and Schönrich, 2013; Preston et al., 1991). Yet, this task can become challenging since even though the (non-smooth) substructures may stand out more clearly as the dominant component at the outer part of the halo, the timescale of phase mixing becomes shorter as we move towards the smaller radii (Helmi and White, 1999). This can dissolve the substructures to a phase mixed and spatially smooth distribution, even if their true origin is from hierarchical accretions.

Searching for halo substructures, as evidence of merger events, also can provide key information to quantify the number and the frequency of such events that have occurred in the galaxy during its evolution. Such estimation can help us to test the ΛCDM cosmology on the galaxy scale, as the model predicts the existence of a large number of satellite subhalos and merger events. In addition, the physical characteristics and the morphology of the stellar streams can provide us with valuable information to constrain the Milky Way's gravitational potential and the distribution of the mass enclosed (e.g., Dehnen et al., 2004; Erkal et al., 2017; Helmi and White, 1999; Koposov et al., 2010). They also can be used to probe the size and the shape of the Galactic dark matter halo and potential dark subhalos, even at the distant outskirts of the galaxy. For example, gaps in the tidal stream can indicate past disturbance during its orbits. Such perturbations in the Milky Way potential would have been induced by the various type of perturbers including giant molecular clouds, Milky Way bar or dark matter subhalos. From the morphological analysis, we can even conjecture the size of the mass of those potential perturbers (Erkal et al., 2017; Ibata et al., 2002; Law and Majewski, 2010; Lux et al., 2012; Pearson et al., 2015). Although it has been suggested that large (thick) and kinematically hot streams may be able to hide such effect of the subhalos that the streams have encountered (Yoon et al., 2011), the stellar streams can be used as a valuable probe for us to prove the existence of the dark matter subhalos (Johnston, 2016).

1.1.3 Dark matter detection with Halo streams

Another potential application of halo substructure of extragalactic origin is dark matter detection. Dark matter halos can contain numerous substructures due to the tidal disruption and stripping of satellite galaxies or dark subhalos of the Milky Way. Extragalactic systems accreted to the Milky Way can give rise to streams of dark matter particles wrapping the galaxy. As already shown from numerical simulations, such substructures of accreted materials can reach the inner region of the Milky Way (Abadi et al., 2006, 2003; Helmi, 2008; Helmi and White, 1999). Since they are highly kinematically localised, they pose excellent prospects for the direct detection of dark matter. There has been a number of papers on the subject of streams and their signals in direct detection experiments (see e.g., Foster et al., 2018; Kavanagh and O'Hare, 2016; Lee and Peter, 2012; O'Hare and Green, 2014,

2017; Savage et al., 2006). Historically, the stream from the Sagittarius dwarf galaxy (Ibata et al., 2001, 1994) was used to motivate such study (Luque et al., 2017; Majewski et al., 2003; Newberg et al., 2003; Purcell et al., 2011, 2012; Yanny et al., 2003). However, the last decade has seen the branches of the Sagittarius stream mapped out in a number of stellar tracers (main sequence-turn-off stars, blue horizontal-branch stars, RR Lyrae) across 360° on the sky. We now know that the Sagittarius stream does not pass close to the Sun (Belokurov et al., 2014; Koposov et al., 2012) and so it will not have have any impact on laboratory experiments for the direct detection of dark matter. Nonetheless, formalisms developed with the Sagittarius stream in mind will be useful. In this regard, the recently discovered halo substructure in the Solar vicinity (S1 stream; Myeong et al., 2018a,b), offers excellent prospects for the direct detection of dark matter (O'Hare et al., 2018).

Based on the spatial and kinematic properties of the S1 stream, as well as its metallicity (abundance matching), its progenitor is believed to be a dwarf galaxy of mass $\approx 10^{10}\mathrm{M}_{\odot}$ in stars and dark matter (Myeong et al., 2018a). The present-day dark matter content of S1 is not known, but is expected to be significant. The S1 stream passes through the Solar neighbourhood on a low inclination retrograde orbit, so the stars in the S1 stream impact on the Solar system at very high speed almost head-on. This suggests a coherent stream of dark matter associated with S1 sweeps the Solar system.

Streams can impact the detection of any dark matter particle to some extent, so we can study the effects of the S1 stream on experiments attempting to discover candidate particles from light axions or axion-like particles (ALPs, $m_a \approx 10^{-10}$–10^{-3} eV) or standard Weakly Interacting Massive Particles (WIMPs, $m_\chi \gtrsim 1$ GeV). Additionally, since it is well known that nuclear recoil-based direct WIMP searches possess limited sensitivity to the dark matter velocity distribution, we can also study the impact of S1 on directional detectors in which more kinematic information is preserved (Billard et al., 2010; Kavanagh and O'Hare, 2016; Lee and Peter, 2012; Mayet et al., 2016; Morgan et al., 2005; O'Hare and Green, 2014).

Relative to nuclear recoil experiments, axion haloscopes (e.g, ADMX (Asztalos et al., 2010; Du et al., 2018), MADMAX (Millar et al., 2017; The MADMAX Working Group et al., 2016), ABRACADABRA (Foster et al., 2018; Henning et al., 2018; Kahn et al., 2016)) have unmatched sensitivity to the local dark matter velocity distribution. Depending on the dispersion, the S1 stream could improve the prospects for detecting axion dark matter. Also, after the axion mass has been identified, properties of the stream can essentially be read from the power spectrum of an axion-induced electromagnetic signal time-stream (O'Hare et al., 2018). The detection of the S1 stream, or any other dark matter substructures that may be present in our local halo, has truly excellent detection prospects if the dark matter in our galaxy is made up of axions.

1.1.4 Phase space

Eggen et al. (1962) advocated the importance of substructure studies for the Milky Way's stellar halo. Their relaxation time is sufficiently long compared to the Milky Way's age, and so their present-day kinematics reflects their initial condition. The halo also consists of some of the oldest and the most metal-poor stars, so their chemical and dynamical properties can provide us valuable knowledge on their origin and the early stage of the galaxy formation.

It has been shown from numerical simulations that accreted stellar materials can reach the inner halo and the disc of the galaxy, which indicates the possibility of finding those remnants in the Solar neighbourhoods (Abadi et al., 2006, 2003; Helmi, 2008; Helmi and White, 1999). Obtaining a sufficient dataset of the local halo stars can be challenging due to their sparseness, especially in comparison to the disc stars in the Solar neighbourhoods. But for those halo stars in the Solar neighbourhood, we can obtain more precise measurements for their kinematics and chemical abundances which would not be possible for the distant halo stars. Recent large area sky surveys such as *Gaia*, SEGUE, RAVE and LAMOST have been expanding our range of sight, allowing us to collect necessary kinematical and chemical information for a larger sample. One thing to note is that at a smaller radius like the Solar neighbourhoods, the dynamical timescale can become very short so that even a single merger event can be disintegrated into hundreds of kinematically cold streams (Gould, 2003; Helmi and White, 1999). As a consequence, the spatial density of each stream can become very low (Gould, 2003; Helmi and White, 1999; Klement, 2010).

One of the most straightforward methods to identify halo substructure is from phase space. The stars forming substructure can show distinguishable signature in the phase space, even after their signal in the configuration space (e.g., surface density) becomes blurred due to the phase mixing after multiple consecutive orbits (e.g. Helmi et al., 1999). The mass of the stellar halo is very low compared to other components of the galaxy and is very sparse in density, so the halo behaves even more like a collisionless system. From stars with full six-dimensional phase space information available, that is, astrometric and kinematic measurements including distance, radial and proper motions, we can construct some optimal multi-dimensional space to look for the coherent signal among the halo stars. For example, we can consider the conserved or approximately conserved elements along the orbit (integrals of motion) since the stars belong to the same substructure will appear clumped (Binney and Tremaine, 2008; Smith, 2016) in such space. The energy and the angular momentum in L_z are conserved in the case of an axisymmetric potential. Exploring phase space with a more sophisticated method can allow us to identify fainter and more ancient substructures that have already faded in configuration space.

One example is the co-moving group of stars identified by Helmi et al. (1999). These authors identified a group of stars with distinctive angular momentum components that appears to be a remnant of a past accretion (Kepley et al., 2007). The authors constructed 2-dimensional space using two components of angular momentum, L_z and $L_\perp = \sqrt{L_x^2 + L_y^2}$, assuming $L_\perp$ is approximately conserved. The L_z is conserved in an axisymmetric potential, and these two angular momentum components are easier to determine, especially in comparison to the energy which requires a good assumption for the Milky Way's gravitational potential (Johnston, 2016). The authors identified a distinct group of stars with high $L_\perp$. While this group of stars appears to have similar v_ϕ to the Sun, they appear to have noticeably high v_z. Interestingly, their distribution in v_z appears to be separated into two groups, almost symmetric to $v_z = 0$, indicating one group is moving upward while the other is moving downward. It was claimed that this is due to the phase mixing and these two groups of stars are the remnant of a single accretion in the past. It was shown in Helmi (2008) based on N-body simulations from Helmi et al. (1999) that, although a substructure can evolve quickly on a short timescale in configuration space, the coherence of the member stars in the phase space (or velocity space) remains relatively distinguishable. Furthermore, they showed in their simulation that multiple kinematic substructures can be found in the Solar neighbourhoods even though they originate from a single merger.

On the other hand, if we assume some suitable model for the Milky Way's potential, the action-angle variables can provide a more sophisticated approach for identifying substructures based on Hamiltonian dynamics (e.g. Binney and Tremaine, 2008; Sanders and Binney, 2014; Sellwood, 2010). Assuming some integrable potential, the stars in regular orbits can be described by the actions and angles variables. The actions and angles are linked via Hamilton's equations where the actions, J, describes the orbit of the star in the phase space while the angles, θ, describes the position of the star on the orbit (Binney and Tremaine, 2008; Johnston, 2016). The action-angle variables provide very clear characterisation of the individual stellar orbits and provide straightforward insights into its dynamics. Since they are a set of canonical coordinates of the Hamiltonian, the action variables are conserved adiabatically so they remain approximately constant even under the slow change of the potential (e.g., Galactic evolution). So, stars from the same origin keep comparable actions and remain identifiable in the action space. In addition, the action variables conserve their quantities from the initial state effectively so the variables inferred based on the present-day data reflect the past state – so they are like "living fossils" (see also, Binney and Tremaine, 2008; Helmi and White, 1999; Johnston, 2016; Klement, 2010). This makes the action-angle variables perfect for revealing the hidden nature of Galaxy formation and evolution.

Historically, there has been no effective method to compute the actions for the "realistic" Milky Way model before. This has only become possible recently (see e.g., Binney, 2012; Sanders and Binney, 2016; Vasiliev, 2019a). For the first time, we computed the action-angle variables based on the "realistic" potential of the Milky Way (e.g., McMillan, 2017), for an unprecedentedly large set of the halo stars.

1.1.5 Rotation of Halo

The general flow of the stellar halo, if it exists, is another important piece of information that can help us to better tune the balance between the pure hierarchical view of Searle and Zinn (1978) and the dissipation scenario of Eggen et al. (1962) for halo formation. For example, from aspects of dynamical friction, prograde rotation (i.e., in the same direction as the Galactic disk rotation) of the halo may indicate that accretions and mergers have occurred preferentially along this particular direction. This is closely related to the efficiency of the dynamical friction, as the efficacy decreases for larger relative velocity between the infalling materials and the disc stars (Quinn and Goodman, 1986). Thus, if the stellar halo has been formed mainly under the hierarchical scenario, it is more likely for the resulted stellar halo, especially at its outer part, has almost no rotation (Norris and Ryan, 1989).

So far, there is a number of studies suggesting different results. Majewski (1992) claimed global retrograde rotation of the halo, while another study based on the main-sequence stars claimed the halo is prograde in the inner part and is retrograde at the outer part (Carollo et al., 2010). Interestingly, Deason et al. (2011b) showed a prograde, metal-rich halo component, and a retrograde, metal-poor halo component independent of the radius from their study of blue-horizontal-branch halo stars. Fermani and Schönrich (2013) however, claimed a non-rotating or weakly prograde halo, without any duality in either the radius or the metallicity as they claimed that distance bias could induce the rotation signal (see also, Schönrich et al., 2012). Helmi et al. (2017) claimed the existence of a retrograde component in the halo based on the L_z distribution of their TGAS-RAVE crossmatched halo samples with low binding energies, but Helmi et al. (2017) underestimated the Solar reflex motion which induces a considerable systematic offset in their result.

Apart from identifying the smooth component of the stellar halo for measuring the rotation signal, one of the main issues is potential contamination in the halo sample. It is important to understand whether the obtained sample can be regarded as a good, unbiased representation of the whole. While it is more challenging to obtain a clean, unbiased halo sample near the Solar neighbourhood, more distant stars currently located in the halo region have to be brighter in order to be observed. The distance estimates (e.g., Ivezić et al., 2008, for the main-sequence-turn-off stars) for these stars are highly correlated with the metallicity

and the surface gravity, which can cause considerable systematic gradients in the inferred kinematics (see e.g., Fermani and Schönrich, 2013; Schönrich et al., 2012). In addition, while it is necessary to obtain the full six-dimensional phase space information to infer the true kinematics of the stars, such information has not been available for sufficient number of halo stars, especially before the *Gaia* mission.

1.2 Halo stars in the *Gaia* era

Gaia is one of the most ambitious space missions of the European Space Agency (ESA), with the main objective of providing a three-dimensional map of the Milky Way with an unprecedented volume and precision (Gaia Collaboration et al., 2016). By measuring the position, parallax, and proper motion (with a precision of the order of a few micro-arcseconds by the end of the nominal mission) of a large number of stars up to the magnitude of 20, *Gaia* will trace $\sim$ 1.3 billion stars (approximately one per cent of the Galaxy's population) across the Milky Way, not only with three-dimensional positions, but also with two- or three-dimensional velocity (the radial velocity will be measured as well for $\sim$ 300 million bright stars) (ESA, 2014). *Gaia* data releases include the spectro-photometry (BP, Blue Photometer 330-680nm, RP, Red Photometer 640-1050nm, in addition to the unfiltered G band of the *Gaia* photometric system) and will also include spectroscopic astrophysical parameters in the future (Gilmore, 2018). This rich variety of information will allow us to conduct a hyper-dimensional analysis for the Milky Way's population that has never been possible before the *Gaia* era.

Due to the sparse density of the Milky Way halo, stars that belong to the halo are very rare especially near the Solar neighbourhood. This means it is difficult to obtain a large sample of halo stars since we only can carry out observations from our current location in the Milky Way. In this perspective, the recent *Gaia* Data Release (DR) 2 (Gaia Collaboration et al., 2018b) can open a new era for the study of Galaxy Dynamics as it provides high precision data for $\sim$ 1.3 billion stars across the Milky Way far beyond the Solar neighbourhood which had remained uncharted so far.

Gaia data can be further reinforced with other spectroscopic surveys which can provide additional kinematical and chemical information for the Milky Way stars. Full six-dimensional phase space coordinates for individual stars enables searches for co-moving groups of stars to be conducted directly in phase space, and the calculation of statistical measures of substructure (Helmi et al., 2017; Lancaster et al., 2018; Myeong et al., 2017a). Together with the astrometric data, the chemical abundances can add valuable information for understanding the chemo-dynamical structure of the Milky Way. The stars born at a similar time and space

will have similar chemical composition, while this environment has been chemically enriched by the previous generations. Therefore, the chemical abundances of individual stars can provide crucial information for identifying different stellar populations (families of stars) in the Milky Way as well as for understanding the past star formation history.

The detailed chemical abundances of the stars or the globular clusters can provide some key information on their origin. For example, the chemical properties of stellar populations in the local dwarf spheroidal galaxies has been investigated in detail based on the spectroscopy of individual stars. Interestingly, the chemical evolution paths between galaxies appear to be quite different according to the abundance patterns of RGB stars (see e.g., α-enrichment in Section 4 of Tolstoy et al., 2009). The neutron-capture elements also can assist us to obtain better understanding on the chemical evolution of the galaxy. The rate of the neutron-capture in comparison to the β decay depends on the environment (i.e., neutron density) and the process can be sub-classified as the slow (s-) and rapid (r-) processes. While the s-process can be found in low to intermediate mass stars, the r-process occurs during massive star nucleosynthesis (Tolstoy et al., 2009). The ratio between the s- and r-process elements can tell us about the self-enrichment history. For example, the r-process from the massive stars dominates the evolution of neutron-capture elements (e.g., Shetrone et al., 2001) at earlier time. Later, the s-process from the low and intermediate mass stars becomes the dominant source eventually. The metallicity of this turnover in the s- and r-process ratio could also tell us about the metallicity of the system at the time when the s-process contribution started in the galaxy (Tolstoy et al., 2009).

If the Milky Way indeed comprises *ex-situ* components, originated from past accretions of lower mass satellites, these remnant populations will show distinct chemical signatures. Such signatures will be most evident from the halo stars (and potentially the halo globular clusters). For example, Haywood et al. (2018) noticed that a population of stars that corresponds to a past major merger event (Belokurov et al., 2018; Myeong et al., 2018c) shows a relatively low sequence of [α/Fe] abundances, across the metallicity range typical for the halo stars (see also, Mackereth et al., 2019).

We can see that the chemical and the dynamical (e.g., action-angle variables) information can be highly complementary to each other. For example, we can search for stars with "extragalactic" origin that were not formed in the Milky Way but were brought in during the Galactic evolution process. Correlated signatures between dynamical and chemical properties can be studied among stars or stellar populations to compile a genealogy of Milky Way evolution.

Based on the data from *Gaia* DR2 and various surveys such as SDSS (SEGUE), APOGEE, LAMOST, RAVE and GALAH, a large dataset of the halo stars can be constructed, with full

six-dimensional phase space (complete spatial and velocity) information, as well as chemical abundances for individual stars. This compiled dataset is much larger than any pre-existing study ever obtained – almost 60 times larger in number, across 5 times greater in spatial volume in the Milky Way.

At this dawn of the *Gaia* era, studying the present-day structure and substructures of the Milky Way halo is one of the most direct ways of understanding the true nature of the Galaxy formation mechanism and evolutionary history. It is also one of the most direct ways of investigating the validity of ΛCDM model on the galaxy scale – which has not yet been tested thoroughly. My study of the Milky Way halo with complete dynamical information and chemical abundance will provide us with a key to unveil the true structure of the Milky Way and its formation mechanism, which is also closely linked to the dark matter and to the current ΛCDM model.

1.3 Algorithm construction

So far, most conventional studies have relied on limited or incomplete phase space information with lower dimensionality and with missing components. Stellar substructures have been mainly identified by searching for stellar concentrations based on astronomical images, sometimes with a one-dimensional radial velocity component. Based on multi-band photometry, it is possible to identify some specific stellar populations (a family of stars with common origin) existing in the field covered by imaging (e.g., matched-filter technique in the colour-magnitude space with a model isochrone. See also, Rockosi et al., 2002). Then by tracing the spatial (projected) distribution of this stellar population, we can study its stellar structure or substructures which reflect the tidal interaction with the Milky Way. Since it is much more challenging to obtain full six-dimensional phase space information for stars further away from the Sun (especially before the era of *Gaia* mission), this conventional method still remains as one of the most effective methods for the substructure study. I also have constructed an algorithm based on the photometric approach that is capable of performing a wide-sky search for the stellar streams (see also, Appendix A).

Although the conventional approach has been widely used with some success, more sophisticated and effective methods can be devised especially at the dawn of the *Gaia* era. Complete phase space information can give us significant advantages in analysing the structure or substructure of the Milky Way halo. The conventional method could have revealed a number of prominent stellar streams. Yet, it is not sufficient to provide full information on a substructure's dynamics which is essential for understanding the origin and the evolutionary history of its progenitor, as well as the potential of the Milky Way. Also,

only those substructures with sufficiently high surface density could have been identified – a big limitation especially in the halo. In contrast, my complete dataset allows us to study the full aspect of the stellar dynamics. For example, we can study the conserved or approximately conserved elements along the orbit (integrals of motion). By inferring the complete orbit of individual stars, we can consider the overall Milky Way structure as a collection of orbits. Any substructures can be identified as a set of stars with similar orbits, and moreover, we can have a better understanding of their dynamics which is essential for investigating the formation and evolution mechanism of the Galaxy.

1.3.1 Multi-dimensional approach

An algorithm was developed to perform a series of data reductions and analysis for investigating the stellar substructures in the local stellar halo based on multi-dimensional information (e.g., six-dimensional phase space, chemical abundances). The algorithm basically searches for any local overdensity in some selected n-dimensional space by comparing the data and the model density, and quantifies the significance of the detected overdensity. The detection space can be chosen freely depending on the purpose of the study, and the algorithm can pre-process the data (e.g., coordinate transformation, orbital integration, action-angle estimation) to obtain the necessary variables for the search. The algorithm consists of three major stages – the data pre-processing, the data/model comparison, and the detection/cleaning stage, and the basic structure is shown in Figure 1.2. More details can be found in Section 5.2.

Based on the input data (e.g., α, δ, ω, $\mu_{\alpha*}$, μ_δ, v_{los}), the algorithm first constructs a catalogue that is suitable for our intended analysis. For example, if the analysis is to be conducted in the action variable space (J_R, J_ϕ, J_z), the algorithm first carries out a series of coordinate transformations and action-angle estimation (with some limited choice of the potential, McMillan (2017) by default) to obtain the necessary variables for the chosen detection space. Once the catalogue is prepared, the algorithm constructs a background model which represents the underlying smooth distribution of the data in the detection space. Then the algorithm searches for local overdensities in the data. It computes the probability percentile of the measured local density (from the data) in comparison to the model density, and gauges the significance. The overdensities with high significance (e.g., $\sigma > 4$) are then classified into several groups based on their relative location in the detection space by hierarchical agglomerative clustering (e.g., Pedregosa et al., 2011). The detection significance is measured for the newly classified group (again in comparison to the model density across the volume occupied by the group) and is used to identify the high significance candidates. The size (number) of the dataset also sets the lower limit for the candidate's size (minimum number of stars that belong to a single candidate) which is necessary for avoiding

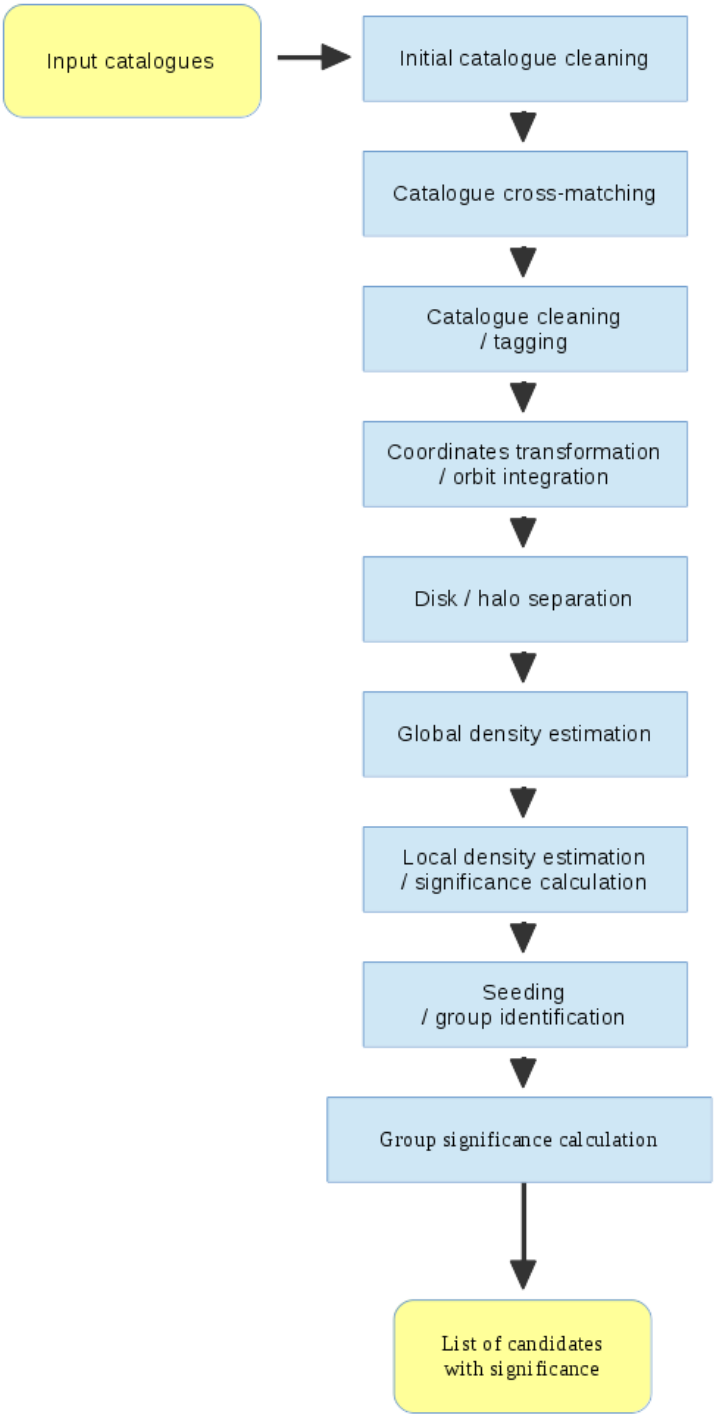

Fig. 1.2 Algorithm structure for the Multi-dimensional approach algorithm

potential false detections by chance. It is also possible to adopt further extra quality cuts. For example, if we are searching for a group of stars with a common origin, comparing the metallicity distributions of the candidate and the entire dataset can be an option to ensure that the candidate shows a reasonable metallicity distribution.

As the result, the algorithm generates a gallery of substructure candidates with their detection significances. The algorithm is designed to be flexible in selecting the variables and the dimensionality of its analysis.

Since we are currently focusing on utilising the astrometric data based on *Gaia*, the algorithm contains a number of useful functionalities applicable for the related analysis. For example, for stars with valid SDSS photometry and metallicity measurements, the algorithm can infer the photometric parallax for main-sequence-turn-off (MSTO) stars (Ivezić et al., 2008) and blue-horizontal-branch (BHB) stars (Deason et al., 2011b) based on the input SDSS photometry and the metallicity. The algorithm also adopted `tact` (Sanders and Binney, 2016) and `AGAMA` (Vasiliev, 2019a) for a fast computational estimation of the action-angle variables (see also, Binney, 2012). The algorithm can perform orbital integration as well to obtain necessary orbital parameters for individual stars. Moreover, the orbital decay can be included during the orbital integration by taking account of a simple dynamical friction from Chandrasekhar (1943) (for the case of some stellar system such as dwarf galaxy).

The algorithm is based on `Python 2.7` (or `3`) with adoptions of various internal and external packages and modules. The algorithm uses a number of functions from `galpy` and `scikit-learn` for some of the processes such as coordinate transformation, or multi-Gaussian fitting. The `OS` module in `Python` is used to manage and operate the OS-dependent functionality and external packages such as `STILTS`. The `Numpy`, `Pandas`, `Scipy`, `Pylab`, `Matplotlib` modules are used for basic data reduction, data management and display.

1.3.2 Photometric approach

A sophisticated algorithm was constructed to investigate the stellar structure of targeted globular clusters or satellite galaxies across a wide field of sky based on imaging data.[1] Figure 1.3 shows the basic structure of the algorithm. When the input imaging data are provided, the algorithm performs a series of image processing, photometry, calibration and de-reddening, and isochrone fitting to construct a stellar catalogue of the targeted stellar population. As a result, the algorithm generates a radial density profile and a spatial density map of this stellar population. The algorithm also can fit a King model to the radial density

[1] Remark: An early version of this algorithm was designed and constructed during my undergraduate study.

profile to infer the core radius, tidal radius, and the concentration. The spatial stellar density is scaled in terms of the significance over the background distribution.

The algorithm can handle as many images (even with different pointings) as desired. It is also capable of performing fast and sophisticated photometry even for some large images with wide field-of-view. It contains various functionalities as well. For example, the user can include or generate weight maps for the corresponding input images, which will help to improve the photometry by means of masking bad or saturated pixels in the image. The user can also choose to perform various image processing with this algorithm, such as image stacking, and masking. The photometry can be fine-tuned easily and can also adopt various techniques such as PSF photometry (generating a model post-spread-function for individual sources) to optimise the result.

The algorithm is based on `Python 2.7` (or 3) with various internal and external packages and modules. The `OS` module in `Python` is used to manage and operate external packages such as `SExtractor`, `PSFEx`, `STILTS`, `IRAF` and `SWarp`. The `Astropy`, `Photutils`, `PyFITS` and `Pywcs` modules are employed to handle FITS format data. The `Numpy`, `Pandas`, `Scipy`, `Pylab`, `Matplotlib` and `Lmfit` modules are used for basic data reduction, model fitting, data management and display.

Furthermore, `SExtractor` and `PSFEx` are adopted to perform the photometry on the input data, providing various photometric and astrometric parameters for each detected source. Especially with the use of `PSFEx`, more effective star/galaxy separation has become possible (see also, Koposov et al., 2015, and Chapter A). `SWarp` is adopted to generate the stacked images or to join the extensions in the "Stacked images" provided by the DECam Community Pipeline (Valdes et al., 2014), if it is necessary. For example, the image stacking from the DECam Community Pipeline can compromise the PSF of the source severely, when the individual images used for the stacking have considerably different seeing values. Moreover, this problem is also correlated to the flux of each source which makes the resulted stacked image not usable for photometry. Also, the stacked image from the DECam Community Pipeline is artificially divided into 9 multi-extensions (Multi-Extension FITS). Since the photometry is performed separately for each extension, this cut can induce various artificial features across the actual field of sky which is critical if we are analysing the stellar distribution across the field. `IRAF` is used for re-masking the "Weight map" provided by the DECam Community Pipeline as these weight maps sometimes contain inappropriate masking for the invalid regions of the image, which can cause problem in the background level estimation during the photometry.

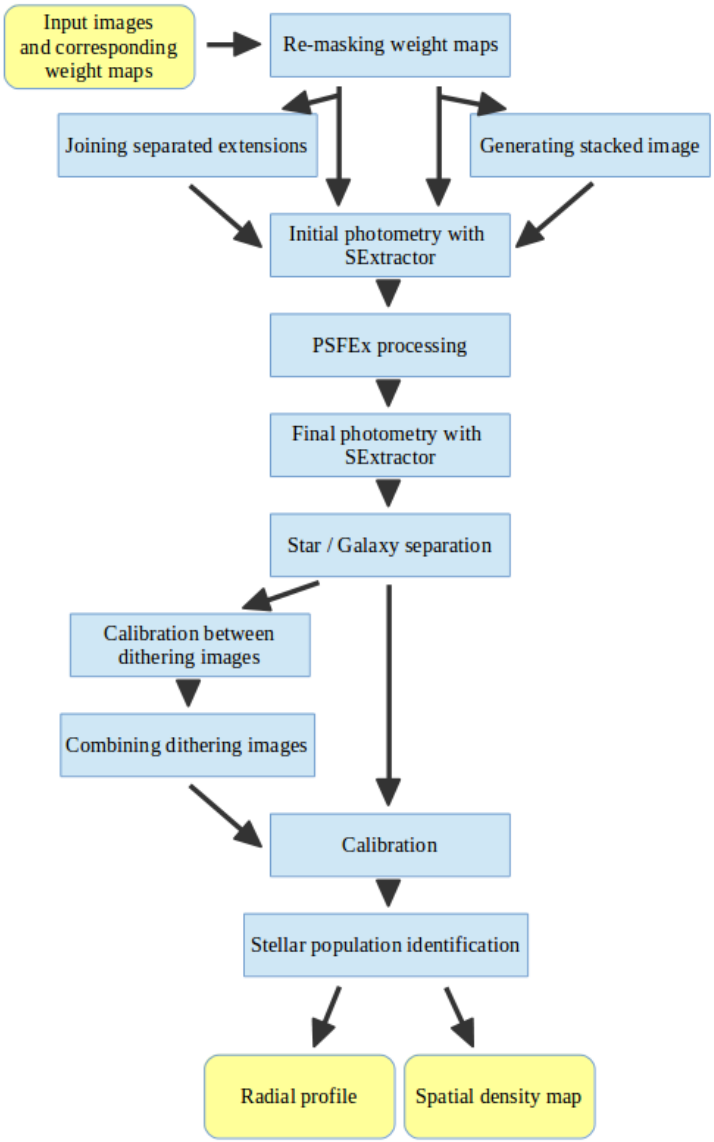

Fig. 1.3 Algorithm structure for the Photometric approach algorithm

1.4 Outline

Chapter 2 is an example of morphological study of the Milky Way halo based on the chemo-dynamical information (action variables and metallicity). It revealed various interesting aspects of the halo and its origin, such as the chemo-dynamical duality (evidence of the most significant merger ever revealed – the *"Gaia Sausage"*), traces of a past retrograde accretion (important clues as to the origin of the retrograde halo component and the potential association with ω Centauri), and the resonant feature (evidence of dynamical influence of the Milky Way bar). Chapter 3, 4 and 5 are examples of a more focused study on the halo substructures with various new methods that differ from the conventional studies. In addition to the discovery of new stellar streams, we investigate the properties of the potential progenitors (past accreted dwarf galaxies) of these substructures, and also the potential association with ω Centauri. Chapter 6 is a study investigating the potential extragalactic origin of the Milky Way globular clusters based on their dynamics and various other information such as age, metallicity, horizontal-branch index. It revealed a collection of globular clusters with extragalactic origin, originating from the *"Gaia Sausage"*. Chapter 7 is a chemo-dynamical study showing the evidence for another early accretion event – the *"Sequoia"* – that contributed to the Milky Way's evolution. From multiple tracers in the Milky Way halo, including the stellar streams and globular clusters, chemo-dynamical signature of the *"Sequoia"* progenitor and its present-day remnants has been investigated. Chapter 8 summaries the thesis. Appendix A is an example of a conventional photometry based study of the tidal features that is imprinted on the stellar structure of the halo globular clusters (dynamical evolution due to the Milky Way's gravity). It reports the discovery of the most distant cold streams known so far, associated with outer halo globular clusters.

Chapter 2

Milky Way Halo in Action Space

G. C. Myeong[1], N. W. Evans[1], V. Belokurov[1], J. L. Sanders[1] and S. E. Koposov[1,2]

[1]Institute of Astronomy, University of Cambridge, Madingley Road, Cambridge CB3 0HA, United Kingdom

[2]McWilliams Center for Cosmology, Department of Physics, Carnegie Mellon University, 5000 Forbes Avenue, Pittsburgh PA 15213, USA

Abstract

We analyse the structure of the local stellar halo of the Milky Way using $\sim 60\,000$ stars with full phase space coordinates extracted from the SDSS–*Gaia* catalogue. We display stars in action space as a function of metallicity in a realistic axisymmetric potential for the Milky Way Galaxy. The metal-rich population is more distended towards high radial action J_R as compared to azimuthal or vertical action, J_ϕ or J_z. It has a mild prograde rotation ($\langle v_\phi \rangle \approx 25 \mathrm{km\,s^{-1}}$), is radially anisotropic and highly flattened with axis ratio $q \approx 0.6 - 0.7$. The metal-poor population is more evenly distributed in all three actions. It has larger prograde rotation ($\langle v_\phi \rangle \approx 50\ \mathrm{km\,s^{-1}}$), a mild radial anisotropy and a roundish morphology ($q \approx 0.9$). We identify two further components of the halo in action space. There is a high energy, retrograde component that is only present in the metal-rich stars. This is suggestive of an origin in a retrograde encounter, possibly the one that created the stripped dwarf galaxy nucleus, ω Centauri. Also visible as a distinct entity in action space is a resonant component, which is flattened and prograde. It extends over a range of metallicities down to [Fe/H] ≈ -3.

[0]Remark: The work presented in this Chapter has been published in Myeong et al. (2018c). I conceived this project and was responsible for the data processing and analysis. My supervisors, N. Wyn Evans and Vasily Belokurov, made an invaluable contribution by consulting and reformatting the first draft into a more logical presentation. Jason L. Sanders and Sergey E. Koposov also provided priceless consultation.

It has a net outward radial velocity $\langle v_R \rangle \approx 12\,\mathrm{km\,s^{-1}}$ within the Solar circle at $|z| < 3.5$ kpc. The existence of resonant stars at such extremely low metallicities has not been seen before.

2.1 Introduction

Samples of halo stars near the Sun provide us with accessible documentation on the early history of the Galaxy. But, like medieval palimpsests, the manuscript pages have been overwritten. Dissipative events, such as the assembly of the Galactic disk, and dissipationless processes, such as phase-mixing in the time-evolving Galactic potential, make the text difficult to read. Nonetheless, the spatial distribution, kinematics and chemistry of local halo stars provides us with important evidence on the nature and timescale of events in the early history of the Galaxy, if we could but decode and interpret it.

Actions are invariant under slow changes (e.g., Goldstein and Poole, 1980). They have often been suggested as the natural coordinates for galactic dynamics (Binney, 1987; Binney and Spergel, 1982), in which of course the potential is evolving in time (though possibly not slowly). One of the advances over the last few years has been the development of fast numerical methods to compute actions in general axisymmetric potentials (Binney, 2012; Bovy, 2015; Sanders and Binney, 2016). For the first time, this allows the study of the local halo in action space using realistic Galactic potentials comprising disks (both stellar and gas), halo and bulge (McMillan, 2017). The only other work known to us that displays the local halo in action space is the pioneering paper of Chiba and Beers (2000). These authors worked with a much smaller sample of stars (~ 1000) and out of necessity used a global Stäckel potential as a model of the Galaxy, as their work predated fast numerical action evaluators.

In this Chapter, we map the halo stars in action space using a new dataset, the SDSS–*Gaia* catalogue. This has six-dimensional phase space information for 62 133 halo stars, an order of magnitude larger than previous studies of the local halo. We use this new dataset, coupled with the recent advances in action evaluation, to provide new maps of the local halo in action space, which graphically illustrate the dichotomy between the metal-rich and metal-poor stars. We identify two new components of the halo. First, there is a high energy retrograde component that is limited to the metal-rich stars. Although retrograde stars have been identified before (Helmi et al., 2017; Majewski et al., 2012), we show here that they are largely restricted to metallicities in the range $-1.9 < \mathrm{[Fe/H]} < -1.3$. Second, we provide strong evidence for the existence of a resonant component. It is present across all metallicities, and it has a strong spatial dependence, which satisfies the characteristics of a dynamically induced resonance. This resonance may be linked to a well-known resonance in disk stars, which causes the Hercules Stream. The presence of resonant stars at such low

metallicities has not been seen before. We conclude with a discussion of how these findings are related to fundamental events in the Galaxy's early history.

2.2 The SDSS–*Gaia* Catalogue

The main SDSS–*Gaia* catalogue was constructed by Sergey Koposov and contains all SDSS stars down to $r = 20.5$. The catalogue was made by recalibrating the Sloan Digital Sky Survey (SDSS) astrometric solution, and then obtaining proper motions from positions in the *Gaia* Data Release 1 (DR1) Source catalogue (Brown et al., 2016; Gaia Collaboration et al., 2016) and their recalibrated positions in SDSS (see e.g., de Boer et al., 2018; Deason et al., 2017, for more details). The individual SDSS–*Gaia* proper motions have statistical errors typically ~ 2 mas yr^{-1}, or $\sim 9.48D$ km s^{-1} for a star with heliocentric distance D kpc. We work here mainly with the subsample of main sequence stars and blue horizontal branch stars with available spectroscopic measurements, in heliocentric distances of $\lesssim 10$ kpc. The spectroscopic measurements such as radial velocities and metallicities are obtained from SDSS DR9 spectroscopy (Ahn et al., 2012) or the crossmatch with LAMOST DR3 (Luo et al., 2015). Finally, photometric parallaxes for stars such as main-sequence turn-offs (MSTOs) or blue horizontal branch stars (BHBs) can be added using the formulae in Ivezić et al. (2008) and Deason et al. (2011b) to give samples with the full six-dimensional phase space coordinates.

The SDSS–*Gaia* catalogue provides one of the most extensive catalogues of halo stars with positions and kinematics, albeit without an easily calculable selection function. This means that some stellar orbits are not properly represented (such as stars with low-J_R and low-J_z orbits in small Galactocentric radius), but this will not change the gross morphological features we describe. The actions and energy of each star are estimated using the numerical method of Binney (2012) and Sanders and Binney (2016) together with the potential of McMillan (2017). The latter also provides the circular speed at the Sun as 232.8 kms^{-1}, whilst for the Solar peculiar motion we use the most recent value from Schönrich et al. (2010), namely $(U,V,W) = (11.1, 12.24, 7.25)$ kms^{-1}. Quality cuts and the disk-halo separation employed by Myeong et al. (2018a), together with an additional cut on distance error < 2.5 kpc, are used to clean the sample. The mode of the distance error is ~ 0.32 kpc. As a result, we obtain a sample of 62 133 halo stars (61 911 MSTO stars and 222 BHB stars; 59 811 stars with SDSS DR9 and 2 322 stars with LAMOST DR3 spectroscopy) with full six-dimensional phase space information, actions and energy (see Myeong et al., 2018a; Williams et al., 2017, for more details on the cuts and the sample). The metallicity distribution of the halo stars shows evidence of at least two subpopulations (see e.g., Figure 1 of Myeong et al., 2018a). A

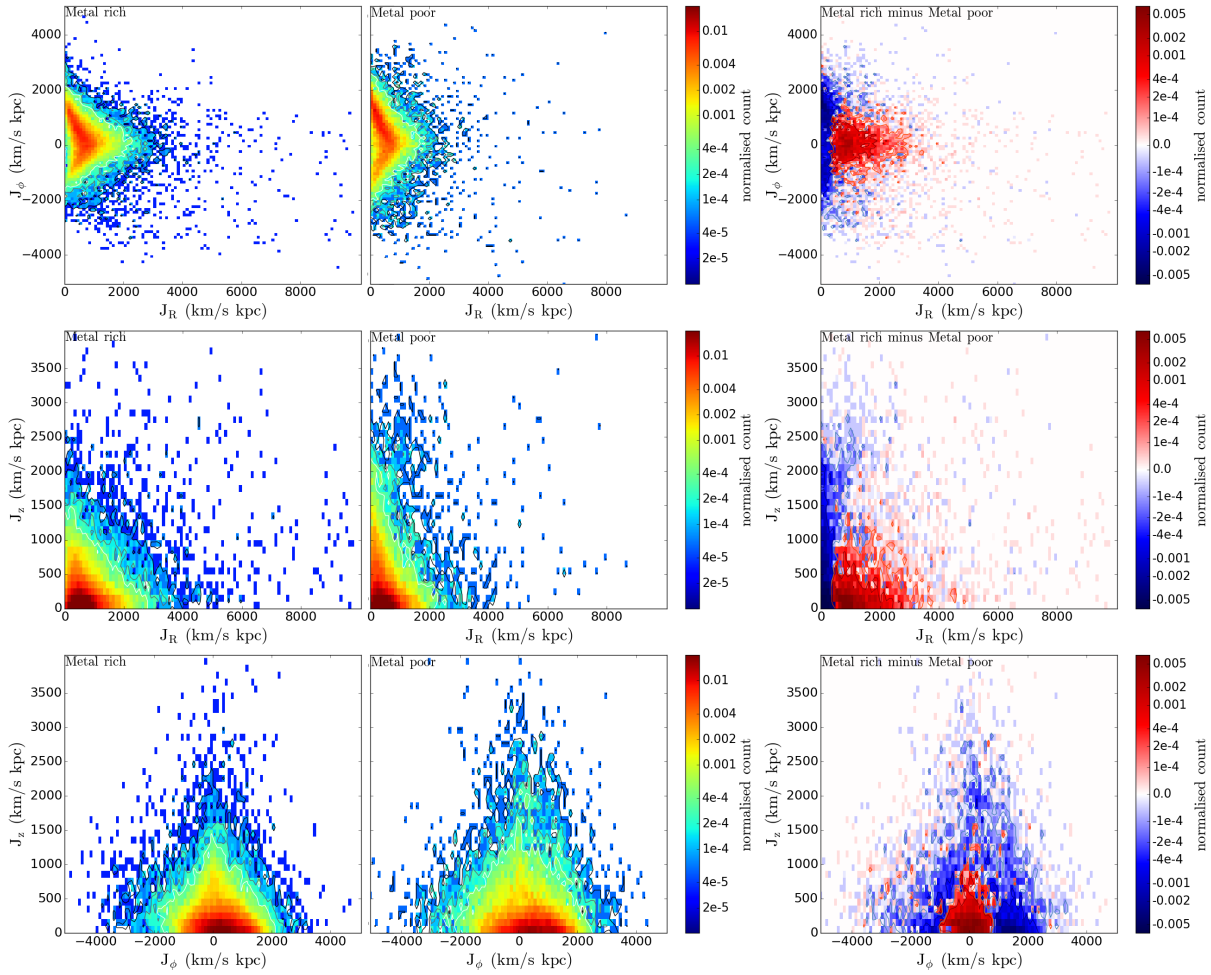

Fig. 2.1 Histograms of the stellar halo in action space (J_R, J_ϕ), (J_R, J_z) and (J_ϕ, J_z) split into metal-rich (left column, $-1.6 <$ [Fe/H] < -1.1) and metal-poor (middle column, $-2.9 <$ [Fe/H] < -1.8). The right column displays the difference, with red showing an excess of metal-rich, blue an excess of metal-poor stars. Notice (i) the metal-rich stars are tightly clustered around $J_\phi \approx 0$ and are much more extended in J_R, and (ii) the metal-poor stars have prograde rotation ($\langle J_\phi \rangle > 0$) and a more isotropic distribution in action space.

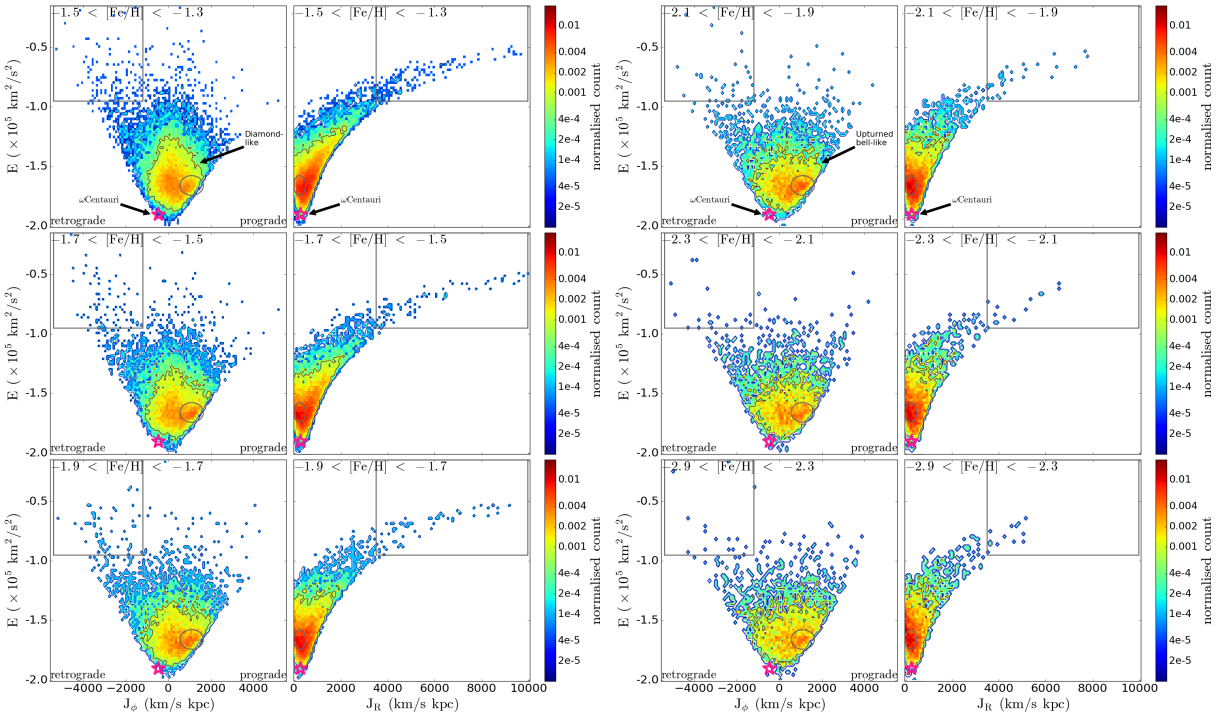

Fig. 2.2 The distribution of halo stars in energy-action space or (J_ϕ, E) and (J_R, E) space, split according to six metallicity bins from $-2.9 <$ [Fe/H] < -1.3. As we move from the most metal-rich to the most metal-poor, notice that (i) the distribution in radial action becomes more compact as the tail melts away by [Fe/H] ≈ -2.0, (ii) the diamond-like shape of the contours in (J_ϕ, E) changes gradually into an upturned bell-like shape, and (iii) the high energy, retrograde stars (marked by rectangular boxes in the left panels) and the high energy, eccentric stars (boxes in the right panels) gradually disappear by [Fe/H] ≈ -1.9, (iv) there is a distinct prograde component at $J_\phi \approx 1100$, $J_R \approx 150$ km s^{-1} kpc, $E \approx -1.6$ km^{2}s^{-2} (marked by ellipses), which is present at all metallicities. The location of ω Centauri is shown by a pink star.

Gaussian Mixture model (GMM) from the `Scikit-learn` (Pedregosa et al., 2011)[1] based on metallicity suggests the subdivision of the halo sample at [Fe/H] ≈ -1.67, with 37 670 metal-rich and 24 463 metal-poor halo stars.

2.3 Characteristics of the Halo in Action Space

2.3.1 The Rich and the Poor

We begin by showing the halo stars in action space (J_R, J_ϕ, J_z). For illustration, we show a metal-rich $(-1.6 <$ [Fe/H] $< -1.1)$ and metal-poor $(-2.9 <$ [Fe/H] $< -1.8)$ sample, together

[1] http://scikit-learn.org

with the difference between them in Fig. 2.1. The stratification on linear combinations of the actions suggested by Williams and Evans (2015) and Posti et al. (2015) is discernible in the triangular shapes of the contours in the left and centre panels. However, the metal-rich sample is clearly much more distended toward high J_R as compared to J_ϕ or J_z. This is most evident in the difference plot in the rightmost plot of Fig. 2.1, in which the red is preponderant at large values of J_R, and at low values of J_ϕ and J_z. The presence of abundant high eccentricity stars indicates that the population is radially anisotropic, whilst the narrow spread in J_z suggests the population is also flattened. In contrast, the metal-poor sample is distributed more equally in all three actions. The blue is preponderant at high J_z and reaches out to larger values of J_ϕ in the rightmost column of Fig. 2.1. This suggests it is rounder and has a mild net prograde rotation. Although correlations between kinematics and metallicities of halo stars have been reported before (e.g., Beers et al., 2012; Chiba and Beers, 2000; Deason et al., 2011a; Hattori et al., 2013), our pictures of the halo in action space provide a dramatic illustration of the dichotomy between the metal-rich and metal-poor stars.

Clearer details can be uncovered by slicing the halo into a sequence of smaller metallicity bins, as in Fig. 2.2. For the most metal-rich stars, the contours in (J_ϕ, E) space at high energy are noticeably "pointy". There is a tight distribution around $J_\phi \approx 0$ km s^{-1} kpc, again indicating the presence of many stars moving on nearly radial orbits. In general, the contours in the metal-rich panel ([Fe/H] > -1.5) are diamond-like in (J_ϕ, E) space, while they resemble an up-turned bell for the metal-poor([Fe/H] < -2.1). Related to this, the metal-rich sample in (J_R, E) space is skewed strongly toward high J_R, while in contrast, the metal-poor sample shows much less spread toward high J_R. In fact, in the more metal-poor panels ($-2.9 <$ [Fe/H] < -1.9), the bulk of the distribution (coloured red) shows the reverse trend of decreasing J_R with increasing energy E.

The metal-rich stars comprise a radially anisotropic and flattened population. The highest energy and most metal-rich stars are strongly retrograde, but the bulk of the population is at lower energies and shows mild prograde rotation. The metal-poor stars form a rounder population. This is also suggested by the broader distribution in J_z in Fig. 2.1. The kinematics are more isotropic, and there is significant prograde rotation. To obtain an idea of the three-dimensional shape, we study their kinematics. Properly speaking, we should decompose the distribution into components in action space, much as Belokurov et al. (2018) do in velocity space. Here, we will simply assume that contamination is mild in the extremal metallicity bins. In the most metal-rich bin, the rotational velocity $\langle v_\phi \rangle = 25$ km s^{-1}, whilst the velocity dispersion tensor is radially anisotropic with $(\sigma_R, \sigma_\phi, \sigma_z) = (155, 77, 88)$ km s^{-1}. So, the ratio of the horizontal to the vertical components of the kinetic energy tensor is ≈ 4.0. This is equal to the ratio of horizontal to vertical components of the potential energy tensor via

the virial theorem. It can be used to calculate the intrinsic shape, as advocated in Agnello and Evans (2012). Using their Figure 1, we see that the axis ratio of the density contours of the metal-rich population is $q \approx 0.6$ - 0.7, depending only modestly on the radial density profile. By contrast, in the most metal-poor bin, the rotational velocity is $\langle v_\phi \rangle = 49$ km s^{-1}, whilst the velocity dispersion tensor is close to isotropic with $(\sigma_R, \sigma_\phi, \sigma_z) = (125, 114, 110)$ km s^{-1}. This gives an axis ratio for the population of $q \approx 0.9$, so that the density contours are very round. These calculations assume that the total Galactic potential (stars plus dark matter) is spherical. Any flattening in the total potential will result in the computed axis ratios becoming flatter.

2.3.2 The Retrograde Stars

Marked by rectangular boxes in the panels of Fig. 2.2 are the general location of the high energy (e.g., $E > -1.1 \times 10^5$ km^{2}s^{-2}), retrograde ($J_\phi < 0$) stars. The box is well-populated in the metal-rich panels (e.g., [Fe/H] > -1.9), but sparsely populated in the metal-poor. These metal-rich, high energy stars have large radial action J_R as well, indicating a highly eccentric, retrograde population. This trend diminishes with decreasing metallicity and the metal-poorer panels (e.g., [Fe/H] < -1.9) show a more evenly balanced J_ϕ distribution of high energy stars. In addition, irrespective of the sign of J_ϕ, there are noticeably more stars with very high energy (e.g., $E > -0.75 \times 10^5$ km^2 s^{-2}) in the metal-rich panels of Fig. 2.2 than the metal-poor. The overdensity of retrograde high energy stars is evidence of a considerable (retrograde) merger or accretion event in the past (e.g., Norris and Ryan, 1989; Quinn and Goodman, 1986).

2.3.3 The Resonant Stars and the Hercules Stream

The panels also show evidence of a prograde component at around $J_\phi \approx 1100$, $J_R \approx 150$ km s^{-1} kpc, $E \approx -1.6 \times 10^5$ km^{2}s^{-2}, which is present at all metallicities as a overdense clump distinct from the general distribution. The component is marked by an ellipse in the panels of Fig. 2.2. We fit a Gaussian with a flat background to isolate this substructure and find a component with mean and dispersion $\langle J_\phi^{\rm C} \rangle \approx 1100$ km s^{-1} kpc and $\sigma_{J_\phi}^{\rm C} \approx 320$ km s^{-1} kpc. It is comprised of stars moving on disk-like prograde orbits with intermediate energies. Surprisingly, these stars show a noticeable positive $\langle v_R^{\rm C} \rangle \approx 12$ km s^{-1}, so that they have a net outward motion in the Galactic rest frame. This is illustrated in the leftmost panel of Fig. 2.3. The positive $\langle v_R \rangle$ signal comes mostly from low Galactic latitudes. The low latitude stars between $|z| < 3.5$ kpc (magenta) show positive mean $\langle v_R \rangle$ signatures at the same J_ϕ range that resembles the signal from the whole sample (black). In contrast, the high latitude stars

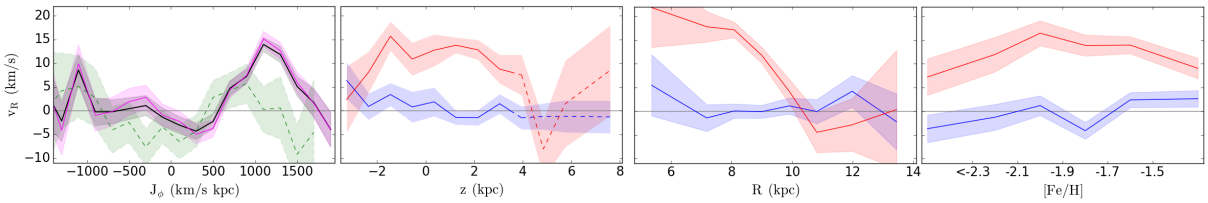

Fig. 2.3 The Outward Moving Stars. Leftmost: The behaviour of the mean radial velocity $\langle v_R \rangle$ as a function of J_ϕ for stars with $|z| < 3.5$ kpc (magenta), as compared to the whole sample (black). All show a signal of positive $\langle v_R \rangle$ at $J_\phi \approx 1100$ km s^{-1} kpc. However, the high latitude stars ($|z| > 3.5$ kpc) shown in green do not contribute to the signal. Center and Rightmost: The panels show the trends in $\langle v_R \rangle$ of the group selected by Gaussian fitting in Sec. 2.3.3 (red) and the rest (blue) against the Galactic position and metallicity. The selected stars with $|z| < 3.5$ kpc (full lines) are the main contributors to the outward moving population. There is no clear correlation with metallicity [Fe/H], but the stars are mainly found interior to the Solar circle. For all panels, the shaded region around each line indicates the corresponding standard error.

with $|z| > 3.5$ kpc (green) show close to zero mean $\langle v_R \rangle$ across the J_ϕ range. The magnitude of positive mean $\langle v_R \rangle$ is significant compared to the corresponding standard error.

We select stars with $\langle J_\phi^{\rm C} \rangle \pm 1.25\sigma_{J_\phi}^{\rm C}$. The remaining panels of Fig. 2.3 show the $\langle v_R \rangle$ trend of this selected group (red) and the rest (blue). The solid and dashed lines indicate the low and high latitude stars for each group (separation at $|z| = 3.5$ kpc). Notice the clear difference in the magnitude of $\langle v_R \rangle$ between the selected stars and the rest in various distributions. We also note that the signal drops by an order of magnitude at or near the solar radius and thereafter is close to zero. Interestingly, there is no clear metallicity dependency as the signal remains at a similar magnitude across the metallicity range. Taken together, these facts strongly suggest the source of the signal is dynamical in origin, namely a resonance. This is the first time that a resonance has been identified in such metal-poor stars. The selected stars at low Galactic latitude have $(\langle v_R^{\rm S} \rangle, \langle v_\phi^{\rm S} \rangle, \langle v_z^{\rm S} \rangle) = (12.2, 140.3, 3.0)$ km s^{-1}. These values are indicative, as the selection is crude and probably blended with the other halo populations. However, the value of the mean rotational velocity $\langle v_\phi^{\rm S} \rangle$ suggests that this component may be associated with the thick disk.

The outward mean radial velocity suggests an association with the Hercules stream, which is also moving outward and is located interior to the Solar circle. Stream is a slight misnomer, as the Hercules stream is really a co-moving group of stars of dynamical origin, induced probably by the Outer Lindblad Resonance of the Galactic bar (Dehnen, 2000). The Hercules stream has a complex structure with outward $\langle v_R \rangle$ somewhat larger than we measure (Antoja et al., 2014; Hunt et al., 2018), though this is likely accounted by contamination in our sample.

It has previously been detected in stars with metallicities $-1.2 <$ [Fe/H] < 0.4 (Bensby et al., 2007). However, we see from the panels in Fig. 2.3 that – if our identification with the Hercules stream is correct – then it is detectable right down to [Fe/H] ≈ -2.9 and so is present in stars of metallicity normally associated with thin disk, thick disk and halo.

2.4 Discussion

There are a number of possible explanations of the properties of the Milky Way stellar halo in action space. The highly flattened metal-rich component is almost certainly the residue of the disruption of accreted dwarf galaxies. The strong radial anisotropy already suggests that the progenitors of this component fell in from large distances. Infall of satellites with random alignments tends to isotropize the dispersion tensor. The easiest way to maintain such extreme radial anisotropy is through the infall of one satellite, or group infall of multiple satellites, from a preferred direction (Belokurov et al., 2018). The eccentric halo substructure discovered by Myeong et al. (2017a) using the Tycho–*Gaia* Astrometric Solution (TGAS) crossmatched with RAVE may well be part of this component. The origin of the rounder, metal-poor component is less clear. The isotropic kinematics of this population, together with its roughly spherical shape and mild prograde rotation, are reminiscent of the halo globular clusters. If these objects were once much more massive than the entities surviving today (Schaerer and Charbonnel, 2011), then they may have contributed most of the stars in the metal-poor component of the halo. Alternatively, the accretion of low mass dwarfs along random directions may have built the metal-poor component. Another contributor could be levitation (Sridhar and Touma, 1996). The growing thin disk can trap stars in the 2:2 resonance and lift them to higher latitude. A pre-existing structure of metal-poor stars could be fattened by such a process.

In addition to these two well-known components, we have identified a high energy subpopulation that is very strongly retrograde. Helmi et al. (2017) noticed that a high fraction of stars more loosely bound than the Sun are retrograde in the local TGAS sample. Here, we have shown that these stars are overwhelmingly metal-rich, and that the feature does not extend to stars with [Fe/H] below -1.9. A candidate for a retrograde invader exists in the anomalous globular cluster ω Centauri, long suspected to be the nucleus of a stripped dwarf galaxy (Bekki and Freeman, 2003). It is known to be on a retrograde orbit. Majewski et al. (2012) showed, on the basis of chemodynamical evidence, that it is a major source of retrograde halo stars in the inner Galaxy. The progenitor of ω Centauri has to be massive, so that the satellite is dragged deep into the potential of the Milky Way and placed on its present low energy orbit, which is marked by a purple star on Fig. 2.2. While ω Centauri is on an

eccentric orbit, it is considerably retrograde as well, given its present-day energy. Estimates of its initial mass are typically $\sim 10^{10} M_{\odot}$(Tsuchiya et al., 2003; Valcarce and Catelan, 2011), while its present-day mass is only $5 \times 10^{6} M_{\odot}$ (Meylan et al., 1995). Its disruption must have sprayed high energy retrograde stars throughout the inner Galaxy, even though it is on a low energy orbit now.

Finally, action space has allowed us to trace a new, resonant component down to very low metallicities. This component is also flattened and has prograde rotation with a mean of $\langle v_{\phi} \rangle \approx 140$ km s^{-1}. Its most unusual feature is a small, but statistically significant, outward mean radial velocity ($\langle v_R \rangle \approx 12$ km s^{-1}). This is present across the swathe of metallicities in our sample, namely $-2.9 <$ [Fe/H]< -1.3, yet is spatially restricted to just within the Solar circle and at $|z| < 3.5$ kpc. The confinement of this prograde feature to a range in Galactocentric radii is unusual and strongly supports a resonance origin. A link with the Hercules stream in disk stars (e.g., Hunt et al., 2018) seems likely.

There are a number of ways the forthcoming *Gaia* Data Release 2 (DR2) can confirm our picture. First, the crossmatches with radial velocity surveys will have well-defined selection functions. This will allow use of halo distribution functions (Posti et al., 2015; Williams and Evans, 2015) to separate the populations in action space as a function of metallicity and hence better characterise their properties. Secondly, the SDSS–*Gaia* catalogue undersamples low latitude stars and so coverage of such substructures is patchy. With *Gaia* DR2, stars with kinematics akin to the Hercules stream can be traced as a function of location throughout the Galaxy. Thirdly, *Gaia* colours, as well as spectroscopic follow-up to obtain alpha-abundances, may confirm the origin of the halo components. For example, if the high energy, retrograde component comes from ω Centauri, the stripped stars in action space must be trackable to their present position through chemodynamical data. Fourthly, the improved proper motions may even permit the use of angles (as opposed to actions) in studying resonances throughout the halo.

Chapter 3

A Halo Substructure in *Gaia* Data Release 1

G. C. Myeong[1], N. W. Evans[1], V. Belokurov[1], S. E. Koposov[1,2] and J. L. Sanders[1]

[1]Institute of Astronomy, University of Cambridge, Madingley Road, Cambridge CB3 0HA, United Kingdom

[2]McWilliams Center for Cosmology, Department of Physics, Carnegie Mellon University, 5000 Forbes Avenue, Pittsburgh PA 15213, USA

Abstract

We identify a halo substructure in the Tycho *Gaia* Astrometric Solution (TGAS) dataset, cross-matched with the RAVE-on data release. After quality cuts, the stars with large radial action ($J_R > 800$ kms^{-1} kpc) are extracted. A subset of these stars is clustered in longitude and velocity and can be selected with further cuts. The 14 stars are centred on $(X,Y,Z) \approx (9.0,-1.0,-0.6)$ kpc and form a coherently moving structure in the halo with median $(v_R, v_\phi, v_z) = (167.33, 0.86, -94.85)$ kms^{-1}. They are all metal-poor giants with median [Fe/H] $= -0.83$. To guard against the effects of distance errors, we compute spectrophotometric distances for the 8 out of 14 stars where this is possible. We find that 6 of the stars are still comoving. These 6 stars also have a much tighter [Fe/H] distribution ~ -0.7 with one exception ([Fe/H] = -2.12). We conclude that the existence of the comoving cluster

[0]Remark: The work presented in this Chapter has been published in Myeong et al. (2017a). I conceived this project and was responsible for the data acquisition and analysis. My supervisors, N. Wyn Evans and Vasily Belokurov, made an invaluable contribution by consulting and reformatting the first draft into a more logical presentation. Sergey E. Koposov and Jason L. Sanders also provided priceless consultation.

is stable against changes in distance estimation and conjecture that this is the dissolving remnant of a long-ago accreted globular cluster.

3.1 Introduction

Over the last decade, many streams have been identified in the stellar halo of the Milky Way, usually as overdensities of main-sequence turn-off stars in resolved star maps from wide area photometric surveys (see e.g., Belokurov et al., 2006b; Grillmair, 2009; Newberg and Carlin, 2016). An alternative method is to identify substructure kinematically as samples of stars with similar chemistry moving in a distinct and coherent way. Though less widely used, this has had some striking successes, including the famous identification of the Sagittarius dwarf (Ibata et al., 1994), the halo stream found by Helmi et al. (1999) in *Hipparcos* data, and the globular cluster streams found by Smith et al. (2009) in Sloan Digital Survey Stripe 82 data.

The first data releases (DR1) of the *Gaia* satellite (Brown et al., 2016; Gaia Collaboration et al., 2016) provides us with a new vista of the Solar neighbourhood. The primary astrometric catalogue in *Gaia* DR1 is TGAS (Tycho *Gaia* Astrometric solution), which uses data from Tycho-2 (Høg et al., 2000) to provide a 30 year baseline for astrometric calculations. It has 2 057 050 entries. When cross-matched with RAVE-on (Casey et al., 2017; Kunder et al., 2017), this gives a catalogue of 180 929 stars with full six-dimensional phase space information, as well as associated stellar spectral quantities. TGAS cross-matches are also possible with LAMOST (Luo et al., 2015) and APOGEE (Anders et al., 2014), though they are somewhat smaller in size with 78 579 and 12 061 entries respectively. Not all the entries in the three cross-matched catalogues are distinct. When stars overlap in the surveys, we take the data with the smallest relative error in radial velocity. This yields a final master catalogue of 268 588 stars where the RAVE-on contribution is 180 454 stars. The master catalogue is a natural arena in which to search for kinematic substructure.

This Chapter identifies a group of stars moving on strongly radial orbits in the TGAS cross-matched master catalogue. The stars have similar metallicities, and the simplest explanation of their unusual kinematics is that they are the residue of an ancient halo structure. Section 3.2 describes our treatment of the data and extraction of the substructure stars. Section 3.3 discusses the selected stars, together with estimates for the age and future evolution of the substructure.

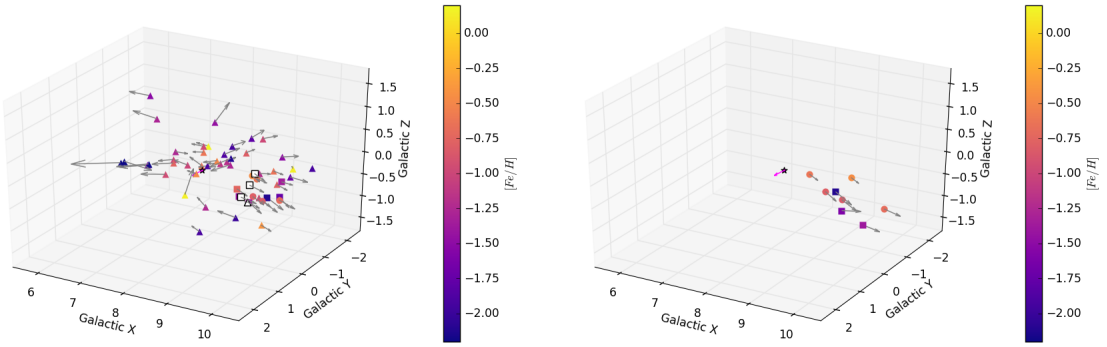

Fig. 3.1 Left: The spatial structure of the 56 stars satisfying the quality cuts and with $J_R > 800$ kms^{-1} kpc. Stars are colour-coded according to metallicity if known, whilst the arrow indicates the magnitude and direction of the spatial velocity. There is a clear clustering of stars at $(X,Y,Z) \approx (9.0,-1.0,-0.6)$ kpc, which have radial motion dominating their total velocity. The 14 stars that may belong to the comoving cluster are shown as circles or squares, while the remainder are shown as triangles. Right: Using spectrophotometric distances, the 14 candidate members are re-examined. 5 stars (circles) are retained as confirmed members as both their distances and metallicities are similar. Of the remaining 9 stars, 6 do not have spectrophotometric distances. However, 2 are not comoving according to the new distances, whilst 1 is comoving but has markedly different metallicity. These 3 objects are marked with squares. Finally, the Sun is marked on both plots as a star.

3.2 Extraction of the Member Stars

First, the proper motions are converted to velocities using the unbiased, inferred distance estimates of Astraatmadja and Bailer-Jones (2016). To ensure a high quality sample, we impose a cut that the error in the radial velocity $\varepsilon_{\rm RV} < 10$ kms^{-1}, the error in the total velocity $\varepsilon_{\rm Vtot} < 25$ kms^{-1} and the relative error in the total velocity is $< 10\%$. This reduces the sample to 73 268 stars (66 891 using the RAVE-on measurements, the remainder from LAMOST and APOGEE). We now use the Galactic potential `MWPotential2014` in Bovy (2015) to compute the radial and azimuthal actions (J_R and J_ϕ, using the adiabatic approximation e.g. Binney, 2010). The bulk of the stars are moving on nearly circular orbits in the thin disk. Nonetheless, there are extensions of stars in the high action regime, which are predominantly metal-poor and are moving on eccentric orbits.

We retain only stars with a radial action $J_R > 800$ kms^{-1} kpc. This cut leave us with 56 stars moving on predominantly eccentric orbits (41 are from the RAVE-on crossmatch, 15 from the other crossmatches). Fig. 3.1 shows the spatial distribution of all these stars, colour-coded according to metallicity (if known), with arrows representing their velocity vectors. The existence of a comoving cohort of stars at $(X,Y,Z) \approx (9.0,-1.0,-0.6)$ kpc

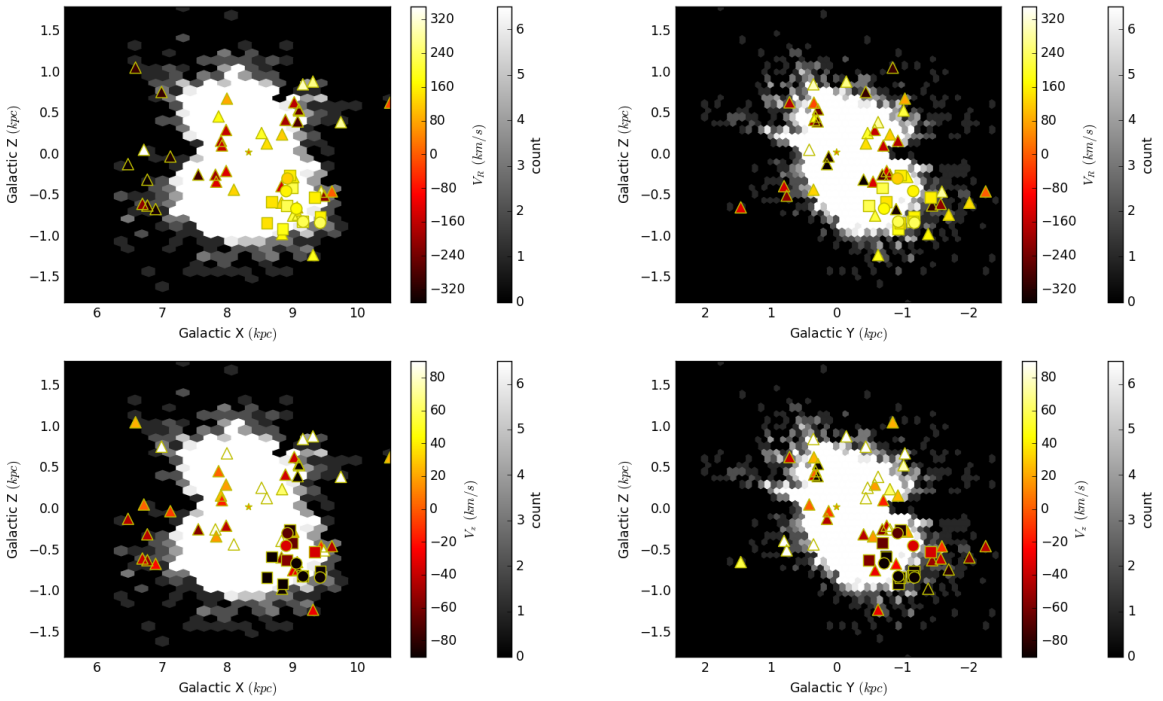

Fig. 3.2 Locations of the 56 high-quality stars with $J_R > 800$ kms^{-1} kpc in the Galactic (X,Y) and (Y,Z) planes using the Astraatmadja and Bailer-Jones (2016) distances. Circles (5 confirmed members) and squares (9 possibles) show stars associated with the comoving clump, whilst triangles show the rejected stars. Symbols are coloured according to the radial velocity (upper panels) or vertical velocity (lower panels). The colours of the symbols show that the stars of interest have quite similar velocities, both vertical and radial.

RAVE ID	RA	DEC
J063314.9-284345	98.312	-28.729
J062653.3-355032	96.722	-35.842
J052906.3-240844	82.276	-24.145
J050209.4-235127	75.539	-23.858
J050519.6-264950	76.332	-26.831

Table 3.1 RAVE identifiers, as well as right ascension and declination, for the 5 confirmed members.

is evident. This is confirmed by a visual inspection of histograms of velocity components resolved with respect to the cylindrical polar coordinate (v_R, v_ϕ, v_z), which betrays clear peaks corresponding to the comoving clump. To formalize their extraction, we perform 2.5σ clipping based on v_R, v_ϕ, v_z and orientation angle Ψ, individually. Here, $\Psi = \arctan(-V/U)$, where U and V are the Galactocentric Cartesian velocity components along the X and Y directions. So, Ψ is the angle of star's motion in Galactic plane. Then, only those stars falling within the range of the median $\pm 2.5\sigma$ (measured after the clipping) are retained. This process is repeated until no further stars are rejected. This leaves a set of 14 stars possibly belonging to a comoving clump with strongly radial orbits. They are shown as circles or squares in the left panel of Fig. 3.1, color-coded according to metallicity. All these stars lie in the TGAS and RAVE-on crossmatch.

For this set of 14 stars, we measured the median and σ (standard deviation) in each (U,V,W) component. To ensure that no possible members have been missed, we returned to the original sample of 73 268 and searched for all stars in the (U,V,W) velocity box bounded by the median $\pm 2\sigma$ in each velocity component. This covers a comparable but wider range then the 'minimum to maximum' range in each velocity component of the 14 initial stars, so it is wide enough to contain our initial sample and any others that may have some comparable motion. However, no further stars are identified as possible members.

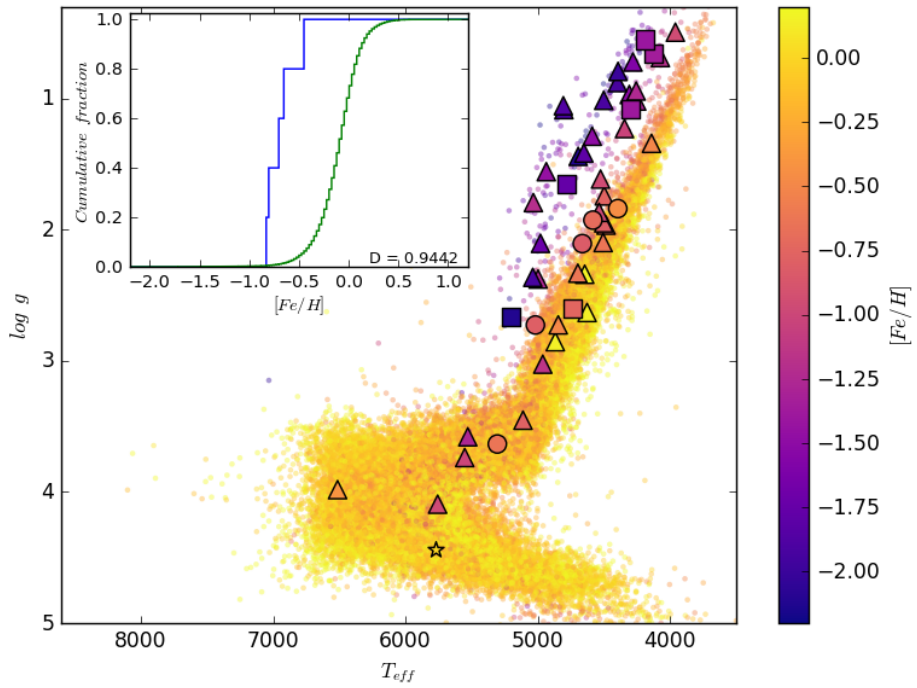

Fig. 3.3 Surface gravity versus effective temperature for all stars in the master catalogue with spectroscopic parameters. The 11 comoving stars with known metallicity are shown as circles (confirmed members) or squares (possibles), the remainder as triangles. The location of the Sun is shown as a star for reference. The inset shows the normalised cumulative histogram of [Fe/H] for the 5 secure comoving stars (in blue) and for the thin disk (in green). The D value for the KS-test indicates that the two distributions are very different.

	[Fe/H]	$\log g$	$T_{\rm eff}$ (K)	(X,Y,Z) (kpc)	(v_R, v_ϕ, v_z) (kms^{-1})	e	$R_{\rm apo}$ (kpc)	$R_{\rm peri}$ (kpc)	$z_{\rm max}$ (kpc)
Median	-0.83	1.93	4662	(9.00,-0.94,-0.62)	(167.33,0.86,-94.85)	0.940	12.79	0.40	3.50
Median Absolute Deviation	0.28	0.74	355	(0.15,0.21,0.18)	(21.47,10.18,30.67)	0.017	1.55	0.11	1.45
Median	-0.70	2.11	4662	(9.06,-0.94,-0.66)	(167.33,8.79,-94.86)	0.948	12.31	0.40	3.50
				(9.13,-0.90,-0.53)	(168.57,11.24,-72.96)	0.947	12.02	0.29	4.50
Median Absolute Deviation	0.10	0.27	268	(0.14,0.21,0.17)	(44.35,8.11,27.22)	0.011	1.98	0.13	1.69
				(0.21,0.37,0.25)	(52.23,1.38,7.13)	0.006	1.92	0.08	2.65

Table 3.2 Upper: The medians and median absolute deviations in spectroscopic and orbital properties of all 14 possible stars in the comoving group. Lower: The same, but for the subset of 5 stars that are unambiguous members. In this case, the velocities and orbital parameters are given first using Astraatmadja and Bailer-Jones (2016) distances, and then using spectrophotometric distances.

Astraatmadja and Bailer-Jones (2016) used a prior suitable for nearby disk stars and they caution that their distances may be underestimates when objects lie beyond 2 kpc from the Sun. Our comoving candidates have heliocentric distance ≈ 1.8 kpc, so it is prudent to cross-check our candidates with another different distance estimator. There are 8 RAVE-on stars among our candidates that satisfy recommendations advocated by Casey et al. (2017), namely they have `teff_sparv` < 8000 K, the RAVE spectral parameters c_1, c_2, c_3 reported as 'n' or normal, and a reduced $\chi^2 < 3$ as recorded by 'the Cannon' pipeline. For these stars, we can use the technique pioneered by Burnett and Binney (2010) to compute the spectrophotometric distance distribution folded with the TGAS parallax distribution for each star. Specifically, we use the PARSEC isochrones (Bressan et al., 2012) and the extinction map of Green et al. (2015) to obtain the probability distribution function of the distance given the spectroscopic parameters ($T_{\rm eff}$, $\log g$, [Fe/H]), apparent 2MASS magnitudes (J, H and K_s) and the TGAS parallaxes along with their associated uncertainties (or covariances where available). We adopt an identical prior to that used in Binney et al. (2014). The right panel of Fig. 3.1 shows the new view of the comoving candidates, Of the 8 stars with spectrophotometric distances, 5 have a common velocity and metallicity. We regard these as confirmed members and they are shown as circles. Their RAVE identifiers, as well as right ascensions and declination, are given in Table 3.1. There are 3 remaining stars, 2 of which are no longer comoving, and 1 of which is comoving but has a discrepant metallicity. We regard these as merely possible members, pending confirmation of the distance or metallicity, and they are shown as squares. In other words, we have 5 confirmed members and 9 possible members, including the stars without spectrophotometric distances.

In the panels of Fig. 3.2, the circles and squares show our selected clump or co-moving group, while the triangles are the rejected stars (but still possessing $\varepsilon_{\rm RV} < 10$ kms^{-1}, $\varepsilon_{\rm Vtot} < 25$ kms^{-1}, relative velocity error $< 10\%$ and $J_R > 800$ kms^{-1} kpc). The stars are colour-coded according to their radial and vertical velocities, so a coherent group stands out as a clump of objects with similar colouring. The significance of the comoving group above the background level can be measured in Galactocentric (X,Y), (X,Z) and (Y,Z) planes. The number of stars (with $\varepsilon_{\rm RV} < 10$ kms^{-1}, $\varepsilon_{\rm Vtot} < 25$ kms^{-1}, relative velocity error $< 10\%$ and $J_R > 800$ kms^{-1} kpc) in the comoving group region (drawn as an aperture that encloses the group) was compared with the number of stars in other regions (representing the background level) across the plane. The significance of the comoving group above the background level is 3.2σ, 7.2σ and 4.8σ for each Galactocentric (X,Y), (X,Z) and (Y,Z) planes respectively.

The comoving sample of 14 stars has median position $(X,Y,Z) = (9.00, -0.94, -0.62)$ kpc and velocity $(v_R, v_\phi, v_z) = (167.33, 0.86, -94.85)$ kms^{-1} in the Galactic rest frame. By integrating orbits in potential `MWPotential2014` from Bovy (2015), we obtain a median

apocentric distance of ~ 13 kpc and pericentric distance of ~ 0.4 kpc for stars in the clump. The high eccentricity (median $e = 0.940$) and low apocentric distances suggest that the clump may be the relic of an object that fell into the halo long ago and whose apocentric distance has been reduced by dynamical friction over a number of pericentric passages. These values are recorded in Table 3.2. where we also give the corresponding figures if the sample is restricted to just the 5 stars with confirmed membership.

Fig. 3.3 shows the spectroscopic properties of the stars. They are all metal-poor giants with median [Fe/H] $= -0.83$. By conducting a Kolmogorov-Smirnov test, we can verify that the metallicities are not consistent with being drawn from the thin disk ($D = 0.944$). This is illustrated in the inset to the figure. The medians and median absolute deviations in the spectroscopic quantities are also noted in Table 3.2. As the stars in the comoving clump are exclusively drawn from the RAVE survey, an immediate concern is that the footprint of the survey may affect the results. The RAVE footprint and the comoving clump are shown in Galactic coordinates in Fig. 3.4. The positions of the 14 stars are marked in red. The distribution of circles (confirmed members) is suggestive of a stream moving from upper left to lower right. The three squares (possibles) at $(\ell \approx 245^\circ, b \approx -40^\circ)$ then lie ~ 300 pc off the stream. This also hints that these three stars are less likely to be members of the structure. However, this is not conclusive as it is conceivable that a globular cluster stream could broaden over time. Note that the substructure does extend towards the edge of the RAVE footprint, and so it is conceivable that it may be larger than is apparent from the TGAS and RAVE cross-match.

3.3 Discussion and Conclusions

Using crossmatches of the Tycho *Gaia* Astrometric Solution (TGAS) with the Radial Velocity Experiment (RAVE-on), we have extracted a sample of 14 stars with unusual kinematics. The stars are all moving on strongly radial orbits and are clumped at $(X, Y, Z) \approx (9.0, -1.0, -0.6)$ kpc. The median eccentricity of the stars is 0.940.

We checked that this comoving group is resilient against distance errors. For 8 out of the 14 stars, it is possible to calculate spectrophotometric distances using the methods of Burnett and Binney (2010). 6 of the stars still show a comoving trend. These 6 stars also have a much tighter [Fe/H] distribution ~ -0.7 with one exception ([Fe/H] = -2.12). The median absolute deviation of [Fe/H] is 0.10. So, the motion, spatial location and metallicity of at least 5 stars are well confined in both distance estimates, suggesting that they are comoving and have a common origin.

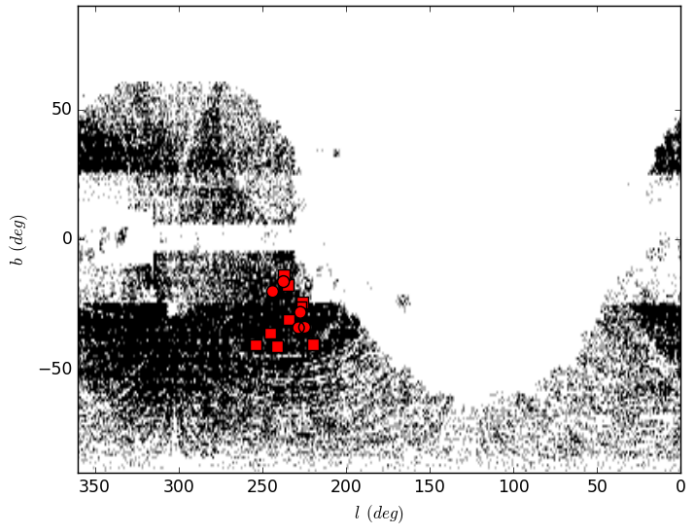

Fig. 3.4 The RAVE footprint in Galactic coordinates. The 14 comoving clump stars are shown as circles (confirmed members) or squares (possibles). As the edge of the footprint abuts the clump, there may be an extension of the substructure that is currently missing.

The simplest interpretation of this coherently moving substructure is that it is the residue of a long past accretion event. The small metallicity spread in the 5 secure members suggests that the progenitor was more likely to be a globular cluster than a dwarf galaxy. The comoving group may be identified with the nucleus of this disintegrating body. Naturally, we would expect tidal streams also to be present, but in an old accretion event, the surface density of stream material may be very low. Although some streams can be caused by resonance effects, such as the Hercules Stream (Dehnen, 2000) and some can be caused by interactions with perturbers, such as the Aquarius Stream (Casey et al., 2014), neither option seems likely here. Resonance effects usually give structures of modest eccentricity, as nearly circular orbits can usually couple most easily to the perturbation.

The large globular cluster ω Centauri has long been thought to be the remnant nucleus of an accreted dwarf galaxy (Freeman, 1993), as it shows evidence of multiple stellar populations with spreads in the age and metallicity (e.g. Villanova et al., 2007). If our comoving group is associated with ω Centauri, for example, by sharing a common progenitor, some clues may be found from stellar parameters or dynamics. RAVE DR4 (Kordopatis et al., 2013) provides an estimate of the age for 14 comoving group members. The mean age is 9.8 Gyr with standard deviation of 0.1 Gyr. The age-metallicity relation for ω Centauri presented by Villanova et al. (2014) shows some stars with metallicity and the age comparable to our comoving group stars, even though this estimated age is a relative age. Yet, the orbit of the comoving group appears to be highly eccentric with v_ϕ close to zero. It is ambiguous as to

whether the group is prograde or retrograde, while ω Centauri clearly has a less eccentric and retrograde orbit (Majewski, 2000). In addition, the estimated values of energy and angular momentum of the comoving group stars do not show a clear link with ω Centauri, suggesting that this comoving group is very unlikely to be associated with it.

Although there have already been searches for halo overdensities in the TGAS-RAVE cross-match by Helmi et al. (2017, herafter H17), the substructure identified in this Chapter appears to be new. It does not correspond to any of the overdensities labelled VelHel-1 to 9 in H17. As the underlying Galactic potential is different between H17 and this work, the estimated values of energy E of the stars are different. As H17 convert parallaxes to distances via the reciprocal rather than using the calculations of Astraatmadja and Bailer-Jones (2016) or using spectrophotometric distances, the azimuthal actions J_ϕ of the stars are also different. This affects the integrity of the substructures identified in H17, which we find to be indistinct and smeared out. As judged by the Tycho-IDs, there are only 4 stars in our substructure that overlap with H17, two in the VelHel-1 and 2 in VelHel-8. The claimed enhancements in H17 therefore do not appear to be related to our substructure, which is a coherent entity in configuration and velocity space.

Chapter 4

Halo Substructure in the SDSS-*Gaia* Catalogue: Streams and Clumps

G. C. Myeong[1], N. W. Evans[1], V. Belokurov[1], N. C. Amorisco[2,3] and S. E. Koposov[1,4]

[1]Institute of Astronomy, University of Cambridge, Madingley Road, Cambridge CB3 0HA, United Kingdom

[2] Max Planck Institute for Astrophysics, Karl Schwarzschild Strasse 1, D-85740 Garching, Germany

[3] Institute for Theory and Computation, Harvard Smithsonian Center for Astrophysics, 60 Garden Street, Cambridge, MA02138, USA

[4]McWilliams Center for Cosmology, Department of Physics, Carnegie Mellon University, 5000 Forbes Avenue, Pittsburgh PA 15213, USA

Abstract

We use the SDSS-*Gaia* Catalogue to identify six new pieces of halo substructure. SDSS-*Gaia* is an astrometric catalogue that exploits SDSS data release 9 to provide first epoch photometry for objects in the *Gaia* source catalogue. We use a version of the catalogue containing 245 316 stars with all phase space coordinates within a heliocentric distance of ~ 10 kpc. We devise a method to assess the significance of halo substructures based on their clustering in velocity space. The two most substantial structures are multiple wraps

[0]Remark: The work presented in this Chapter has been published in Myeong et al. (2018a). I conceived this project and was responsible for the data acquisition and analysis. My supervisors, N. Wyn Evans and Vasily Belokurov, made an invaluable contribution by consulting and reformatting the first draft into a more logical presentation. Nicola C. Amorisco provided model analogues (see Amorisco, 2017, for more details) for interpreting some of the results. Sergey E. Koposov also provided priceless consultation.

of a stream which has undergone considerable phase mixing (S1, with 94 members) and a kinematically cold stream (S2, with 61 members). The member stars of S1 have a median position of (X,Y,Z) = $(8.12,-0.22,2.75)$ kpc and a median metallicity of [Fe/H] $=-1.78$. The stars of S2 have median coordinates (X,Y,Z) = $(8.66,0.30,0.77)$ kpc and a median metallicity of [Fe/H] $=-1.91$. They lie in velocity space close to some of the stars in the stream reported by Helmi et al. (1999). By modelling, we estimate that both structures had progenitors with virial masses $\approx 10^{10} M_{\odot}$ and infall times $\gtrsim 9$ Gyr ago. Using abundance matching, these correspond to stellar masses between 10^6 and $10^7 M_{\odot}$. These are somewhat larger than the masses inferred through the mass-metallicity relation by factors of 5 to 15. Additionally, we identify two further substructures (S3 and S4 with 55 and 40 members) and two clusters or moving groups (C1 and C2 with 24 and 12) members. In all 6 cases, clustering in kinematics is found to correspond to clustering in both configuration space and metallicity, adding credence to the reliability of our detections.

4.1 Introduction

Lord Rutherford briskly asserted "All Science is either Physics or Stamp Collecting". The study of the stellar halo of the Milky Way has seen much philately over the last decade with the discovery of abundant streams and substructure (e.g., Belokurov et al., 2006b; Grillmair, 2009; Newberg and Carlin, 2016). These have usually been identified as overdensities from resolved star maps. Substructures remain kinematically cold and identifiable in phase space long after they have ceased to be recognizable in star counts against the stellar background of the Galaxy. In principle, searches in velocity space or in phase space are much more powerful than direct searches in configuration space. There are believed to be hundreds of accreted dwarf galaxies and globular clusters in the halo of the Milky Way which could be found through searches in velocity space.

In practice, kinematic data has been so fragmentary to date that such substructure searches have been difficult to perform. There have been some successes, such as the group of 8 stars in the Hipparcos data clumped in metallicity and phase space found by Helmi et al. (1999) or the discrete kinematic overdensities in Sloan Digital Sky Survey (SDSS) Stripe 82 identified by Smith et al. (2009). Nonetheless, given the ostensible power of the method, results have been meagre.

The advent of data from the *Gaia* satellite (Gaia Collaboration et al., 2016) is a pivotal moment for identifying the hundreds of partially mixed phase space structures that numerical simulations suggest should be present in the halo. Many of these have dissolved sufficiently

to fall below the surface brightness threshold of current imaging surveys, and thus will remain unnoticed without kinematic data from *Gaia*.

The first *Gaia* data release provided TGAS, or the Tycho-*Gaia* Astrometric Solution, which used the earlier Tycho catalogue as the first epoch for the astrometric solution (Brown et al., 2016). TGAS gives the proper motions and parallaxes of just over 2 million stars. Subsets of these stars are in ongoing radial velocity surveys such as LAMOST, RAVE or RAVE-on (Casey et al., 2017; Kunder et al., 2017; Luo et al., 2015). Already, claims of a coherently moving feature in velocity space (Myeong et al., 2017a) as well as over-densities in "integrals of motion space" (Helmi et al., 2017) have been made.

Cross-matches between TGAS and radial velocity surveys produce catalogues of $\sim$ 250 000 stars. These are primarily local samples, dominated by denizens of the local disk within 1 kpc. It would be advantageous to use a much larger and deeper sample of stars with full phase space information. Along with TGAS, *Gaia* data release 1 also comprised the *Gaia* source photometric catalogue, which provides the locations of $\sim 10^9$ sources. Koposov (2017, in prep.) recalibrated the SDSS astrometric solution and then obtained proper motions from *Gaia* positions and their recalibarted positions in SDSS. This catalogue is also discussed in some detail in Deason et al. (2017) and de Boer et al. (2018). The individual SDSS-*Gaia* proper motions have statistical errors typically ~ 2 mas yr^{-1}, or $\sim 9.48D$ km s^{-1} for a star with heliocentric distance D kpc. As the SDSS data were taken over a significant period of time, the error is primarily controlled by the time baseline. However, there are no systematic effects down to a level of $0.1-0.2$ mas yr^{-1} in the astrometry with regard to magnitude or colour (see e.g., Figure 2 of Deason et al., 2017), so this makes the SDSS-*Gaia* catalogue suitable for searching for large-scale velocity signatures corresponding to streams and substructures.

The depth of SDSS-*Gaia* enables us to search out to heliocentric distances of ~ 10 kpc, which is a substantial advantage over TGAS. Cross-matching SDSS-*Gaia* with spectroscopic surveys can add radial velocities. Finally, photometric parallaxes for stars such as main-sequence turn-offs (MSTOs) or blue horizontal branch stars (BHBs) gives samples with the full six-dimensional phase space coordinates. Although the SDSS-*Gaia* catalogue will be superseded in April 2018 by the next *Gaia* data release, it currently provides the best catalogue in which to search for halo substructure by kinematic means.

The overall aim of this activity is to constrain the fraction of halo stars in clumps and substructures. This is of great interest as it encodes the accretion history of the stellar halo and by extension of the Milky Way itself. Nonetheless, the optimum algorithms for substructure identification, as well as the best methodologies to match detected substructures to disrupting subhalos in numerical simulations, are ripe for exploration with SDSS-*Gaia*. Ultimately,

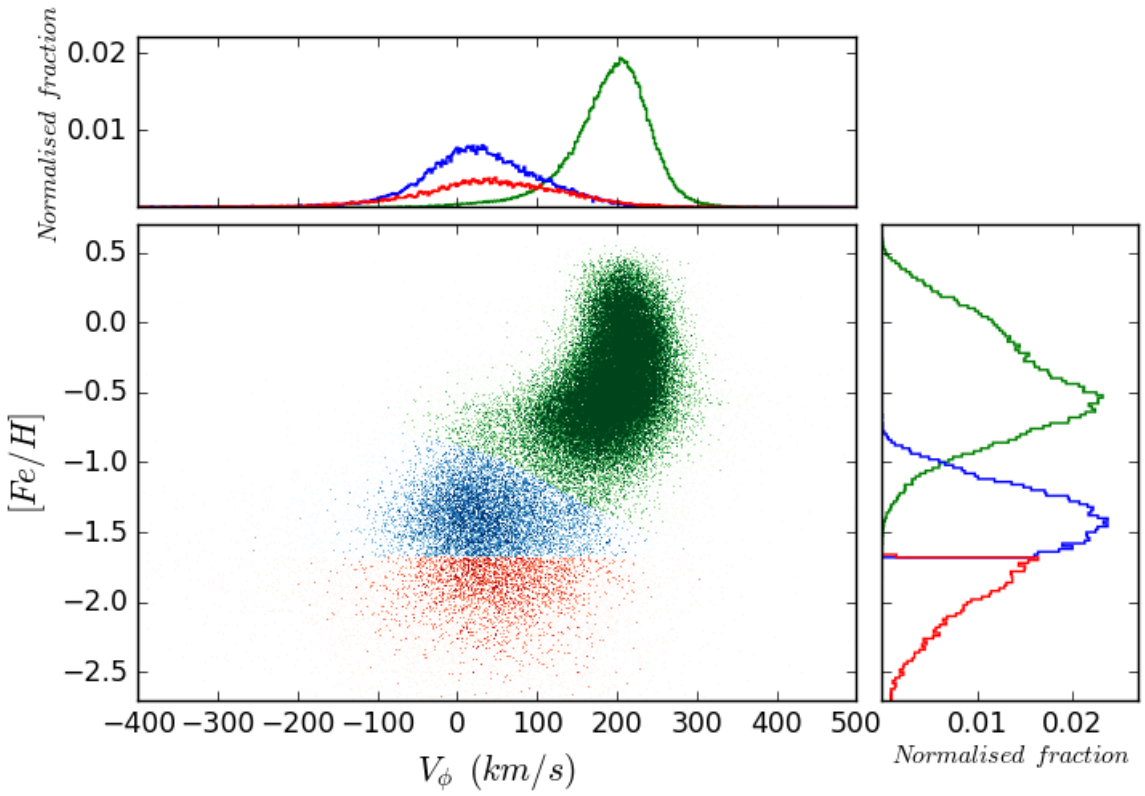

Fig. 4.1 The cleaned sample is shown in the $(v_\phi, [\mathrm{Fe/H}])$ plane. There is a clear separation of the halo stars from the disk (thin and thick) populations. Green represents the disk, blue the relatively metal-rich halo ([Fe/H] > -1.65), and red the relatively metal-poor halo ([Fe/H] < -1.65). For the one dimensional v_ϕ and [Fe/H] distributions, the normalisation is performed separately for the disk, and for the entire halo group, so the sum of the area under the green histogram is unity, as is that for the blue and red combined.

a better understanding of such algorithms is needed to convert the 'stamp collecting' into astrophysics.

In this spirit, Section 4.2 introduces a new method to search for substructure in velocity space in the SDSS-*Gaia* catalogue. The six most significant halo substructures are studied in detail in Section 4.3. They include a gigantic stream with cold kinematics, two moving groups and three hotter substructures in which the velocity distribution in at least one component is very broad. By matching with substructure in a library of numerical simulations in Section 4.4, we argue that hotter substructures probably correspond to multiply-wrapped streams in the later stages of disruption. For the two largest substructures, we provide estimates of the likely mass of the progenitor and infall time. Finally, Section 4.5 sums up with an eye to possible extensions and elaborations of our new method.

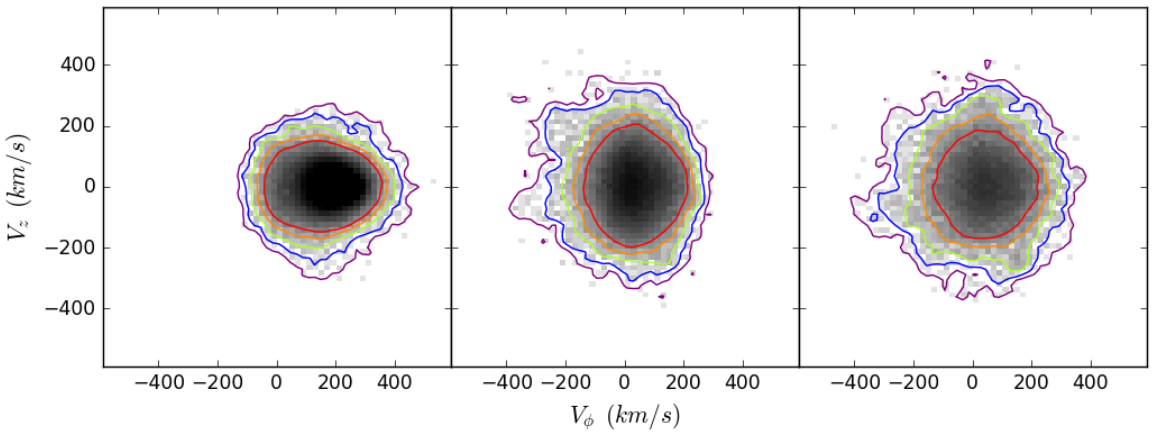

Fig. 4.2 The data are shown in the plane of (v_ϕ, v_z) for the disk (left), metal-rich halo (middle) and metal-poor halo (right). The contours levels are logarithmic. We can see visible substructure evident in the metal-rich ([Fe/H] > -1.65) and metal-poor ([Fe/H] < -1.65) halo groups. It is apparent that the sequence from disk to metal-rich halo to metal-poor halo is one of increasing lumpiness and substructure. The pixel size is 20 kms^{-1} on each side. The outermost contour is 2 stars per pixel, and the contours increase by a factor of $10^{0.35} \approx 2.24$ on moving inwards.

4.2 Method

4.2.1 Sample

Our starting sample is the crossmatch between *Gaia* data release 1 (DR1), the Sloan Digital Sky Survey data release 9 (PhotoObjAll for the photometric and sppParams for the spectroscopic), APOGEE, LAMOST DR2 and RAVE-on (see e.g., Anders et al., 2014; Casey et al., 2017; Kunder et al., 2017; Luo et al., 2015). There are 466 414 stars in this sample with five-dimensional phase space information. The sample contains MSTO stars and BHB stars, which can be extracted using methods similar to Sections 3.1 and 3.2 of Williams et al. (2017). The MSTO stars are extracted using the cuts: extinction $\varepsilon_r < 0.5$, g, r, i magnitudes satisfying $14 < g < 20$, $14 < r < 20$, $14 < i < 20$, $0.2 < (g-r)_0 < 0.8$ with surface gravity $3.5 < \log g < 5.0$ and effective temperature $4500 < T_{\rm eff} < 8000$. The BHB stars are chosen from $-0.25 < (g-r)_0 < 0.0$, $0.9 < (u-g)_0 < 1.4$ with spectroscopic parameters satisfying $3.0 < \log g < 3.5$ and $8300 < T_{\rm eff} < 9300$. We apply a set of quality cuts to both the photometric and spectroscopic data to remove stars with uncertain measurements as well as stars with a heliocentric radial velocity error > 15 kms^{-1} and a heliocentric distance > 10 kpc. The cuts cause the sample to be reduced to 245 316 in size with 245 078 MSTO stars and 238 BHB stars. The median heliocentric radial velocity error is 2.9 kms^{-1} and the median

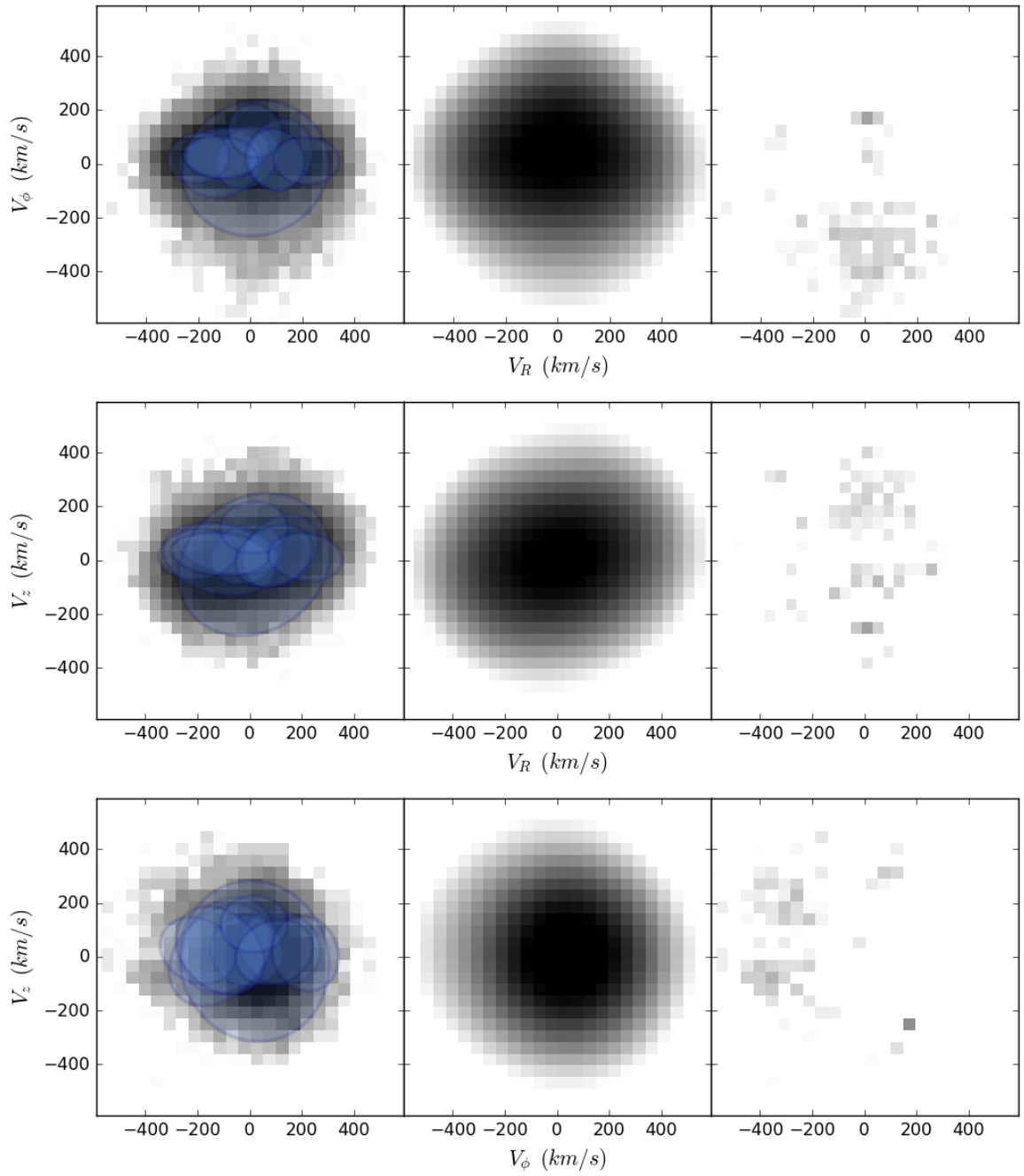

Fig. 4.3 For the entire halo sample, we show from left to right the data, the smooth Gaussian Mixture model, and the residuals. Superposed on the data are blue ellipses representing the Gaussians with orientation and sizes scaled according to their principal axes. The rows show the principal planes in velocity space (v_R, v_ϕ), (v_R, v_z) and (v_ϕ, v_z) respectively. Although the Gaussian mixture model is a good representation of the halo, substructure is already apparent in the plots in the rightmost column. The residuals demonstrate the locations of the main pieces of substructure, as well as highlighting the lumpy nature of the distribution.

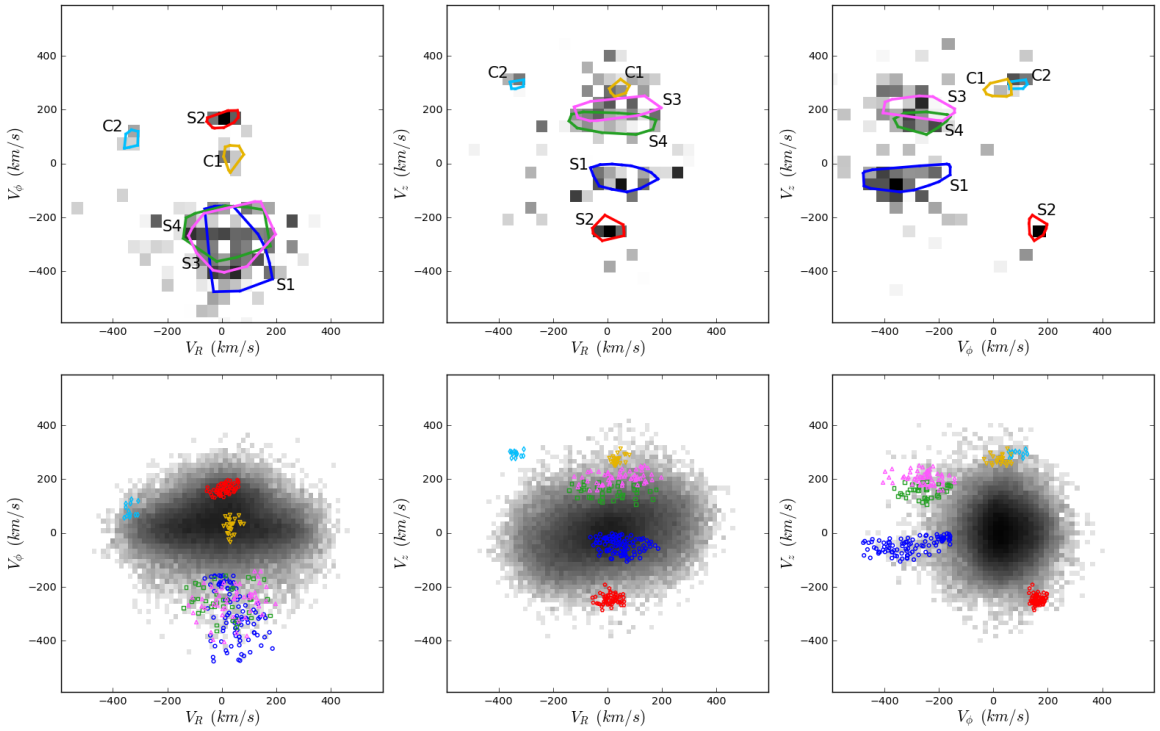

Fig. 4.4 The velocity distributions of the full halo sample (bottom row) and the residuals (top row) are shown in the three principal planes in velocity space, (v_R, v_ϕ), (v_R, v_z) and (v_ϕ, v_z). Stars belonging to the two most prominent substructures are shown as blue circles and red pentagons (S1 and S2). Also shown are two smaller substructures as upward-pointing magenta triangles and green squares (S3 and S4), and two moving clumps as downward-pointing brown triangles and pale blue diamonds (C1 and C2).

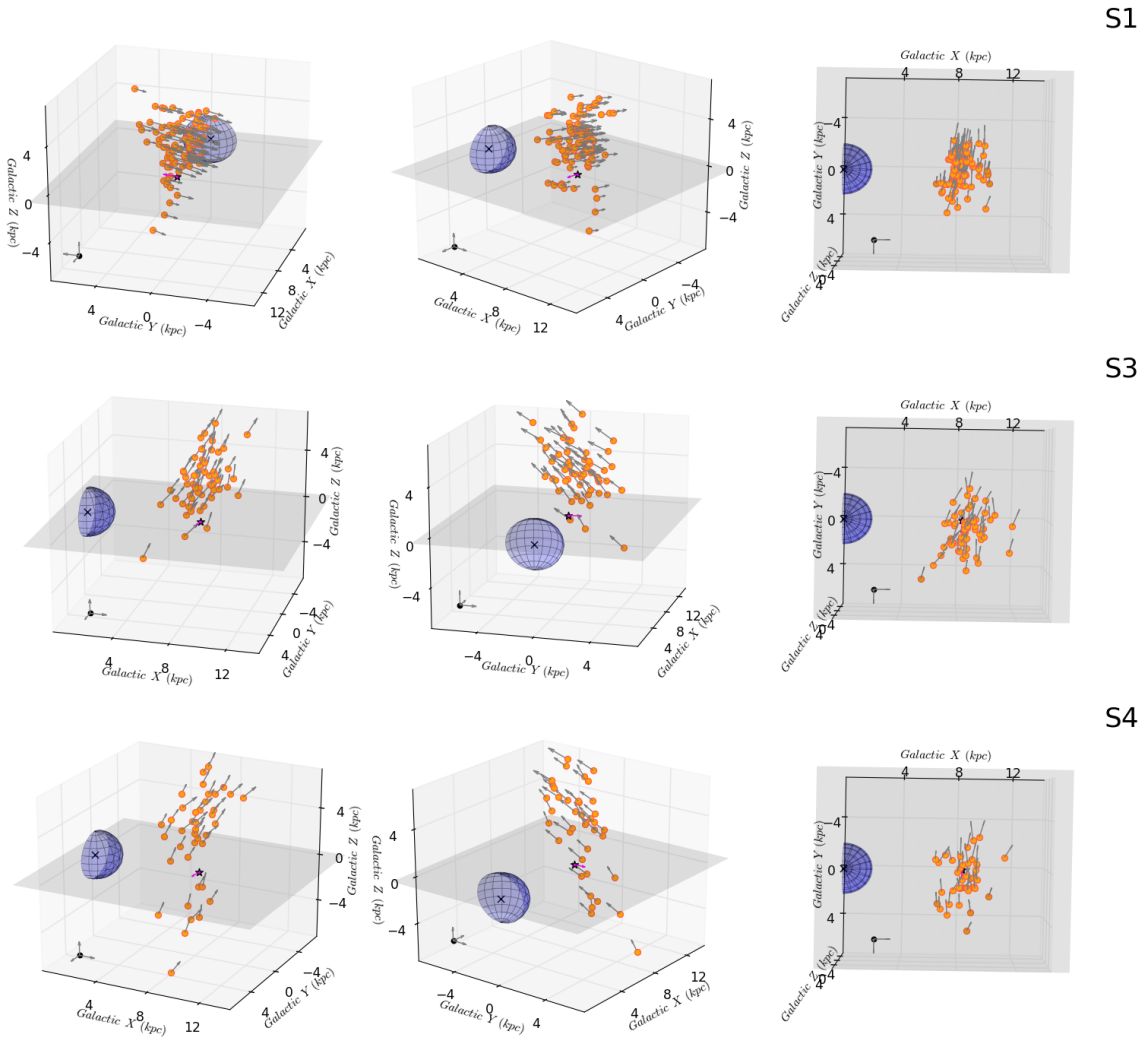

Fig. 4.5 The properties of stars belonging to the three substructures S1, S3 and S4. We have grouped them together because of the morphological similarity. The left and middle panes show two views of the substructure with the intention of depicting the overall shape. The right panel is a projection of the substructure onto the Galactic plane. The arrows show the total velocity in the Galactic rest-frame. The Sun is marked as a star at the centre, whilst the Sun's motion is marked by an arrow in magenta. A sphere of radius 2 kpc (which is a crude representation of the Galactic bulge), as well as a grey sheet representing the Galactic plane, are shown to give a sense of the scale and position of the substructure in relation to the familiar Galactic landscape. A triad of velocity vectors of scale 300 kms^{-1} is shown in the bottom left corner.

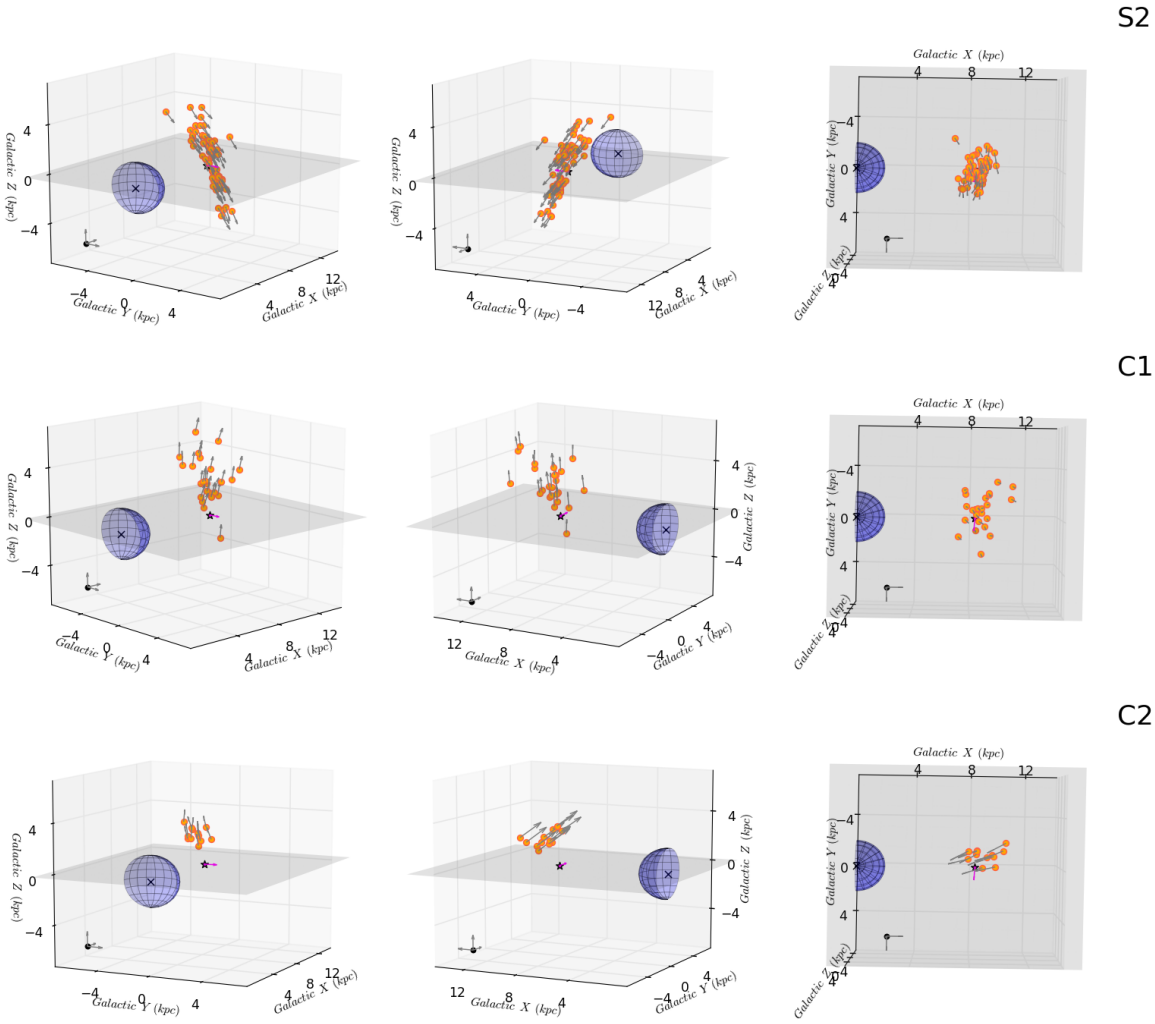

Fig. 4.6 As Fig. 4.5, but for the stream S2 and the two moving clumps (C1 and C2).

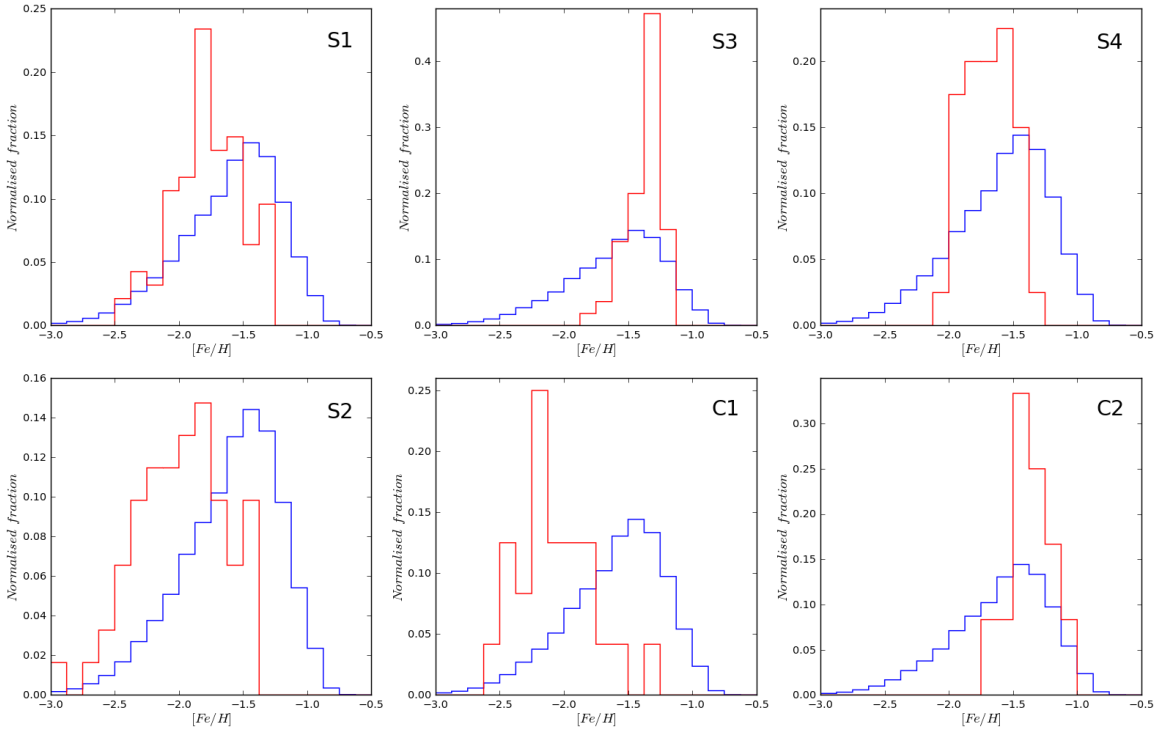

Fig. 4.7 The metallicity distribution function for the six substructures is shown in red, whilst the blue is the entire halo sample for comparison. Note that the substructures are narrower in metallicity than the entire halo, which is consistent with expectations.

proper motion error is 17.8 kms^{-1}. Parallaxes can be obtained via the formulae in Ivezić et al. (2008) for MSTOs (using spectroscopic metallicities) and in Deason et al. (2011b) for BHBs to give full six-dimensional phase space information. For the MSTOs that comprise the bulk of the sample, mean distance error scales linearly with distance and reaches ~ 1 kpc at a distance of 4.5 kpc. The mode of the distance error for the whole MSTO sample is ~ 0.47 kpc.

Velocities in the Galactic rest-frame are resolved in the cylindrical polar coordinate system to give (v_R, v_ϕ, v_z). From the histogram in the $(v_\phi, [\mathrm{Fe/H}])$ plane in Fig. 4.1, we see a reasonably clear separation of the halo population from the thin and thick disk populations. We define a polygon (converted from a contour) representing each population, and then calculate the distance of each star from two contours (one representing the halo, the other representing the thin and thick disks). This enables us to classify each star as either halo or disk. For the halo stars, we perform a Gaussian fitting decomposition based on the metallicity, and then subdivide the halo group into the relatively metal-rich, and the relatively metal-poor halo. As the result of the Gaussian decomposition, the division occurs at $[\mathrm{Fe/H}] \approx -1.65$. Our sample then comprises 181 574 disk stars (green), 40 293 relatively metal-rich halo stars (blue), and 23 449 relatively metal-poor halo stars (red), as shown in Fig. 4.1.

This subdivision of the stars into disk and halo groups is crude, but we only wish to use it to demonstrate that the sequence from thin and thick disk through metal-rich halo to metal-poor halo is one of increasing substructure. This is evident from Fig. 4.2 in which the logarithmic contours of the velocity distribution in the (v_R, v_ϕ) plane moves from smoothness to raggedness with increasing numbers of outliers and subgroups. Some of this effect is statistical in origin as there are between 4 and 8 times fewer stars in the halo populations. However, some prominent pieces of halo substructure can be picked out by eye, and so some of the effect is real. Accordingly, we proceed to develop a systematic way of identifying the substructure.

4.2.2 Detection

Henceforth, we use the entire halo sample (the blue and red distributions in Fig. 4.1). We first develop a smooth underlying background model, which is then used as the global density estimator against which substructure is identified. Using Galactocentric velocities resolved with respect to cylindrical polar coordinates (v_R, v_ϕ, v_z), we fit a basic Gaussian Mixture model from the `Scikit-learn` (Pedregosa et al., 2011) python software package [1]. Note that if we use too many Gaussian components, some of the actual signals from genuine

[1] http://scikit-learn.org

substructures get diluted by some of the fitted Gaussians. To avoid such dilution, we decide to use considerably less Gaussian components than the estimate of the number of components obtained from minimization of the Akaike Information Criterion or AIC test (56 components). We ensure that each of the fitted Gaussians has a width wider than 150 kms^{-1} on each axis to avoid including small scale features in our velocity distribution model. We find that 10 Gaussians provide a reasonable description of the velocity space for the halo stars, as shown in Fig. 4.3. The data, together with the superposed Gaussians are shown in the left panels, whilst the smooth model and residuals are shown in the middle and right. It is evident that there is substructure, and much of it corresponds to prominent clumps in Fig 4.2.

Next, we look for significant overdensities over the Gaussian Mixture model. We measure the local density of each star in our data, and compare this to the density value predicted by the smooth model. We do this by carrying out a k-nearest neighbours search with $k = 5$ (or 6 including the star itself). Using `Scikit-learn`, we obtain the radius r_5 required to encounter the $k = 5$ nearest neighbours and hence an estimate of the local density. The probability of the star's location in the 3-dimensional velocity space is predicted by the Gaussian Mixture model. We multiply this by the sample size and the volume of the sphere with radius r_5 to give the expected number. We assume Poisson sampling and from the expected number of stars in the sphere, we compute the tail probability of having 6 stars (5 neighbours and the star itself) in the sphere given this distribution. We then convert the tail probability to the number of sigma.

We use any stars with significance > 4 as the "seeds" for finding an overdensity in our 3-dimensional velocity space. First, we classify these seeds by the Friends-of-Friends method – that is, any seeds that are close to each other (< 30 kms^{-1} radius sphere) are considered as the same group. For each seed, we then take all stars within a spherical volume of radius 35 kms^{-1} around the seed. During this process, we discard any seeds and corresponding stars if there exist less than 5 stars within this spherical volume. We classify the stars around the seeds by using the Nearest Neighbours Classification from `Scikit-learn`. This stage is necessary because there are cases in which a star is picked up by more than one seed. So we train the classifier using the classified seeds, and then perform a distance-weighted k neighbours classification ($k = 3$) for the stars around the seeds. The weight here is the inverse of the distance. This gives us a list of candidates.

Now, we find the centre of each group in our 3-dimensional space. The measured number of group members is the number of stars in the ellipsoid in velocity space occupied by the group. This ellipsoid has a volume $4\pi abc/3$, where (a,b,c) is the extent of the group in each axis. The expected number of field stars in the volume ellipsoid is then the probability predicted by the Gaussian Mixture Model at the central location multiplied by the data size

and by the volume. The Poisson uncertainty is the square root of the expected number. This provides us with a crude measure of the significance of each substructure.

We will provide the list of substructures elsewhere, but here we describe the six most significant pieces of halo substructure, which is ~ 20 per cent of the detected potential candidates with $\sigma > 4$. They are labelled S for stream or shell-like substructures and C for clusters or moving groups. The locations of the stars in velocity space belonging to the substructures are shown in Fig. 4.4. Note that, as the stars lie within the SDSS footprint, proper motions contribute mainly to the radial v_R and azimuthal v_z components, whilst the line of sight velocities contribute mainly to v_z. This causes kinematic features to appear colder in v_z than in the other two directions which are more affected by errors. The two largest substructures in terms of the number of member stars are S1, coloured blue, with 94 identified members ($\sigma = 8.94$) and S2, coloured red, with 61 members ($\sigma = 8.95$). Just behind them in terms of the number of member stars are: S3, coloured magenta, with 55 members ($\sigma = 8.41$) and S4, coloured green, with 40 ($\sigma = 8.49$) members. There are also two clumps or moving groups: C1, coloured brown, with 24 members ($\sigma = 8.46$) and C2, coloured pale blue, with 12 members ($\sigma = 18.66$). Table 4.1 provides the median, mean absolute deviation and dispersion for kinematical and spectroscopic quantities of the substructures. A list of stars in the substructures is available electronically from the authors.

Name		[Fe/H]	$\log g$	$T_{\rm eff}$ (K)	(X,Y,Z) (kpc)	(v_R,v_ϕ,v_z) (kms^{-1})	(U,V,W) (kms^{-1})	KE (km^{2}s^{-2})	L (kpc kms^{-1})
	Median	-1.78	3.96	6073.2	(8.1,-0.2,2.8)	(44.8,-313.8,-42.7)	(32.9,-322.6,-42.7)	55872	2911
S1	MAD	0.19	0.21	265.7	(0.4,0.9,1.1)	(38.4,75.7,21.3)	(25.8,65.4,21.3)	22621	519
	Dispersion	0.27	0.25	335.2	(0.8,1.2,1.9)	(56.2,93.4,26.5)	(39.2,86.5,26.5)	26815	822
	Median	-1.91	4.00	5847.0	(8.7,0.3,0.8)	(8.9,160.2,-249.9)	(-1.2,164.9,-249.9)	46048	2632
S2	MAD	0.26	0.26	392.4	(0.3,0.6,1.5)	(19.7,12.1,11.7)	(17.1,10.2,11.7)	2527	127
	Dispersion	0.35	0.32	473.8	(0.6,1.0,2.0)	(28.2,16.8,17.5)	(35.6,15.5,17.5)	4962	233
	Median	-1.34	4.05	6114.3	(8.6,0.5,3.5)	(50.6,-245.5,206.7)	(77.3,-257.0,206.7)	59857	2901
S3	MAD	0.08	0.20	196.8	(0.6,1.0,1.0)	(67.3,30.5,19.0)	(60.1,40.6,19.0)	11230	448
	Dispersion	0.13	0.30	334.2	(1.1,1.5,1.9)	(80.1,58.7,22.4)	(66.1,61.5,22.4)	17604	792
	Median	-1.70	3.83	6144.1	(8.5,0.6,4.1)	(4.0,-250.5,157.7)	(14.7,-262.7,157.7)	49617	2755
S4	MAD	0.14	0.14	203.8	(0.5,1.2,1.8)	(68.2,43.8,18.5)	(41.3,38.3,18.5)	11436	351
	Dispersion	0.19	0.28	290.7	(1.0,,1.7,3.6)	(84.4,54.3,22.2)	(61.6,56.2,22.2)	14708	719
	Median	-2.11	3.85	6081.4	(8.7,-0.8,2.5)	(32.0,32.3,271.6)	(33.7,29.4,271.6)	38235	2311
C1	MAD	0.16	0.25	285	(0.4,1.0,1.1)	(8.5,18.6,11.2)	(10.7,20.4,11.2)	2502	107
	Dispersion	0.29	0.31	360	(0.9,1.4,1.6)	(17.8,26.9,15.8)	(18.2,28.3,15.8)	4807	191
	Median	-1.39	4.05	5998.7	(8.9,-1.0,2.1)	(-337.5,75.4,295.0)	(-322.7,121.0,295.0)	105895	3498
C2	MAD	0.12	0.21	258.9	(0.6,0.3,0.3)	(13.1,16.9,8.2)	(15.3,27.8,8.2)	3319	147
	Dispersion	0.17	0.25	320.1	(0.85,0.5,0.6)	(16.2,23.9,10.0)	(18.6,32.3,10.0)	6631	293

Table 4.1 The median, median absolute deviation and dispersions in spectroscopic and kinematic properties of the six substructures.

4.3 Candidates

4.3.1 The Hotter Substructures: S1, S3 and S4

Fig. 4.5 shows the discovery panels for the three hotter substructures. For each, we provide two views of the morphology in the left and middle panels, as well as a projection onto the Galactic plane on the right. The metallicity distribution function of each substructure is compared against that of the full halo sample in Fig. 4.7.

S1 is a large piece of halo substructure, containing 94 member stars. The members correspond to an obvious narrow tail-like overdensity in the (v_ϕ, v_z) velocity distribution in Figs 4.2 or 4.4, visible by eye. The medians of the positions of the stars provide a location of $(X,Y,Z) = (8.1, -0.2, 2.8)$ kpc, so the structure lies just beyond the Sun's location. It has a substantial extension in both Y and Z as indicated by the median absolute deviations of ~ 1 kpc, so it is distended vertically and azimuthally. Therefore, the spatial configuration is shell-like, pirouetting around the Sun's location. The vertical or v_z velocities are tightly constrained around a median of -42.7 kms^{-1} with a median absolute deviation of 21.3 kms^{-1}. The structure is counter-rotating with a median v_ϕ of -313.8 kms^{-1}. The median radial velocity v_R is 44.8 kms^{-1} with a comparatively large median absolute deviation of 38.4 kms^{-1}, mainly caused by the extent of the structure. It is natural to inquire whether this is a diminutive analogue of the shell-like features seen in elliptical galaxies (Hernquist and Quinn, 1987) or in the Milky Way halo (Belokurov et al., 2007b; Rocha-Pinto et al., 2004). However, shells are known to be associated with radial infall of galaxies or clusters (e.g., Amorisco, 2015; Hendel and Johnston, 2015; Pop et al., 2017), whereas the strongly counter-rotating nature of the substructure indicates that the progenitor orbit has high angular momentum. We will elaborate on the true nature of this structure in the next Section.

The detection algorithm used to identify substructures is based on kinematics alone. However, in all our presented substructures, it is possible to identify clumpiness in configuration space and in chemical properties. Fig. 4.7 shows the metallicities of the S1 stars in red are much spikier than the halo metallicity distribution function in green. They have a median metallicity of -1.78 with a narrow median absolute deviation of 0.19, making this a convincing detection.

S3 and S4 share some similarities with S1 in that the radial and azimuthal velocity distributions are broad, but the vertical velocity distribution is narrower, suggesting a highly inclined orbital plane. S3 and S4 are more obviously stream-like, as the stars are moving along the extent of the structure, whereas S1 moves almost perpendicularly. All three substructures are on retrograde orbits. They all lie just beyond the Solar position, though the preponderance of substructure here is a selection effect of the SDSS-*Gaia* catalogue. The stars belonging to

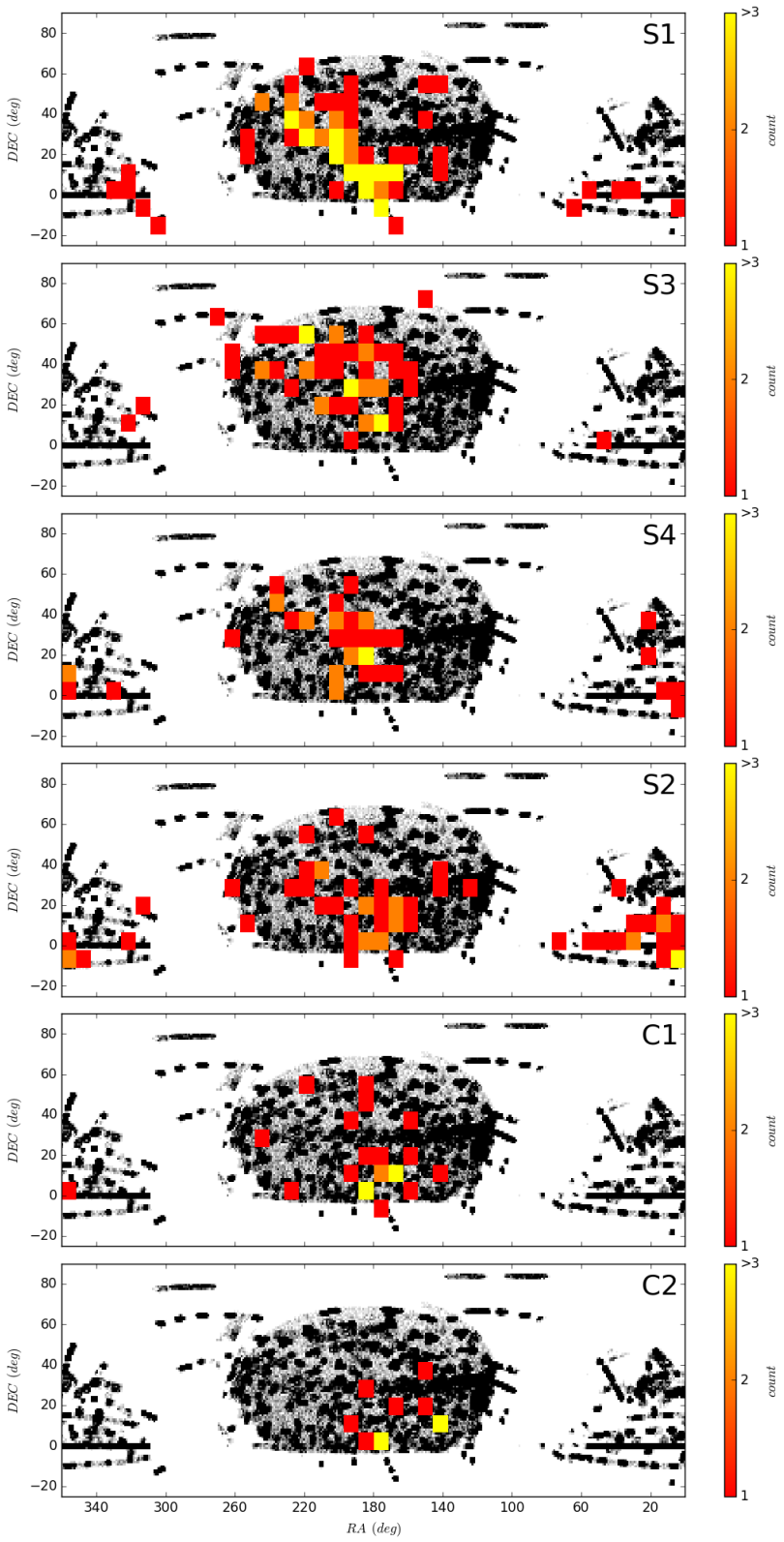

Fig. 4.8 The location of the stars belong to the substructures are shown in the plane of right ascension versus declination. The pixel size is 8.5 deg on each side.

both S3 and S4 are tightly clustered in metallicity with median values of -1.34 and -1.70 respectively. Although S3 and S4 occupy similar region in the 3-dimensional velocity space, they show clear deviation in their metallicity distribution as well as in their v_z distribution which suggest they are separate substructures. This has been further checked by the Gaussian fitting decomposition on the 4-dimensional space (3-dimensional velocity components and the metallicity) which shows the separation between two substructures more clearly. Notice that S3 is comparatively metal-rich and is visible by eye as a distortion in the outermost contours of the velocity distribution of the metal-rich halo in the middle panel of Fig. 4.2 at $(v_\phi, v_z) \simeq (-250, 200)$ kms^{-1}. There is also a possibility that S3 and S4 are not fully distinct substructures. Despite their different metallicity distributions, their close overlap in velocity space (Fig. 4.4) and similar spatial distribution (middle and bottom rows of Fig. 4.5) suggest a possibility of a single large substructure with some internal metallicity variations being torn apart over time.

4.3.2 The Colder Substructures: S2, C1 and C2

The top row of Fig. 4.6 shows the discovery panels for substructure S2 comprising 73 member stars, which has the characteristics of a halo stream. S2 corresponds to an obvious overdensity in the (v_ϕ, v_z) velocity distribution. It can be seen as an underhanging blob of stars in the lower rightmost panel of Fig. 4.2 at $(v_\phi, v_z) \simeq (160, -250)$ kms^{-1}. The member stars also comprise a tight grouping in the (v_R, v_ϕ) and (v_R, v_z) planes. The coldness of this substructure in velocity space is emphasised by the narrow velocity distributions. The median absolute deviation in (v_R, v_ϕ, v_z) are $(19.7, 12.1, 11.7)$ kms^{-1}, though these are of course averages over the spatial extent of the stream and so are not indicative of the velocity dispersion or the size of the progenitor.

The median values of the spatial coordinates are (X, Y, Z) = $(8.7, 0.3, 0.8)$ kpc, so that this substructure is again close to the Sun. Nearby objects have the highest proper motions and stand out from the bulk of the stars in the catalogue, so it is not surprising that our detection is more sensitive to the substructures close to the Solar radius. As Fig. 4.6 shows, S2 is a stream plunging through the Galactic disk, moving on a nearly polar orbit. The fact that the stream is aligned along the velocity vectors of the stars, as is natural for a stream, adds confidence to our detection. The stars have a median metallicity [Fe/H] of -1.91 and a median absolute deviation of 0.26. As is clear from Fig. 4.7, the metallicity distribution function of the substructure is poorer and narrower than the stellar halo as a whole.

In fact, S2 lies at a very similar location in velocity space as 4 stars belonging to the halo stream identified in Hipparcos data by Helmi et al. (1999, see especially the upper panels of their Fig. 2). Their stars are clumped in “integrals of motion space”, while the two structures

have no direct member stars in common, presumably due to the use of different dataset. The relationship of S2 with the stream of Helmi et al. (1999) will be discussed in detail elsewhere. As the associated substructure has been identified both in velocity space and in "integrals of motion space", it provides an interesting test case for assessing the advantages and disadvantages of each search arena and algorithm.

The middle and bottom rows of Fig. 4.6 show panels for the two clumps C1 and C2. These comprise 24 and 12 members respectively, and so are less substantial and extensive than S1-S4. Their velocity histograms are very narrow with the vertical velocity distribution being the coldest. The structures are tightly confined in space and in metallicity. The median metallicity [Fe/H] of C1 is -2.11, making it the most metal-poor of all our substructures, whilst C2 has a median metallicity of -1.39 (see Fig. 4.7).

4.3.3 Distribution on the Sky

The locations of the stars in right ascension and the declination for all the substructures are shown in Fig. 4.8. Notice that the substructure are difficult to discern, with the exceptions of S1 and S4. In general, the substructures are both nearby and extended, so their member stars are scattered across the sky. The stream S2 is hard to make out, as it is traversing the Galactic disk. Fig. 4.8 vindicates the power of kinematic searches, as the substructures would be nearly impossible to identify any other way.

4.4 Interpretation

We use the library of accretion events created by Amorisco (2017) to find model analogues for the two largest substructures S1 and S2. The library uses minor merger N-body simulations to study how stellar material is deposited onto the host. Both host and infalling satellites are assumed to have spherical Navarro-Frenk-White profiles (Navarro et al., 1997), meaning that the Milky Way disk is not properly accounted for. The disk is not expected to cause substantial additional satellite disruption in satellites with total masses $M_{sat} \gtrsim 10^9 M_\odot$ (D'Onghia et al., 2010; Garrison-Kimmel et al., 2017), but can alter the debris' orbits and it does increase the speed of the phase-mixing process (e.g., Helmi and White, 1999). This initial exploration neglects these effects. Specifically, we search for accretion events that result in substructures located close to the Solar radius and that provide reasonable matches to the velocity histograms. To do so, we use spherical polar coordinate, $(v_r, v_\theta, v_\varphi)$, defined by the mean angular momentum vector of the substructure itself. Therefore, v_φ refers to rotation in the mean orbital plane, while the scatter in v_θ is a proxy of the structure's hotness.

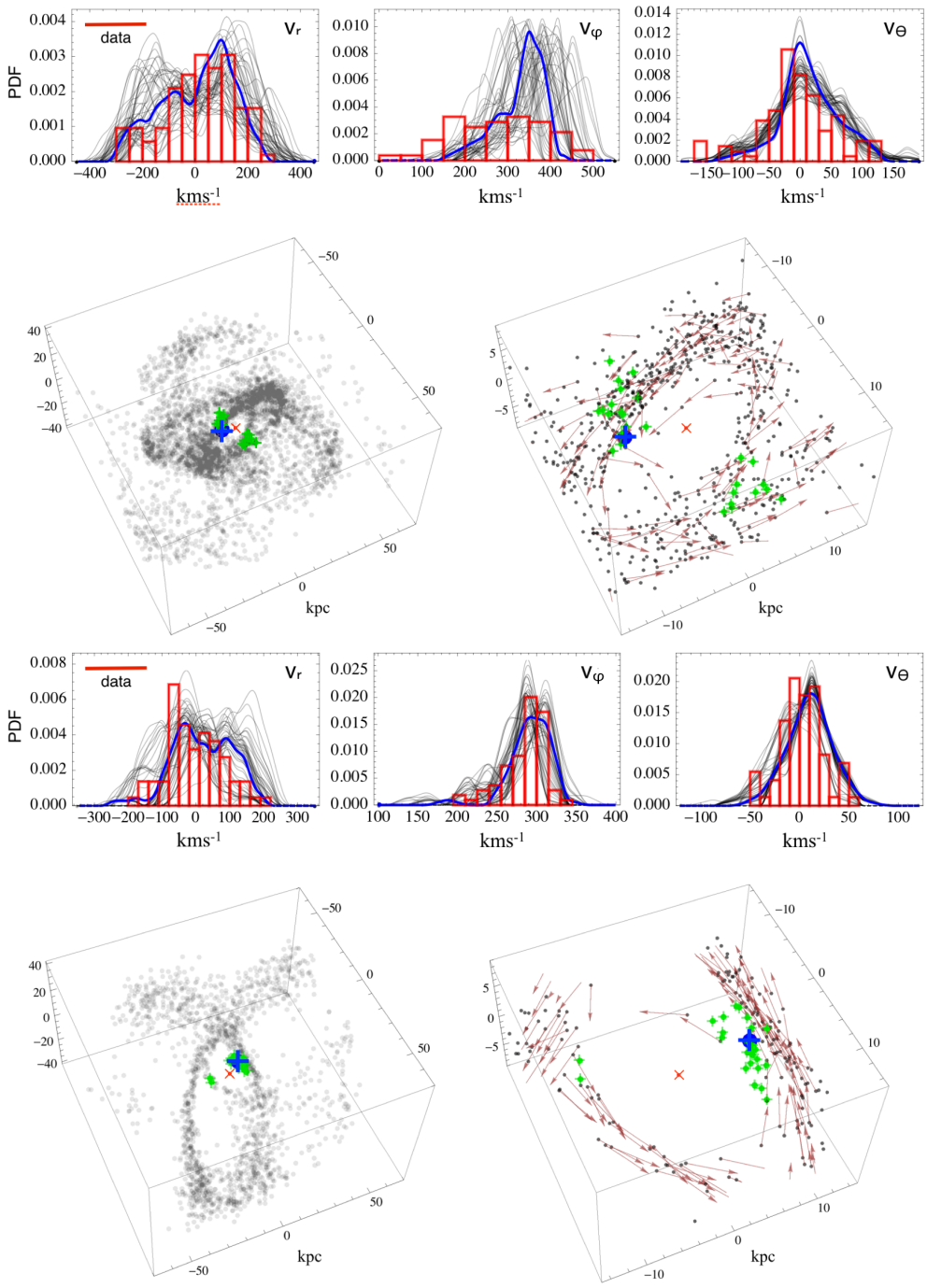

Fig. 4.9 Matches to substructures S1 (upper two rows of panels) and S2 (lower two rows of panels) in the library of Amorisco (2017). For each substructure, the observed kinematics (red histograms) is compared with the chosen model in the upper trios of panels. There, thin grey lines illustrate the debris' kinematics corresponding to different viable positions of the Sun. The thick blue line identifies the best-fitting model, corresponding to the best Sun's position. The lower-left panels illustrate the three-dimensional structure of the simulated tidal debris. Grey points are model particles and the red X symbol identifies the Galactic centre. Green + symbols identify the Sun's positions corresponding to the kinematic distributions shown in the upper trio of panels. The best Sun's position is displayed with a large blue + symbol. The panel in the lower-right is a zoomed version that best shows the position of the simulated debris material with respect to the selected Sun's locations. Symbols are as in the lower-left panels. Additionally, a fraction of the model particles are accompanied by their velocity vectors, to illustrate the debris kinematics.

By automating this, we can explore a large number of models in the library with a variety of mass ratios ($-2 \lesssim \log M_{sat}/M_{halo} \lesssim -0.5$), infall circularities ($0.2 < j < 0.8$, where j is the ratio between angular momentum and the maximum angular momentum at the same energy) and infall times. For each model we look for matches by considering thousands of possible Sun's locations, together with slightly different mass and length normalisations. The former exploits the lack of a stellar disk in the models, the second explores the possible scatter in the values of the Galaxy's mass and concentration at the time of infall.

Despite the size of this library, there do not seem to be that many models that fit reasonably when actually compared with the histograms of S1. For a randomly picked Sun's location, most model structures feature the presence of multiple phase-space wraps, resulting in sharply double peaked v_r distributions, with average close to zero or $\langle v_r \rangle \approx 0$. Instead, S1 is characterised by a broad and unimodal v_r distribution, which contains $v_r = 0$ and is not double peaked. To reproduce this, the Sun is required to lie very close to the pericenter of the debris' orbit. Among those models for which feasible locations for the Sun can be found, we illustrate one of the most successful in the upper panel of Fig. 4.9, in which green points display a selection of feasible Sun's locations. Each of these produce the velocity distributions plotted as thin black lines in the upper panels. The best choice for the Sun's location is shown in blue. The corresponding blue velocity distributions reproduce most of the features of the velocity histograms, though the match to the v_φ distribution is poor. It corresponds to a virial mass ratio of $M_{sat}/M_{halo} = 1:20$ at infall, implying that the progenitor had a starting mass of $\approx 2 \times 10^{10} M_\odot$ at infall time ≈ 10 Gyr ago, for a circularity at infall of $j = 0.8$.

As shown in the lower plot of the upper panel of Fig. 4.9, S1 is identified as a stream in an advanced state of disintegration. The Sun appears to lie within the stream's wraps, while these are at pericenter. The quite advanced state of phase mixing and partial superposition of multiple stream wraps helps in reproducing the broad v_φ distribution, although the model distributions still appear to remain somewhat tighter than suggested by the data. The stream does indeed pirouette around the Sun, but the substructure S1 is not a shell. In fact, its angular momentum is still high, as permitted by the low initial virial mass ratio. The v_r distribution encompasses $v_r = 0$, but it does so while the Sun is close to the stream's pericenter rather than to the apocenter as in a more classical shell. The fact that one of the velocity distributions is poorly fit does mean that our conclusions regarding the properties of the progenitor of S1 are preliminary. It may be that we have a restricted view of S1 owing to the incompleteness of our sample, though integration of the orbits of the stars does not reveal a connection to other known substructures.

The v_r histogram of the substructure S2 has a similar distinguishing property, implying that the Sun's preferred position is again very close to pericentre. The main difference is that the dispersions are smaller, which drives the model to lower mass ratios, and therefore to less phase-mixed morphologies. The lower panel of Fig. 4.9 illustrates a model that provides a good match: it has a virial mass ratio of 1 : 100 at infall, implying that the progenitor had a starting mass of $\approx 5 \times 10^9 M_\odot$ at infall time ≈ 11 Gyr ago, and an initial circularity of $j = 0.5$. However, a number of models that are close in parameter space can also roughly reproduce the features of the substructure. For example, one can trade a slightly higher initial mass ratio ($\approx 1 : 50$) for a somewhat later infall time (≈ 8 Gyr) or a marginally higher angular momentum. These coupled changes can compensate each other, without affecting much the degree of the stream's phase mixing, and therefore its kinematic properties.

As shown by the analysis above, a significant variety of models have a pericentric distance that is comparable with the Sun's radius. These are models with comparatively old progenitors, which helps them to fall deeper in the Milky Way halo, but not overly massive, which would instead cause excessive dynamical friction and phase mixing. Despite the limits of the models we adopted, it is clear that the progenitors of both S1 and S2 belong to this class.

The inferred total masses of S1 ($\approx 10^{10} M_\odot$) and S2 ($\approx 5 \times 10^9 M_\odot$) are about a factor of 10 smaller than the total mass of the Large Magellanic Cloud. According to the abundance matching of Garrison-Kimmel et al. (2014), these correspond to stellar masses between 10^6 and $10^7 M_\odot$, and so are comparable to present-day objects like the Fornax dwarf spheroidal. The stellar masses inferred for S1 and S2 through the mass-metallicity relation of Kirby et al. (2013a) are $10^{5.7} M_\odot$ and $10^{5.3} M_\odot$, which are somewhat lower by factors of 5 to 15. However, this does not take into account the redshift evolution of the mass-metallicity relation (see e.g., Ma et al., 2016), which though uncertain may remove these inconsistencies entirely. In addition, there is substantial scatter in both abundance matching, the mass-metallicity relation and the data of Kirby et al. (2013a). Hence, metallicity and kinematics appear to be painting a broadly consistent picture.

Nonetheless, there are some clear shortcomings to our methodology. First, we did not use the footprint of the SDSS-*Gaia* survey and so this weakens our claim to a proper comparison with the data. Secondly, the proper motion errors are not known on a star by star basis, though on average they are reckoned to be ~ 2 mas yr^{-1}. The effect of the proper motion errors is to broaden the distributions in the angular coordinates especially and this may partially explain our failure to reproduce the broadness of the v_φ distribution for S1. Finally, the underlying galaxy models used to generate our substructure library are spherical and so somewhat idealised.

4.5 Conclusions

We have devised a method to search algorithmically for substructure. We model the distribution of the underlying smooth component as a Gaussian Mixture model. We use this to identify enhancements against the background, by comparing the local density around any star with the prediction from the Gaussian Mixture model and thence computing the significance. Stars with significance greater than 4 are then grouped by a Friends-of-Friends algorithm to give substructures. In our application, the underlying smooth component is the velocity distribution of the stellar halo, and we were seeking kinematically coherent substructures that are the residue of long-disrupted dwarf galaxies.

Our method has a number of advantages. First, the entire algorithm is very fast. For the halo samples studied here (63 742 stars), substructures can be identified and their significance computed in $\sim$ 100s. It is estimated that there will be 2×10^7 halo stars in *Gaia* Data Release 2 (Robin et al., 2012), so the algorithm remains competitive and feasible in the face of the much larger datasets expected shortly. Secondly, the algorithm is easily adapted to different search spaces. Here, we chose to search only in velocity space and use any metallicity data as confirmation. However, it would have been easy to add extra dimensions in chemistry (such as metallicity or abundances) and search in a chemo-dynamical space. Alternatively, we could have applied the algorithm in action or 'integral of motion' space.

We implemented the new algorithm on a sample of stars extracted from the SDSS-*Gaia* catalogue (see e.g. Deason et al., 2017). This uses Sloan Digital Sky Survey (SDSS) photometry as the first epoch for sources in *Gaia* DR1. When cross-matched with available spectroscopic surveys, such as RAVE, APOGEE or LAMOST, we obtain the line-of-sight velocities and metallicity. By photometrically selecting main sequence turn-off stars or BHB stars, for which distance estimators are available, we construct a sample of 245 316 stars with full phase space coordinates. The velocity distributions show a strong trend of increasing substructure with diminishing metallicity. The most metal-poor stars ([Fe/H] < -1.65) exhibit abundant substructure in their velocity distributions. Some of the substructures are visible by eye.

Our new algorithm enabled us to identify six new substructures in the local stellar halo. The most substantial (S1) is a stream in an advanced state of disruption just beyond the Solar radius. The Sun is located close to the pericentre of multiple wraps, giving rise to a broad distribution in two of the velocity components. This is the relic of an old accretion event in which a satellite was engulfed on a retrograde orbit. Modelling suggests that the progenitor was relatively massive at $\approx 2 \times 10^{10} M_{\odot}$ at infall time ≈ 10 Gyr ago. The next most substantial (S2) is a stream, though it is more intact. Again, it is located close to the Solar radius, but is plunging through the Galactic disk. It has characteristic stream kinematics, with the

velocity vectors of the stars aligned with the elongation of the substructure. The cold velocity distributions suggest that the progenitor was less massive – at most perhaps $\approx 5 \times 10^9 M_\odot$ at infall time ≈ 11 Gyr ago. The stars belonging to these substructures are clustered not just kinematically but also chemically, which adds confidence to the detections. Abundance matching suggests that both S1 and S2 correspond to galaxies with stellar masses between 10^6 and $10^7 M_\odot$. This is comparable to the largest dwarf spheroidal galaxies surrounding the Milky Way today. The metallicities of S1 and S2 ([Fe/H] ≈ -1.78 and -1.91 respectively) are consistent with stellar masses of $\sim 10^{5.5} M_\odot$ through the mass-metallicity relation (Kirby et al., 2013a). Although such masses are slightly lower than our modelling suggests, it must be remembered that there is considerable scatter in both the abundance matching and the redshift dependence of the mass-metallicity relations.

We identified four further pieces of substructure; namely, two moving groups or clumps (C1 and C2) and two substructures (S3 and S4). The latter two share some similarities with S1 and are also probably streams in the later stages of disintegration. As all our substructures are nearby, the member stars are candidates for high resolution spectroscopic follow-up to provide abundances and ages. The larger substructures probably extend beyond the volume accessible in SDSS-*Gaia*, and it would be valuable to trace their full extent.

The overall aim of activity in this field is to provide an assessment of the fractional mass in substructure as a function of Galactic position and metallicity. Nevertheless, in Rutherford's words, the 'Stamp Collecting' is still insightful. It is useful to understand the largest substructures in the nearby halo and the nature of the accretion events that gave rise to them. Our matches with the remnants of accretion events in libraries of numerically constructed stellar halos have provided insights, but they are not perfect – for example, we failed to reproduce the full broadness of the azimuthal velocity distribution in the case of S1. In fact, it was difficult to find perfect matches, even though our task was eased by the absence of a Galactic disk in the library of Amorisco (2017). This suggests that the problem of matching substructures in *Gaia* DR2 to accreted subhalos in simulations may be challenging.

Chapter 5

Discovery of New Retrograde Substructures: The Shards of ω Centauri?

G. C. Myeong[1], N. W. Evans[1], V. Belokurov[1], J. L. Sanders[1], S. E. Koposov[1,2]

[1]Institute of Astronomy, University of Cambridge, Madingley Road, Cambridge CB3 0HA, United Kingdom

[2]McWilliams Center for Cosmology, Department of Physics, Carnegie Mellon University, 5000 Forbes Avenue, Pittsburgh, PA 15213, USA

Abstract

We use the SDSS-*Gaia* catalogue to search for substructure in the stellar halo. The sample comprises 62 133 halo stars with full phase space coordinates and extends out to heliocentric distances of ~ 10 kpc. As actions are conserved under slow changes of the potential, they permit identification of groups of stars with a common accretion history. We devise a method to identify halo substructures based on their clustering in action space, using metallicity as a secondary check. This is validated against smooth models and numerical constructed stellar halos from the Aquarius simulations. We identify 21 substructures in the SDSS-*Gaia* catalogue, including 7 high significance, high energy and retrograde ones.

[0]Remark: The work presented in this Chapter has been published in Myeong et al. (2018b). I conceived this project and was responsible for the data acquisition and analysis. My supervisors, N. Wyn Evans and Vasily Belokurov, made an invaluable contribution by consulting and reformatting the first draft into a more logical presentation. Jason L. Sanders and Sergey E. Koposov also provided priceless consultation.

We investigate whether the retrograde substructures may be material stripped off the atypical globular cluster ω Centauri. Using a simple model of the accretion of the progenitor of the ω Centauri, we tentatively argue for the possible association of up to 5 of our new substructures (labelled Rg1, Rg3, Rg4, Rg6 and Rg7) with this event. This sets a minimum mass of $5 \times 10^8 M_\odot$ for the progenitor, so as to bring ω Centauri to its current location in action – energy space. Our proposal can be tested by high resolution spectroscopy of the candidates to look for the unusual abundance patterns possessed by ω Centauri stars.

5.1 Introduction

The spatial structure of the stellar halo has already been explored using either multiband photometry from surveys like the Sloan Digital Sky Survey and Pan-STARRS (e.g., Bell et al., 2008; Belokurov et al., 2006b; Slater et al., 2014) or variable stars such as RR Lyrae characteristic of old metal-poor stellar populations (Iorio et al., 2018; Watkins et al., 2009). At least within heliocentric distances of ~ 30 kpc and for declinations northward of $\delta = -30^\circ$, the most prominent halo substructures in resolved star density maps have now been identified by matched filter searches (Newberg and Carlin, 2016).

Nowadays, we are so familiar with maps such as the "Field of Streams" (Belokurov et al., 2006b) that we forget how surprising they really are. Substructure identification in configuration space is grossly inefficient compared to searches in phase space (Helmi and White, 1999; Johnston, 1998). Streams remain kinematically cold and identifiable as substructure in phase space long after they have ceased to be recognisable in star counts against the stellar background of the galaxy. Given what has already been discovered with multiband photometry, the local phase space structure of the stellar halo must be bristling with abundant substructure.

Astrometric satellites have the ability to transform this terrain. Already using data from the *Hipparcos* satellite, Helmi and White (1999) identified 13 stars which form an outlier in the plane defined by two components of angular momentum (see also Myeong et al., 2018a, for later developments). The first *Gaia* data release (DR1) in 2016 has already inspired two such searches. Helmi et al. (2017) used the Tycho-*Gaia* Astrometric Solution (TGAS) cross-matched with RAVE (Kunder et al., 2017) to identify overdensities in "integrals of the motion space", or energy and angular momentum space, which they ascribed to halo substructure. Myeong et al. (2017a) used TGAS cross-matched with RAVE-on (Casey et al., 2017) to search for halo substructure in action space, identifying a subset of stars with large radial action. These stars are all moving on highly eccentric orbits and are clustered in both configuration space and metallicity, thus providing a convincing candidate.

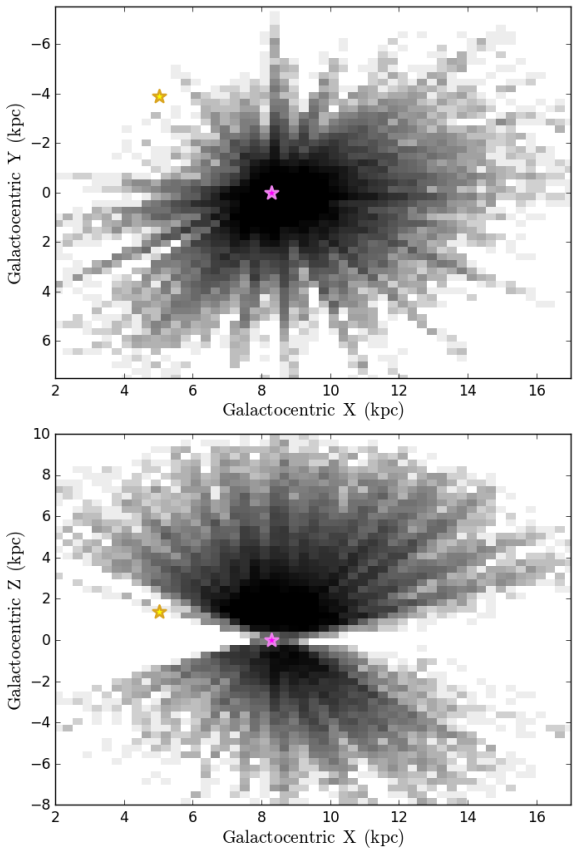

Fig. 5.1 Distribution of the stellar halo sample in the SDSS-*Gaia* catalogue in spatial coordinates projected onto the principal planes (X,Y) and (X,Z) in Galactocentric Cartesian coordinates (X,Y,Z). There are 62 133 halo stars with full phase space coordinates and the sample extends out to heliocentric distances of ~ 10 kpc. The golden star in each panel represents the present position of ω Centauri, while the mauve star is the position of the Sun. Note that ω Centauri is at the low galactic latitude limit of the survey, so some of its debris may be missed.

Crossmatches between TGAS and radial velocity surveys provide catalogues of $\sim 2\,000$ halo stars largely within ~ 1 kpc of the Sun. This is too parochial for studies of the stellar halo. The SDSS-*Gaia* catalogue contains a much larger and deeper sample of $\sim 60\,000$ halo stars out to ~ 10 kpc. This catalogue was made by recalibrating the Sloan Digital Sky Survey (SDSS) astrometric solution, and then obtaining proper motions from positions in the *Gaia* DR1 Source catalogue and their recalibrated positions in SDSS (see e.g., de Boer et al., 2018; Deason et al., 2017, for more details). The individual SDSS-*Gaia* proper motions have statistical errors typically ~ 2 mas yr^{-1}, or $\sim 9.48D$ km s^{-1} for a star with heliocentric distance D kpc. The SDSS-*Gaia* catalogue is the natural intermediary between *Gaia* DR1 and the recently released *Gaia* DR2 (Gaia Collaboration et al., 2018b).

Myeong et al. (2018c) recently provided new pictures of the Milky Way halo in action space as a function of metallicity using a sample of $\sim 60\,000$ halo stars with full phase space coordinates present in the SDSS-*Gaia* catalogue. The comparatively metal-rich halo ($-1.9 <$ [Fe/H] < -1.3) is strongly retrograde at high energies (see e.g., Figure 2 of Myeong et al., 2018c). By contrast, at lower metallicities, there are very few halo stars that are retrograde and high energy. This is evidence of a considerable retrograde merger or accretion event in the recent past (e.g., Norris and Ryan, 1989; Quinn and Goodman, 1986).

Here, we carry out a search for halo substructure in action space using the SDSS-*Gaia* catalogue. This is a modification of our earlier search for halo substructure in velocity space (Myeong et al., 2018a). There are a number of advantages to using actions. Unlike integrals of motion, actions preserve their invariance under slow changes (e.g., Goldstein and Poole, 1980). They have often been suggested as the natural coordinates for galactic dynamics (see e.g., Binney and Spergel, 1982), in which of course the potential is evolving in time. Helmi and White (1999) first argued that fossil structures in the stellar halo may be identifiable as clusters in action space. This idea has been tested extensively with numerical simulations both in static analytical potentials and in time-varying cosmological potentials (Gómez et al., 2010; Helmi and White, 1999; Knebe et al., 2005).

The identification of substructures enables us to map out the accretion history of the Milky Way. For example, Myeong et al. (2018a) found two prominent substructures in velocity space (S1 and S2) and used a library of accreted remnants to estimate that they correspond to dwarf galaxies with virial masses of $\approx 10^{10} M_{\odot}$ that fell into the Milky Way $\gtrsim 9$ Gyr ago. Likewise, Belokurov et al. (2018) have suggested that the highly radially anisotropic velocity distribution of halo stars may be the imprint of a massive merger event, for which evidence also exits in the radial profile of the stellar halo density law (Deason et al., 2013).

Retrograde substructures are interesting, because they may be related to the anomalous globular cluster ω Centauri. This has a present-day mass of $5 \times 10^6 M_\odot$ (Meylan et al., 1995) and is believed to be the stripped nucleus of a dwarf galaxy (Bekki and Freeman, 2003). This is bolstered by the fact that ω Centauri has long been known to contain multiple stellar populations (Bedin et al., 2004; Norris et al., 1996; Suntzeff and Kraft, 1996). Not merely do the stars in ω Centauri exhibit a large metallicity spread (Norris and Da Costa, 1995), but there are extreme star-to-star variations in many light elements (Marino et al., 2012; Milone et al., 2017). If ω Centauri was once a dwarf galaxy, then its virial mass may have been as high as $10^{10} M_\odot$ based on models of the chemical evolution of multi-population clusters (Valcarce and Catelan, 2011). Dynamical evolutionary models find similar, though somewhat lower, starting values of $\sim 10^8 - 10^9 M_\odot$ (e.g., Bekki and Freeman, 2003; Tsuchiya et al., 2003, 2004). Therefore, ω Centauri must have disgorged much of its initial mass of stars (and dark matter) as tidal debris in its passage to the inner Galaxy.

Searches for tidal debris in the solar neighbourhood date back to at least Dinescu (2002), who found a retrograde signature in the solar neighbourhood for stars in the metallicity range $-2.0 \leq$[Fe/H] ≤ -1.5. Further kinematic searches followed, though primarily with small samples of stars concentrated in the solar neighbourhood (e.g., Brook et al., 2003; Fernández-Trincado et al., 2015; Meza et al., 2005; Mizutani et al., 2003). Majewski et al. (2012) examined the line of sight velocities of ~ 3000 metal-poor stars within 5 kpc and conjectured that most of the retrograde stars in the inner halo may be related to the disruption of ω Centauri. There have also been suggestions of evidence of material torn from ω Centauri by Morrison et al. (2009) and Helmi et al. (2017) based on their studies with 246 metal-poor stars and 1912 halo stars respectively. However, some specific groups that have been suggested as likely contenders for material stripped off – such as Kapteyn's Moving Group (Wylie-de Boer et al., 2010) and the so-called ω Centauri Moving Group (Meza et al., 2005) – have not survived detailed scrutiny based on the chemical evidence (Navarrete et al., 2015).

This Chapter is organised as follows. Section 5.2 describes our algorithm for substructure search in action space using the SDSS-*Gaia* catalogue. We identify 21 substructures in total with coherent kinematics and narrow metallicity distributions. Remarkably, we find that some of the most significant substructures are comparatively metal-rich, high energy and retrograde. Section 5.3 describes the properties of our retrograde candidates, and uses simple models of dynamical friction to investigate whether at least some of the new retrograde substructures are likely to be the shards of ω Centauri. We draw our conclusions in Section 5.4.

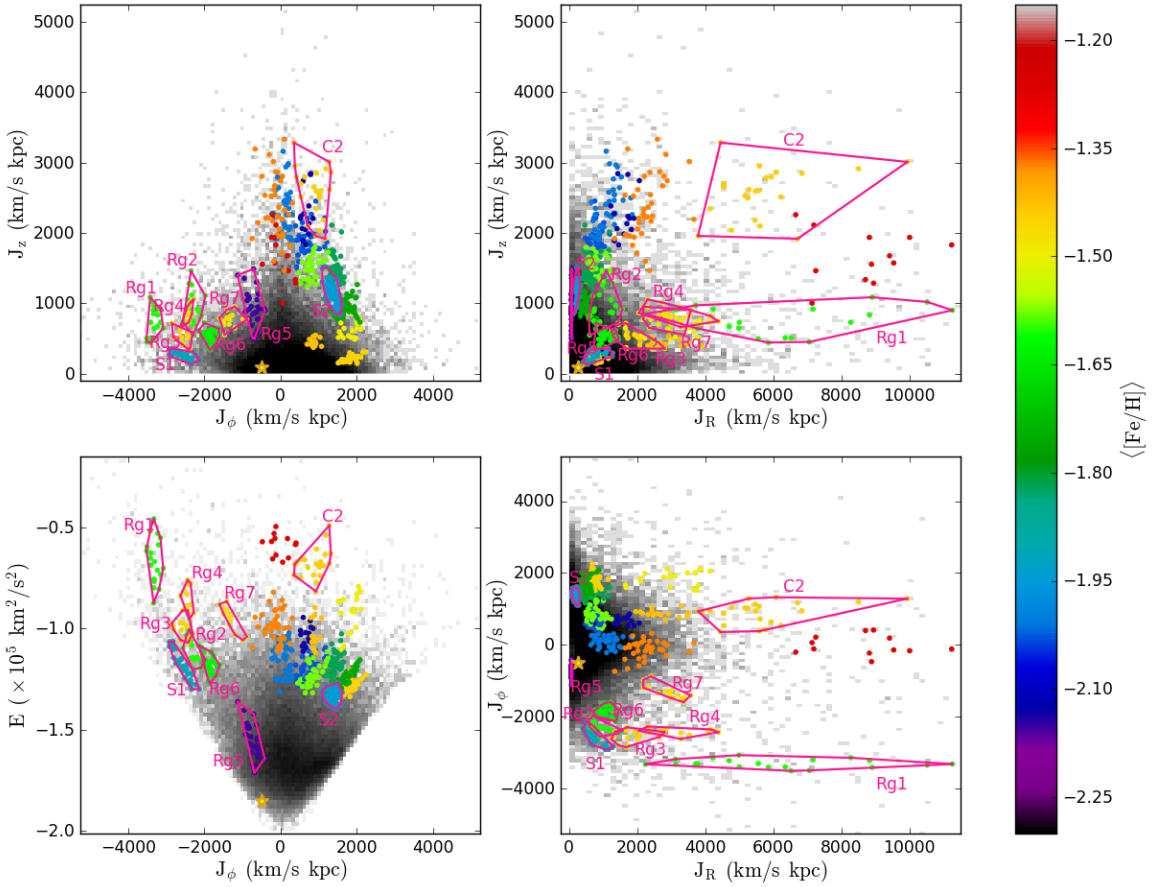

Fig. 5.2 Distribution of the stellar halo sample and substructure candidates in action – energy space. Top left: (J_ϕ, J_z). Top right: (J_z, J_R). Bottom left: (J_ϕ, E). Bottom right: (J_R, J_ϕ). The 21 most significant substructures are colour-coded according to metallicity. Previously found substructures (S1, S2, C2) and seven highlighted candidates (Rg1 – Rg7) are further highlighted with a magenta outline. The golden star in each panel represents the present position of ω Centauri.

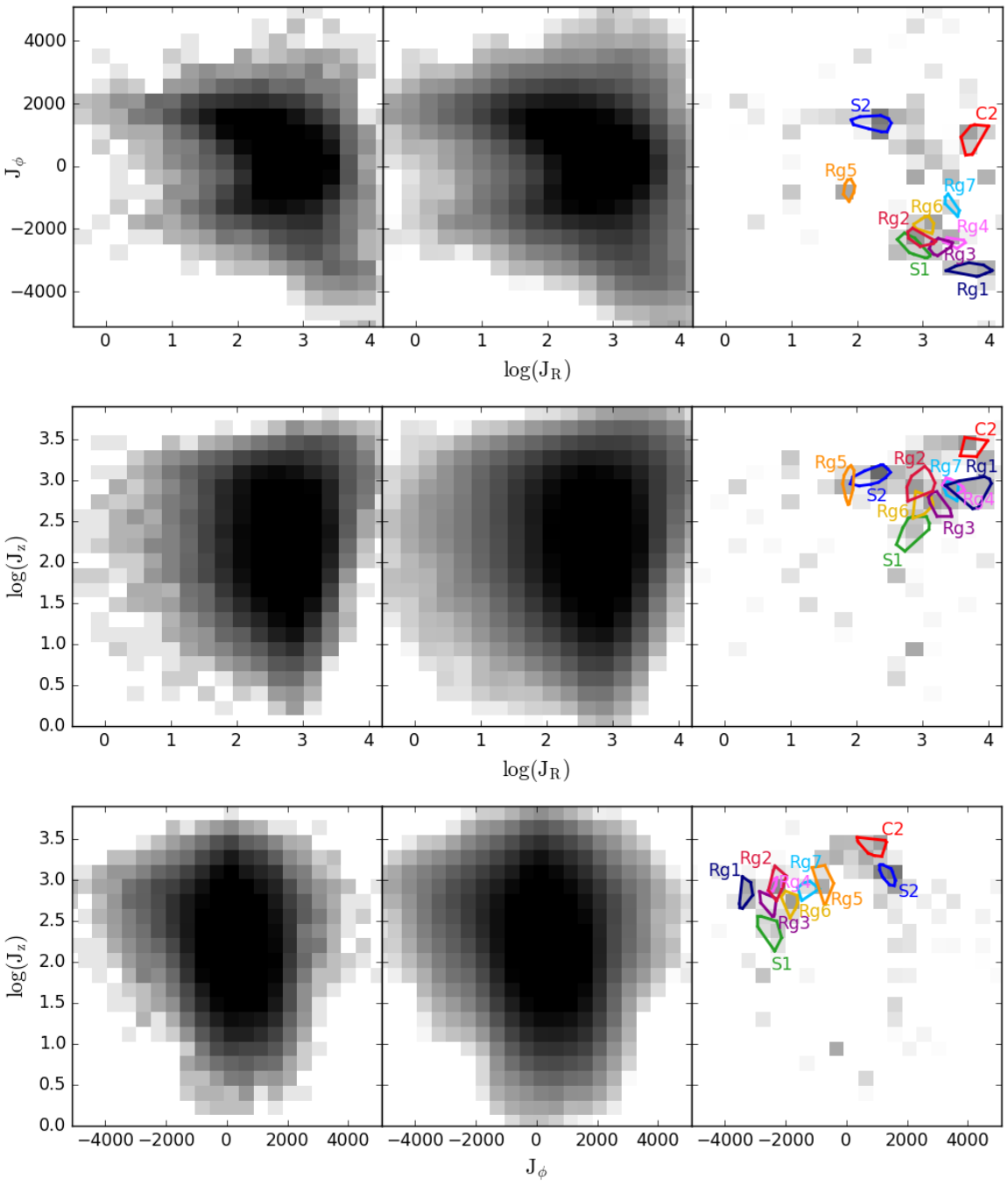

Fig. 5.3 Two-dimensional projection of the detection space. We show from left to right the data, the smooth Gaussian kernel density model, and the residuals. The rows show the principal planes in action space $(\log J_R, J_\phi)$, $(\log J_R, \log J_z)$ and $(J_\phi, \log J_z)$ respectively. Reassuringly, the residuals correspond to the locations of the main pieces of substructure.

5.2 Detection of Substructures

5.2.1 Method

We use the SDSS-*Gaia* catalogue. This is created by the crossmatch between Gaia data release 1 (DR1), the Sloan Digital Sky Survey data release 9 and LAMOST data release 3 (see, Ahn et al., 2012; Luo et al., 2015). Briefly, the main sequence turn-off stars (MSTOs) are extracted using the cuts: extinction $\varepsilon_r < 0.5$, g,r,i magnitudes satisfying $14 < g < 20$, $14 < r < 20$, $14 < i < 20$, $0.2 < (g-r)_0 < 0.8$ with surface gravity $3.5 < \log g < 5.0$ and effective temperature $4500 < T_{\rm eff} < 8000$. The rationale for the cuts is described in detail in Williams et al. (2017). The blue horizontal branch stars (BHBs) are chosen from $-0.25 < (g-r)_0 < 0.0$, $0.9 < (u-g)_0 < 1.4$ with spectroscopic parameters satisfying $3.0 < \log g < 3.5$ and $8300 < T_{\rm eff} < 9300$. Photometric parallaxes based on the SDSS photometry are used for MSTOs and BHBs using the formulae in Ivezić et al. (2008) and in Deason et al. (2011b) to give full six-dimensional phase space coordinates. We apply a series of quality cuts to both the photometric and spectroscopic data to remove stars with poor measurements as well as stars with a heliocentric radial velocity error > 15 kms^{-1}, distance error > 2.5 kpc, and a heliocentric distance > 10 kpc.

We then convert the observables to velocities in the Galactic rest-frame. We use the Milky Way potential of McMillan (2017), which gives the circular speed at the Sun as 232.8 km s^{-1}. For the Solar peculiar motion, we use the most recent value from Schönrich et al. (2010), namely $(U,V,W) = (11.1, 12.24, 7.25)$ km s^{-1}. The separation between the disk and the halo stars is carried out based on their azimuthal velocity and their metallicity (e.g., Myeong et al., 2018a). The equation for the excision of disk stars is

$$[\mathrm{Fe/H}] \gtrsim -0.002\, v_\phi - 0.9 \tag{5.1}$$

where v_ϕ is the azimuthal velocity in direction of the Milky Way rotation and [Fe/H] the metallicity. This equation gives a good description of the more elaborate statistical separation displayed in Figure 1 of Myeong et al. (2018a). After the cuts, we obtain a sample of 62 133 halo stars comprising 61 911 MSTO stars and 222 BHB stars (59 811 stars with SDSS DR9 and 2 322 stars with LAMOST DR3 spectroscopy). The locations of these stars are shown projected onto the principal planes of the Galaxy in Fig. 5.1. Notice that the sample extends well beyond the solar neighbourhood out to heliocentric distances of 10 kpc. There are clear spatial selection effects, and the footprint of the Sloan Digital Sky Survey can be readily discerned. Nonetheless, the sample is kinematically unbiased and has already proved to be a treasure trove for substructure searches in velocity space (Myeong et al., 2018a).

Next, the actions of each star are computed using the numerical method of Binney (2012) and Sanders and Binney (2016). We construct a background model representing the underlying smooth distribution of the data in the 3-dimensional action space $(\log(J_R), J_\phi, \log(J_z))$. We perform our search in logarithmic scale for J_R and J_z to compensate for the increase in spread of J_R and J_z which can reach large values for halo stars (see e.g., Figure 7 of Sanderson et al., 2015). The density estimation with a Gaussian kernel (KDE) from `Scikit-learn` (Pedregosa et al., 2011) is used with the optimal bandwidth determined by cross-validation. From this model, we generate 200 random samples with the same size as the data. For each sampling, we use a k-nearest neighbour search with $k = 5$ to measure the density at the location of each star in the actual data. The mean of these 200 independent measurements is considered as the local density S_0 expected by the model (computationally faster than deriving the model density by Gaussian KDE itself). The similar k-nearest neighbours search is applied on the original data to obtain the actual measured density S. From the probability density function, $P(S) \approx S^{-k-1} \exp(-kS_0/S)$, we compute the probability percentile of the measured density and convert it to the number of sigma indicating the significance.

Stars with significance > 4 are used as "seeds" for searching for overdensities in action space. The seeds are first classified into several groups based on their relative location in the action space by the hierarchical agglomerative clustering implementation in `Scikit-learn`. For each seed, we collect nearby stars within a local volume of ellipsoid with semi-axes corresponding to one third of the standard deviation of each action. We discard any seeds that have less than 5 stars within this volume. The collected stars are classified by the Nearest Neighbours Classification from `Scikit-learn`. The classifier is trained on the pre-classified seeds and performs a distance-weighted $(k = 3)$ neighbours classification on stars. This provides us with a list of substructure candidates.

For each candidate, we measure the volume of ellipsoid in action space occupied by its member. The expected density (predicted by the model) at the centre of this volume is used to estimate the expected number of stars for the candidate, and hence obtain the significance (using the same method as described above). To obtain a high quality list, we require that a candidate (i) has significance > 4, (ii) contains more than 10 stars and (iii) has a metallicity distribution function (MDF) strongly peaked in comparison with the halo MDF. The latter is judged by first decomposing the halo MDF into two Gaussians (with dispersions 0.38 and 0.27 as the result of Gaussian mixture model. see e.g., Figure 1 of Myeong et al., 2018a). We require that a Gaussian fit to our candidate MDF should have a dispersion less than 0.27, ensuring that it is peakier than the halo MDF. This gives us 21 candidate substructures.

5.2.2 Algorithm Validation

Before proceeding, we report two cross-checks. Using the public software package AGAMA (Vasiliev, 2019a), we generated a smooth model of a stellar halo (Williams and Evans, 2015) in the potential of McMillan (2017). We created a catalogue of 250 000 stars within a heliocentric distance of 10 kpc around the Sun with the disk and the bulge region eliminated using $|z| > 1.5$ kpc and $r > 3.0$ kpc. The algorithm identified no substructures as it found no "seeds".

Secondly, we tested on publicly available stellar haloes created by cosmological zoom-in simulations. We used the Aquarius catalogue provided by Lowing et al. (2015). The catalogue lists the "TreeID" for each star providing the information of the parent satellite that brought the star into the main halo. We obtained the catalogue of 250 000 stars with 49 TreeIDs in the local volume of 10 kpc around the Sun with disk and bulge region excluded. However, some of the TreeIDs contribute very few stars in the local volume. There are 34 TreeIDs with > 50 stars. This seems a reasonable figure against which to measure performance of our method.

Our algorithm identified 28 candidate substructures after applying the significance $\sigma > 4$ and number of member stars > 10 cuts. The smallest candidate has 40 stars. Although all the substructures identified by the algorithm are real, there is not a one-to-one correspondence between TreeIDs and candidates. Of these, 2 TreeIDs are detected as multiple candidates (4 candidates and 3 candidates respectively) and 2 candidates show significant internal blending of multiple TreeIDs. For the case of blended candidates, we note that these multiple TreeIDs in the same candidate have virtually the same actions. Interestingly, they also occupy the same region in the configuration space with the indistinguishable streaming motion – therefore the same actions. This may be a case of multiple satellites accreted to the main halo along the same dark matter filament at a similar redshift. In this case, multiple TreeID groups are accreted with almost identical kinematics.

We conclude that the present algorithm works well, in the sense of identifying overdensities with high significance and generating candidate lists for these overdensities. In particular, the tunable parameters in the algorithm (bandwidth, linking procedure, number of nearest neighbours) have been set conservatively. Although some highly disrupted structures are missed, most substructures get picked up, unless they are too small in size.

Our method has some points of similarity with Helmi et al. (2017) and also some points of difference, which it is useful to summarise. Both algorithms use the data to derive a smooth background model. However, our search proceeds in action space, whereas Helmi et al. (2017) use an 'integral of motion space' that is most appropriate for a spherical potential. Secondly, Helmi et al. (2017) begins with a two-dimensional search in (E, J_ϕ)

with a corroborating check for projections in the third integral of motion, whereas we carry out our search in the three-dimensional action space (J_R, J_ϕ, J_z) from the beginning. Thirdly, Helmi et al. (2017) do not account for the Solar peculiar motion and take the Local Standard of Rest as 220 kms^{-1}, whereas we use the circular speed at the Sun as 232.8 $\mathrm{km\,s}^{-1}$ and the Solar peculiar motion from Schönrich et al. (2010), namely $(U,V,W) = (11.1, 12.24, 7.25)$ $\mathrm{km\,s}^{-1}$. These differences are important, as for very local stars they can cause a change from prograde to retrograde. Fourthly, we require that the metallicity distribution functions of our substructures to be strongly peaked, whereas no such requirement is imposed in Helmi et al. (2017). These differences in methodology mean that we do not detect any of the "VelHels" identified by Helmi et al. (2017). Many of the "VelHels" have rather broad metallicity distribution functions (Veljanoski and Helmi, 2018) and would fail our criteria.

Although the algorithms are related, the main difference is the size of the dataset through which we search. Helmi et al. (2017) uses a sample of 1912 halo stars extracted from TGAS crossmatched with RAVE. Our algorithm has been applied to a sample of 62 133 stars with full six-dimensional phase space information in the SDSS-*Gaia* catalogue (see e.g., de Boer et al., 2018; Deason et al., 2017). We identified 21 high significance substructures. These all have morphological features that resemble segments of orbits close to pericentre, as well as compact metallicity distributions. The stars belonging to the substructures are therefore kinematically and chemically similar.

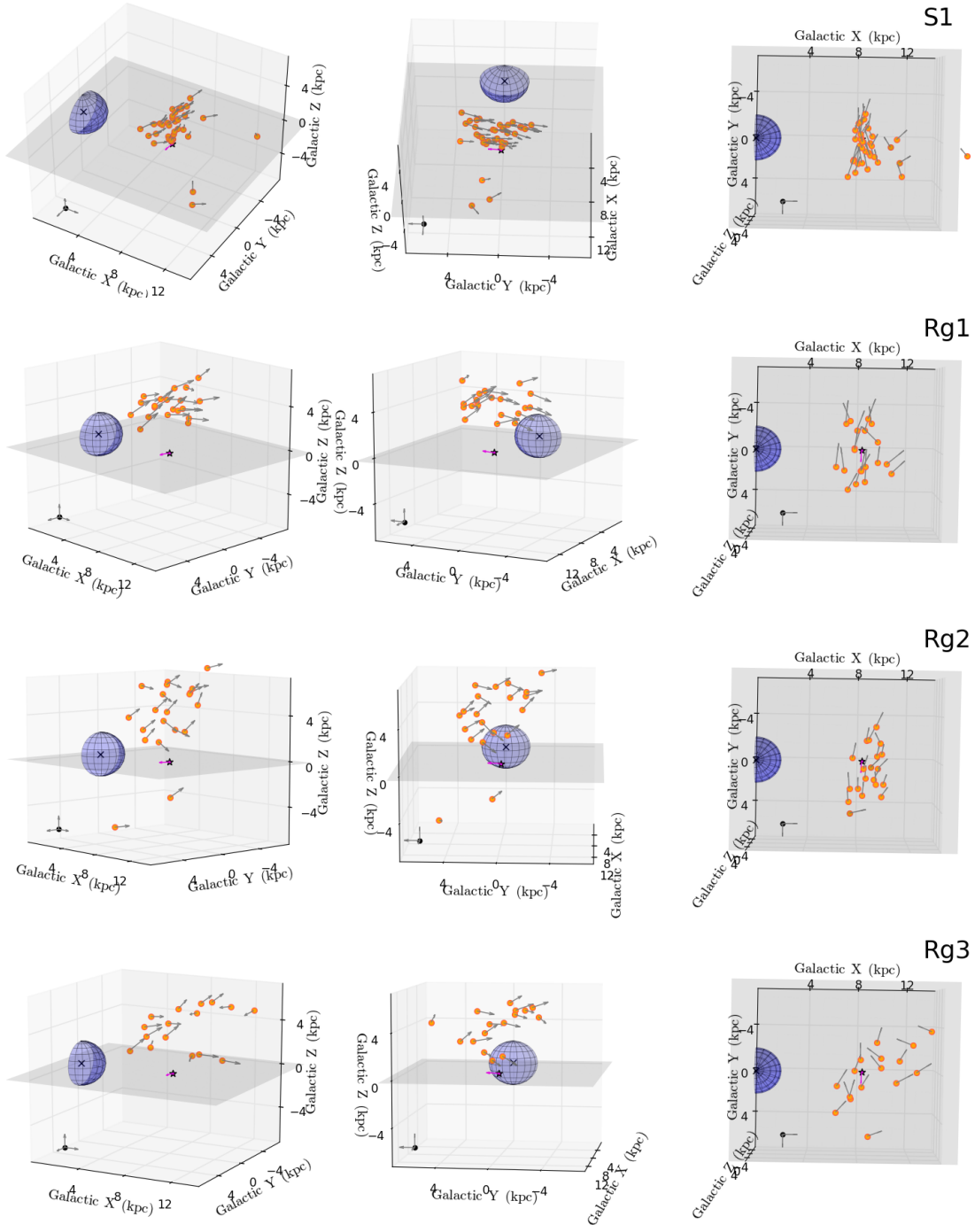

Fig. 5.4 Spatial distribution of 4 selected retrograde substructures, the previously known S1 and the new Rg1, Rg2, and Rg3. Left and Middle: Two views of the substructure depicting the overall shape and motion. Right: Projection of the substructure onto the Galactic plane. The arrow shows the total Galactocentric velocity. The Sun and the Sun's motion are marked as a star and a magenta arrow. A 2 kpc radius sphere and a grey plane are crude representation of the Galactic bulge and the Galactic plane to give a sense of substructure's scale and location in Galactic frame. A black triad of velocity vectors (scale of 300 km s^{-1}) is marked in each panel.

Table 5.1 The mean, mean absolute deviation and dispersions in positional and kinematic properties of the already known S1 and 7 new retrograde candidate substructures (Rg1 – Rg7). Also given are metallicity [Fe/H], as well as orbital properties, including energy E, circularity η (or ratio of total angular momentum to the angular momentum of a circular orbit of the same energy), and orbital inclination i. An electronic list of substructure member stars is available from the authors.

Name		[Fe/H]	(J_R, J_ϕ, J_z) ($\mathrm{kms}^{-1}kpc$)	η	incl. i (deg)	(X,Y,Z) (kpc)	(v_R, v_ϕ, v_z) (kms^{-1})	E ($\mathrm{km}^2\mathrm{s}^{-2}$)	Mem. no.
	Mean	-1.91	(749.7,-2551.1,253.4)	0.74	157.43	(8.9,0.6,2.5)	(-8.6,-286.7,-67.9)	-118958	
S1	MAD	0.22	(186.6,180.9,51.2)	0.04	2.25	(1.0,1.2,1.2)	(104.5,40.9,45.8)	5761	34
	Dispersion	0.26	(234.8,210.4,60.3)	0.05	2.56	(1.6,1.4,1.9)	(115.3,49.9,60.0)	6933	
	Mean	-1.60	(6066.6,-3309.0,759.5)	0.36	145.37	(8.3,0.2,4.3)	(54.1,-393.8,68.3)	-65634	
Rg1	MAD	0.14	(2033.8,94.2,174.8)	0.08	3.94	(0.8,1.7,0.8)	(121.8,37.2,135.7)	9459	20
	Dispersion	0.17	(2452.3,116.3,197.0)	0.09	4.54	(1.1,1.9,1.0)	(147.2,45.7,149.4)	11260	
	Mean	-1.60	(980.5,-2307.8,930.0)	0.71	136.29	(8.8,0.8,4.0)	(47.8,-254.6,71.8)	-109787	
Rg2	MAD	0.12	(270.5,109.3,175.2)	0.05	3.56	(0.7,1.7,2.4)	(91.5,22.6,149.4)	6027	20
	Dispersion	0.11	(303.1,140.8,221.0)	0.06	4.47	(0.8,2.0,3.2)	(110.2,27.8,172.1)	6578	
	Mean	-1.46	(1844.3,-2550.5,503.5)	0.54	148.35	(9.3,0.1,4.2)	(28.0,-275.1,18.0)	-99899	
Rg3	MAD	0.17	(356.7,136.6,90.4)	0.05	3.01	(1.8,1.9,1.4)	(160.4,54.6,123.2)	3978	16
	Dispersion	0.22	(445.8,163.5,112.2)	0.07	3.52	(2.1,2.3,1.6)	(186.0,62.7,136.5)	4769	
	Mean	-1.47	(3228.6,-2423.1,850.8)	0.42	138.64	(8.2,1.7,5.0)	(177.6,-287.9,117.9)	-84803	
Rg4	MAD	0.14	(683.5,64.8,89.8)	0.06	2.40	(1.1,1.5,1.4)	(88.5,35.5,142.1)	5541	13
	Dispersion	0.19	(781.9,85.2,111.4)	0.07	3.03	(1.6,1.8,1.7)	(114.6,46.0,162.7)	6217	
	Mean	-2.16	(75.4,-723.5,937.4)	0.89	114.98	(8.2,0.3,1.7)	(-10.0,-82.3,-0.6)	-155848	
Rg5	MAD	0.23	(5.7,124.9,188.6)	0.02	3.71	(0.8,1.1,2.1)	(72.3,17.2,158.2)	7073	29
	Dispersion	0.20	(7.2,154.4,247.1)	0.03	4.68	(1.1,1.4,3.0)	(83.2,21.2,162.7)	8588	
	Mean	-1.63	(1074.5,-1837.7,522.9)	0.60	141.76	(8.2,0.7,3.0)	(-11.9,-222.1,88.0)	-117935	
Rg6	MAD	0.17	(174.0,94.8,74.4)	0.04	2.96	(1.4,1.3,2.0)	(178.6,35.4,115.1)	3336	30
	Dispersion	0.22	(210.2,125.2,91.4)	0.05	3.72	(2.0,1.7,2.5)	(187.6,44.0,134.9)	4439	
	Mean	-1.48	(2883.7,-1314.8,770.6)	0.33	129.61	(8.6,0.1,4.4)	(-92.3,-160.2,-33.4)	-95342	
Rg7	MAD	0.17	(385.4,148.8,70.7)	0.02	3.24	(1.6,1.1,2.0)	(255.2,53.2,138.0)	5236	14
	Dispersion	0.24	(447.6,190.7,96.6)	0.03	4.07	(2.0,1.4,2.6)	(274.6,66.5,178.1)	6073	

Table 5.2 The mean, mean absolute deviation and dispersions in positional and kinematic properties of the prograde or radial candidate substructures. This includes the previously known S2 and C2, as well as the new candidates (Cand8 – Cand18). Also given are metallicity [Fe/H], as well as orbital properties, including energy E, circularity η (or ratio of total angular momentum to the angular momentum of a circular orbit of the same energy), and orbital inclination i. A list of substructure member stars is available from the authors electronically.

Name		[Fe/H]	(J_R, J_ϕ, J_z) ($\mathrm{kms}^{-1}kpc$)	η	incl. i (deg)	(X, Y, Z) (kpc)	(v_R, v_ϕ, v_z) (kms^{-1})	E ($\mathrm{km}^2\mathrm{s}^{-2}$)	Mem. no.
	Mean	-1.94	(206.1,1363.3,1144.6)	0.88	58.64	(9.1,0.3,0.9)	(-11.2,159.6,-166.5)	-133500	
S2	MAD	0.19	(45.6,101.2,118.8)	0.02	2.33	(1.0,0.9,2.6)	(46.7,16.6,110.7)	2488	73
	Dispersion	0.23	(55.8,120.0,146.5)	0.03	2.96	(1.5,1.2,3.2)	(65.6,21.9,151.7)	2987	
	Mean	-1.45	(5718.7,896.5,2577.4)	0.30	75.55	(9.0,-0.6,2.3)	(-242.4,109.9,180.7)	-67927	
C2	MAD	0.11	(938.3,247.9,282.7)	0.03	3.66	(0.9,0.8,1.9)	(155.1,28.5,189.5)	4916	22
	Dispersion	0.13	(1359.0,296.6,354.3)	0.04	4.45	(1.2,0.9,2.5)	(229.2,35.9,236.1)	7011	
	Mean	-1.76	(498.5,1695.6,940.0)	0.77	51.72	(9.3,0.2,1.9)	(8.2,192.0,-25.0)	-125103	
Cand8	MAD	0.21	(92.3,162.7,84.4)	0.03	2.01	(1.6,1.9,3.6)	(104.4,32.9,169.6)	3537	49
	Dispersion	0.22	(117.4,197.9,109.0)	0.04	2.60	(2.0,2.4,4.2)	(124.0,40.2,186.6)	4317	
	Mean	-1.82	(672.2,1423.6,1488.1)	0.75	61.75	(9.1,-0.1,1.7)	(48.4,164.5,-171.1)	-118088	
Cand9	MAD	0.15	(182.1,101.2,150.0)	0.04	1.90	(0.9,1.2,2.5)	(118.3,18.0,125.1)	4324	44
	Dispersion	0.18	(221.4,123.2,201.3)	0.05	2.40	(1.2,1.6,3.4)	(139.6,24.2,172.0)	5626	
	Mean	-2.01	(1127.1,94.2,2345.9)	0.61	88.01	(8.7,0.0,1.8)	(-115.6,17.4,169.3)	-115259	
Cand10	MAD	0.13	(255.7,123.3,269.8)	0.04	2.73	(1.4,1.0,2.0)	(175.1,15.1,137.8)	6958	39
	Dispersion	0.18	(306.7,144.5,329.2)	0.06	3.23	(1.9,1.3,2.8)	(200.3,18.5,197.5)	7929	
	Mean	-2.03	(795.4,722.1,1903.9)	0.69	74.93	(9.1,-0.2,2.5)	(-82.8,91.7,41.4)	-119169	
Cand11	MAD	0.20	(113.3,181.1,139.5)	0.04	2.68	(1.7,0.9,2.5)	(153.8,26.0,221.2)	4128	37
	Dispersion	0.13	(144.3,222.8,185.1)	0.04	3.33	(2.1,1.2,3.2)	(171.1,36.6,239.8)	4980	
	Mean	-1.57	(800.8,828.0,1505.6)	0.66	70.26	(9.6,-0.8,3.7)	(-33.3,94.4,60.9)	-122892	
Cand12	MAD	0.17	(174.1,152.3,129.1)	0.05	2.46	(1.6,2.1,3.2)	(151.8,21.9,173.4)	4141	36
	Dispersion	0.19	(204.5,197.8,153.0)	0.06	3.01	(2.0,2.5,4.2)	(175.4,26.8,197.5)	5021	

Table 5.2 continued.

Name		[Fe/H]	(J_R, J_ϕ, J_z) (kms^{-1}kpc)	η	incl. i (deg)	(X, Y, Z) (kpc)	(v_R, v_ϕ, v_z) (kms^{-1})	E (km^{2}s^{-2})	Mem. no.
	Mean	-1.37	(2272.7,-125.6,2356.9)	0.44	92.40	(9.1,1.0,3.1)	(-101.3,-9.3,98.4)	-98737	
Cand13	MAD	0.13	(360.1,183.8,373.0)	0.04	3.71	(1.9,1.6,3.2)	(223.1,22.0,203.0)	5956	36
	Dispersion	0.18	(481.6,239.5,449.8)	0.06	4.88	(2.5,2.0,4.1)	(246.4,30.4,238.1)	7373	
	Mean	-1.45	(777.4,1837.4,219.4)	0.65	30.97	(11.5,0.2,1.6)	(-51.6,170.5,-7.5)	-128409	
Cand14	MAD	0.15	(91.2,130.2,37.5)	0.04	1.36	(1.6,1.4,3.1)	(155.1,20.9,79.9)	2408	36
	Dispersion	0.17	(116.0,169.3,44.3)	0.05	1.75	(1.9,1.8,3.6)	(166.6,27.0,90.1)	3050	
	Mean	-1.49	(3041.5,1850.1,625.0)	0.37	43.60	(10.4,0.8,3.4)	(-73.6,186.4,-29.2)	-91662	
Cand15	MAD	0.09	(635.1,170.2,93.3)	0.05	2.17	(1.6,1.7,3.9)	(272.3,25.4,108.5)	6905	19
	Dispersion	0.10	(760.4,195.2,108.6)	0.05	2.63	(1.9,2.3,4.8)	(285.9,34.7,129.2)	8796	
	Mean	-1.43	(2769.2,875.5,450.8)	0.25	50.53	(8.7,1.1,2.3)	(114.6,107.3,90.7)	-102594	
Cand16	MAD	0.12	(450.5,66.2,44.9)	0.04	2.88	(1.2,1.6,3.8)	(255.8,15.6,122.5)	5501	17
	Dispersion	0.09	(538.2,88.9,53.4)	0.05	3.57	(1.5,2.0,4.4)	(283.2,19.3,146.9)	6526	
	Mean	-2.13	(1614.4,673.3,2263.4)	0.56	77.22	(9.7,-0.3,2.6)	(29.0,77.5,116.5)	-103328	
Cand17	MAD	0.15	(210.4,89.7,251.5)	0.03	1.40	(1.0,0.8,1.7)	(171.1,10.6,230.6)	4013	14
	Dispersion	0.18	(240.2,101.4,317.8)	0.04	1.67	(1.3,0.9,2.5)	(201.1,13.2,269.9)	4778	
	Mean	-1.27	(8654.9,-18.1,1665.1)	0.14	89.88	(7.2,-0.1,5.3)	(-151.7,-8.3,-26.3)	-58877	
Cand18	MAD	0.12	(1060.5,223.2,294.1)	0.02	6.96	(2.3,1.6,1.4)	(398.6,35.0,117.5)	4395	12
	Dispersion	0.14	(1304.9,257.8,350.7)	0.03	8.00	(3.1,1.8,1.6)	(424.7,40.6,142.8)	5216	

5.3 Substructure Forensics

Fig. 5.2 shows the 21 high significance substructures in action space and integral of motion space. The data, the underlying smooth model from the Gaussian kernel density estimator and the residuals are shown in the left, middle and right panels of Fig. 5.3. Reassuringly, the identified substructures correspond to prominent residuals, mainly in the outer, relatively less dense parts of the distribution. This is an effect due to the imposition of high significance in candidate selection. Candidates detected at the central denser regions are more vulnerable to blending with random contaminants. Since we use compactness of the MDF of the candidates as one of the criteria for validation, it is natural for us to identify more substructures with high significance in less dense regions. Another thing to notice is that a significant number are in a retrograde tail of stars that emanates from the main body of the distribution in Fig. 5.2. In fact, two of the top three most significant substructures are retrograde. The population of high energy retrograde stars provides a very happy hunting ground for halo substructure in general.

We list the properties of all the retrograde candidates in Table 5.1. The table gives their mean locations, velocities in the Galactic rest-frame and metallicity. We also report their orbital properties, including mean energy E and circularity η, which is the ratio of total angular momentum to the angular momentum of a circular orbit of the same energy $L/L_{\rm circ}(E)$. Another orbital quantity of interest is the inclination to the Galactic plane, defined as $i = \arccos(J_\phi/J)$ where J is the absolute value of the total angular momentum. Although we do not study the new prograde substructure candidates in detail in this Chapter, we list their basic properties in Table 5.2. Electronic tables of member stars are available from the authors.

5.3.1 Cross-checks: Known Candidates (S1, S2, C2)

Myeong et al. (2018a) already identified six halo substructures in the SDSS-*Gaia* catalogue from a search in velocity space. Only three are recovered here with high significance, namely S1, S2 and C2. What happened to the remaining substructures? Two (S3, S4) are found, but at lower significance than we imposed here. C1 is also identified with a large portion of new members, but it fails the requirement that we insisted that the substructure have a compact metallicity distribution. The velocity-based search was more successful in recovering seemingly clean stream-like structures for S2 and C2. However, the power of action space is that it can associate patches of substructures from different pericentric passages (Helmi and White, 1999). This means that more highly phase-mixed material can be associated with the substructure, and so we expect more disrupted morphologies.

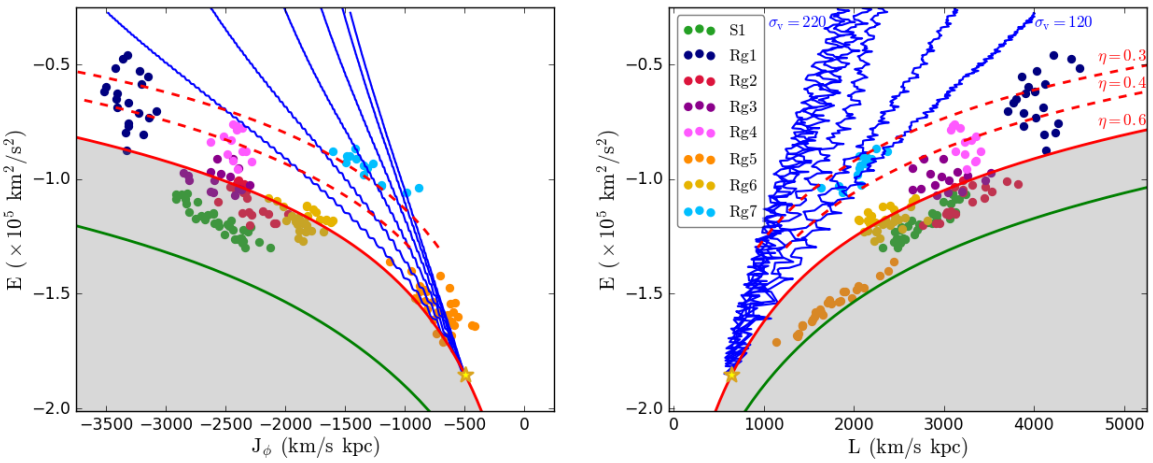

Fig. 5.5 Orbital tracks of ω Centauri in action space (E, J_ϕ) and (E, L) as the progenitor sinks to its present location, together with the retrograde substructures (S1 and Rg1–7). The golden star marks the present position of ω Centauri. The blue tracks the trajectory of the progenitor to the present-day ω Centauri, as given by numerical integration assuming Chandrasekhar dynamical friction with the velocity dispersion of the dark matter varying from 120 kms^{-1} to 220 kms^{-1} in steps of 20 kms^{-1}. We also show the evolution tracks of an object with a constant circularity $\eta \approx 0.6$ (solid red line) corresponding to ω Centauri today, whilst dashed red lines show further constant circularity tracks (0.4 and 0.3). The grey shaded area shows the range of locations in which tidally-torn streams may not reside, as ω Centauri's circularity cannot have diminished during its orbital evolution. The green lines mark the (retrograde) circular orbit limit.

5.3.2 The Retrograde Candidates

These include the previously known S1, and the seven new retrograde candidates (Rg1–7, in order of decreasing significance). The morphology of some of the retrograde substructures is shown in Fig. 5.4. Their shapes are strongly affected by the footprint, as the stars must lie in the SDSS so the coverage of the Southern Galactic hemisphere is patchy. Occasionally, there are stars that do not seem to agree with the overall morphology of the substructure (e.g., in Rg3 there are two stars whose velocity vectors run counter to the trends seen in the remaining stars in the arm). These could be contaminants, but they could also be phase-mixed material. Nonetheless, the overall shapes of the substructures, as well as their velocity distributions, are consistent with orbital segments close to pericentre. The candidates all share similar characteristics in that they are retrograde and all (but one) belong to Myeong et al. (2018c)'s categorisation of the comparatively metal-rich halo ($-1.9 <$ [Fe/H] < -1.3). They are tightly clustered in azimuthal action J_ϕ, but typically have much larger spreads in J_R and J_z. It is interesting to compare S1 as selected in action space with the more ragged view of the same substructure as selected in velocity space and given in Figure 5 of Myeong et al. (2018a). This retrograde substructure passes right through the solar neighbourhood. If there is a dark matter stream associated with this substructure, then it may have important consequences for direct detection experiments.

Of course, ω Centauri is known to be on a retrograde orbit. Its proper motion has recently been re-measured by Libralato et al. (2018) and differs somewhat from the previous value. Using the potential of McMillan (2017), the present energy of ω Centauri is -1.85×10^5 km^2 s^2, whilst its actions (J_R, J_ϕ, J_z) are (264.5, -496.4, 93.5) kms^{-1} kpc. Its position is marked as a golden star in the action plots of Fig. 5.2. This gives a total angular momentum of 646.62 kms^{-1} kpc and a present day circularity of $\eta \approx 0.60$ for ω Centauri. Usually, the effect of dynamical friction on orbits of moderate eccentricity is to circularize orbits. However, van den Bosch et al. (1999) find that the orbital circularity can sometimes stay roughly constant throughout the decay. The eccentricity decreases near the pericentre, but increases near the apocentre such that there is only mild net circularisation or radialisation in their simulations in an admittedly spherical potential (see Figure 9 of van den Bosch et al., 1999). It is reasonable to conjecture that the orbit of ω Centauri can only get more circular with time, or – in this limiting case – stay constant. Thus, the circularity $\eta = 0.6$ line is a limit below which it is not sensible to associate substructure with ω Centauri. This rules out S1, Rg2 and Rg5 as belonging to the sinking ω Centauri.

The circularity $\eta = 0.6$ line is shown in Fig 5.5 with the region below it shaded grey as forbidden. We also show the tracks in red for objects evolving with constant circularity of 0.4 and 0.5 in action space. In addition, we have supplemented these with blue tracks showing

the simple model trajectory of an ω Centauri progenitor (represented as a point mass of $5 \times 10^8 M_\odot$) moving in the Galactic potential of McMillan (2017) and under the influence of dynamical friction as judged by the Chandrasekhar (1943) formula, with the velocity dispersion of the dark matter particles as 120 kms^{-1} to 220 kms^{-1} in 20 kms^{-1} intervals (see also, Chapter 8.1 of Binney and Tremaine, 2008). We use the factor Λ in the Coulomb logarithm from the equation (8.1b) in Binney and Tremaine (2008). We note that these tracks are simple model trajectories and although the Chandrasekhar formula can provide a good description for orbital decay under dynamical friction (Binney and Tremaine, 2008), a more realistic picture will require more sophisticated methods such as N-body simulations (see also, Fujii et al., 2006; Weinberg, 1989). Although we consider ω Centauri as a point mass, its internal velocity dispersion could produce scatter about the tracks. Still, at $5 \times 10^8 M_\odot$, the scatter would have a modest effect on the overall direction of the trajectory. The rate of circularisation does depend on the choice of parameters, especially the velocity dispersion of the halo. These tracks are much steeper, but it is actually difficult to push the trajectories to lower values of J_ϕ than that of the present day ω Centauri. Of course, this calculation omits any effects due to mass loss from ω Centauri or evolution of the Milky Way potential. Given that the structure of the progenitor and the workings of dynamical friction in the Galaxy are not well-known, we regard the region between the constant circularity line $\eta = 0.60$ and the most extreme Chandrasekhar curve as the likely area in which tidal fragments are to be sought and found. This suggests that the substructures Rg1, Rg3, Rg4, Rg6 and Rg7 are all possible candidates.

Further evidence can be provided by the inclinations of the substructures, which are listed in Table 5.1. Here, we use the traditional convention that inclinations greater than 90° describe retrograde orbits. The effect of dynamical friction is to drag the orbit of a sinking satellite down towards the Galactic plane. Unsurprisingly ω Centauri is now on a rather low inclination orbit $i_{\mathrm{OC}} = 140.15°$. So, candidates with more inclined retrograde orbits (that is, smaller i), or within the range of their dispersion with the present day inclination of ω Centauri, are feasible. Rg1 has a slightly less inclined orbit ($i = 145.37°$), but considering its dispersion of 4.54°, it is still plausible. Rg3 has a less inclined orbit ($i = 148.35°$), and even taking into account its dispersion, it does not cause it to overlap with i_{OC}. Rg4 has comparable but more inclined orbit (138.64°). Rg6 has a slightly less inclined orbit (141.76°), while its dispersion takes it within the range. Rg7 has considerably more inclined orbit (129.61°) – more than 10° difference. This leaves Rg1, Rg4, Rg6 as the strongest candidates, with Rg3 and Rg7 somewhat less favoured.

The validity of the claims can be established by seeing which substructures are chemically consistent with ω Centauri via high resolution spectroscopy. Navarrete et al. (2015) studied

two prominent pieces of retrograde substructure, Kapteyn's Moving Group, and the so-called ω Centauri group. Both have been previously been claimed to be material shed by ω Centauri on its journey to the inner Galaxy (Meza et al., 2005; Wylie-de Boer et al., 2010). However, both groups are not related to ω Centauri, based on abundances from Na, O, Mg, Al, Ca and Ba derived from optical spectra. In particular, ω Centauri has characteristic Na-O and Mg-Al patterns of abundances for moderately metal-rich halo stars, as well as an overabundance of Ba, that are different from the halo field stars. The GALAH survey (Buder et al., 2018), with its range of elemental abundances, may also be useful here.

If the substructures are not related to ω Centauri, then they are perhaps even more interesting and puzzling! Presumably they must then be the remnants of objects that are highly phase-mixed and so little now remains even of the nucleus. Studying the elemental abundance ratios of the retrograde substructure will greatly benefit the unravelling of their true origin. In particular, we would obtain evidence on the importance of rapid (r) and slow (s) process enrichment. It would be interesting to see if they show evidence for the anomalous r-process enhancement, already detected for some of the faintest dwarf galaxies (Ji et al., 2016; Roederer, 2017). To this end, the authors happily make available electronic tables of the member stars in the retrograde substructures as target lists for spectroscopy.

5.4 Conclusions

This Chapter has developed a new algorithm to search for substructure in action space. As actions are conserved under slow evolution of the potential, stars accreted onto the Milky Way halo in the same merger event should be clustered in action space. Thus, the algorithm searches for significant overdensities with respect to the data-derived background model. The metallicity distribution function of the substructures is required to be more strongly peaked than the stellar halo metallicity distribution function itself. The final substructure candidates are therefore clustered both in action and in metallicity. Our algorithm has been validated against mock catalogues of substructure in the Aquarius cosmological zoom-in simulations provided by Lowing et al. (2015).

This algorithm is similar in spirit to our earlier search strategy in velocity space, though here we have used a Kernel density estimator to model the background rather than a Gaussian mixture model (Myeong et al., 2018a). We applied our algorithm to a sample of 62 133 halo stars with full phase space coordinates extracted from the SDSS-*Gaia* catalogue. The sample size is at least an order of magnitude greater than any previous substructure search in phase space (see e.g., Helmi et al., 2017; Morrison et al., 2009). The stars extend out to heliocentric

distances of ~ 10 kpc, and this permits us to identify coherent features in phase space in an unprecedently large volume of the Galaxy.

Altogether, we identified 21 high significance substructures in action space. Here, we have focussed on eight substructures that lie in the retrograde, high energy portion of action space. This includes the previously discovered S1 substructure (Myeong et al., 2018a), as well as seven new candidates (Rg1–7). Myeong et al. (2018c) already showed that the retrograde, high energy stars in the local halo are confined to a restricted range of metallicities ($-1.9 <$ [Fe/H] < -1.3). The origin of this high energy and clumpy component of the local stellar halo remains a puzzle. Although the substructure must have come from mergers of retrograde satellites, it remains unclear whether one large satellite or multiple smaller ones are responsible.

One possible source of the abundant retrograde substructure is the anomalous globular cluster, ω Centauri. There is a long history of searches in the solar neighbourhood for stars tidally torn from ω Centauri (e.g., Dinescu, 2002; Meza et al., 2005; Morrison et al., 2009). On studying a sample of metal-poor halo giants within ~ 5 kpc, Majewski et al. (2012) made the bold conjecture that the disruption of the progenitor of ω Centauri may have generated a very substantial part of the retrograde population in the stellar halo. It is this hypothesis that we can hope to test with substructure searches in deeper halo catalogues like SDSS-*Gaia*.

Here, we have shown based on kinematic evidence that three of our substructures (Rg1, Rg4, Rg6) could be the shards of ω Centauri. Rg3 and Rg7 are also possible, though they are somewhat disfavoured on the grounds of their present inclination. S1, Rg2 and Rg5 seem ruled out on the grounds of their present circularity. The timescale of the orbital decay due to the dynamical friction depends on the mass of the satellite (e.g. van den Bosch et al., 1999). Since this timescale must be shorter than a Hubble time, then, given the current energy and location of ω Centauri, the progenitor must have had a mass of at least $5 \times 10^8 M_\odot$, comparable to the value found by Bekki and Freeman (2003). This sets a lower bound, as this is an average mass throughout the orbital decay over the Hubble time. Moreover, the mass loss from the tidal stripping and the evolution of the Milky Way potential could cause the actual initial mass to be greater by perhaps an order of magnitude (e.g., Tsuchiya et al., 2003).

The most direct way to test the claims of this Chapter is by obtaining high resolution spectroscopy of the candidate stars in the substructures. In particular, ω Centauri has characteristic Na-O and Mg-Al patterns of abundances for moderately metal-rich halo stars, as well as an overabundance of Ba, that are different from the halo field stars (c.f. Navarrete et al., 2015). Furthermore, suppose for example we establish that Rg3 and Rg4 (but not the others) were associated with ω Centauri. Then, this would provide significant constraints

on the progenitor and the action of dynamical friction, as we would know whether the orbit is circularising. Another intriguing possibility is that the highest energy substructures may have been stripped before extended star formation and multiple population enrichment, and so it may even be possible to see gradients across the substructures.

If chemical evidence disproves our assertion that some of the retrograde substructures belong to ω Centauri, then the situation is perhaps even more interesting. It leaves us with two major puzzles. First, where are the substantial amounts of debris that must have been shed by the ω Centauri progenitor? And second, what is the origin of the high energy, retrograde halo which is riven with substructure? The recent release of the Gaia DR2 dataset (Gaia Collaboration et al., 2018b) offers further golden prospects for resolving these puzzles, as well as for harnessing the power of substructure identification algorithms to build a complete inventory of merger remnants in the stellar halo. The algorithms and techniques that we have developed here will have no small part to play.

Chapter 6

The Sausage Globular Clusters

G. C. Myeong[1], N. W. Evans[1], V. Belokurov[1], J. L. Sanders[1] and S. E. Koposov[1,2]

[1]Institute of Astronomy, University of Cambridge, Madingley Road, Cambridge CB3 0HA, United Kingdom

[2]McWilliams Center for Cosmology, Department of Physics, Carnegie Mellon University, 5000 Forbes Avenue, Pittsburgh PA 15213, USA

Abstract

The *Gaia Sausage* is an elongated structure in velocity space discovered by Belokurov et al. (2018) using the kinematics of metal-rich halo stars. They showed that it could be created by a massive dwarf galaxy ($\sim 5 \times 10^{10} M_{\odot}$) on a strongly radial orbit that merged with the Milky Way at a redshift $z \lesssim 3$. This merger would also have brought in globular clusters. We seek evidence for the associated *Sausage Globular Clusters* by analysing the structure of 91 Milky Way globular clusters (GCs) in action space using the *Gaia* Data Release 2 catalogue, complemented with *Hubble Space Telescope* proper motions. There is a characteristic energy $E_{\rm crit}$ which separates the *in situ* objects, such as the bulge/disc clusters, from the accreted objects, such as the young halo clusters. There are 15 old halo GCs that have $E > E_{\rm crit}$. Eight of the high energy, old halo GCs are strongly clumped in azimuthal and vertical action, yet strung out like beads on a chain at extreme radial action. They are very radially anisotropic ($\beta \sim 0.95$) and move on orbits that are all highly eccentric ($e \gtrsim 0.80$). They also form a

[0]Remark: The work presented in this Chapter has been published in Myeong et al. (2018d). I conceived this project and was responsible for the data acquisition and analysis. My supervisors, N. Wyn Evans and Vasily Belokurov, made an invaluable contribution by consulting and reformatting the first draft into a more logical presentation. Jason L. Sanders and Sergey E. Koposov also provided priceless consultation.

track in the age-metallicity plane compatible with a dwarf galaxy origin. These properties are consistent with GCs associated with the merger event that gave rise to the Gaia Sausage.

6.1 Introduction

There are multiple and striking pieces of evidence for the existence of a massive ancient merger which provides the bulk of the stars in the inner halo of the Milky Way galaxy. For example, the radial density profile of the stellar halo shows a dramatic break at around 30 kpc in tracers such as RR Lyrae and blue horizontal branch stars (e.g., Deason et al., 2011b; Watkins et al., 2009). Deason et al. (2013) argued that this could be interpreted as the last apocentre of a massive progenitor galaxy accreted between 8 and 10 Gyr ago. Myeong et al. (2018c) showed that the kinematics of metal-rich halo stars ($-1.9 <$ [Fe/H] < -1.1) betray extensive evidence of recent accretion using the SDSS-*Gaia* catalogue. The variation in Oosterhoff classes of RR Lyraes with radius (Belokurov et al., 2018) similarly shows evidence that the bulk of the field RRab is provided by a single massive progenitor. Finally, Belokurov et al. (2018) demonstrated that the shape of the velocity ellipsoid of the inner metal-rich stellar halo is highly non-Gaussian and sausage-shaped. They interpreted this *Gaia Sausage* as evidence that two thirds of the local stellar halo could have been deposited via the disruption of a massive ($\gtrsim 10^{10} M_{\odot}$) galaxy on a strongly radial orbit between redshift $z = 3$ and $z = 1$. Although identified in the SDSS-*Gaia* catalogue, recent investigations by Haywood et al. (2018) with the new *Gaia* Data Release 2 (DR2) catalogue (Gaia Collaboration et al., 2018c) support the original hypothesis. If so, then this beast must have brought with it a population of globular clusters (GCs), now dispersed in the inner halo. After all, the similarly massive Sagittarius galaxy (Sgr) is now known to have brought at least 4 and possibly 7 GCs with it (e.g., Forbes and Bridges, 2010; Sohn et al., 2018).

The main aim of this Chapter is to search for the *Sausage Globular Clusters*. The identification of objects accreted in the same merger event is easiest in action space. Actions have the property of adiabatic invariance, so that they stay approximately constant when changes in the potential occur slowly (e.g., Binney and Spergel, 1982; Goldstein and Poole, 1980). Globular clusters accreted in the same event are identifiable as clumped and compact substructures in action space (as is indeed the case for the 4 Sgr GCs – Terzan 7, Terzan 8, Arp 2, Pal 12). Historically, actions were cumbersome to calculate, but recent theoretical advances have transformed the situation (e.g., Binney, 2012; Sanders and Binney, 2016). The power of actions has recently been demonstrated by the identification of the tidal disgorgements of ω Centauri (Myeong et al., 2018b). Here, we display the Milky Way globular clusters in action space using a realistic Galactic potential comprising flattened stellar and gas discs,

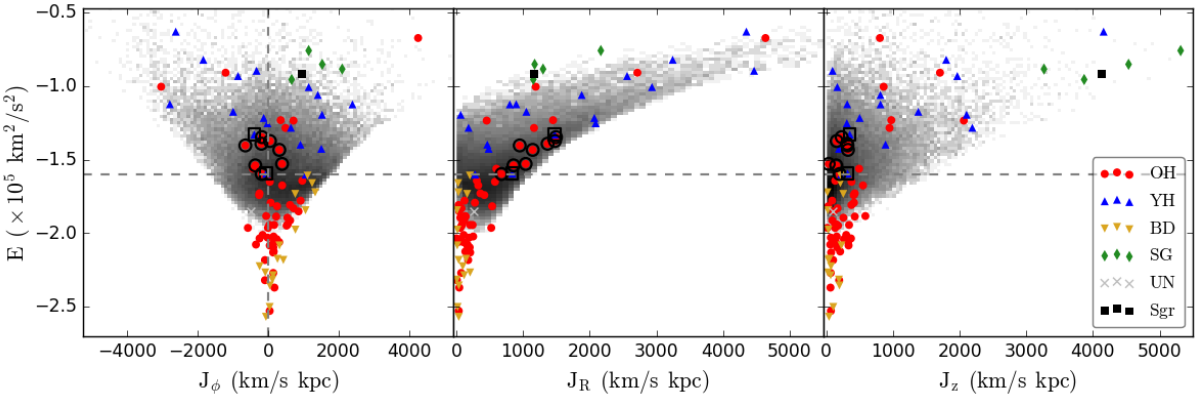

Fig. 6.1 The distribution of globular clusters (GCs) in energy-action space or (J_ϕ, E), (J_R, E) and (J_z, E) space. The grey-scale background shows the halo main-sequence turn-off (MSTO) stars from Myeong et al. (2018c) as a comparison. There are 75 GCs with *Gaia* DR2 proper motions and a further 16 with *Hubble Space Telescope* proper motions; 53 old halo (OHs, red circles), 17 young halo (YHs, blue triangles), 16 bulge/disc (BDs, yellow triangles), and 4 Sgr GCs (SG, green diamonds) together with 1 of unknown classification (grey cross). The Sagittarius galaxy (Sgr) is also marked as a black filled square. The vertical dashed line marks the division between prograde ($J_\phi > 0$) and retrograde ($J_\phi < 0$). The horizontal dashed line signifies the characteristic energy above which all the YHs lie, and below which all the BDs lie. The eight OH globular clusters whose symbols are enclosed by black open circles are grouped together in (J_ϕ, E) and (J_z, E), whilst in (J_R, E) they are stretched out close to the boundary of J_R at corresponding energy (as judged from the MSTOs). They are the Sausage GCs. The 2 YHs enclosed with black open squares form an extended selection that may also be related. They have horizontal branch morphology similar to OHs, and have similar actions.

halo and bulge (McMillan, 2017) with the specific aim of identifying the *Sausage Globular Clusters*.

6.2 The Globular Clusters in Action Space

The Milky Way globular clusters are a disparate group: some were formed *in situ* in the Milky Way, some acquired by the engulfment of dwarf galaxies. A classification was introduced by Zinn (1993), in which globular clusters are divided into bulge/disc, old halo and young halo on the basis of cluster metallicity and horizontal branch morphology. The bulge/disc systems are concentrated in the Galactic bulge and inner disc, whilst the old halo clusters are predominantly in the inner halo. They are mostly believed to have been formed in the Milky Way, though $\sim$ 15–17 per cent might have been accreted. The young halo clusters can extend

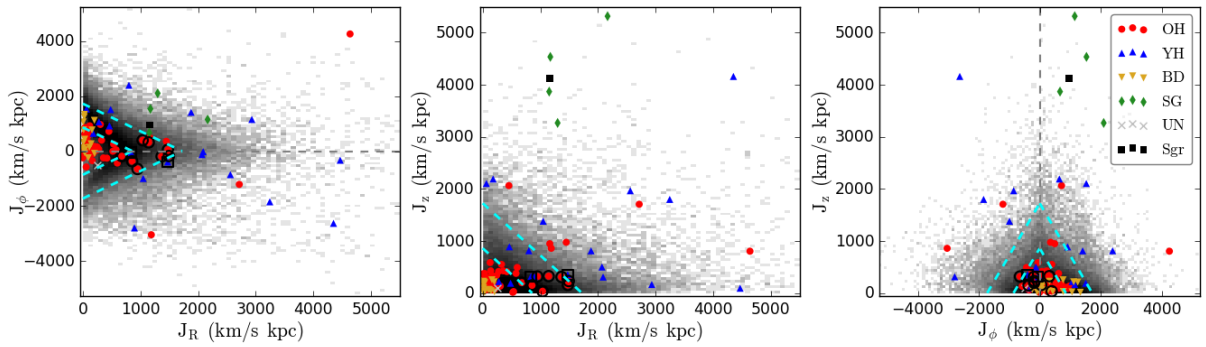

Fig. 6.2 The same data as Fig. 6.1, but now in action space. The Sausage GCs form an extended sequence in J_R, but are tightly clustered in J_ϕ and especially J_z. Again black circles enclose probable members, black open squares possibles; red circles are OHs, blue triangles are YHs, yellow triangles are BDs, green diamonds are SGs and grey cross is unknown. The black filled square is Sgr itself. The grey dashed line marks $J_\phi = 0$. The two cyan dashed lines mark two constant-energy surfaces projected onto the principal planes to provide a rough idea of the action space morphology (see e.g., Figure 3.25 of Binney and Tremaine, 2008).

to large radii and are all believed to have been accreted (see e.g., Mackey and Gilmore, 2004; Mackey and van den Bergh, 2005).

The combination of observables from the Gaia Collaboration et al. (2018c), Sohn et al. (2018) and Harris (1996, 2010 edition) allows us to obtain full six-dimensional information for 91 globular clusters (out of a total of ~ 150 in the Galaxy). To convert from observables to the Galactic rest-frame, we use the circular speed of 232.8 kms^{-1} at the Sun's position of 8.2 kpc, consistent with the McMillan (2017) potential, whilst for the Solar peculiar motion we use the most recent value from Schönrich et al. (2010), namely $(U,V,W) = (11.1, 12.24, 7.25)$ kms^{-1}. These values differ from those used by the Gaia Collaboration et al. (2018c) or Posti and Helmi (2018), so there are small differences in quantities such as apocentres and eccentricities. We use the numerical method of Binney (2012) and Sanders and Binney (2016) to compute the action variables of each globular cluster (J_R, J_ϕ, J_z). Globular clusters associated with the Gaia Sausage must lie on highly radial orbits, and so have low J_ϕ and J_z, but very large J_R. The uncertainty in proper motions is the main contributor to the median (total) velocity error of ~ 9 kms^{-1}. This leads to median errors in the actions of $\sim 10\%$, and so features in action space are robust against uncertainties. Fig. 6.1 presents the distribution of globular clusters in energy and action space, while Fig. 6.2 presents the projections onto the principal planes of action space. In both cases, we also show as grey pixels the distribution of main sequence turn-off stars (MSTOs) from Myeong et al. (2018c). This is to give an idea of the range in action at any energy level occupied by the stellar

halo. Both plots are colour-coded according to the conventional classification from Mackey and van den Bergh (2005): red circles mark the old halo globular clusters (OHs), the blue triangles the young halo globular clusters (YHs), yellow triangles the bulge/disc ones (BDs) and green diamonds the Sagittarius GCs (SG). The Sagittarius dwarf (Sgr) is also marked as a black filled square. The young halo globular clusters all lie above a critical energy of $E_{\rm crit} = -1.6 \times 10^5$ km^{2}s^{-2}. The bulge/disc globulars all lie below this critical energy. We regard the identification of this critical energy $E_{\rm crit}$ as a reference level. Though the value of $E_{\rm crit}$ does depend on potential, the existence of a critical energy level is robust – it is the value of the most bound YH cluster. We argue that globular clusters with comparable or higher energy are all accreted from dwarf galaxies.

The bulge/disc and old halo clusters form tracks in Figs. 6.1 and 6.2. We can see that the bulge/disc clusters branch out towards positive J_ϕ, while maintaining low J_R and low J_z values, as befit disc orbits. They are entirely limited to $E \leq E_{\rm crit}$. For the old halo clusters, we can see a similar branching towards positive J_ϕ at low energy ($E < E_{\rm crit}$). The low energy old halo clusters are all concentrated at low J_R. There are similarities in the morphology of the (J_R, E) distribution for the low energy old halo clusters and the MSTOs as illustrated in Myeong et al. (2018c). In the (J_z, E) plane, the old halo clusters seemingly break up into two separate branches at low energy, though it is unclear whether this is caused by dynamical or selection effects.

There are 15 old halo clusters above the critical energy ($E \gtrsim E_{\rm crit}$). Their azimuthal action J_ϕ distribution is narrower than the low energy ones. It resembles the tips of the 'diamond-like' contours seen in the distribution of MSTOs in the metal-rich halo (Myeong et al., 2018c). Also, the radial action J_R distribution of high energy old halo clusters is extremely distended. Most of them have high radial action, tracing out a structure similar to the picture of the metal-rich halo.

Of the 15 high energy old halo clusters, there are 6 with high vertical action ($J_z \gtrsim 1000$ km s^{-1} kpc). They lie well apart from the main group. They have a wide spread in azimuthal (J_ϕ) and radial (J_R) actions, similar to the YHs suggesting an accretion origin. The main group are concentrated at large J_R, low J_z and low J_ϕ region in the action space, indicating radial orbits. They show surprisingly low vertical action ($J_z \lesssim 500$ km s^{-1}) – they are actually less extended in J_z than the low energy old halo clusters and much less extended than the MSTO stars with similar energy. This tight concentration, especially in J_z, is interesting since the range of J_z becomes wider as we move to higher energy, as is demonstrated by the MSTO sample. The 8 high energy OHs forming this main group (NGCs 1851, 1904, 2298, 2808, 5286, 6864, 6779 and 7089) are marked with black circles in Figs. 6.1 and 6.2. For this group of 8, the maximum J_z is ~ 360 km s^{-1} kpc, the maximum $|J_\phi|$ is ~ 500 km s^{-1} kpc, while

the *minimum* J_R is ~ 700 km s^{-1} kpc. In action space, their distribution is highly flattened and sausage-like. Interestingly, there are no old halo clusters with comparable energy that have high vertical action J_z (see e.g., the middle panel of Fig. 6.2). Mackey and Gilmore (2004) suggest that 15–17 per cent of the old halo clusters might have been accreted. In our picture, at least 8 Sausage GCs (or 14 including those with very high J_z) out of 53 are accreted, in rough accord with the estimate.

The young halo globular clusters all have $E > E_{\rm crit}$, and show a broad spread in all actions. They include extreme prograde and retrograde members in the sample, as well as the ones with largest radial J_R and vertical J_z actions (excluding the Sgr GCs). The 2 black open squares in Figs. 6.1 and 6.2 provide an extended selection to the Sausage GCs. They are 2 young halo globular clusters (NGC 362, and NGC 1261) with a rather similar horizontal branch morphology to old halo clusters (see later) that also have similar actions and energy to the Sausage GCs. These are possibles rather than probables.

The left panel of Fig. 6.3 shows the apocentres and pericentres of the sample, with lines of constant eccentricity superposed. The Gaia Collaboration et al. (2018c) already noted the tendency for GCs with larger apocentres to have larger eccentricities. The 8 probable and 2 possible Sausage GCs are denoted by black open circles and open squares. They form a clump concentrated at high J_R, low J_z and low J_ϕ and they all have high orbital eccentricity $\gtrsim 0.80$. We can also see that most of the bulge/disc clusters have low eccentricity. There are also many old halo clusters with comparably low eccentricity. The young halo clusters are again widely dispersed, as they have high energy and highly spread actions.

Finally, we must consider whether selection effects could cause this. As the Gaia Collaboration et al. (2018c) point out, GCs with high energy are more likely to be observed if they are on eccentric orbits. Even so, the middle panel of Fig. 6.2 demonstrates that there are no old halo clusters in this energy range that have high J_z. By taking the positions of GCs in our sample, and sampling their velocities from velocity distribution tensors based on Figure 4 of Belokurov et al. (2018), we show the expected distribution in action space in the right panel of Fig. 6.3. Grey pixels represent the metal-poor halo with $\beta \sim 0.3$ and red contours represent the metal-rich halo with $\beta \sim 0.8$. Notice that there is only a mild bias towards low J_z in the grey pixels, and *Gaia* should have seen any high J_z GCs at this energy range, if they existed. For the red contours with the velocity distribution representing the metal-rich halo (i.e. highly anisotropic), we can see better correlation with the Sausage GCs.

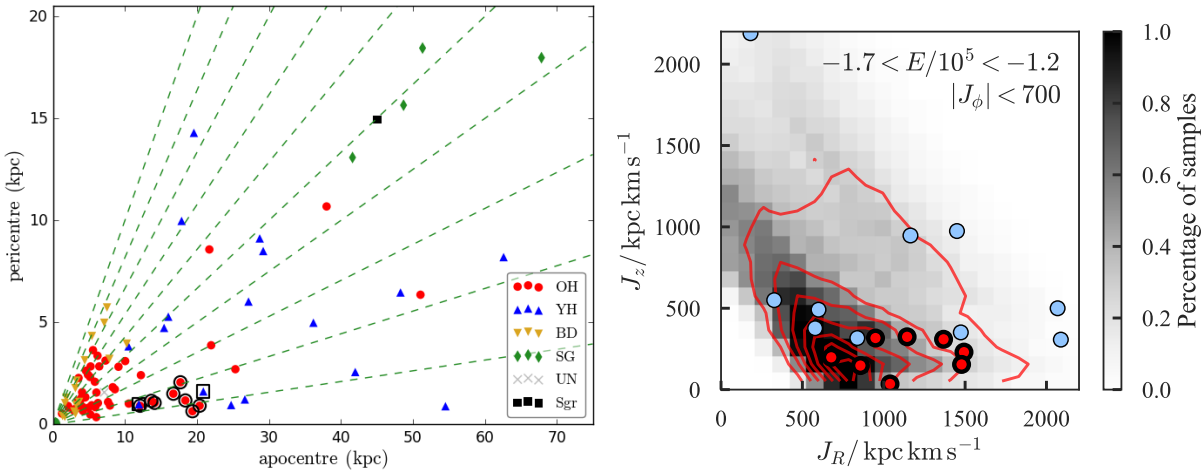

Fig. 6.3 Left Panel: Apocentres and pericentres of the GCs, colour coded according to old halo (red circles), young halo (blue triangles), bulge/disc (yellow triangles), Sgr GCs (green diamonds), and unknown (grey cross). Sagittarius galaxy (Sgr) is also marked (black filled square). Lines of constant eccentricity from 0 to 0.9 in steps of 0.1 are shown in green. Note the Sausage GCs (black open circles as probables and open squares as possibles) all have eccentricity $\gtrsim 0.80$. Right Panel: *Gaia* Selection Effects. The grey pixels and red contours show the distribution of samples in action space of GCs at the observed locations of GCs, but with velocities randomly drawn from velocity distribution tensors based on Figure 4 of Belokurov et al. (2018). Grey pixels represent the metal-poor halo with $\beta \sim 0.3$ and the red contours represent the metal-rich halo with $\beta \sim 0.8$. Only samples with $-1.7 < E/10^5\,(\mathrm{km^2/s^2}) < -1.2$ and $|J_\phi| < 700$ kms^{-1}kpc are shown. Although there is a weak bias to low J_z, it is clear that *Gaia* could have detected objects at high J_z in this energy range if they existed. The actual locations of the Sausage GCs (red) and other GCs (pale blue) with $-1.7 < E/10^5\,(\mathrm{km^2/s^2}) < -1.2$ and $|J_\phi| < 700$ kms^{-1}kpc are superposed.

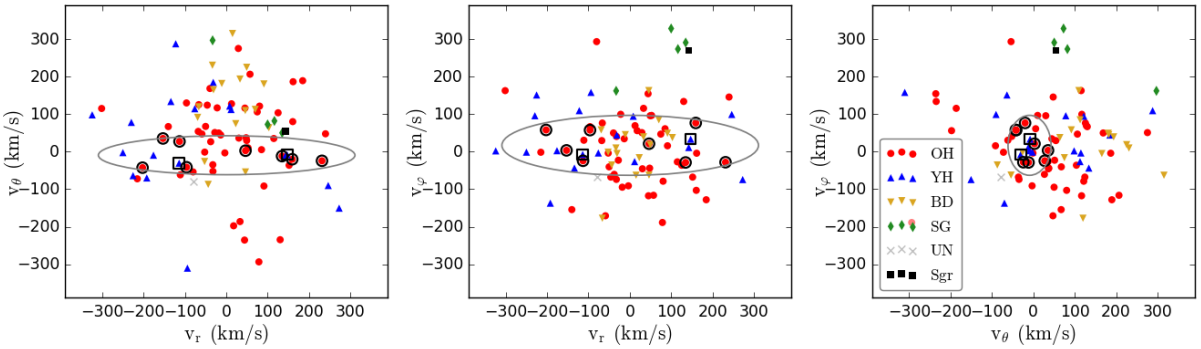

Fig. 6.4 The velocity distribution of the GC sample, resolved with respect to spherical polar coordinates (v_r, v_θ, v_ϕ). The Sausage GCs are marked with their customary black open circles (probables) and open squares (possibles). Their extreme radial anisotropy is illustrated by the superposed ellipses with semiaxes given by the velocity dispersion in each coordinate. This plot should be compared with Fig. 2 of Belokurov et al. (2018), which shows the sausage-like velocity distributions of main-sequence turn-off stars in the SDSS-*Gaia* catalogue.

Name (NGC)	$(v_r, v_\theta, v_\varphi)$ (kms^{-1})	e	(J_R, J_ϕ, J_z) (kms^{-1}kpc)	E (km^{2}s^{-2})
1851	(134.8,11.6,28.6)	0.91	(1493,-178,230)	-134706
1904	(46.5,-2.9,-21.5)	0.93	(1477,51,155)	-137390
2298	(-96.1,41.3,-57.7)	0.79	(949,-648,317)	-140391
2808	(-152.9,-35.5,-3.7)	0.86	(1038,394,35)	-152947
5286	(-202.3,42.4,-58.3)	0.84	(856,-366,148)	-153940
6864	(-113.0,-27.6,24.1)	0.83	(1144,316,324)	-143397
6779	(159.4,19.9,-76.9)	0.86	(677,-182,199)	-159799
7089	(231.3,24.1,28.0)	0.88	(1368,-192,309)	-139217
362	(147.1,7.9,-33.5)	0.85	(837,-57,317)	-159510
1261	(-113.8,30.5,7.2)	0.86	(1474,-393,351)	-132973

Table 6.1 The kinematic properties of the 8 probable and 2 possible Sausage GCs. The Galactic rest frame velocity in spherical polars, the actions in cylindrical polars, the energy and orbital eccentricity $e = (r_{\rm apo} - r_{\rm peri})/(r_{\rm apo} + r_{\rm peri})$ are all given.

6.3 The Sausage Globular Clusters

The properties of the 8 probable and 2 possible Sausage GCs in energy and action space are listed in Table 6.1.

The identification of the Gaia Sausage in main-sequence turn-off stars is most evident in velocity space. Belokurov et al. (2018) show that the velocity anisotropy parameter $\beta_{\rm MSTO}$ is very extreme,

$$\beta_{\rm MSTO} = 1 - \frac{\sigma^2_{v_\theta} + \sigma^2_{v_\varphi}}{2\sigma^2_{v_r}} \approx 0.9, \tag{6.1}$$

Here, v_φ is the azimuthal velocity in the direction of the Milky Way's rotation, v_θ is increasing towards the Milky Way's north pole and v_r is the radial velocity in spherical coordinates. Given that the $\beta = 1$ implies that all orbits are linear straight lines through the Galactic Centre, then the metal-rich local halo stars are very radially anisotropic. This gives the Sausage its name, as the structure (which is also highly non-Gaussian) looks sausage-shaped in velocity space. Fig. 6.4 shows the velocities of the GCs resolved with respect to spherical polar coordinates. The Sausage GCs have an even more extreme value of the anisotropy parameter than the Sausage MSTOs, with $\beta_{\rm GCs} \approx 0.95$. Of course, both here and in Belokurov et al. (2018), cuts have been used to remove stars and GCs to isolate the Sausage component.

The left panel of Fig. 6.5 shows age versus metallicity for the Sausage GCs, as well as 7 GCs that have been claimed as associates of the Sagittarius (Sgr), specifically Terzan 7, Terzan 8, Arp 2, Pal 12, NGC 4147, NGC 6715 and Whiting 1 (Forbes and Bridges, 2010). As noted by Forbes and Bridges (2010), the age-metallicity relation for the Milky Way's GCs reveals two distinct tracks. There is broad swathe of bulge/disc and old halo globular clusters with a roughly constant old age of ~ 12.8 Gyr. This comprises the bulk of the sample. However, Forbes and Bridges (2010) pointed out that the Sgr GCs form a separate track that branches to younger ages, and is shown as open diamonds in Fig. 6.5. We find that the Sausage GCs similarly follow a track that is very different from the bulk of the Milky Way's *in situ* GCs. It is similar to, but vertically offset from, the Sgr track. The right panel of Fig. 6.5 shows the horizontal branch index versus metallicity using data from Mackey and van den Bergh (2005). The plot emphasises the ambiguous nature of the two clusters, NGC 362, NGC 1261. Although Mackey and van den Bergh (2005) classified them as young halo clusters based on their horizontal branch morphology, they are in fact close to the dividing line. We therefore suggest that this classification can be debatable. They are kinematically close to the Sausage GCs, who may well be their true brethren.

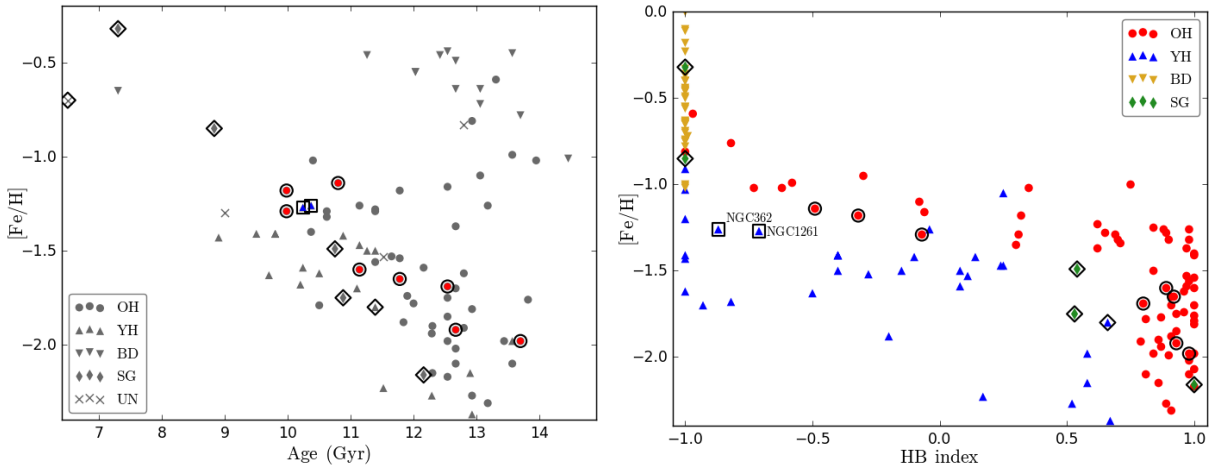

Fig. 6.5 Left panel: Plot of the age of GCs versus metallicity using data from Forbes and Bridges (2010). The Sausage GCs are shown with circular (probables) and square (possibles) black boundaries. 7 GCs that are claimed former denizens of the Sagittarius (Sgr) dwarf are shown as unfilled black diamonds. The sequences of Sgr GCs and Sausage GCs lie on two distinct, though closely matched, tracks. They are different from the bulk of the Milky Way GCs which show a constant age of $\sim$ 13 Gyr independent of metallicity. Right panel: Plot of horizontal branch morphology versus metallicity using data from Mackey and van den Bergh (2005). The locations of the two young halo clusters (NGC 362, NGC 1261) are close to the boundary and their designation is open to debate. We have included them in our extended sample of Sausage GCs, as they are kinematically similar.

6.4 Discussion

We argues that there are at least eight and possibly ten halo globular clusters that belong to a single, ancient massive merger event identified by Belokurov et al. (2018) and responsible for the Gaia Sausage in velocity space. The evidence is threefold. First, there is a strong prior expectation of finding a population of radially anisotropic GCs. Evidence for a major accretion event is provided by studies of the kinematics of halo main-sequence turn-off stars in the SDSS-*Gaia* catalogue (Belokurov et al., 2018; Myeong et al., 2018c), as well as in *Gaia* DR2 (Haywood et al., 2018). It explains the peculiar, highly non-Gaussian, radial anisotropic local velocity distribution of halo stars (hence the "Gaia Sausage"). The existence of the Sausage GCs supports the idea of a single event and allows us to put estimates on the mass of the progenitor. Judging from GC numbers, it must have been more massive than Fornax and comparable to the Sgr progenitor, which Gibbons et al. (2017) estimated as $5 \times 10^{10} M_{\odot}$ in total mass. This is in good agreement with the mass estimate provided in Belokurov et al. (2018).

Secondly, just as the GCs associated with the Sgr can be identified by their agglomeration in action space, so can the GCs associated with the "Gaia Sausage". A critical energy separates the young halo clusters (which have all been accreted) from the bulge/disc clusters (which are all formed *in situ*). The old halo clusters are mainly formed *in situ*, though Mackey and Gilmore (2004) suggest that 15–17 per cent were accreted. They straddle the critical energy. Eight of the old halo clusters with $E > E_{\rm crit}$ form a narrow, clumped and compact distribution in action space. They have characteristic low vertical (J_z) and high radial (J_R) action. They show strong radial anisotropy ($\beta \approx 0.95$) and highly radial, eccentric orbits ($e \gtrsim 0.80$). These are exactly the characteristics expected for the Sausage GCs. There may even be 2 further members – if we, for example, permit the inclusion of young halo clusters.

Thirdly, the 8 globular clusters identified as belonging to the "Gaia Sausage" were chosen without any regard to their age or metallicity. However, these 8 clusters show the typical age-metallicity trend expected from dwarf galaxies, which is additional evidence supporting their extragalactic origin. The time of infall can also be roughly reckoned from the tracks in age-metallicity space as ~ 10 Gyrs or $z \sim 3$, in accord with the estimate in Belokurov et al. (2018).

Could this peculiarity of the data be due to a selection effect, against which the Gaia Collaboration et al. (2018) already caution? High energy GCs are more likely to be observed if they are on eccentric orbits. We have demonstrated that there is a weak preference for GCs in the Sausage GC energy and angular momentum range to have larger J_R than J_z. However, the Sausage GCs are a significantly more radially anisotropic population than expected purely

from selection effects. This indicates that the selection effects have limited impact on our conclusions.

Chapter 7

Evidence for Two Early Accretion Events That Built the Milky Way Stellar Halo

G. C. Myeong[1], E. Vasiliev[1,2], G. Iorio[1], N. W. Evans[1], V. Belokurov[1]

[1]Institute of Astronomy, University of Cambridge, Madingley Road, Cambridge CB3 0HA, United Kingdom

[2]Lebedev Physical Institute, Leninsky Prospekt 53, Moscow 119991, Russia

Abstract

The Gaia Sausage is the major accretion event that built the stellar halo of the Milky Way galaxy. Here, we provide dynamical and chemical evidence for a second substantial accretion episode, distinct from the Gaia Sausage. The Sequoia Event provided the bulk of the high energy retrograde stars in the stellar halo, as well as the recently discovered globular cluster FSR 1758. There are up to 6 further globular clusters, including ω Centauri, as well as many of the retrograde substructures in Myeong et al. (2018), associated with the progenitor dwarf galaxy, named the Sequoia. The stellar mass in the Sequoia galaxy is $\sim 5 \times 10^7 M_\odot$, whilst the total mass is $\sim 10^{10} M_\odot$, as judged from abundance matching or from the total sum of the globular cluster mass. Although clearly less massive than the Sausage, the Sequoia has a distinct chemo-dynamical signature. The strongly retrograde Sequoia stars have a typical eccentricity of ~ 0.6, whereas the Sausage stars have no clear net rotation and move on

[0]Remark: The work presented in this Chapter is currently in press (Myeong et al., 2019). I conceived the original project which was better refined by discussions with Cambridge Streams group. I was responsible for the data acquisition and analysis, except for Section 7.2. The work presented in Section 7.2 was conducted by Eugene Vasiliev who is the second author of a publication based on this Chapter. My supervisors, N. Wyn Evans and Vasily Belokurov, made an invaluable contribution by consulting and reformatting the first draft into a more logical presentation. Giuliano Iorio also provided priceless consultation.

predominantly radial orbits. On average, the Sequoia stars have lower metallicity by ~ 0.3 dex and higher abundance ratios as compared to the Sausage. We conjecture that the Sausage and the Sequoia galaxies may have been associated and accreted at a comparable epoch.

7.1 Introduction

The Gaia Data Release 2 (DR2, Gaia Collaboration et al., 2018d) is proving transformational in the identification of substructure in the Milky Way galaxy. This is because substructure retains coherence in phase space over very long timescales (Johnston et al., 1996; Tremaine, 1999). The acquisition of kinematic data, particularly accurate stellar proper motions courtesy of the Gaia satellite, is therefore the key to unlocking the accretion history of the stellar halo. The long-term goal of understanding the building blocks of at least the stellar halo, and perhaps even the entire Galaxy, seems to be within our grasp.

Already, Gaia has provided compelling evidence for the nearly head-on collision of a Magellanic-sized dwarf galaxy with the nascent Milky Way some 8 to 10 billion years ago, the so-called 'Gaia Sausage' (see e.g. Belokurov et al., 2018; Fattahi et al., 2019; Haywood et al., 2018; Myeong et al., 2018c,d). This name describes the elongated shape of the structure in velocity space. The radial velocity dispersion of the Sausage stars is ≈ 180 kms^{-1}, while the azimuthal and longitudinal dispersions are only ≈ 60 kms^{-1} (see e.g., Figure 4 of Belokurov et al., 2018). The name therefore follows the long-standing scientific practice of being descriptive and informative.

The aftermath of this accretion event is detectable in the inner stellar halo of the Galaxy as a giant cloud of relatively metal-rich ([Fe/H]$\gtrsim -1.5$) stars on highly radial orbits. Originally traced with nearby Main Sequence stars (Belokurov et al., 2018; Myeong et al., 2018c), the Sausage debris has now been found over a large distance range with a number of distinct tracers, including Blue Horizontal Branch stars (Deason et al., 2018; Lancaster et al., 2019) and RR Lyrae (Iorio and Belokurov, 2019; Simion et al., 2019). The characteristic property of the residue of this collision is that the orbits are eccentric with little or no net angular momentum. The debris of this event does not provide any strongly prograde or retrograde material, as befits an almost head-on collision.

Alternatively, it was proposed that an ancient major merger – dubbed 'Gaia-Enceladus' – could have given rise to the bulk of the retrograde stars in the halo, as well as some of the low-angular momentum debris (Helmi et al., 2018). The fundamental difference between the two hypotheses is that the 'Gaia-Enceladus' encompasses not just the highly eccentric component of the halo, but also the strongly retrograde component. For example, in Helmi et al. (2018), the 'Gaia-Enceladus' stars have angular momentum component satisfying

$-1500 < J_\phi < 150$ kms^{-1} kpc^{-1}, independent to the total energy, and so span a range from mild prograde through highly eccentric to strongly retrograde. The question of whether a single collision could produce such a spray of debris with different kinematical properties remains open.

In fact, the suggestion that the retrograde component of the halo may have been accreted already predates the arrival of the Gaia data by many years (see e.g., Beers et al., 2012; Carollo et al., 2007; Majewski et al., 2012; Norris and Ryan, 1989). The retrograde and peculiar globular cluster ω Centauri has also long been suspected of playing a role in the supply of retrograde stars, as it may be the stripped nucleus of a dwarf galaxy (Bekki and Freeman, 2003). The Gaia data releases have provided new samples of the retrograde halo component, which have been scoured for evidence of multiple minor mergers and accretion events (e.g., Helmi et al., 2017; Myeong et al., 2018b,c). The question therefore at issue is: did one merger event provide both the eccentric and retrograde components of the stellar halo (as in the 'Gaia-Enceladus' theory) or does the retrograde component have a different origin from the eccentric component (the 'Gaia-Sausage' theory)?

We provide a possible answer to this question in this Chapter, but our line of reasoning begins in a roundabout way with another unusual retrograde object, FSR 1758. This was originally discovered by Froebrich et al. (2007) as a claimed open cluster and later identified as a globular cluster (Cantat-Gaudin et al., 2018). Barbá et al. (2019) recently reported the first estimate of its distance and noticed its unusual size, using a combination of data from the DECam Plane Survey (DECaPS, Schlafly et al. 2018) and the VISTA Variables in the Via Lactea (VVV) Extended Survey, complemented with Gaia DR2. It is an extended agglomeration of stars, located at $(\ell = 349^\circ, b = 3^\circ)$ and with a heliocentric distance of $10-12$ kpc. They determined the core radius of FSR 1758 to be ≈ 10 pc, and estimated the tidal radius to be ≈ 150 pc. Considering its unusual size, Barbá et al. (2019) questioned whether FSR 1758 is the remnant of a dwarf galaxy or an unusually large globular cluster. Subsequently, Simpson (2019) found 3 stars in the centre of FSR 1758 with line-of-sight velocities from the Gaia Radial Velocity Spectrograph (RVS) and argued that the object has a line-of-sight velocity of 227 ± 1 kms^{-1}. Although the 3 stars are insufficient to come to a definite conclusion as regards FSR 1758's internal velocity dispersion, nonetheless Simpson (2019) argued on the basis of its highly retrograde orbit that it is an accreted halo globular cluster.

In fact, the globular cluster (GC) datasets have been scrutinised carefully for evidence of accretion events in recent years. They have proved surprisingly powerful tracers of the merger events that build the stellar halo of the Galaxy. This was made clear in Forbes and Bridges (2010), who showed that the globular clusters that formerly belonged to the

Sagittarius galaxy follow a different track in the plane of age-metallicity as compared to the bulk of the primordial or in situ clusters. Subsequently, Myeong et al. (2018d) identified a sample of 10 high eccentricity, high-energy, old halo GCs strongly clumped in action space that belonged to the 'Gaia Sausage' event. More speculatively, Kruijssen et al. (2019) used the age–metallicity distribution of Galactic globular clusters to reconstruct the entire merger history, claiming three substantial events. If FSR 1758 is indeed an accreted GC, then this suggests that a systematic search for companion GCs accreted in the same event, as well as other stellar debris such as substructures and tidal tails, may provide a picture of the progenitor.

In Section 7.2, we use Gaia's kinematic data in combination with photometry from DECaPS to determine structural parameters and the proper motion dispersion profile for FSR 1758, and show that its declining fall-off is characteristic of a GC. The nature of FSR 1758 having been established, we search for companion GCs and stellar substructures moving on orbits of similar eccentricity and inclination that may have joined the Milky Way in the same accretion event in Section 7.3. Barbá et al. (2019) introduced the picturesque term Sequoia to describe the size of FSR 1758. We retain the term and slightly adapt it for our own use. In our picture, FSR 1758 is one of about five or more GCs that populated the Sequoia dwarf galaxy, whose existence was already conjectured from our stellar substructure searches (Myeong et al., 2018b,c). Its disruption brought these GCs into the Milky Way on similar orbits, as well as abundant retrograde high energy stellar substructure. We argue that the remnants of the Sequoia galaxy are dynamically distinct from the Gaia Sausage as they are retrograde, whereas the Sausage was an almost head-on collision. The dual pattern of these accretion events is evident in energy and actions, and is also shown clearly when the chemical evidence is analysed. The stars and substructures associated with the Sequoia have different mean metallicities and different abundance ratios. In Section 7.4, we provide estimates of the age and mass of the Sequoia galaxy and compare with the Gaia Sausage. Finally, we summarise our results in our concluding Section 7.5.

7.2 The Nature of FSR 1758

7.2.1 Data

First, we cross-match the positions of stars between Gaia and DECaPS, using a search radius of 0.5". DECaPS provides roughly two magnitudes deeper photometry than Gaia, but it is saturated for bright stars and has patchy spatial coverage, so we study the union of the two datasets. We use the following combinations of r and i DECaPS photometric bands as a

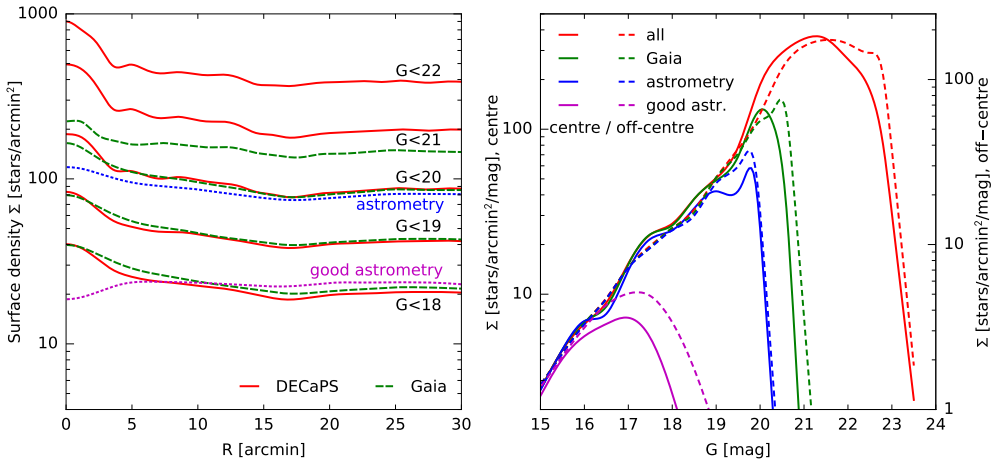

Fig. 7.1 Left: Radial profiles of the surface density of FSR 1758. Solid red curves show the DECaPS data and dashed green the Gaia data; the former have been converted to Gaia G magnitude using eqn 7.1. If the magnitude distribution of stars were not spatially varying, these curves would have a constant vertical offset (in logarithmic units). It is clear that the Gaia data is reasonably complete up to $G \leq 19$ in the centre and up to $G \leq 20$ elsewhere, while the DECaPS data is fairly complete up to $G \approx 21$. Right: Distribution of stars as a function of magnitude in the central 2 arcmin (solid lines) and in an off-centred field at $R \sim 11$ arcmin to the north (dashed lines); the latter is vertically offset by a factor of 2 to compensate for the lower overall density of stars. It illustrates the same points about the completeness of Gaia data as compared to DECaPS (the difference between red and green lines starts to appear at $G \gtrsim 20$). In the central area, there is an excess of stars with $20 \leq G \leq 21$. These are numerous main-sequence stars of the cluster, absent in off-centred fields. Therefore, we need to include the stars up to $G \leq 21$ in order to have a faithful representation of surface density of the cluster.

proxy for Gaia G and $G_{\rm BP} - G_{\rm RP}$ (derived by comparing the magnitudes of cross-matched stars):

$$\begin{aligned} G &\approx r + 0.1 + 0.3(r-i) - 0.5(r-i)^2, \\ G_{\rm BP} - G_{\rm RP} &\approx\ 0.65\ + 2.35(r-i) - 0.3(r-i)^2. \end{aligned} \tag{7.1}$$

Fig. 7.1 shows the surface density profiles of stars in different ranges of magnitudes, and their distributions by magnitudes at different spatial locations. By comparing the density of stars in Gaia and DECaPS datasets, we conclude that the former is reasonably complete up to $G \lesssim 20$. The subset of stars with astrometric measurements also extends roughly to $G = 20$, but is less complete in the central area. We wish to include the fainter stars without astrometry in order to mitigate the bias in representation of the spatial density profile of the cluster. We chose to use stars up to $G = 21$, of which roughly 70% are present in the Gaia dataset, and only 40% have astrometric measurements. During fitting, we also infer the total mass from the intrinsic (error-deconvolved) proper motion (PM) dispersion. We only use a high-quality subset of stars (marked as "good astrometry" in the figure) for this inference, ignoring all sources with `astrometric_excess_noise` > 1 or `phot_bp_rp_excess_factor` $> 1.3 + 0.06(G_{\rm BP} - G_{\rm RP})^2$, as suggested by Gaia Collaboration et al. (2018d).

7.2.2 Dynamical Modelling

We use a probabilistic model, in which the stars are drawn from a mixture of two populations: the cluster and the field. The distribution of field stars is assumed to be spatially uniform, and described by a sum of two bivariate Gaussians in the PM plane. We assume that the density of cluster stars follows a generalized King profile, also known as the LIMEPY family of models (Gieles and Zocchi, 2015), which has been shown to adequately describe realistic globular clusters (Hénault-Brunet et al., 2019). It has the following free parameters: mass M, scale (core) radius R_c, dimensionless potential depth at the centre (King parameter) W_0, and truncation parameter g controlling the density profile in the outer parts. For the models in this Section, we do not assume any particular relation between the total cluster mass and the number of observed cluster members $N^{\rm clust}$ (this relation is examined in the next Section). Rather, the total mass of the cluster manifests itself only kinematically, through the overall amplitude of velocity dispersion. We assume a Gaussian distribution for the PM of cluster stars, centred around its mean PM, and with a spatially-variable width.

We measure the parallax distribution of field stars directly from the data using stars outside the central 5 arcmin and represent it by a mixture of three Gaussian components, with parameters fixed throughout the rest of the modelling. The intrinsic (error-free) parallaxes of cluster stars are assumed to be equal to the inverse distance to the cluster (fixed to $D = 10$ kpc),

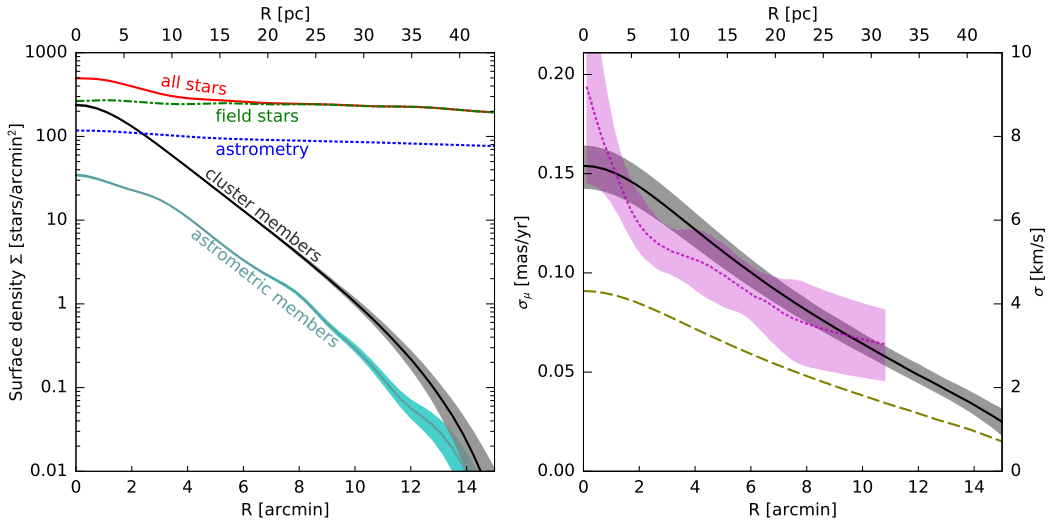

Fig. 7.2 Left: Surface density profiles for different subsets of stars. Red solid line: all stars with $G < 21$ (same as the corresponding curve in Fig. 7.1). Black solid line and gray shaded region: all cluster members. Green dot-dashed line: field stars (the difference between the previous two curves). Blue dotted line: all stars with astrometric measurements. Cyan shaded region: cluster stars with astrometric measurements. Right: PM dispersion profile of cluster stars. Black line and shaded region: parametric profile of the generalized King model, with 68% confidence interval. Purple dotted line and shaded region: non-parametric estimate from stars with $\gtrsim 80\%$ membership probability. Olive dashed line: the profile of a King model with the total mass $2.5 \times 10^5\,M_\odot$, as inferred by the photometric fit (Fig. 7.3).

plus the constant zero-point parallax offset -0.03 mas (Gaia Collaboration et al., 2018d). We do not use any information about colours and magnitudes for membership determination, because they are severely affected by spatially-variable reddening.

The likelihood of observing a star i at a given distance from the cluster centre, with or without further astrometric information, is given by a sum of likelihoods of the two alternative hypotheses:

$$\mathscr{L}_i = \mathscr{L}_i^{\rm clust} + \mathscr{L}_i^{\rm field}. \tag{7.2}$$

Let $N^{\rm clust}$ be the (unknown) total number of cluster members in our sample of stars within the radius $R_{\rm max}$. We choose $R_{\rm max} \gg R_c$, so that all possible cluster members are included, and normalize the cluster surface density $\Sigma^{\rm clust}(R)$ so that $\int_0^{R_{\rm max}} \Sigma^{\rm clust}(R)\, 2\pi R\, {\rm d}R = N^{\rm clust}$. The remaining $N^{\rm field} \equiv N^{\rm total} - N^{\rm clust}$ observed stars are then attributed to the field population with a spatially-uniform density $\Sigma^{\rm field} \equiv N^{\rm field}/(\pi R_{\rm max}^2)$. Then the likelihoods of a given star to belong to either population are

$$\mathscr{L}_i^{\rm clust} \equiv \Sigma^{\rm clust}(R_i)\, A_i^{\rm clust}, \qquad \mathscr{L}_i^{\rm field} \equiv \Sigma^{\rm field}\, A_i^{\rm field}, \tag{7.3}$$

where the factors $A_i^{\rm clust}$, $A_i^{\rm field}$ are unity for stars without astrometric measurements, or describe the likelihood of measuring the observed parallax and PM, given the intrinsic distribution functions of either population, convolved with measurement uncertainties. For the cluster population, this factor is a product of the parallax likelihood and the PM likelihood (ignoring correlations between them):

$$\begin{aligned} A_i^{\rm clust} &\equiv \mathscr{N}(\varpi_i - \varpi^{\rm clust},\, \varepsilon_{\varpi,i}^2)\;\; \mathscr{N}(\mu_i - \mu^{\rm clust},\, \mathsf{S}_i), \\ \mathsf{S}_i &\equiv \begin{pmatrix} \varepsilon_{\mu_\alpha,i}^2 + \sigma_\mu^2(R_i) & \rho_i\, \varepsilon_{\mu_\alpha,i}\, \varepsilon_{\mu_\delta,i} \\ \rho_i\, \varepsilon_{\mu_\alpha,i}\, \varepsilon_{\mu_\delta,i} & \varepsilon_{\mu_\delta,i}^2 + \sigma_\mu^2(R_i) \end{pmatrix}, \end{aligned} \tag{7.4}$$

where $\mathscr{N}$ is the uni- or bivariate normal distribution, ϖ is the parallax, $\mu \equiv \{\mu_\alpha, \mu_\delta\}$ is the PM with associated measurement uncertainties ε, ρ_i is the correlation coefficient between the two components of PM uncertainty matrix, R_i is the distance of the star from the cluster centre, $\sigma_\mu(R)$ is the spatially-dependent intrinsic PM dispersion of cluster stars, whose amplitude is proportional to the square root of the cluster mass. We use only a subset of stars with reliable PM measurements outside the central 2 arcmin for inferring the intrinsic dispersion, since the stars in the centre may be affected by crowding. The PM of remaining (mostly faint) stars are still used to determine the membership, but in doing so, we use a conservative value $\sigma_\mu = 0$. For the field population, the expressions are similar, but involve several Gaussian components (two for PM and three for parallax), with the intrinsic PM dispersion being a spatially-constant symmetric 2×2 matrix rather than a single spatially-varying quantity.

The fitting procedure optimizes the model parameters ($N^{\rm clust}, \mu^{\rm clust}, \mu^{\rm field}$, covariance matrices of the field population, parameters of the cluster density profile) to maximize the total log-likelihood

$$\ln \mathscr{L} \equiv \sum_{i=1}^{N^{\rm total}} \ln \mathscr{L}_i, \tag{7.5}$$

via Markov Chain Monte Carlo as implemented in the EMCEE package (Foreman-Mackey et al., 2013). We then evaluate the posterior probability of membership for each star as

$$P_i^{\rm clust} = \frac{\mathscr{L}_i^{\rm clust}}{\mathscr{L}_i^{\rm clust} + \mathscr{L}_i^{\rm field}}. \tag{7.6}$$

The total number of cluster members is $N^{\rm clust} = \sum_i P_i^{\rm clust}$. We stress that we do not make hard cuts in any of the observed quantities (parallax, PM, radius) to separate the cluster and the field populations. For stars with astrometric measurements, the membership probability distribution is strongly bimodal (the two populations are well separated), while for stars without astrometry, the membership probability smoothly drops with radius from ~ 0.5 in

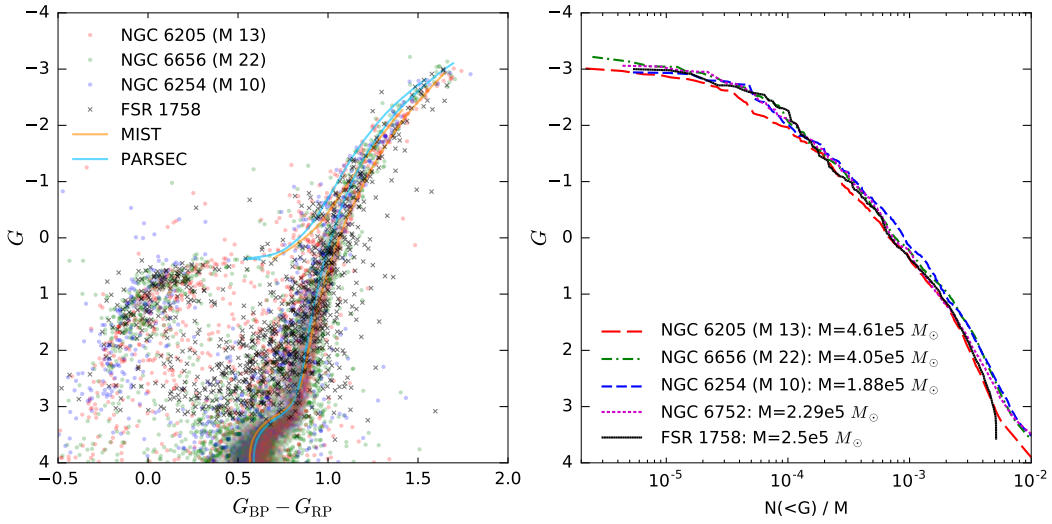

Fig. 7.3 Left: De-reddened colour–absolute magnitude diagrams (CMD) of several Galactic globular clusters with similar metallicity [Fe/H]≈ -1.5, shown by coloured dots, together with the one for FSR 1758, shown by black crosses (they are shifted leftward from the isochrone at faint magnitudes because of crowding issues in Gaia BP/RP photometry). We used the distance $D = 10$ kpc and reddening $E(B-V) = 0.73$ for the latter cluster, and the literature values for the remaining ones. Overplotted are theoretical isochrones for 12.5 Gyr old population from two stellar-evolution models: MIST (Choi et al., 2016) and PARSEC (Bressan et al., 2012). Right: Cumulative number of stars brighter than the given magnitude (horizontal axis) as a function of magnitude (vertical axis), scaled to the mass of each cluster. The masses of 4 NGC clusters are from Baumgardt et al. (2019), while the mass of FSR 1758 is inferred as the best match to the remaining clusters.

the centre down to zero at large radii. In total, we have $N^{\rm clust} \simeq 7500$ member stars, of which only ~ 1600 are astrometrically selected, and only ~ 350 are used in the dynamical mass determination through the intrinsic PM dispersion.

Fig. 7.2 shows the inferred cluster density and the PM dispersion profiles. The best-fit parameters of the generalized King model are: King radius of 3 arcmin (~ 8.5 pc for the assumed distance $D = 10$ kpc), King parameter $W_0 \simeq 3$, truncation radius ~ 15 arcmin, and truncation parameter $g \simeq 1$. The core radius (defined as the projected distance from the cluster centre where the surface density drops to 1/2 its central value) is ~ 6.5 pc, and the half-light radius (the projected distance enclosing half of the cluster stars) is ~ 9 pc. The core radius is somewhat smaller than determined by Barbá et al. (2019) from their fit to the DECaPS photometric sample (without considering astrometry). On the other hand, the truncation radius (~ 50 pc) is three times smaller than found in that paper. We stress that the

density profile in the outer parts, and in particular the truncation radius, is determined mainly by Gaia astrometry, so is more reliably constrained than just using the photometry alone.

Overall, the modelling procedure makes good use of both the deeper DECaPS photometry in the cluster centre and the Gaia astrometry in the outer parts. However, the inferred cluster mass (equivalently, the intrinsic PM dispersion) appears to be rather high, $M \simeq (7 \pm 1) \times 10^5 M_\odot$, compared to the photometric model of the next Section. We stress that the width of the intrinsic PM distribution is inferred by convolving it with the measurement uncertainties and comparing the error-broadened distribution with the actually observed one. Hence, it strongly depends on the reliability of uncertainty estimates ε_μ of stars in the Gaia dataset. Even for the high-quality subsample, these errors are in the range $0.1 - 0.3$ mas yr^{-1}, comparable to or exceeding the inferred value of intrinsic PM dispersion. It is known that the formal uncertainties in Gaia PMs are underestimated (e.g., Gaia Collaboration et al., 2018d). We multiplied the uncertainties quoted in the catalogue by a correction factor 1.1, as suggested in that paper, before running the fit. If we instead increase the uncertainties by a factor 1.3, this reduces the PM dispersion by a third, bringing it into agreement with the total cluster mass estimated from photometry.

Finally, to check if the PM dispersion profile could be biased by the assumed parametric form of the generalized King model, we also determined it non-parametrically from the subset of high-quality stars classified as cluster members with $\geq 80\%$ probability. We used the method of Vasiliev (2018), representing $\sigma_\mu(R)$ as a cubic spline with the values at four control points adjustable during the fit, while taking into account spatially correlated measurement errors. The result, shown in the right panel of Fig. 7.2, agrees reasonably well with the parametric profile, but is higher in the very centre. This is likely caused by crowding issues, and for this reason we have excluded the stars in the central two arcmin from the high-quality sample used to determine the PM dispersion in the parametric fit. In any case, the PM dispersion profile appears to be declining with radius, which is natural to expect for a globular cluster, but not for a dwarf galaxy.

7.2.3 Photometric modelling

Since almost all stars with magnitudes $G \lesssim 19 - 20$ have astrometric measurements and are well separated into the cluster and the field populations, we may use the sample of astrometrically confirmed members to determine the total cluster mass. The idea is to compare the distribution of stars by magnitudes with those of several other clusters with similar colour-magnitude diagrams (CMDs), for which the total mass and the distance are known. By normalizing the number of stars brighter than the given absolute magnitude by the cluster mass, we constructed the cumulative magnitude distribution profiles for a

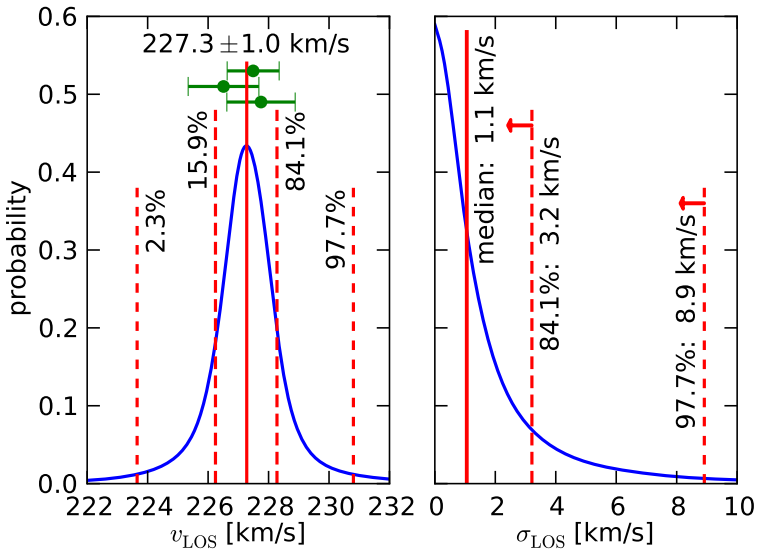

Fig. 7.4 Estimate of the mean line-of-sight velocity (left panel) and its dispersion (right panel) from the three stars detected by the Gaia RVS instrument. The measured values, shown by green dots with error bars, are very similar and consistent with zero intrinsic dispersion, however, the probability distributions as shown in this figure are heavy-tailed, and the chances of σ exceeding 5 km s^{-1} are around 10%.

dozen globular clusters in the range of metallicities $-2 \lesssim [\mathrm{Fe/H}] \lesssim -1$. The masses and distances of these clusters are taken from Baumgardt et al. (2019), who used a large library of N-body simulations and a variety of observational constraints to measure the masses. Three clusters have very similar CMDs to FSR 1758, particularly with regards to the location of blue horizontal branch (BHB): NGC 6205 (M 13), NGC 6254 (M 10) and NGC 6656 (M 22). They all have metallicities $\simeq -1.5$ and masses $(2-5)\times 10^5\,M_\odot$.

Fig. 7.3, left panel, shows the composite CMDs of these three clusters, with the astrometrically detected members of FSR 1758 overplotted by black crosses. The measured colour $G_{\rm BP}-G_{\rm RP}$ and the G-band magnitude are de-reddened using the coefficients given in Table 2 of Gaia Collaboration et al. (2018a), and the observed magnitude is converted to the absolute magnitude. By matching the stars of FSR 1758 to the empirically determined isochrones, we infer the reddening coefficient $E(B-V)=0.73$ and the distance $D=10$ kpc, in reasonable agreement with Barbá et al. (2019). Stars in the lower part of the red giant branch (RGB) are systematically offset to the left from the isochrone, but this is expected for such a dense and highly reddened region. If we use DECaPS r and i bands instead of Gaia $G_{\rm BP}-G_{\rm RP}$, as per eqn 7.1, the scatter and offset of member stars from the isochrone curve at faint magnitudes are substantially reduced. The upper part of the RGB and the BHB of FSR 1758 match well the location of these features in the other three clusters.

The right panel of Fig. 7.3 shows the cumulative number of stars as a function of magnitude, normalized by the mass of each cluster. The three clusters listed above have similar profiles, and in fact almost all other clusters also follow the same trend (we show additionally the cluster NGC 6752, which has a somewhat higher metallicity). By matching, we infer the mass of FSR 1758 to be $\sim 2.5 \times 10^5 M_\odot$, with an uncertainty $\lesssim 20\%$.

As noticed by Simpson (2019), three bright stars in the centre of FSR 1758 are actually present in the Gaia RVS sample, having values of line-of-sight velocity around 227 km s^{-1}. Simpson (2019) additionally reported a fourth star with a very similar line-of-sight velocity at a projected distance $\sim 0.6^\circ$ from the cluster. Given that its PM, G magnitude and colour are all very close to those of the three other stars, it is unlikely to be a field star, but it also cannot be a current cluster member, being more than twice as far as the inferred cutoff radius. This star may have been tidally stripped from the cluster.

With only three stars, it is not possible to put strong constraints on the internal velocity dispersion σ. The measured values are very close to each other and consistent with zero intrinsic scatter, but values of σ up to 5–10 km s^{-1} are not strongly excluded (Fig 7.4). These values are also consistent with the photometrically estimated mass, which corresponds to the central velocity dispersion ~ 4 km s^{-1}, and even with the higher values inferred from PM, although these are less reliable.

7.3 Tracers of the Sequoia Galaxy

FSR 1758 has a very retrograde, eccentric orbit (e.g., Simpson, 2019). An accretion origin for the strongly retrograde components of the stellar halo has long been suspected (e.g., Beers et al., 2012; Carollo et al., 2007; Norris and Ryan, 1989; Quinn and Goodman, 1986). Analyses of the *Gaia* data (Helmi et al., 2017; Myeong et al., 2018b,c) have convincingly shown that the highest energy stars in the halo are typically retrograde, reinvigorating these earlier suspicions. This rotational asymmetry could be the consequence of dynamical interaction between accreted satellites and the Milky Way. For example, Quinn and Goodman (1986) and Norris and Ryan (1989) show that retrograde accretion events – especially with some inclination – experience much less drag than prograde ones. So, the effect of many random infalls can produce an overall rotational asymmetry at high energy. A sharp feature traced by the retrograde stellar substructure has already been seen in energy-action space with a specific metallicity range. This is especially obvious in the subpanels of metallicity $-1.9 < [\mathrm{Fe/H}] < -1.5$ in Figure. 2 of Myeong et al. (2018c). This is a clear signature of an individual event of retrograde accretion in the past, distinct from other, numerous, past accretions.

Table 7.1 The kinematic, action, and orbital properties of the probable and possible GCs from Monte Carlo sampling.

Name	(J_R, J_ϕ, J_z) (kpc km s^{-1})	E (km^{2}s^{-2})	pericentre (kpc)	apocentre (kpc)	ecc.	incl. (deg)
FSR 1758	$(620^{+160}_{-130}, -1250^{+150}_{-150}, 230^{+50}_{-40})$	-142500^{+8100}_{-8400}	$3.8^{+0.5}_{-0.5}$	$16.2^{+3.0}_{-2.6}$	$0.62^{+0.02}_{-0.01}$	$146.5^{+1.4}_{-1.4}$
NGC 3201	$(900^{+140}_{-120}, -2800^{+80}_{-90}, 310^{+20}_{-20})$	-112300^{+3200}_{-3000}	$8.4^{+0.1}_{-0.1}$	$29.3^{+2.6}_{-2.1}$	$0.55^{+0.03}_{-0.02}$	$152.6^{+0.3}_{-0.3}$
ω Centauri	$(270^{+30}_{-30}, -520^{+30}_{-30}, 100^{+20}_{-20})$	-185000^{+900}_{-800}	$1.5^{+0.1}_{-0.1}$	$7.2^{+0.1}_{-0.2}$	$0.65^{+0.02}_{-0.03}$	$139.7^{+2.2}_{-2.1}$
NGC 6101	$(1400^{+240}_{-210}, -3210^{+200}_{-210}, 800^{+60}_{-50})$	-97200^{+4400}_{-4400}	$10.7^{+0.5}_{-0.5}$	$41.4^{+4.7}_{-4.2}$	$0.59^{+0.02}_{-0.02}$	$143.1^{+0.5}_{-0.5}$
NGC 6535	$(140^{+30}_{-30}, -350^{+30}_{-30}, 66^{+8}_{-7})$	-207600^{+800}_{-700}	$1.3^{+0.1}_{-0.1}$	$4.5^{+0.2}_{-0.1}$	$0.56^{+0.05}_{-0.04}$	$159.0^{+2.2}_{-2.4}$
NGC 6388	$(80^{+10}_{-5}, -250^{+40}_{-30}, 71^{+1.4}_{-1.3})$	-222300^{+3800}_{-3300}	$0.9^{+0.1}_{-0.1}$	$3.5^{+0.2}_{-0.5}$	$0.59^{+0.03}_{-0.02}$	$149.2^{+3.2}_{-4.3}$
NGC 6401	$(54^{+10}_{-7}, -590^{+110}_{-110}, 150^{+30}_{-30})$	-194000^{+8200}_{-8900}	$2.5^{+0.5}_{-0.5}$	$4.9^{+0.9}_{-0.8}$	$0.34^{+0.02}_{-0.02}$	$142.5^{+0.9}_{-1.1}$

Fig. 7.5 shows the Milky Way GCs from Vasiliev (2019b), together with the substructures found by Myeong et al. (2018b), in the plot of scaled action. GCs on retrograde orbits, including FSR 1758, lie on the far left-hand side of the plot. Specifically, the horizontal axis is the (normalized) azimuthal action $J_\phi/J_{\rm tot}$, while the vertical axis is the (normalized) difference between the vertical and radial actions $(J_z - J_R)/J_{\rm tot}$, where $J_{\rm tot}$ is the sum of absolute values of all three actions. Colour represents the radius of the circular orbit with the same energy, and so gives an idea of the typical distances probed by an object. The observational uncertainties such as the distance, line-of-sight velocities and proper motions are Monte Carlo sampled, with error ellipse transforming in action space to distended shapes. The gravitational potential used to represent the Milky Way is the one recommended as the best amongst the suite studied by McMillan (2017). It is an axisymmetric model with bulge, thin, thick and gaseous disks and an NFW (Navarro et al., 1997) halo.

The portion of the plot occupied by FSR 1758 (coloured green) overlaps with a number of GCs, in particular ω Centauri. Using a 'Friends-of-Friends' clustering algorithm in this scaled action space, we identify 6 GCs that form an agglomeration. They are FSR 1758, NGC 3201, ω Centauri (NGC 5139), NGC 6101, NGC 5635, and NGC 6388. All 6 are listed in Table 7.1, which gives their actions, energies and orbital characteristics. Also shown on Fig. 7.5 are all the retrograde stellar substructures identified by Myeong et al. (2018b). These are depicted as irregularly shaped polygons that include all the stars believed to be members. Apart from Rg5 and Rg7, it is striking that all the retrograde substructures overlap with our group of GCs associated with FSR 1758. Fig. 7.6 shows the same objects, but now plotted in the plane of eccentricity and inclination. We see that the GCs listed in Table 7.1 are restricted to a narrow range of inclinations ($140^\circ - 160^\circ$) and eccentricities ($e \sim 0.6$). We remark that additionally NGC 6401 may be associated with the group, at least as judged by inclination. However, its eccentricity is somewhat less than the other members. As a possible member, the orbital properties of NGC 6401 are also listed in the lower part of Table 7.1. It is noteworthy that the inclination range of our group appears to be distinct from the orbital plane of the Magellanic system (e.g., D'Onghia and Lake, 2009; Nichols et al., 2011) or the plane of Milky Way satellites (Kroupa et al., 2005) known to be near perpendicular to the Galactic plane.

In addition to the GCs (Vasiliev, 2019b) and retrograde stellar substructures (Myeong et al., 2018b), a retrograde stellar stream, GD-1 (Grillmair and Dionatos, 2006b) is also marked on Fig. 7.5, 7.6 and 7.7 based on a representative six-dimensional phase space information from Webb and Bovy (2019). Interestingly, the orbital inclination, (normalized) azimuthal action and energy of GD-1 appear to be comparable to our group of GCs and retrograde substructures. But, its other action components and orbital eccentricity noticeably

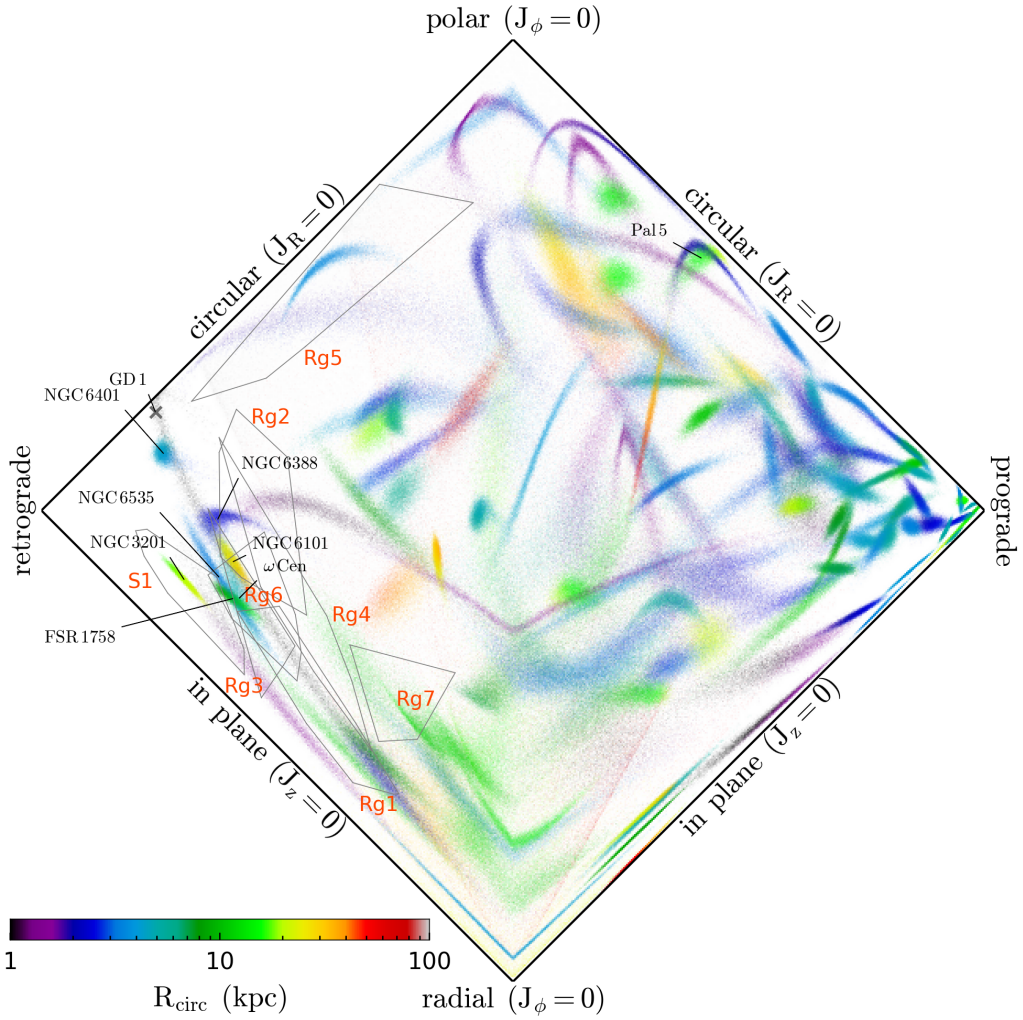

Fig. 7.5 The action-space map for the Milky Way GCs (Vasiliev, 2019b) and retrograde substructures (Myeong et al., 2018b). The GD-1 stream (Grillmair and Dionatos, 2006b) is also marked with a cross based on a representative 6D phase space information from Webb and Bovy (2019). The horizontal axis is $J_\phi/J_{\rm tot}$, and the vertical axis is $(J_z - J_R)/J_{\rm tot}$, analogous (but not exactly identical) to Fig. 5 of Vasiliev (2019b). Colour marks the circular orbit radius for the corresponding total energy $R_{\rm circ}(E_{\rm tot})$. Each object is shown with 1000 Monte Carlo representations of the orbit as drawn from the observational errors. The geometry of the figure can be thought as a projection of the energy-scaled three-dimensional action-space, viewed from the top (cf. Fig. 3.25 of Binney and Tremaine 2008).

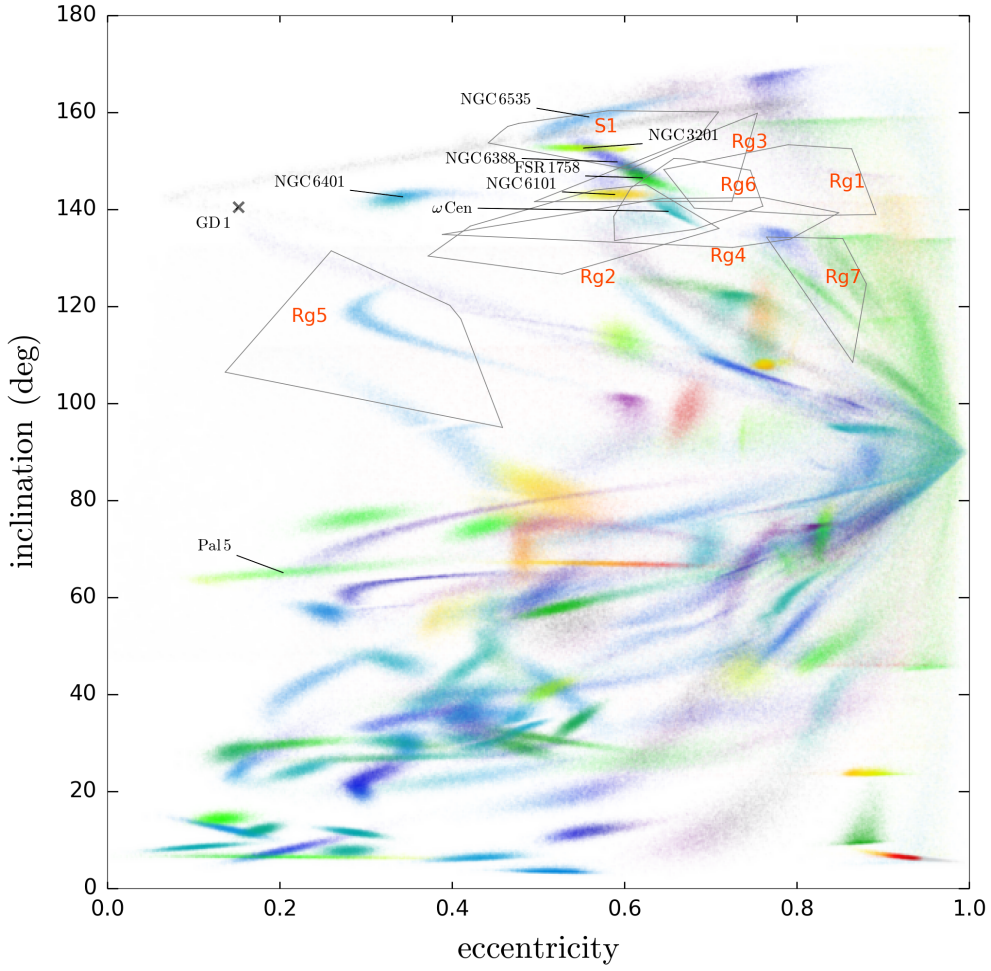

Fig. 7.6 Distribution of orbital eccentricity and inclination for the Milky Way GCs (Vasiliev, 2019b) and retrograde substructures (Myeong et al., 2018b). The GD-1 stream (Grillmair and Dionatos, 2006b; Webb and Bovy, 2019) is marked with a cross. Colours have the same meaning as in Fig. 7.5.

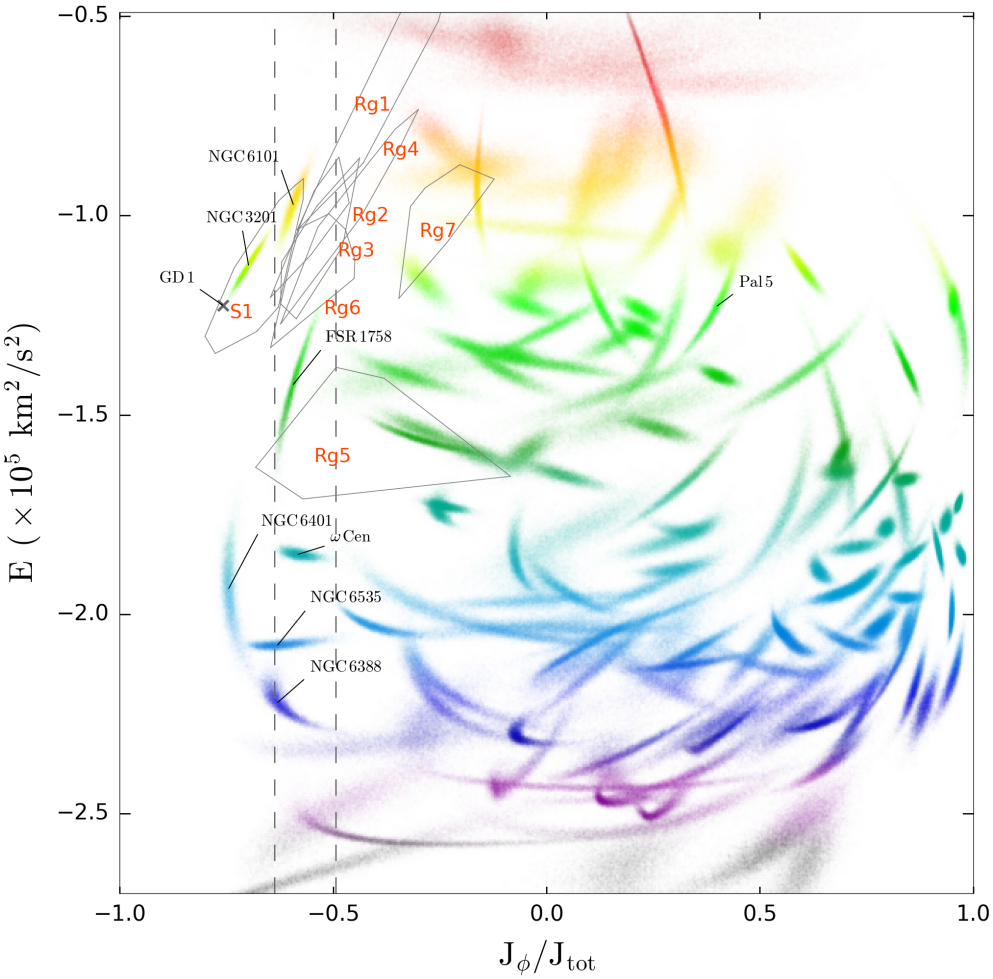

Fig. 7.7 Distribution of energy and normalised azimuthal action $J_\phi/J_{\rm tot}$ for the Milky Way GCs (Vasiliev, 2019b) and retrograde substructures (Myeong et al., 2018b). The GD-1 stream (Grillmair and Dionatos, 2006b; Webb and Bovy, 2019) is marked with a cross. Grey dashed lines are marking the 3σ range of ω Centauri (NGC 5139) in $J_\phi/J_{\rm tot}$, which traces the orbital inclination roughly. Candidate members associated with the accretion event that included ω Centauri are expected to lie within this range.

differ from our group. According to the complex morphology of GD-1 (see e.g., Malhan et al., 2019; Price-Whelan and Bonaca, 2018), there is a possibility that the current orbital characteristics of GD-1 may not be a good reflection of its past state or its progenitor or its parent dwarf galaxy. Nonetheless, it will require more detailed investigation to find out any potential connection between our group and GD-1.

There have been long-held suspicions over the intriguing and anomalous globular cluster, ω Centauri. Normal globular clusters often have multiple populations, but show homogeneous abundances in heavy elements (such as calcium and iron) together with variations in light elements (such as the oxygen-sodium anticorrelation). However, ω Centauri hosts multiple stellar populations with different heavy element abundances enriched by supernovae, as well as spreads in the light elements (see e.g., Bedin et al., 2004; D'Antona et al., 2011; D'Orazi et al., 2011; Joo and Lee, 2013; Lee et al., 1999). This necessitates the existence of different channels for enrichment to account for the chemical peculiarities of ω Centauri (e.g., Bekki and Norris, 2006; Marcolini et al., 2007; Romano et al., 2007). Already Freeman (1993) and Bekki and Freeman (2003) suggested it is the nucleus of a stripped dwarf galaxy, inspired by its very bound retrograde orbit. A number of authors have argued that the retrograde components in the stellar halo may be related to the disruption of ω Centauri (e.g., Brook et al., 2003; Dinescu, 2002; Helmi et al., 2017; Majewski et al., 2012; Myeong et al., 2018b,c). We amplify this hypothesis here by associating it with the Sequoia Event. Either ω Centauri is the remnant core of the Sequoia galaxy, or it was the largest GC member. For dwarf galaxies in cored haloes, the nucleus may be completely dissolved by the merging process, leaving only the GCs and stellar debris. For nucleated dwarfs or dwarfs in cusped haloes, the nucleus can survive intact, even if the outer parts are stripped. Whichever picture is correct, it is reasonable to conclude that the Sequoia dwarf once possessed an entourage of up to 7 GCs (5 probable and 2 possible).

Fig. 7.7 shows the distribution in energy and normalised azimuthal action. We show the azimuthal action of ω Centauri with its 3σ uncertainty as dashed vertical lines. If inclination is roughly preserved under the action of dynamical friction for these strongly retrograde mergers, then the dashed lines will delineate GCs and substructure associated with the ω Centauri, and hence the Sequoia. We see that FSR 1758, as well as the objects in Table 7.1, all lie within this band. GCs with higher energy were stripped earlier and/or composed the trailing tail. In this picture, FSR 1758 was one of the most massive GCs in the precursor dwarf galaxy, residing near the centre of the progenitor. So, it has ended up with comparable, if higher, energy. Objects with lower energy may have come from the disruption of the leading tail. This includes NGC 6535 (and possibly NGC 6388), which have been deposited closer to the centre of the Milky Way on tighter orbits.

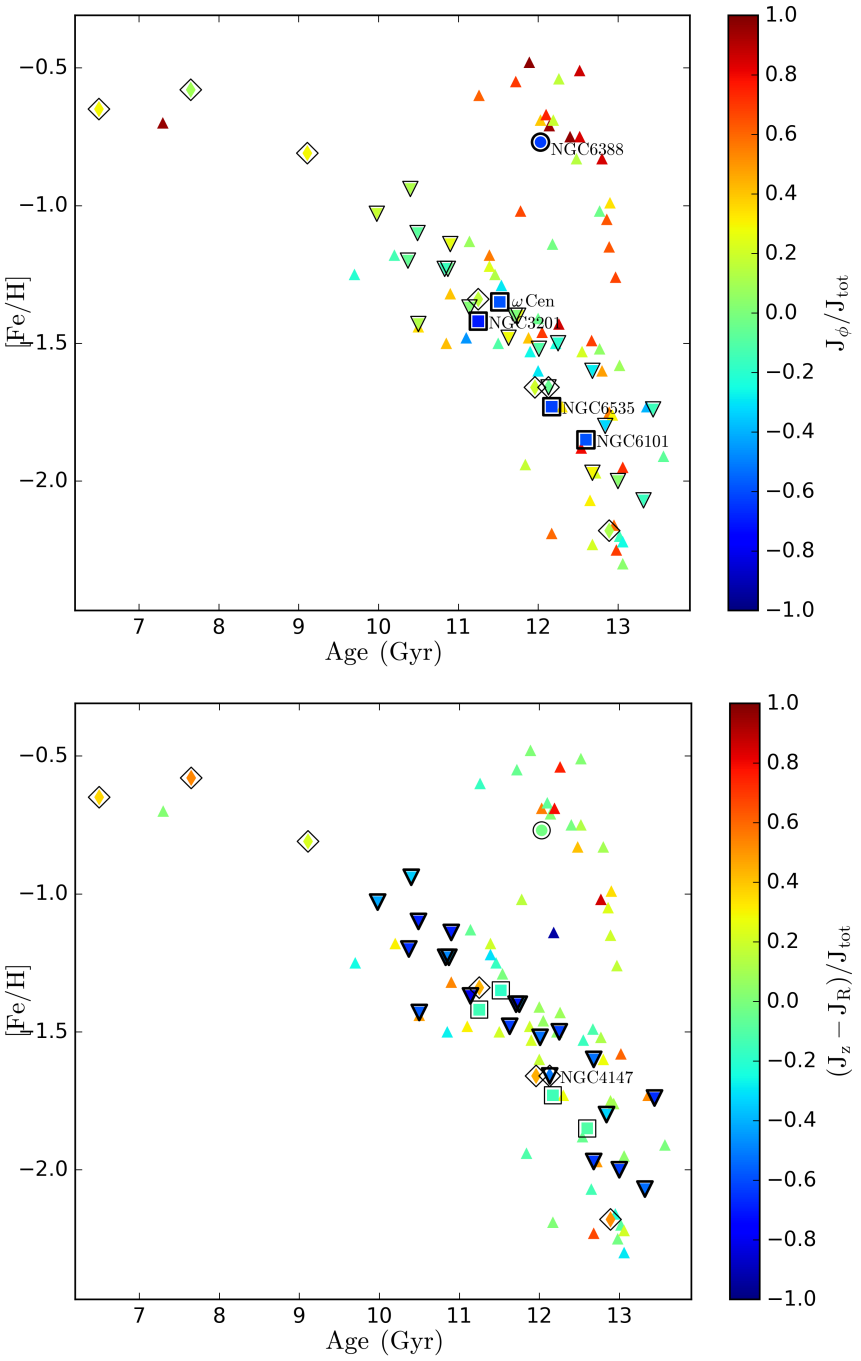

Fig. 7.8 Distribution of age and metallicity for the Milky Way GCs from Kruijssen et al. (2019) and the references therein. Five Sequoia member GCs with existing estimates are marked with squares (probable) and circle (possible). Sausage GCs (see e.g., Myeong et al., 2018d; Vasiliev, 2019b) are marked with downward-pointing triangles. Sgr GCs (see e.g., Forbes and Bridges, 2010) are marked as diamonds. Upper panel: Colour shows the normalised azimuthal action $J_\phi/J_{\rm tot}$. The member GCs stand out clearly with $J_\phi/J_{\rm tot} \sim -0.6$. Lower panel: Colour shows the normalised difference between the vertical and radial actions $(J_z - J_R)/J_{\rm tot}$. Sausage GCs stand out clearly with $(J_z - J_R)/J_{\rm tot} \sim -0.6$.

From energy arguments, the retrograde substructures (Myeong et al., 2018b) are more likely to be the remnant debris of the Sequoia than direct tidal debris from ω Centauri. The retrograde stellar substructures are stripped well before the progenitor became severely destroyed. In this case, if its core is indeed ω Centauri, we do not expect the retrograde substructures to show the unique chemical abundance patterns observed from ω Centauri (e.g., Na–O and Mg–Al patterns, Ba overabundance; cf. Navarrete et al., 2015). These may have been imprinted on ω Centauri by subsequent accretion of gas onto the nucleus, after the stripping process removed the retrograde substructures. It would be interesting to revisit Kapteyn's Moving Group (Wylie-de Boer et al., 2010) or the ω Centauri Moving group (Meza et al., 2005) – which were disproved to be ω Centauri's tidal debris based on the chemical abundances (Navarrete et al., 2015) – for the possibility that they are remnant debris of the Sequoia. By contrast, the freshly discovered Fimbulthul stream (Ibata et al., 2019) is probably stripped from ω Centauri itself rather than Sequoia and in this case should show the unique abundance patterns.

The age–metallicity relation of the GCs is shown in Fig. 7.8 based on data complied by Kruijssen et al. (2019). Among five member GCs estimates four GCs (except NGC 6388) form a distinct track in the age–metallicity relation that is different from the Milky Way's in-situ GCs. This is most visible in the upper panel of Fig. 7.8. This branching is similar to what has already been seen for GCs associated with major accretion events – in particular, the Sagittarius (Sgr) GCs (Terzan 7, Terzan 8, Arp 2, Pal 12, NGC 4147[1], NGC 6715, and Whiting 1, Forbes and Bridges, 2010, and marked as diamonds) or the Sausage GCs (see e.g., Myeong et al., 2018d, and marked as downward-pointing triangles). The track of the Sausage GCs stands out clearly especially at the lower panel of Fig. 7.8. This track in the age–metallicity plot of Fig. 7.8 is remarkable especially since the original membership of the GCs is established purely based on dynamical information. This is independent evidence of the extragalactic origin of the member GCs from an individual merger event.

Halo stars can be identified effectively based on chemical abundances such as [Al/Fe] and [Mg/Fe] (Hawkins et al., 2015). With APOGEE DR14 (Abolfathi et al., 2018), Mackereth et al. (2019) showed that halo stars with high eccentricity orbits tend to have lower [Mg/Fe] on average compared to the rest of the halo stars. In Fig. 7.9, we show more specifically that the highly radial Gaia Sausage remnant stars ($e \sim 0.9$ with $|J_\phi/J_{\rm tot}| < 0.07$ and $(J_z - J_R)/J_{\rm tot} < -0.3$) and the high energy retrograde substructure stars ($e \sim 0.6$ with $J_\phi/J_{\rm tot} < -0.5$ and $(J_z - J_R)/J_{\rm tot} < 0.1$) have clearly different [Fe/H] distribution and different abundance patterns. The Sausage remnants show a metallicity distribution function peak at [Fe/H]$= -1.3$, whereas the high energy retrograde stars are more metal poor, with the

[1] As will be discussed later, this cluster is unlikely to belong to the Sgr group, based on its kinematics.

peak at [Fe/H]$= -1.6$ (both in good agreement with Matsuno et al., 2019; Myeong et al., 2018c). While the metallicity distributions of the Sausage and Sequoia stars overlap, at fixed [Fe/H], the two galaxies show distinct patters in the abundance of alpha elements. For example, at [Fe/H]~ -1.5, the Sequoia debris are clearly more enhanced in Al compared to the Sausage. Such differences in the abundances provide additional evidence that the accretion event that made the high energy retrograde stars in the halo is also chemically different from the Sausage event. Interestingly, their chemical characteristics – the Sausage having higher [Fe/H] and lower abundance ratios compared to the Sequoia progenitor – are in line with the trend observed by Mackereth et al. (2019) from the EAGLE simulations (Schaye et al., 2015).

Matsuno et al. (2019) searched through the SAGA database, which contains ~ 880 metal-poor stars with [Fe/H] < -0.7. They also found that the high energy retrograde stars are clearly distinct from the stars of the Sausage which dominates the inner halo (Belokurov et al., 2018). They reported that the 'knee' in the abundance and metallicity plane differs by about 0.5 dex (at [Fe/H]~ -2 for the Sausage and ~ -2.5 for the retrograde stars) which is another indication of their different origin.

Our hypothesis is distinct from the proposal of Helmi et al. (2018), who made a broad selection based on the azimuthal action -1500 kpc km s^{-1} $< J_\phi <$ 150 kpc km s^{-1} only, as opposed to using additional integrals of motion. Helmi et al. (2018) used this sample to suggest the 'Gaia-Enceladus' accretion event. In our picture, this sample contains stars belonging to both the Gaia Sausage and the Sequoia. Our hypothesis is more closely related to the work of Mackereth et al. (2019), who divided halo stars according to eccentricity and showed that the low and high eccentricity groups have different abundance ratios and probably different origin. For the low eccentricity group, Mackereth et al. (2019) suggested they are likely to be a mixture of in situ halo stars and many smaller accreted materials – which includes the Sequoia debris. Matsuno et al. (2019) finding of a different 'knee' is important corroboratory evidence of this as well.

7.4 The Sequoia and the Sausage

The progenitor of the Sausage had a total mass in stars and dark matter $\gtrsim 10^{11} M_\odot$ (Belokurov et al., 2018). This was also derived in Fattahi et al. (2019) using cosmological hydrodynamical simulations (Grand et al., 2017), and is consistent with the estimates from Mackereth et al. (2019) and Vincenzo et al. (2019). Myeong et al. (2018d) identified 10 GCs associated with the Sausage event from one of the earliest kinematics dataset of 75 Milky Way GCs based on the Gaia DR2 (Gaia Collaboration et al., 2018c). This Sausage GC membership has

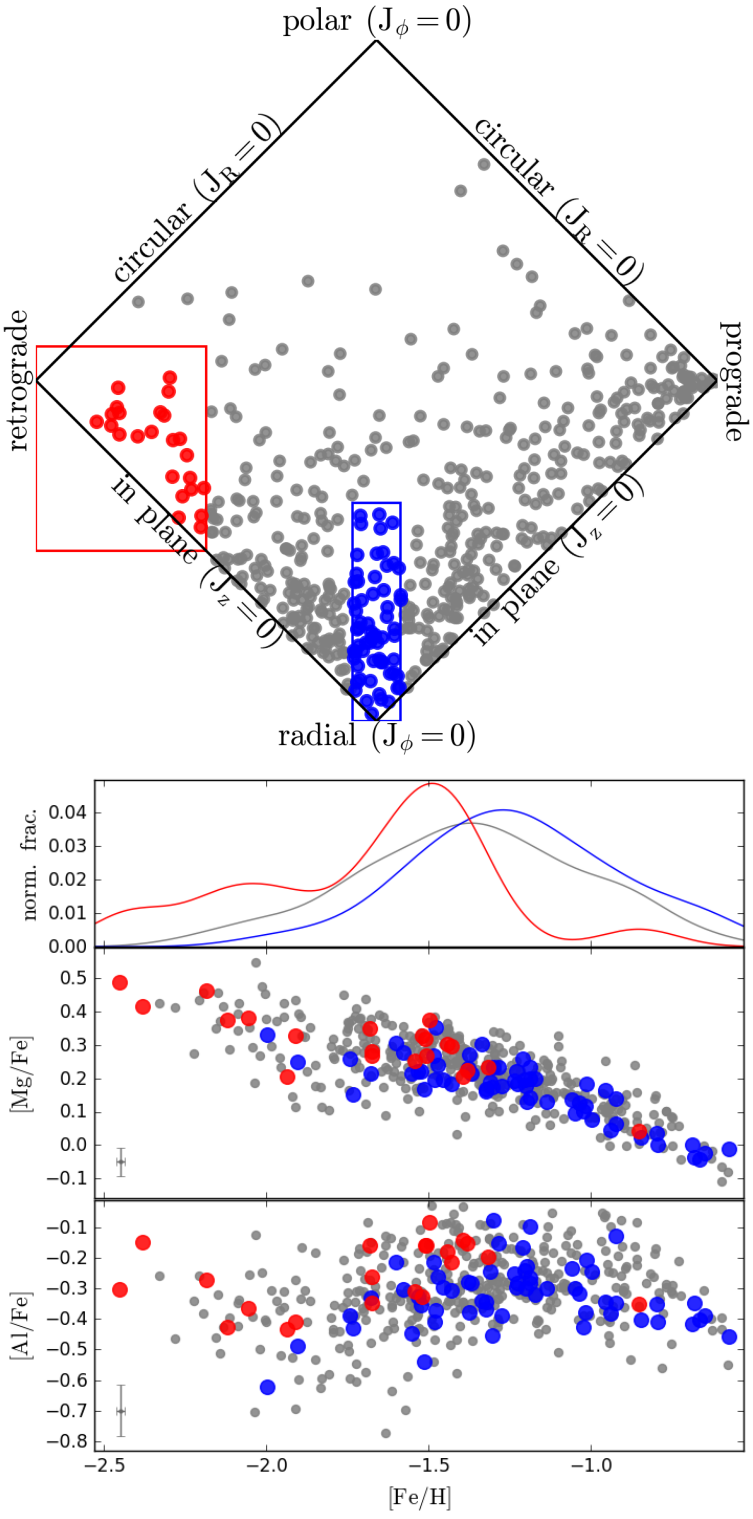

Fig. 7.9 The action-space map, metallicity distribution and abundance patterns for the halo stars in APOGEE DR14 (Abolfathi et al., 2018; Leung and Bovy, 2019). Gaia Sausage remnant set ($e \sim 0.9$ with $|J_\phi/J_{\rm tot}| < 0.07$ and $(J_z - J_R)/J_{\rm tot} < -0.3$) and the high energy retrograde set ($e \sim 0.6$ with $J_\phi/J_{\rm tot} < -0.5$ and $(J_z - J_R)/J_{\rm tot} < 0.1$) are shown with blue and red. Rest of the halo stars are shown in grey.

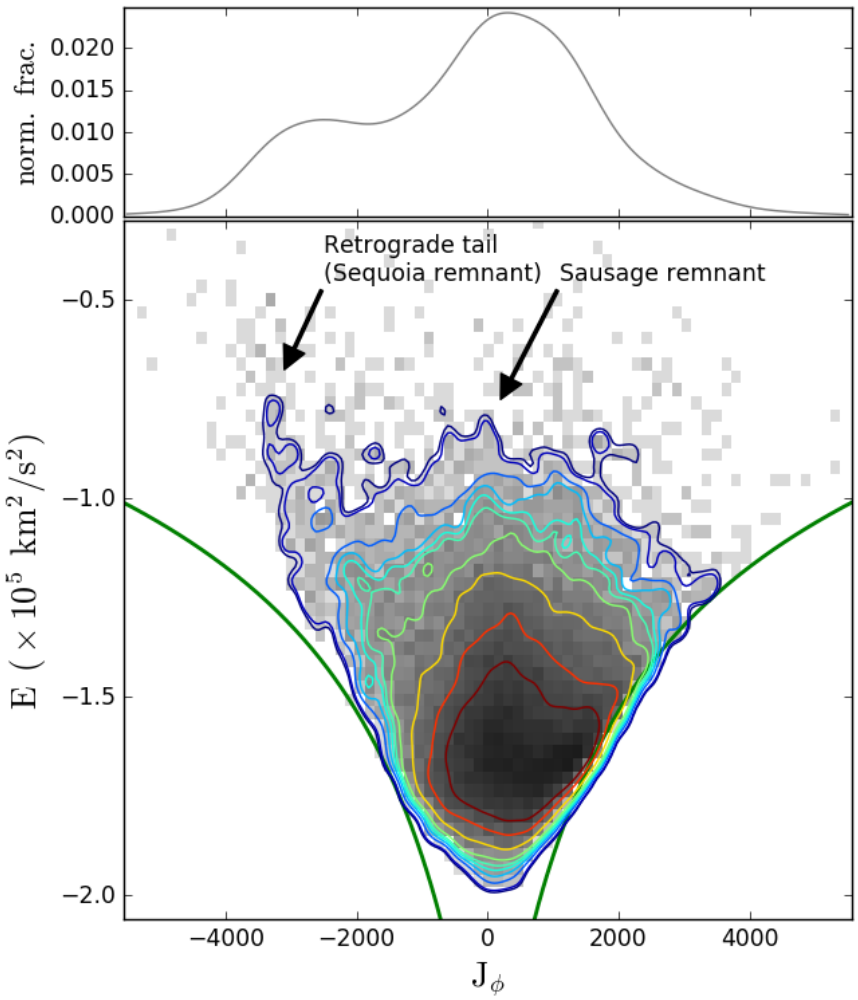

Fig. 7.10 Distribution of energy and azimuthal action for the halo stellar sample similar to Figure. 2 of Myeong et al. (2018c). The top panel is showing the distribution function of the azimuthal action for the stars with high energy ($E > -1.1 \times 10^5$ km^{2}s^{-2}). The signature of Gaia Sausage remnants is visible as a peak at low J_ϕ. A separate trace of a retrograde accretion (Sequoia event) is clearly visible as a sharp tail around $J_\phi \sim -3000$ kpc km s^{-1} (Myeong et al., 2018b). Green lines mark the circular orbit.

been revised with the more complete catalogue of 150 Milky Way GCs (Vasiliev, 2019b) and also with the age–metallicity relation (see e.g., lower panel of Fig. 7.8). The original identification by Myeong et al. (2018d) was also limited to GCs with noticeably high energy only. These authors used the total energy of the young halo (YH) clusters (see e.g., Mackey and Gilmore, 2004; Mackey and van den Bergh, 2005; Zinn, 1993, for more details on the GC classification) known at that time as a reference energy in order to concentrate on the old halo (OH) GCs with the most certain ex situ origin, judging from their noticeably high total energy. As we now have better knowledge on the typical chemo-dynamical characteristics of the Sausage GCs (e.g., $e \sim 0.9$, $(J_z - J_R)/J_{tot} \sim -0.6$ with age–metallicity branching from Fig. 5 of Vasiliev (2019b) and Fig. 7.8 in this work), we can revise the search in the larger catalogue of Milky Way GCs, without any artificial energy cut. We note that only the GCs with full kinematics, age and metallicity information have been examined. This gives up to 21 potential GCs showing typical chemo-dynamical characteristics of the Sausage, specifically NGC 362 [2], 1261 [2], 1851, 1904, 2298, 2808, 4147 [23], 4833, 5286, 5694, 6544, 6584 [2], 6712, 6779, 6864, 6934 [2], 6981 [2], 7006 [2], 7089, Pal 14 [2], Pal 15. Note that there are 8 YH classified GCs among the set with red horizontal branch (HB) morphology (see e.g., Mackey and Gilmore, 2004; Mackey and van den Bergh, 2005; Zinn, 1993). Since the Sausage progenitor was considerably massive, its original GCs might have HB morphology similar to the Milky Way OH clusters (see Mackey and Gilmore, 2004; Mackey and van den Bergh, 2005, for more detail), while some of the younger GCs with red HB morphology might have been formed during the wet merger of the Sausage and the Milky Way (see e.g., Renaud, 2018), or have been acquired by the Sausage from separate accretion events before it merged with the Milky Way. Interestingly, this number, 13, of Sausage GCs with OH classification is in agreement with the suggested number of expected GCs originally formed in a major merger satellite of the Milky Way (see e.g., Kruijssen et al., 2019).

The Sequoia event has at least 4 GCs, excluding ω Centauri (as is right if it is the stripped core). The total stellar mass of GCs is known to be correlated with the (halo) mass of the host, albeit with some scatter. Based on the current and the initial masses of the GCs from Baumgardt et al. (2019) and using the fractional mass $\langle \eta \rangle = M_{\rm GCs}/M_{\rm halo} \sim 4 \times 10^{-5}$ derived by Hudson et al. (2014), we can estimate the progenitor mass. In the case of the Gaia Sausage with 13 OH clusters, the progenitor mass is at least $1 \times 10^{11} M_{\odot}$ (from the current mass of the GCs) or up to $4 \times 10^{11} M_{\odot}$ (from the initial mass of the GCs). Hudson et al. (2014)

[2]YH clusters (see e.g., Mackey and Gilmore, 2004; Mackey and van den Bergh, 2005; Zinn, 1993)

[3]Note that NGC 4147 is among the potential Sausage GCs. NGC 4147 has previously been suggested as a Sgr GC (e.g., Bellazzini et al., 2003; Forbes and Bridges, 2010), while there are studies suggesting no connection with Sgr dwarf (e.g., Law and Majewski, 2010). Here, we consider NGC 4147 to be a potential Sausage GC as the orbital characteristics of NGC 4147 are very different from the Sgr dwarf and other Sgr GCs, while they are similar to other Sausage GCs.

also provides a fractional value for the GC mass in terms of the stellar halo mass, which yields corresponding lower bounds on the stellar mass of the Sausage progenitor of $5 \times 10^8 M_\odot$ or up to $5 \times 10^9 M_\odot$ respectively. The abundance matching relation of Garrison-Kimmel et al. (2014) gives similar estimates as well. Since our estimates are not redshift corrected, we note that they are overestimates of the actual progenitor mass at the merger time.

In comparison, the mass of the Sequoia galaxy is at least $1 \times 10^{10} M_\odot$ (from the current mass of the GCs) or $5 \times 10^{10} M_\odot$ (from the initial mass[4] of the GCs). Valcarce and Catelan (2011) suggested the mass of the progenitor of ω Centauri may be as high as $10^{10} M_\odot$ from chemical evolution modelling of its multiple populations which is in broad agreement. The lower bound of the stellar mass from abundance matching gives $5 \times 10^6 M_\odot$ (current mass of GCs) or $7 \times 10^7 M_\odot$ (initial mass), while the relation from Hudson et al. (2014) gives higher stellar mass estimates by a factor of two. The mass-metallicity relation of Kirby et al. (2013b) with a metallicity of -1.6 gives a broadly consistent stellar mass of $2 \times 10^7 M_\odot$, but if we take account of the redshift evolution of the relation, this could be larger (see e.g., Ma et al., 2016). For example, for $z = 1.3$, the relation gives $1.7 \times 10^8 M_\odot$ which is again comparable to other estimates.

Although less massive then the Gaia Sausage, the Sequoia was a notable accretion in the evolutionary history of the Milky Way. In terms of the mass, the Fornax dwarf spheroidal could be a rough representation of the Sequoia progenitor. The fact that the Fornax dSph hosts a comparable number of GCs is also a similarity. Among its six GCs, Fornax 4 has been considered for possible ex situ origin (see e.g., Buonanno et al., 1999; van den Bergh, 2000), leaving Fornax with five probable in situ GCs. This is comparable to our estimates of the current number of member GCs of the Sequoia galaxy.

It is noteworthy that NGC 3201 is one of the probable members of the Sequoia event. It has already been pointed out that NGC 3201 is potentially associated with the S1 stellar stream (Myeong et al., 2018a; O'Hare et al., 2018). In fact, NGC 3201 and the S1 stream have almost identical actions and energy. Myeong et al. (2018a) identified the S1 stream as a stellar remnant of an accreted dwarf, and inferred its progenitor mass to be in order of $\sim 10^{10} M_\odot$ based on the library of accretion events using minor merger N-body simulations (Amorisco, 2017). Interestingly, in this study, we already derived the lower bound mass of the Sequoia to be in order of $\sim 10^{10} M_\odot$ as well, based on completely different methods. Such agreement from independent approaches adds credence to the authenticity of this likely the same event discovered from two separate studies.

[4]For the mass fraction $M_{\rm current}/M_{\rm initial}$ for FSR 1758, we used the mean mass fraction of the other member GCs.

Now, the infall time for the S1 stream's progenitor is $\gtrsim 9$ Gyr (Myeong et al., 2018a). If the S1 progenitor is indeed the Sequoia, this provides a consistent picture, as the youngest GC associated with the event (NGC 3201) is ~ 11 Gyr. In fact, the S1 stream and NGC 3201 bracket the range of possible infall times between 9 and 11 Gyr. Interestingly, Marcolini et al. (2007) suggested that ω Centauri is a remnant of a dwarf spheroidal galaxy accreted ~ 10 Gyr ago based on their study with hydrodynamical and chemical modelling. This is in a good agreement with our range. Also, we note that this suggested age range (9 Gyr to 11 Gyr) agrees very well with the suggested infall time of the Gaia Sausage itself. There is a possibility that the Sausage and the Sequoia galaxies were accreted at a comparable epoch. This suggests that here may have been a global association between them – perhaps the Sequoia was a satellite galaxy of the Sausage? The currently observed higher angular momentum of the Sequoia debris could reflect its binary orbital velocity at the time of accretion. More generally, any small differences in the initial condition at the early stage of the infall can easily cause the current difference between the orbital characteristics of the Gaia Sausage (highly radial with very low azimuthal action) and the Sequoia event (clearly retrograde).

7.5 Conclusions

The starting point of our investigation is an unusual object FSR 1758 (Froebrich et al., 2007). Its enigmatic nature was recently pointed out by Barbá et al. (2019), who raised the question as to whether FSR 1758 is an unusually large globular cluster or a dwarf galaxy remnant. Using Gaia data, we derived its proper motion dispersion profile, which is strongly declining, and so we concur with Simpson (2019) that FSR 1758 is an accreted, retrograde globular cluster. Our modelling suggests that FSR 1758 has a half-light radius of ~ 9 pc and a baryonic mass of $\sim 2.5 \times 10^5 M_{\odot}$ with an uncertainty $\lesssim 20\%$.

It is natural to look for other retrograde globular clusters with similar actions as FSR 1758, which may have fallen in to the Milky Way at the same merger. This led us to the identification of Sequoia Event, which was already conjectured from our studies of stellar substructures (e.g., Myeong et al., 2018b,c). Other investigators before us (e.g., Beers et al., 2012; Carollo et al., 2007; Majewski et al., 2012; Norris and Ryan, 1989; Quinn and Goodman, 1986) have concurred that the highly retrograde parts of the stellar halo are most likely accreted.

The Sequoia Event is distinct from other known accretions, particularly the Gaia Sausage (Belokurov et al., 2018; Myeong et al., 2018c,d). It has been seen in three tracers. First, there are at least 6 globular clusters, packed in action space around FSR 1758. These

include ω Centauri itself, the most massive of the Milky Way globular clusters. Based on its kinematics and its spread of stellar ages, metallicities and abundances, this has long been suggested as the stripped core of a dwarf galaxy remnant (e.g., Bekki and Freeman, 2003; D'Antona et al., 2011). It may therefore be the remnant of the Sequoia galaxy. However, it is also possible that ω Centauri may have been a core globular cluster of a now wholly destroyed progenitor. Whichever hypothesis is correct, it still remains the case that FSR 1758 is also one of the Sequoia's largest globular clusters. Of the agglomeration of 6 globular clusters, 4 have existing age and metallicity estimates (see e.g., Kruijssen et al., 2019, and the references therein). They form a distinct track in the age–metallicity relation, different from the Milky Way's in situ globular clusters. Additionally, this track shows evidence of an offset from the track of the Sausage globular clusters (Myeong et al., 2018a), supporting the identification of a separate event.

Secondly, the Sequoia Event is discernible in the retrograde stellar substructures, which are clearly visible in energy and action space (Myeong et al., 2018b). They form a separate grouping from the bulk of the Gaia Sausage, which has close to zero net angular momentum. This is clearly shown in Fig. 7.10, where the morphology of the contours in the high energy region shows the pattern of bimodal accretion tracks. The distribution of the azimuthal action for the stars with high energy (e.g., $E > -1.1 \times 10^5$ km^2/s^2) shows the existence of this extra retrograde component, clearly separated from the Sausage at zero angular momentum. Myeong et al. (2018b,c) showed the signal of this extra component is concentrated at a specific range of metallicity ([Fe/H] ~ -1.6). Thus, the Sequoia Event is also distinct from the Gaia-Enceladus structure (Helmi et al., 2018), which appears to combine parts of the Gaia Sausage and the Sequoia.

Thirdly, the very metal poor stars that are retrograde also have a chemical signature in the abundance and metallicity plane that is distinct from both the Sausage and the overall halo. This was already hinted at in Mackereth et al. (2019), who used APOGEE data release 14 (DR14, Abolfathi et al., 2018) to demonstrate that the retrograde halo stars have lower [Mg/Fe] compared to the rest of the halo. The argument was further substantiated by Matsuno et al. (2019), who found evidence that the knee in the abundance and metallicity plane occurs at different spots separated by 0.5 dex for the stars in the Sausage and in the retrograde component or Sequoia. We have provided further evidence from APOGEE DR14 that the metallicity distribution and the abundance patters of Sausage and Sequoia stars are different (see Fig. 7.9). The peak of the metallicity distribution function of the Sausage is higher with [Fe/H] $= -1.3$ as compared to the Sequoia at [Fe/H] $= -1.6$. The abundance ratios of Sausage stars are lower than Sequoia stars.

These three lines of evidence all argue for two different accretion events. A number of arguments (abundance matching, mass in globular clusters today) suggest that the Sausage progenitor had a total mass of $\sim 1-5\times10^{11}M_{\odot}$, whilst the Sequoia had a mass of $\sim 1-5\times10^{10}M_{\odot}$. In terms of stellar mass, the Sausage weighs in at $\sim 5-50\times10^{8}M_{\odot}$, whilst the Sequoia is $\sim 5-70\times10^{6}M_{\odot}$. Modern day analogues would be the Large Magellanic Cloud and Fornax dSph, respectively. The infall time is somewhat comparable, and so the two progenitors may have been a binary pair or association.

Different tracers (e.g., globular clusters, retrograde stellar substructures) stripped from the progenitor at different times now occupy different portions of energy and action space. They are like stepping stones that enable us to recreate the history of the event and trace out the time evolution of the disruption of the progenitor. To carry out such a re-creation, we need to be certain which substructures can be definitely associated with the Sequoia event. Here, detailed studies of abundances of stars with high resolution spectroscopy can play a crucial role. The chemical signature of the Sequoia event is seemingly evident both in Fig. 7.9, as well as in Mackereth et al. (2019) and Matsuno et al. (2019). The current limitation is the size or the quality of the sample and so dedicated medium or high resolution spectroscopic follow-up study is essential.

Chapter 8

Summary and Future Prospects

The stellar halo of the Milky Way is an interesting component of the Galaxy. It is believed to be mainly formed by the extragalactic materials as a result of the past accretions (see e.g., Abadi et al., 2006; Font et al., 2006; Searle and Zinn, 1978). In addition to its *ex-situ* origin, the timescale for the dynamical relaxation is much longer in this region of the Galaxy which means their present-day dynamics can better preserve the traces of the past accretion/merger events. Studying the present-day structure and substructure of the Milky Way halo is therefore one of the most direct ways of understanding the formation and the evolutionary history of the Galaxy. Yet, obtaining a sample of halo stars with sufficient size and quality has been a challenge due to the sparse density of the stellar halo, and the detailed study on the halo has been largely limited so far.

In this perspective, the current and the future *Gaia* Data Releases (DR) can open a new era for the study of Galactic Archaeology. The recent *Gaia* DR2 provides data that is incomparable in volume and quality compared to any pre-existing data. Precise astrometric information is now available for ~ 1.3 billion stars across the Milky Way which had remained uncharted so far. The combination of the recent *Gaia* dataset with various spectroscopic surveys such as SDSS (SEGUE), APOGEE, LAMOST, RAVE and GALAH can give us an access to the largest dataset of the Milky Way halo stars, comprising full six-dimensional phase space (complete spatial and velocity) information and chemical abundances. This dataset is almost 60 times larger in number, across 5 times greater spatial volume in the Milky Way.

So far, most conventional studies have relied on limited or incomplete phase space information with lower dimensionality and with missing components – insufficient to fully understand the substructure's dynamics or to trace the evolutionary history of its progenitor. Also, only those substructures with sufficiently high surface density could have been identified, which has been a big limitation for halo substructure study.

In contrast, the full six-dimensional phase space information allows us to study the stellar dynamics by inferring the conserved elements along the orbit (e.g., integrals of motion) for individual stars. The action-angle variables (a set of canonical coordinates of the Hamiltonian) provide clear characterisation of the individual stellar orbits. They are adiabatic invariant so remain approximately constant even under the slow change in the potential (i.e., Galactic evolution). This means they are effectively conserved, so the variables inferred based on the present-day data reflect the past state – they are like "living fossils". This makes them ideal for the "Galactic Archaeology" as they allow us to trace the hidden history of Galaxy formation and evolution. For the first time, I computed the action-angle variables based on a "realistic" potential of the Milky Way (e.g., McMillan, 2017) for an incomparably large set of the halo stars.

In addition to the dynamical information, chemical abundances for individual stars provide key information for identifying different stellar populations. This chemical information can be complementary to the dynamical analysis. For example, the chemo-dynamical correlation among stars or stellar populations can be studied to compile a genealogy of Milky Way evolution. Such a study of the Milky Way halo with complete dynamical information and chemical abundances has been and will continue to provide us with a key to unveil the true structure of the Milky Way and its formation mechanism which is also closely linked to the dark matter and to the current picture of the Λ Cold Dark Matter Cosmology.

In Chapter 2, I have studied the morphology of the stellar halo of the Milky Way based on their action space distribution, as a function of metallicity. This study showed many interesting features of the halo, such as the chemo-dynamical duality of the halo (the evidence of the most significant merger revealed so far – the *"Gaia Sausage"* Belokurov et al., 2018; Myeong et al., 2018c), the trace of a past retrograde accretion (contributed by the current high energy retrograde halo component), and a resonant feature (evidence of the dynamical influence of the Milky Way bar).

Chapter 3, 4 and 5 are examples of a more focused study on the halo substructures with a new detection algorithm that differs from the conventional studies. These studies reveal the existence of halo substructures. The majority of them appear to be retrograde stellar streams which are highly likely to be the remnant of past retrograde accretions. I have investigated the properties of the potential progenitors (past accreted dwarf galaxies) of these substructure. I also have looked for potential association of these substructures with ω Centauri which has long been suggested to be a remaining core of a dissolved dwarf galaxy that could be the major contributor of retrograde stars in the inner halo.

I also compiled a catalogue of Milky Way globular clusters with six-dimensional phase space information as well as their age, metallicity, horizontal-branch (HB) index and the

classification based on the HB index (e.g., Forbes and Bridges, 2010; Mackey and van den Bergh, 2005; Vasiliev, 2019b). If the radially anisotropic metal-rich halo population (see e.g., Chapter 2) is a result of a radial merger of one or a group of satellites in the past (the *"Gaia Sausage"*), any globular clusters originated from them are likely to have similarly radial orbits. Indeed, a collection of globular clusters with strong chemo-dynamical similarity to the *"Gaia Sausage"* remnant is identified in Chapter 6. Their age–metallicity relations also support their extragalactic origin and adds more credence to the association with the *"Gaia Sausage"*.

The age, metallicity and dynamical information of the Milky Way globular clusters reveals a group of globular clusters with comparable orbital characteristics (eccentric and highly retrograde) that also forms a separate age–metallicity track differs from the bulk of the *in-situ* Milky Way globular clusters. More interestingly, their orbital characteristics and the metallicity distribution are in good agreement with the majority of the retrograde stellar streams identified in Chapter 4 and 5. Chapter 7 shows the chrono-chemo-dynamical evidence of another early retrograde accretion event – the *"Sequoia"* – that contributed to the Milky Way's evolution, especially to the retrograde halo population. From multiple tracers in the Milky Way halo, including the stellar substructures and globular clusters, the chemical and dynamical signature of the *"Sequoia"* and its present-day remnants has been investigated.

Most of the work mentioned so far is based on the first *Gaia* data release with some updates from the second data release. This is a foretaste of what to come. Future data releases from *Gaia*, LSST, 4MOST, and many more will come in a few years time. Here I am closing the chapter with brief descriptions on some of the research ideas to pursue as a next step to take from the current results. One example is a study on the stellar structures associated with the Milky Way globular clusters. Such structures could be a result of the dynamical evolution of the globular cluster itself or the globular cluster's parent, such as a past-accreted dwarf galaxy. If a globular cluster has extragalactic origin and was released into the Milky Way as a result of the tidal disruption of its parent, it will have orbital characteristics similar to some other (extragalactic) stellar materials in the halo originating from the same parent. Since the traces of such stellar contents can be elusive by themselves, the globular cluster can be a powerful tracer in the phase space to capture the sign of such remnants of the past accretion/merger. Here, dynamical information such as the action-angle variables or orbital parameters can be used based on the full six-dimensional phase space information with a realistic Milky Way potential model. The globular cluster's actions can be used as a seed to capture the stars with comparable actions (similar orbit). The study also can be extended to the samples without the full phase space information by marginalising over

the missing components. This method will be more effective than the conventional studies which only rely on photometric imaging, as it is more sensitive to the low surface brightness structure and is much more resistant to the phase-mixing. This also provides more complete information about the dynamics of the structure. We can trace the evolutionary history of it and its progenitor as a result of dynamical interactions with the Milky Way. This can provide powerful constraint on the physical characteristics of its progenitor and the Milky Way.

The chemo-chrono-dynamical correlations between the Milky Way globular clusters can provide constraint on the portion of Milky Way globular clusters with extragalactic origin which is related to the significance of the role of the accretion/merger process in the galaxy formation and evolution – in line with the ΛCDM cosmology. Combined information of chemical abundances, age, horizontal-branch morphology, action-angle variables and orbital characteristics (e.g., inclination, precession rate, eccentricity) can provide an effective arena for the study of chemo-chrono-dynamical correlations between globular clusters. Each identified globular cluster pair or group could indicate a separate accretion/merger event in the past that brought corresponding globular clusters into the Milky Way. Their progenitors (e.g., dwarf galaxy) also can be characterised. For example, the number and the age of the member globular clusters tell us about the progenitor's mass and the time of infall. Its action variables and orbital characteristics are also closely related to the initial condition of infall (e.g., angle or eccentricity). Any preferred infall direction or the possibility of "group infall" can be examined among those identified cases. This can be compared with the existing satellite galaxies around the Milky Way. Also, this can reveal the existence of "dark matter filaments" which is another characteristic features predicted in the ΛCDM model.

The existence of shell structures in the Milky Way associated with the *"Gaia Sausage"* is another interesting topic. The *"Gaia Sausage"* appears to be one of the most massive mergers that occurred in the Milky Way. The range of apocentres of these *"Sausage"* stars is closely related to the size of the progenitor, and the number of orbits during its orbital decay. While these stars show considerable spread of apocentre, the distribution of the apocentre, mean (time-averaged over orbits) and current Galactocentric radius of the associated stars can be analysed in detail. Particularly since the *"Gaia Sausage"* was a radial infall (or quickly radialised), it is highly likely for the orbital decay of the progenitor to leave noticeable structures such as "stellar shells" which will appear as patterns or peaks in these distributions. Thus, such traces can provide us with a crucial understanding of the orbital decay process under the dynamical friction, and so can provide constraint on the potential (structure and mass distribution) of the Milky Way and the *"Gaia Sausage"*.

In addition, newly discovered stellar streams with extragalactic origins (e.g., S1 and Rg streams) are other good tracers for investigating the Milky Way potential and the orbital

decay process with regard to the dynamical friction. Moreover, these cases provide important clues for investigating the potential existence of the associated dark matter component at the inner Galaxy. Such information is crucial for the direct dark matter detection experiments based on the recoil energy regarding the streams which have very good prospects for the purpose.

The follow-up study of retrograde stellar streams is another topic of great interest. For example, more detailed chemical abundance analysis will aid the confirmation of the extragalactic nature of these retrograde stellar streams, and will provide insight into their detailed chemical and star formation history. This can be achieved from medium/high-resolution spectroscopy of the member stars. While the current analysis on the metallicity ([Fe/H]) and the kinematics of the stars in these stellar streams strongly hint at the likely progenitors being dwarf galaxies, it is crucial to obtain chemical evidence to assess their extragalactic origin, to study their star-formation history and to make comparisons with the surviving dwarf galaxy population or the stripped dwarf galaxy nucleus ωCentauri. Our retrograde stellar streams could be a new evidence of a past retrograde accretion (the *"Sequoia"*, contributing to the retrograde halo component) with a clear trace of orbital decay. They also could be the first confirmed discovery of significant halo substructures associated with ωCentauri and its progenitor. On the other hand, a possible globular cluster origin can also be explored through a very tight metallicity distribution and the presence of the well-known abundance anti-correlations (e.g., Na–O, Mg–Al) which are universal in globular cluster stars.

Another interesting topic is a study of traces of radialisation in the metal-poor halo component. Previous study on the Milky Way halo based on the action-angle variables revealed a massive major merger *"Gaia Sausage"* which created a highly radial, metal-rich halo component. In addition to this, a possible trace of an anti-correlation between the energy and the radial action from the metal-poor halo population was observed. Such anti-correlation may be a result of a significant radialisation during the orbital decay of a massive merger. The existence of such traces at the inner Galaxy can be a clue for unveiling the nature of the metal-poor halo, especially regarding the origin, formation and evolution mechanism of it and the Milky Way.

Similar chemo-dynamical analysis can be made to the disc component of the milky Way to identify the substructures in the disc. The detected comoving candidates can be studied in details with their chemical and dynamical characteristics, and also can be compared to the known comoving bodies such as open clusters. Similarly, the kinematics of the known open clusters can be used as tracers to look for further members with comparable dynamics. Also, potential associations between the known open clusters can be examined. Although

the vast majority of the disc stars are expected to show strong rotation corresponding to the Galactic rotation, we may be able to find specific correlations or trends among the disc stars and classify them into subgroups. We may be able to identify outlier comoving groups as well. In addition, any sign of radial mixing could be traced.

The recent *Gaia* data releases already have opened a new chapter for the field of Galactic Archaeology. The *Gaia* mission is highly complementary to many other existing and forthcoming surveys and indeed have brought an incredible synergy. The current and the future *Gaia* data releases and the upcoming surveys (e.g., wide-sky spectroscopic survey such as 4MOST) will continue to be the driving force for our voyage to the uncharted ocean of knowledge.

References

Abadi, M., Navarro, J., and Steinmetz, M. (2006). Stars beyond galaxies: the origin of extended luminous haloes around galaxies. *Monthly Notices of the Royal Astronomical Society*, 365:747–758.

Abadi, M., Navarro, J., Steinmetz, M., and Eke, V. (2003). Simulations of galaxy formation in a lambda cold dark matter universe. ii. the fine structure of simulated galactic disks. *The Astrophysical Journal*, 597:21–34.

Abolfathi, B., Aguado, D. S., Aguilar, G., Allende Prieto, C., Almeida, A., Ananna, T. T., Anders, F., Anderson, S. F., Andrews, B. H., and Anguiano, B. (2018). The Fourteenth Data Release of the Sloan Digital Sky Survey: First Spectroscopic Data from the Extended Baryon Oscillation Spectroscopic Survey and from the Second Phase of the Apache Point Observatory Galactic Evolution Experiment. *The Astrophysical Journal Supplement Series*, 235(2):42.

Agnello, A. and Evans, N. W. (2012). Virial sequences for thick discs and haloes: flattening and global anisotropy. *Monthly Notices of the Royal Astronomical Society*, 422:1767–1778.

Ahn, C. P., Alexandroff, R., Allende Prieto, C., Anderson, S. F., Anderton, T., Andrews, B. H., Aubourg, É., Bailey, S., Balbinot, E., Barnes, R., Bautista, J., Beers, T. C., Beifiori, A., Berlind, A. A., Bhardwaj, V., Bizyaev, D., Blake, C. H., Blanton, M. R., Blomqvist, M., Bochanski, J. J., Bolton, A. S., Borde, A., Bovy, J., Brandt, W. N., Brinkmann, J., Brown, P. J., Brownstein, J. R., Bundy, K., Busca, N. G., Carithers, W., Carnero, A. R., Carr, M. A., Casetti-Dinescu, D. I., Chen, Y., Chiappini, C., Comparat, J., Connolly, N., Crepp, J. R., Cristiani, S., Croft, R. A. C., Cuesta, A. J., da Costa, L. N., Davenport, J. R. A., Dawson, K. S., de Putter, R., De Lee, N., Delubac, T., Dhital, S., Ealet, A., Ebelke, G. L., Edmondson, E. M., Eisenstein, D. J., Escoffier, S., Esposito, M., Evans, M. L., Fan, X., Femenía Castellá, B., Fernández Alvar, E., Ferreira, L. D., Filiz Ak, N., Finley, H., Fleming, S. W., Font-Ribera, A., Frinchaboy, P. M., García-Hernández, D. A., García Pérez, A. E., Ge, J., Gé nova-Santos, R., Gillespie, B. A., Girardi, L., González Hernández, J. I., Grebel, E. K., Gunn, J. E., Guo, H., Haggard, D., Hamilton, J.-C., Harris, D. W., Hawley, S. L., Hearty, F. R., Ho, S., Hogg, D. W., Holtzman, J. A., Honscheid, K., Huehnerhoff, J., Ivans, I. I., Ivezić, Ž., Jacobson, H. R., Jiang, L., Johansson, J., Johnson, J. A., Kauffmann, G., Kirkby, D., Kirkpatrick, J. A., Klaene, M. A., Knapp, G. R., Kneib, J.-P., Le Goff, J.-M., Leauthaud, A., Lee, K.-G., Lee, Y. S., Long, D. C., Loomis, C. P., Lucatello, S., Lundgren, B., Lupton, R. H., Ma, B., Ma, Z., MacDonald, N., Mack, C. E., Mahadevan, S., Maia, M. A. G., Majewski, S. R., Makler, M., Malanushenko, E., Malanushenko, V., Manchado, A., Mandelbaum, R., Manera, M., Maraston, C., Margala, D., Martell, S. L., McBride, C. K., McGreer, I. D., McMahon, R. G., Ménard, B., Meszaros,

S., Miralda-Escudé, J., Montero-Dorta, A. D., Montesano, F., Morrison, H. L., Muna, D., Munn, J. A., Murayama, H., Myers, A. D., Neto, A. F., Nguyen, D. C., Nichol, R. C., Nidever, D. L., Noterdaeme, P., Nuza, S. E., Ogando, R. L. C., Olmstead, M. D., Oravetz, D. J., Owen, R., Padmanabhan, N., Palanque-Delabrouille, N., Pan, K., Parejko, J. K., Parihar, P., Pâris, I., Pattarakijwanich, P., Pepper, J., Percival, W. J., Pérez- Fournon, I., Pérez-Ràfols, I., Petitjean, P., Pforr, J., Pieri, M. M., Pinsonneault, M. H., Porto de Mello, G. F., Prada, F., Price-Whelan, A. M., Raddick, M. J., Rebolo, R., Rich, J., Richards, G. T., Robin, A. C., Rocha-Pinto, H. J., Rockosi, C. M., Roe, N. A., Ross, A. J., Ross, N. P., Rossi, G., Rubiño-Martin, J. A., Samushia, L., Sanchez Almeida, J., Sánchez, A. G., Santiago, B., Sayres, C., Schlegel, D. J., Schlesinger, K. J., Schmidt, S. J., Schneider, D. P., Schultheis, M., Schwope, A. D., Scóccola, C. G., Seljak, U., Sheldon, E., Shen, Y., Shu, Y., Simmerer, J., Simmons, A. E., Skibba, R. A., Skrutskie, M. F., Slosar, A., Sobreira, F., Sobeck, J. S., Stassun, K. G., Steele, O., Steinmetz, M., Strauss, M. A., Streblyanska, A., Suzuki, N., Swanson, M. E. C., Tal, T., Thakar, A. R., Thomas, D., Thompson, B. A., Tinker, J. L., Tojeiro, R., Tremonti, C. A., Vargas Magaña, M., Verde, L., Viel, M., Vikas, S. K., Vogt, N. P., Wake, D. A., Wang, J., Weaver, B. A., Weinberg, D. H., Weiner, B. J., West, A. A., White, M., Wilson, J. C., Wisniewski, J. P., Wood-Vasey, W. M., Yanny, B., Yèche, C., York, D. G., Zamora, O., Zasowski, G., Zehavi, I., Zhao, G.-B., Zheng, Z., Zhu, G., and Zinn, J. C. (2012). The Ninth Data Release of the Sloan Digital Sky Survey: First Spectroscopic Data from the SDSS-III Baryon Oscillation Spectroscopic Survey. *The Astrophysical Journal Supplement Series*, 203:21.

Amorisco, N. C. (2015). On feathers, bifurcations and shells: the dynamics of tidal streams across the mass scale. *Monthly Notices of the Royal Astronomical Society*, 450:575–591.

Amorisco, N. C. (2017). Contributions to the accreted stellar halo: an atlas of stellar deposition. *Monthly Notices of the Royal Astronomical Society*, 464:2882–2895.

Anders, F., Chiappini, C., Santiago, B. X., Rocha- Pinto, H. J., Girardi, L., da Costa, L. N., Maia, M. A. G., Steinmetz, M., Minchev, I., Schultheis, M., Boeche, C., Miglio, A., Montalbán, J., Schneider, D. P., Beers, T. C., Cunha, K., Allende Prieto, C., Balbinot, E., Bizyaev, D., Brauer, D. E., Brinkmann, J., Frinchaboy, P. M., García Pérez, A. E., Hayden, M. R., Hearty, F. R., Holtzman, J., Johnson, J. A., Kinemuchi, K., Majewski, S. R., Malanushenko, E., Malanushenko, V., Nidever, D. L., O'Connell, R. W., Pan, K., Robin, A. C., Schiavon, R. P., Shetrone, M., Skrutskie, M. F., Smith, V. V., Stassun, K., and Zasowski, G. (2014). Chemodynamics of the Milky Way. I. The first year of APOGEE data. *Astronomy and Astrophysics*, 564:A115.

Antoja, T., Helmi, A., Dehnen, W., Bienaymé, O., Bland-Hawthorn, J., Famaey, B., Freeman, K., Gibson, B. K., Gilmore, G., Grebel, E. K., Kordopatis, G., Kunder, A., Minchev, I., Munari, U., Navarro, J., Parker, Q., Reid, W. A., Seabroke, G., Siebert, A., Steinmetz, M., Watson, F., Wyse, R. F. G., and Zwitter, T. (2014). Constraints on the Galactic bar from the Hercules stream as traced with RAVE across the Galaxy. *Astronomy and Astrophysics*, 563:A60.

Astraatmadja, T. L. and Bailer-Jones, C. A. L. (2016). Estimating Distances from Parallaxes. III. Distances of Two Million Stars in the Gaia DR1 Catalogue. *The Astrophysical Journal*, 833:119.

Asztalos, S. J., Carosi, G., Hagmann, C., Kinion, D., van Bibber, K., Hotz, M., Rosenberg, L. J., Rybka, G., Hoskins, J., Hwang, J., Sikivie, P., Tanner, D. B., Bradley, R., Clarke, J., and ADMX Collaboration (2010). SQUID-Based Microwave Cavity Search for Dark-Matter Axions. *Physical Review Letters*, 104:041301.

Balbinot, E., Yanny, B., Li, T. S., Santiago, B., Marshall, J. L., Finley, D. A., Pieres, A., Abbott, T. M. C., Abdalla, F. B., Allam, S., Benoit-Lévy, A., Bernstein, G. M., Bertin, E., Brooks, D., Burke, D. L., Carnero Rosell, A., Carrasco Kind, M., Carretero, J., Cunha, C. E., da Costa, L. N., DePoy, D. L., Desai, S., Diehl, H. T., Doel, P., Estrada, J., Flaugher, B., Frieman, J., Gerdes, D. W., Gruen, D., Gruendl, R. A., Honscheid, K., James, D. J., Kuehn, K., Kuropatkin, N., Lahav, O., March, M., Martini, P., Miquel, R., Nichol, R. C., Ogando, R., Romer, A. K., Sanchez, E., Schubnell, M., Sevilla-Noarbe, I., Smith, R. C., Soares-Santos, M., Sobreira, F., Suchyta, E., Tarle, G., Thomas, D., Tucker, D., Walker, A. R., and DES Collaboration (2016). The Phoenix Stream: A Cold Stream in the Southern Hemisphere. *The Astrophysical Journal*, 820:58.

Barbá, R. H., Minniti, D., Geisler, D., Alonso-García, J., Hempel, M., Monachesi, A., Arias, J. I., and Gómez, F. A. (2019). A Sequoia in the Garden: FSR 1758—Dwarf Galaxy or Giant Globular Cluster? *The Astrophysical Journal*, 870(2):L24.

Baumgardt, H., Hilker, M., Sollima, A., and Bellini, A. (2019). Mean proper motions, space orbits, and velocity dispersion profiles of Galactic globular clusters derived from Gaia DR2 data. *Monthly Notices of the Royal Astronomical Society*, 482(4):5138–5155.

Bedin, L. R., Piotto, G., Anderson, J., Cassisi, S., King, I. R., Momany, Y., and Carraro, G. (2004). ω Centauri: The Population Puzzle Goes Deeper. *The Astrophysical Journal*, 605:L125–L128.

Beers, T. C., Carollo, D., Ivezić, Ž., An, D., Chiba, M., Norris, J. E., Freeman, K. C., Lee, Y. S., Munn, J. A., Re Fiorentin, P., Sivarani, T., Wilhelm, R., Yanny, B., and York, D. G. (2012). The Case for the Dual Halo of the Milky Way. *The Astrophysical Journal*, 746:34.

Bekki, K. and Freeman, K. C. (2003). Formation of ω Centauri from an ancient nucleated dwarf galaxy in the young Galactic disc. *Monthly Notices of the Royal Astronomical Society*, 346:L11–L15.

Bekki, K. and Norris, J. E. (2006). The Origin of the Double Main Sequence in ω Centauri: Helium Enrichment due to Gas Fueling from Its Ancient Host Galaxy? *The Astrophysical Journal*, 637:L109–L112.

Bell, E. F., Zucker, D. B., Belokurov, V., Sharma, S., Johnston, K. V., Bullock, J. S., Hogg, D. W., Jahnke, K., de Jong, J. T. A., Beers, T. C., Evans, N. W., Grebel, E. K., Ivezić, Ž., Koposov, S. E., Rix, H.-W., Schneider, D. P., Steinmetz, M., and Zolotov, A. (2008). The Accretion Origin of the Milky Way's Stellar Halo. *The Astrophysical Journal*, 680:295–311.

Bellazzini, M., Ferraro, F. R., and Ibata, R. (2003). Building Up the Globular Cluster System of the Milky Way: The Contribution of the Sagittarius Galaxy. *The Astronomical Journal*, 125(1):188–196.

Belokurov, V., Erkal, D., Evans, N. W., Koposov, S. E., and Deason, A. J. (2018). Co-formation of the disc and the stellar halo. *Monthly Notices of the Royal Astronomical Society*, 478:611–619.

Belokurov, V., Evans, N., Irwin, M., Lynden-Bell, D., Yanny, B., Vidrih, S., Gilmore, G., Seabroke, G., Zucker, D., Wilkinson, M., Hewett, P., Bramich, D., Fellhauer, M., Newberg, H., Wyse, R., Beers, T., Bell, E., Barentine, J., Brinkmann, J., Cole, N., Pan, K., and York, D. (2007a). An orphan in the "field of streams". *The Astrophysical Journal*, 658:337–344.

Belokurov, V., Evans, N. W., Bell, E. F., Irwin, M. J., Hewett, P. C., Koposov, S., Rockosi, C. M., Gilmore, G., Zucker, D. B., Fellhauer, M., Wilkinson, M. I., Bramich, D. M., Vidrih, S., Rix, H. W., Beers, T. C., Schneider, D. P., Barentine, J. C., Brewington, H., Brinkmann, J., Harvanek, M., Krzesinski, J., Long, D., Pan, K., Snedden, S. A., Malanushenko, O., and Malanushenko, V. (2007b). The Hercules-Aquila Cloud. *The Astrophysical Journal*, 657:L89–L92.

Belokurov, V., Evans, N. W., Irwin, M. J., Hewett, P. C., and Wilkinson, M. I. (2006a). The Discovery of Tidal Tails around the Globular Cluster NGC 5466. *The Astrophysical Journal*, 637:L29–L32.

Belokurov, V., Koposov, S. E., Evans, N. W., Peñarrubia, J., Irwin, M. J., Smith, M. C., Lewis, G. F., Gieles, M., Wilkinson, M. I., Gilmore, G., Olszewski, E. W., and Niederste-Ostholt, M. (2014). Precession of the Sagittarius stream. *Monthly Notices of the Royal Astronomical Society*, 437:116–131.

Belokurov, V., Zucker, D. B., Evans, N. W., Gilmore, G., Vidrih, S., Bramich, D. M., Newberg, H. J., Wyse, R. F. G., Irwin, M. J., Fellhauer, M., Hewett, P. C., Walton, N. A., Wilkinson, M. I., Cole, N., Yanny, B., Rockosi, C. M., Beers, T. C., Bell, E. F., Brinkmann, J., Ivezić, Ž., and Lupton, R. (2006b). The Field of Streams: Sagittarius and Its Siblings. *The Astrophysical Journal*, 642:L137–L140.

Bensby, T., Oey, M. S., Feltzing, S., and Gustafsson, B. (2007). Disentangling the Hercules Stream. *The Astrophysical Journal*, 655:L89–L92.

Bertin, E. (2011). Automated Morphometry with SExtractor and PSFEx. In Evans, I. N., Accomazzi, A., Mink, D. J., and Rots, A. H., editors, *Astronomical Data Analysis Software and Systems XX*, volume 442, page 435.

Bertin, E. and Arnouts, S. (1996). SExtractor: Software for source extraction. *Astronomy and Astrophysics Supplement Series*, 117:393–404.

Billard, J., Mayet, F., Macías-Pérez, J. F., and Santos, D. (2010). Directional detection as a strategy to discover Galactic Dark Matter. *Physics Letters B*, 691:156–162.

Binney, J. (1987). The Galaxy in Action Space. In Gilmore, G. and Carswell, B., editors, *NATO Advanced Science Institutes (ASI) Series C*, volume 207, page 399.

Binney, J. (2010). Distribution functions for the Milky Way. *Monthly Notices of the Royal Astronomical Society*, 401:2318–2330.

Binney, J. (2012). Actions for axisymmetric potentials. *Monthly Notices of the Royal Astronomical Society*, 426:1324–1327.

Binney, J., Burnett, B., Kordopatis, G., McMillan, P. J., Sharma, S., Zwitter, T., Bienaymé, O., Bland-Hawthorn, J., Steinmetz, M., Gilmore, G., Williams, M. E. K., Navarro, J., Grebel, E. K., Helmi, A., Parker, Q., Reid, W. A., Seabroke, G., Watson, F., and Wyse, R. F. G. (2014). New distances to RAVE stars. *Monthly Notices of the Royal Astronomical Society*, 437:351–370.

Binney, J. and Spergel, D. (1982). Spectral stellar dynamics. *The Astrophysical Journal*, 252:308–321.

Binney, J. and Tremaine, S. (2008). *Galactic Dynamics: Second Edition*. Princeton University Press.

Blumenthal, G. R., Faber, S. M., Primack, J. R., and Rees, M. J. (1984). Formation of galaxies and large-scale structure with cold dark matter. *Nature*, 311:517–525.

Bovy, J. (2015). galpy: A python Library for Galactic Dynamics. *The Astrophysical Journal Supplement Series*, 216:29.

Bressan, A., Marigo, P., Girardi, L., Salasnich, B., Dal Cero, C., Rubele, S., and Nanni, A. (2012). PARSEC: stellar tracks and isochrones with the PAdova and TRieste Stellar Evolution Code. *Monthly Notices of the Royal Astronomical Society*, 427:127–145.

Brook, C. B., Kawata, D., Gibson, B. K., and Flynn, C. (2003). Galactic Halo Stars in Phase Space: A Hint of Satellite Accretion? *The Astrophysical Journal*, 585:L125–L129.

Brown, A. G. A., Vallenari, A., Prusti, T., de Bruijne, J. H. J., Mignard, F., Drimmel, R., Babusiaux, C., Bailer-Jones, C. A. L., Bastian, U., Biermann, M., Evans, D. W., Eyer, L., Jansen, F., Jordi, C., Katz, D., Klioner, S. A., Lammers, U., Lindegren, L., Luri, X., O'Mullane, W., Panem, C., Pourbaix, D., Randich, S., Sartoretti, P., Siddiqui, H. I., Soubiran, C., Valette, V., van Leeuwen, F., Walton, N. A., Aerts, C., Arenou, F., Cropper, M., Høg, E., Lattanzi, M. G., Grebel, E. K., Holland, A. D., Huc, C., Passot, X., Perryman, M., Bramante, L., Cacciari, C., Castañeda, J., Chaoul, L., Cheek, N., De Angeli, F., Fabricius, C., Guerra, R., Hernández, J., Jean-Antoine-Piccolo, A., Masana, E., Messineo, R., Mowlavi, N., Nienartowicz, K., Ordóñez- Blanco, D., Panuzzo, P., Portell, J., Richards, P. J., Riello, M., Seabroke, G. M., Tanga, P., Thévenin, F., Torra, J., Els, S. G., Gracia-Abril, G., Comoretto, G., Garcia-Reinaldos, M., Lock, T., Mercier, E., Altmann, M., Andrae, R., Astraatmadja, T. L., Bellas-Velidis, I., Benson, K., Berthier, J., Blomme, R., Busso, G., Carry, B., Cellino, A., Clementini, G., Cowell, S., Creevey, O., Cuypers, J., Davidson, M., De Ridder, J., de Torres, A., Delchambre, L., Dell'Oro, A., Ducourant, C., Frémat, Y., García-Torres, M., Gosset, E., Halbwachs, J. L., Hambly, N. C., Harrison, D. L., Hauser, M., Hestroffer, D., Hodgkin, S. T., Huckle, H. E., Hutton, A., Jasniewicz, G., Jordan, S., Kontizas, M., Korn, A. J., Lanzafame, A. C., Manteiga, M., Moitinho, A., Muinonen, K., Osinde, J., Pancino, E., Pauwels, T., Petit, J. M., Recio-Blanco, A., Robin, A. C., Sarro, L. M., Siopis, C., Smith, M., Smith, K. W., Sozzetti, A., Thuillot, W., van Reeven, W., Viala, Y., Abbas, U., Abreu Aramburu, A., Accart, S., Aguado, J. J., Allan, P. M., Allasia, W., Altavilla, G., Álvarez, M. A., Alves, J., Anderson, R. I., Andrei, A. H., Anglada Varela, E., Antiche, E., Antoja, T., Antón, S., Arcay, B., Bach, N., Baker, S. G., Balaguer-Núñez, L., Barache, C., Barata, C., Barbier, A., Barblan, F., Barrado y Navascués, D., Barros, M., Barstow, M. A., Becciani, U., Bellazzini, M., Bello García, A., Belokurov, V., Bendjoya, P., Berihuete, A., Bianchi, L., Bienaymé, O.,

Billebaud, F., Blagorodnova, N., Blanco-Cuaresma, S., Boch, T., Bombrun, A., Borrachero, R., Bouquillon, S., Bourda, G., Bouy, H., Bragaglia, A., Breddels, M. A., Brouillet, N., Brüsemeister, T., Bucciarelli, B., Burgess, P., Burgon, R., Burlacu, A., Busonero, D., Buzzi, R., Caffau, E., Cambras, J., Campbell, H., Cancelliere, R., Cantat-Gaudin, T., Carlucci, T., Carrasco, J. M., Castellani, M., Charlot, P., Charnas, J., Chiavassa, A., Clotet, M., Cocozza, G., Collins, R. S., Costigan, G., Crifo, F., Cross, N. J. G., Crosta, M., Crowley, C., Dafonte, C., Damerdji, Y., Dapergolas, A., David, P., David, M., De Cat, P., de Felice, F., de Laverny, P., De Luise, F., De March, R., de Martino, D., de Souza, R., Debosscher, J., del Pozo, E., Delbo, M., Delgado, A., Delgado, H. E., Di Matteo, P., Diakite, S., Distefano, E., Dolding, C., Dos Anjos, S., Drazinos, P., Duran, J., Dzigan, Y., Edvardsson, B., Enke, H., Evans, N. W., Eynard Bontemps, G., Fabre, C., Fabrizio, M., Faigler, S., Falcão, A. J., Farràs Casas, M., Federici, L., Fedorets, G., Fernández-Hernández, J., Fernique, P., Fienga, A., Figueras, F., Filippi, F., Findeisen, K., Fonti, A., Fouesneau, M., Fraile, E., Fraser, M., Fuchs, J., Gai, M., Galleti, S., Galluccio, L., Garabato, D., García-Sedano, F., Garofalo, A., Garralda, N., Gavras, P., Gerssen, J., Geyer, R., Gilmore, G., Girona, S., Giuffrida, G., Gomes, M., González-Marcos, A., González-Núñez, J., González-Vidal, J. J., Granvik, M., Guerrier, A., Guillout, P., Guiraud, J., Gúrpide, A., Gutiérrez-Sánchez, R., Guy, L. P., Haigron, R., Hatzidimitriou, D., Haywood, M., Heiter, U., Helmi, A., Hobbs, D., Hofmann, W., Holl, B., Holland, G., Hunt, J. A. S., Hypki, A., Icardi, V., Irwin, M., Jevardat de Fombelle, G., Jofré, P., Jonker, P. G., Jorissen, A., Julbe, F., Karampelas, A., Kochoska, A., Kohley, R., Kolenberg, K., Kontizas, E., Koposov, S. E., Kordopatis, G., Koubsky, P., Krone-Martins, A., Kudryashova, M., Kull, I., Bachchan, R. K., Lacoste-Seris, F., Lanza, A. F., Lavigne, J. B., Le Poncin-Lafitte, C., Lebreton, Y., Lebzelter, T., Leccia, S., Leclerc, N., Lecoeur-Taibi, I., Lemaitre, V., Lenhardt, H., Leroux, F., Liao, S., Licata, E., Lindstrøm, H. E. P., Lister, T. A., Livanou, E., Lobel, A., Löffler, W., López, M., Lorenz, D., MacDonald, I., Magalhães Fernandes, T., Managau, S., Mann, R. G., Mantelet, G., Marchal, O., Marchant, J. M., Marconi, M., Marinoni, S., Marrese, P. M., Marschalkó, G., Marshall, D. J., Martín-Fleitas, J. M., Martino, M., Mary, N., Matijevič, G., Mazeh, T., McMillan, P. J., Messina, S., Michalik, D., Millar, N. R., Miranda, B. M. H., Molina, D., Molinaro, R., Molinaro, M., Molnár, L., Moniez, M., Montegriffo, P., Mor, R., Mora, A., Morbidelli, R., Morel, T., Morgenthaler, S., Morris, D., Mulone, A. F., Muraveva, T., Musella, I., Narbonne, J., Nelemans, G., Nicastro, L., Noval, L., Ordénovic, C., Ordieres-Meré, J., Osborne, P., Pagani, C., Pagano, I., Pailler, F., Palacin, H., Palaversa, L., Parsons, P., Pecoraro, M., Pedrosa, R., Pentikäinen, H., Pichon, B., Piersimoni, A. M., Pineau, F. X., Plachy, E., Plum, G., Poujoulet, E., Prša, A., Pulone, L., Ragaini, S., Rago, S., Rambaux, N., Ramos- Lerate, M., Ranalli, P., Rauw, G., Read, A., Regibo, S., Reylé, C., Ribeiro, R. A., Rimoldini, L., Ripepi, V., Riva, A., Rixon, G., Roelens, M., Romero-Gómez, M., Rowell, N., Royer, F., Ruiz-Dern, L., Sadowski, G., Sagristà Sellés, T., Sahlmann, J., Salgado, J., Salguero, E., Sarasso, M., Savietto, H., Schultheis, M., Sciacca, E., Segol, M., Segovia, J. C., Segransan, D., Shih, I. C., Smareglia, R., Smart, R. L., Solano, E., Solitro, F., Sordo, R., Soria Nieto, S., Souchay, J., Spagna, A., Spoto, F., Stampa, U., Steele, I. A., Steidelmüller, H., Stephenson, C. A., Stoev, H., Suess, F. F., Süveges, M., Surdej, J., Szabados, L., Szegedi-Elek, E., Tapiador, D., Taris, F., Tauran, G., Taylor, M. B., Teixeira, R., Terrett, D., Tingley, B., Trager, S. C., Turon, C., Ulla, A., Utrilla, E., Valentini, G., van Elteren, A., Van Hemelryck, E., van Leeuwen, M., Varadi, M., Vecchiato, A., Veljanoski, J., Via, T., Vicente, D., Vogt, S., Voss, H., Votruba, V., Voutsinas, S., Walmsley, G., Weiler, M., Weingrill, K., Wevers, T., Wyrzykowski, Ł., Yoldas, A., Žerjal, M., Zucker, S., Zurbach, C., Zwitter, T., Alecu, A., Allen, M., Allende Prieto, C., Amorim,

A., Anglada-Escudé, G., Arsenijevic, V., Azaz, S., Balm, P., Beck, M., Bernstein, H. H., Bigot, L., Bijaoui, A., Blasco, C., Bonfigli, M., Bono, G., Boudreault, S., Bressan, A., Brown, S., Brunet, P. M., Bunclark, P., Buonanno, R., Butkevich, A. G., Carret, C., Carrion, C., Chemin, L., Chéreau, F., Corcione, L., Darmigny, E., de Boer, K. S., de Teodoro, P., de Zeeuw, P. T., Delle Luche, C., Domingues, C. D., Dubath, P., Fodor, F., Frézouls, B., Fries, A., Fustes, D., Fyfe, D., Gallardo, E., Gallegos, J., Gardiol, D., Gebran, M., Gomboc, A., Gómez, A., Grux, E., Gueguen, A., Heyrovsky, A., Hoar, J., Iannicola, G., Isasi Parache, Y., Janotto, A. M., Joliet, E., Jonckheere, A., Keil, R., Kim, D. W., Klagyivik, P., Klar, J., Knude, J., Kochukhov, O., Kolka, I., Kos, J., Kutka, A., Lainey, V., LeBouquin, D., Liu, C., Loreggia, D., Makarov, V. V., Marseille, M. G., Martayan, C., Martinez-Rubi, O., Massart, B., Meynadier, F., Mignot, S., Munari, U., Nguyen, A. T., Nordlander, T., Ocvirk, P., O'Flaherty, K. S., Olias Sanz, A., Ortiz, P., Osorio, J., Oszkiewicz, D., Ouzounis, A., Palmer, M., Park, P., Pasquato, E., Peltzer, C., Peralta, J., Péturaud, F., Pieniluoma, T., Pigozzi, E., Poels, J., Prat, G., Prod'homme, T., Raison, F., Rebordao, J. M., Risquez, D., Rocca-Volmerange, B., Rosen, S., Ruiz-Fuertes, M. I., Russo, F., Sembay, S., Serraller Vizcaino, I., Short, A., Siebert, A., Silva, H., Sinachopoulos, D., Slezak, E., Soffel, M., Sosnowska, D., Straižys, V., ter Linden, M., Terrell, D., Theil, S., Tiede, C., Troisi, L., Tsalmantza, P., Tur, D., Vaccari, M., Vachier, F., Valles, P., Van Hamme, W., Veltz, L., Virtanen, J., Wallut, J. M., Wichmann, R., Wilkinson, M. I., Ziaeepour, H., and Zschocke, S. (2016). Gaia Data Release 1. Summary of the astrometric, photometric, and survey properties. *Astronomy and Astrophysics*, 595:A2.

Buder, S., Asplund, M., Duong, L., Kos, J., Lind, K., Ness, M. K., Sharma, S., Bland-Hawthorn, J., Casey, A. R., De Silva, G. M., D'Orazi, V., Freeman, K. C., Lewis, G. F., Lin, J., Martell, S. L., Schlesinger, K. J., Simpson, J. D., Zucker, D. B., Zwitter, T., Amarsi, A. M., Anguiano, B., Carollo, D., Casagrande, L., Čotar, K., Cottrell, P. L., Da Costa, G., Gao, X. D., Hayden, M. R., Horner, J., Ireland, M. J., Kafle, P. R., Munari, U., Nataf, D. M., Nordlander, T., Stello, D., Ting, Y.-S., Traven, G., Watson, F., Wittenmyer, R. A., Wyse, R. F. G., Yong, D., Zinn, J. C., and Žerjal, M. (2018). The GALAH Survey: second data release. *Monthly Notices of the Royal Astronomical Society*, 478:4513–4552.

Buonanno, R., Corsi, C. E., Castellani, M., Marconi, G., Fusi Pecci, F., and Zinn, R. (1999). Hubble Space Telescope Photometry of the Fornax Dwarf Spheroidal Galaxy: Cluster 4 and Its Field. *The Astronomical Journal*, 118:1671–1683.

Burnett, B. and Binney, J. (2010). Stellar distances from spectroscopic observations: a new technique. *Monthly Notices of the Royal Astronomical Society*, 407:339–354.

Cantat-Gaudin, T., Jordi, C., Vallenari, A., Bragaglia, A., Balaguer-Núñez, L., Soubiran, C., Bossini, D., Moitinho, A., Castro-Ginard, A., and Krone-Martins, A. (2018). A Gaia DR2 view of the open cluster population in the Milky Way. *Astronomy and Astrophysics*, 618:A93.

Capuzzo Dolcetta, R., Di Matteo, P., and Miocchi, P. (2005). Formation and Evolution of Clumpy Tidal Tails around Globular Clusters. *The Astronomical Journal*, 129:1906–1921.

Carballo-Bello, J. A., Gieles, M., Sollima, A., Koposov, S., Martínez-Delgado, D., and Peñarrubia, J. (2012). Outer density profiles of 19 Galactic globular clusters from deep and wide-field imaging. *Monthly Notices of the Royal Astronomical Society*, 419:14–28.

Carballo-Bello, J. A., Muñoz, R. R., Carlin, J. L., Côté, P., Geha, M., Simon, J. D., and Djorgovski, S. G. (2015). A Megacam Survey of Outer Halo Satellites. IV. Two Foreground Populations Possibly Associated with the Monoceros Substructure in the Direction of NGC 2419 and Koposov 2. *The Astrophysical Journal*, 805:51.

Carlberg, R. G., Grillmair, C. J., and Hetherington, N. (2012). The Pal 5 Star Stream Gaps. *The Astrophysical Journal*, 760:75.

Carollo, D., Beers, T. C., Chiba, M., Norris, J. E., Freeman, K. C., Lee, Y. S., Ivezić, Ž., Rockosi, C. M., and Yanny, B. (2010). Structure and Kinematics of the Stellar Halos and Thick Disks of the Milky Way Based on Calibration Stars from Sloan Digital Sky Survey DR7. *The Astrophysical Journal*, 712:692–727.

Carollo, D., Beers, T. C., Lee, Y. S., Chiba, M., Norris, J. E., Wilhelm, R., Sivarani, T., Marsteller, B., Munn, J. A., Bailer-Jones, C. A. L., Fiorentin, P. R., and York, D. G. (2007). Two stellar components in the halo of the Milky Way. *Nature*, 450:1020–1025.

Casey, A. R., Hawkins, K., Hogg, D. W., Ness, M., Rix, H.-W., Kordopatis, G., Kunder, A., Steinmetz, M., Koposov, S., Enke, H., Sanders, J., Gilmore, G., Zwitter, T., Freeman, K. C., Casagrande, L., Matijevič, G., Seabroke, G., Bienaymé, O., Bland-Hawthorn, J., Gibson, B. K., Grebel, E. K., Helmi, A., Munari, U., Navarro, J. F., Reid, W., Siebert, A., and Wyse, R. (2017). The RAVE-on Catalog of Stellar Atmospheric Parameters and Chemical Abundances for Chemo-dynamic Studies in the Gaia Era. *The Astrophysical Journal*, 840:59.

Casey, A. R., Keller, S. C., Alves-Brito, A., Frebel, A., Da Costa, G., Karakas, A., Yong, D., Schlaufman, K. C., Jacobson, H. R., Yu, Q., and Fishlock, C. (2014). The Aquarius comoving group is not a disrupted classical globular cluster. *Monthly Notices of the Royal Astronomical Society*, 443:828–851.

Chambers, K. C., Magnier, E. A., Metcalfe, N., Flewelling, H. A., Huber, M. E., Waters, C. Z., Denneau, L., Draper, P. W., Farrow, D., Finkbeiner, D. P., Holmberg, C., Koppenhoefer, J., Price, P. A., Saglia, R. P., Schlafly, E. F., Smartt, S. J., Sweeney, W., Wainscoat, R. J., Burgett, W. S., Grav, T., Heasley, J. N., Hodapp, K. W., Jedicke, R., Kaiser, N., Kudritzki, R. P., Luppino, G. A., Lupton, R. H., Monet, D. G., Morgan, J. S., Onaka, P. M., Stubbs, C. W., Tonry, J. L., Banados, E., Bell, E. F., Bender, R., Bernard, E. J., Botticella, M. T., Casertano, S., Chastel, S., Chen, W. P., Chen, X., Cole, S., Deacon, N., Frenk, C., Fitzsimmons, A., Gezari, S., Goessl, C., Goggia, T., Goldman, B., Grebel, E. K., Hambly, N. C., Hasinger, G., Heavens, A. F., Heckman, T. M., Henderson, R., Henning, T., Holman, M., Hopp, U., Ip, W. H., Isani, S., Keyes, C. D., Koekemoer, A., Kotak, R., Long, K. S., Lucey, J. R., Liu, M., Martin, N. F., McLean, B., Morganson, E., Murphy, D. N. A., Nieto-Santisteban, M. A., Norberg, P., Peacock, J. A., Pier, E. A., Postman, M., Primak, N., Rae, C., Rest, A., Riess, A., Riffeser, A., Rix, H. W., Roser, S., Schilbach, E., Schultz, A. S. B., Scolnic, D., Szalay, A., Seitz, S., Shiao, B., Small, E., Smith, K. W., Soderblom, D., Taylor, A. N., Thakar, A. R., Thiel, J., Thilker, D., Urata, Y., Valenti, J., Walter, F., Watters, S. P., Werner, S., White, R., Wood- Vasey, W. M., and Wyse, R. (2016). The Pan-STARRS1 Surveys. *ArXiv e-prints*, page arXiv:1612.05560.

Chandrasekhar, S. (1943). Dynamical Friction. I. General Considerations: the Coefficient of Dynamical Friction. *The Astrophysical Journal*, 97:255.

Chiba, M. and Beers, T. C. (2000). Kinematics of Metal-poor Stars in the Galaxy. III. Formation of the Stellar Halo and Thick Disk as Revealed from a Large Sample of Nonkinematically Selected Stars. *The Astronomical Journal*, 119:2843–2865.

Choi, J., Dotter, A., Conroy, C., Cantiello, M., Paxton, B., and Johnson, B. D. (2016). Mesa Isochrones and Stellar Tracks (MIST). I. Solar-scaled Models. *The Astrophysical Journal*, 823:102.

Choi, J.-H., Weinberg, M. D., and Katz, N. (2007). The dynamics of tidal tails from massive satellites. *Monthly Notices of the Royal Astronomical Society*, 381:987–1000.

Combes, F., Leon, S., and Meylan, G. (1999). N-body simulations of globular cluster tides. *Astronomy and Astrophysics*, 352:149–162.

Da Costa, G. and Armandroff, T. (1995). Abundances and kinematics of the globular cluster systems of the galaxy and of the sagittarius dwarf. *The Astronomical Journal*, 109:2533–2552.

D'Antona, F., D'Ercole, A., Marino, A. F., Milone, A. P., Ventura, P., and Vesperini, E. (2011). The Oxygen versus Sodium (Anti)Correlation(S) in ω Cen. *The Astrophysical Journal*, 736:5.

de Boer, T. J. L., Belokurov, V., and Koposov, S. E. (2018). The fall of the Northern Unicorn: tangential motions in the Galactic anticentre with SDSS and Gaia. *Monthly Notices of the Royal Astronomical Society*, 473:647–662.

Deason, A. J., Belokurov, V., and Evans, N. W. (2011a). Rotation of halo populations in the Milky Way and M31. *Monthly Notices of the Royal Astronomical Society*, 411:1480–1494.

Deason, A. J., Belokurov, V., and Evans, N. W. (2011b). The Milky Way stellar halo out to 40 kpc: squashed, broken but smooth. *Monthly Notices of the Royal Astronomical Society*, 416:2903–2915.

Deason, A. J., Belokurov, V., Evans, N. W., and Johnston, K. V. (2013). Broken and Unbroken: The Milky Way and M31 Stellar Halos. *The Astrophysical Journal*, 763:113.

Deason, A. J., Belokurov, V., Koposov, S. E., Gómez, F. A., Grand, R. J., Marinacci, F., and Pakmor, R. (2017). The slight spin of the old stellar halo. *Monthly Notices of the Royal Astronomical Society*, 470:1259–1273.

Deason, A. J., Belokurov, V., Koposov, S. E., and Lancaster, L. (2018). Apocenter Pile-up: Origin of the Stellar Halo Density Break. *The Astrophysical Journal*, 862(1):L1.

Dehnen, W. (2000). The Effect of the Outer Lindblad Resonance of the Galactic Bar on the Local Stellar Velocity Distribution. *The Astronomical Journal*, 119:800–812.

Dehnen, W., Odenkirchen, M., Grebel, E. K., and Rix, H.-W. (2004). Modeling the Disruption of the Globular Cluster Palomar 5 by Galactic Tides. *The Astronomical Journal*, 127:2753–2770.

Dinescu, D., Majewski, S., Girard, T., and Cudworth, K. (2000). The absolute proper motion of palomar 12: A case for tidal capture from the sagittarius dwarf spheroidal galaxy. *The Astronomical Journal*, 120:1892–1905.

Dinescu, D. I. (2002). A Solar Neighborhood Search for Tidal Debris from ω Centauri's Hypothetical Parent Galaxy. In van Leeuwen, F., Hughes, J. D., and Piotto, G., editors, *Omega Centauri, A Unique Window into Astrophysics*, volume 265, page 365.

D'Onghia, E. and Lake, G. (2009). The Magellanic Group and the Seven Dwarfs. In Van Loon, J. T. and Oliveira, J. M., editors, *The Magellanic System: Stars, Gas, and Galaxies*, volume 256 of *IAU Symposium*, pages 473–478.

D'Onghia, E., Springel, V., Hernquist, L., and Keres, D. (2010). Substructure Depletion in the Milky Way Halo by the Disk. *The Astrophysical Journal*, 709:1138–1147.

D'Orazi, V., Gratton, R. G., Pancino, E., Bragaglia, A., Carretta, E., Lucatello, S., and Sneden, C. (2011). Chemical enrichment mechanisms in ω Centauri: clues from neutron-capture elements. *Astronomy and Astrophysics*, 534:A29.

Du, N., Force, N., Khatiwada, R., Lentz, E., Ottens, R., Rosenberg, L. J., Rybka, G., Carosi, G., Woollett, N., Bowring, D., Chou, A. S., Sonnenschein, A., Wester, W., Boutan, C., Oblath, N. S., Bradley, R., Daw, E. J., Dixit, A. V., Clarke, J., O'Kelley, S. R., Crisosto, N., Gleason, J. R., Jois, S., Sikivie, P., Stern, I., Sullivan, N. S., Tanner, D. B., and Hilton, G. C. (2018). Search for Invisible Axion Dark Matter with the Axion Dark Matter Experiment. *Physical Review Letters*, 120:151301.

Eggen, O. J., Lynden-Bell, D., and Sandage, A. R. (1962). Evidence from the motions of old stars that the Galaxy collapsed. *The Astrophysical Journal*, 136:748.

Erkal, D., Koposov, S., and Belokurov, V. (2017). A sharper view of pal 5's tails: discovery of stream perturbations with a novel non-parametric technique. *Monthly Notices of the Royal Astronomical Society*, 470:60–84.

ESA (2014). Gaia mission science objective.

Eyre, A. and Binney, J. (2011). The mechanics of tidal streams. *Monthly Notices of the Royal Astronomical Society*, 413:1852–1874.

Fattahi, A., Belokurov, V., Deason, A. J., Frenk, C. S., Gómez, F. A., Grand , R. J. J., Marinacci, F., Pakmor, R., and Springel, V. (2019). The origin of galactic metal-rich stellar halo components with highly eccentric orbits. *Monthly Notices of the Royal Astronomical Society*, 484(4):4471–4483.

Fermani, F. and Schönrich, R. (2013). Rotational signature of the milky way stellar halo. *Monthly Notices of the Royal Astronomical Society*, 432:2402–2419.

Fernández-Trincado, J. G., Robin, A. C., Vieira, K., Moreno, E., Bienaymé, O., Reylé, C., Valenzuela, O., Pichardo, B., Robles-Valdez, F., and Martins, A. M. M. (2015). RAVE stars tidally stripped or ejected from the ω Centauri globular cluster. *Astronomy and Astrophysics*, 583:A76.

Flaugher, B., Diehl, H. T., Honscheid, K., Abbott, T. M. C., Alvarez, O., Angstadt, R., Annis, J. T., Antonik, M., Ballester, O., Beaufore, L., Bernstein, G. M., Bernstein, R. A., Bigelow, B., Bonati, M., Boprie, D., Brooks, D., Buckley- Geer, E. J., Campa, J., Cardiel-Sas, L., Castander, F. J., Castilla, J., Cease, H., Cela- Ruiz, J. M., Chappa, S., Chi, E., Cooper, C.,

da Costa, L. N., Dede, E., Derylo, G., DePoy, D. L., de Vicente, J., Doel, P., Drlica-Wagner, A., Eiting, J., Elliott, A. E., Emes, J., Estrada, J., Fausti Neto, A., Finley, D. A., Flores, R., Frieman, J., Gerdes, D., Gladders, M. D., Gregory, B., Gutierrez, G. R., Hao, J., Holland, S. E., Holm, S., Huffman, D., Jackson, C., James, D. J., Jonas, M., Karcher, A., Karliner, I., Kent, S., Kessler, R., Kozlovsky, M., Kron, R. G., Kubik, D., Kuehn, K., Kuhlmann, S., Kuk, K., Lahav, O., Lathrop, A., Lee, J., Levi, M. E., Lewis, P., Li, T. S., Mandrichenko, I., Marshall, J. L., Martinez, G., Merritt, K. W., Miquel, R., Muñoz, F., Neilsen, E. H., Nichol, R. C., Nord, B., Ogando, R., Olsen, J., Palaio, N., Patton, K., Peoples, J., Plazas, A. A., Rauch, J., Reil, K., Rheault, J. P., Roe, N. A., Rogers, H., Roodman, A., Sanchez, E., Scarpine, V., Schindler, R. H., Schmidt, R., Schmitt, R., Schubnell, M., Schultz, K., Schurter, P., Scott, L., Serrano, S., Shaw, T. M., Smith, R. C., Soares-Santos, M., Stefanik, A., Stuermer, W., Suchyta, E., Sypniewski, A., Tarle, G., Thaler, J., Tighe, R., Tran, C., Tucker, D., Walker, A. R., Wang, G., Watson, M., Weaverdyck, C., Wester, W., Woods, R., Yanny, B., and DES Collaboration (2015). The Dark Energy Camera. *The Astronomical Journal*, 150:150.

Font, A., Johnston, K., Bullock, J., and Robertson, B. (2006). Chemical abundance distributions of galactic halos and their satellite systems in a lambda-cdm universe. *The Astrophysical Journal*, 638:585–595.

Font, A., McCarthy, I., Crain, R., Theuns, T., Schaye, J., Wiersma, R., and Dalla Vecchia, C. (2011). Cosmological simulations of the formation of the stellar haloes around disc galaxies. *Monthly Notices of the Royal Astronomical Society*, 416:2802–2820.

Forbes, D. A. and Bridges, T. (2010). Accreted versus in situ Milky Way globular clusters. *Monthly Notices of the Royal Astronomical Society*, 404:1203–1214.

Foreman-Mackey, D., Hogg, D. W., Lang, D., and Goodman, J. (2013). emcee: The MCMC Hammer. *The Publications of the Astronomical Society of the Pacific*, 125:306.

Foster, J. W., Rodd, N. L., and Safdi, B. R. (2018). Revealing the dark matter halo with axion direct detection. *Physical Review D*, 97:123006.

Freeman, K. and Bland-Hawthorn, J. (2002). The new galaxy: Signatures of its formation. *Annual Review of Astronomy and Astrophysics*, 40:487–537.

Freeman, K. C. (1993). Globular Clusters and Nucleated Dwarf Ellipticals. In Smith, G. H. and Brodie, J. P., editors, *The Globular Cluster-Galaxy Connection*, volume 48, page 608.

Froebrich, D., Scholz, A., and Raftery, C. L. (2007). A systematic survey for infrared star clusters with |b| <20° using 2MASS. *Monthly Notices of the Royal Astronomical Society*, 374:399–408.

Fujii, M., Funato, Y., and Makino, J. (2006). Dynamical Friction on Satellite Galaxies. *Publications of the Astronomical Society of Japan*, 58:743–752.

Gaia Collaboration, Babusiaux, C., van Leeuwen, F., Barstow, M. A., Jordi, C., Vallenari, A., Bossini, D., Bressan, A., Cantat-Gaudin, T., and van Leeuwen, M. (2018a). Gaia Data Release 2. Observational Hertzsprung-Russell diagrams. *Astronomy and Astrophysics*, 616:A10.

Gaia Collaboration, Brown, A. G. A., Vallenari, A., Prusti, T., de Bruijne, J. H. J., Babusiaux, C., Bailer-Jones, C. A. L., Biermann, M., Evans, D. W., Eyer, L., Jansen, F., Jordi, C., Klioner, S. A., Lammers, U., Lindegren, L., Luri, X., Mignard, F., Panem, C., Pourbaix, D., Randich, S., Sartoretti, P., Siddiqui, H. I., Soubiran, C., van Leeuwen, F., Walton, N. A., Arenou, F., Bastian, U., Cropper, M., Drimmel, R., Katz, D., Lattanzi, M. G., Bakker, J., Cacciari, C., Castañeda, J., Chaoul, L., Cheek, N., De Angeli, F., Fabricius, C., Guerra, R., Holl, B., Masana, E., Messineo, R., Mowlavi, N., Nienartowicz, K., Panuzzo, P., Portell, J., Riello, M., Seabroke, G. M., Tanga, P., Thévenin, F., Gracia-Abril, G., Comoretto, G., Garcia-Reinaldos, M., Teyssier, D., Altmann, M., Andrae, R., Audard, M., Bellas-Velidis, I., Benson, K., Berthier, J., Blomme, R., Burgess, P., Busso, G., Carry, B., Cellino, A., Clementini, G., Clotet, M., Creevey, O., Davidson, M., De Ridder, J., Delchambre, L., Dell'Oro, A., Ducourant, C., Fernández-Hernández, J., Fouesneau, M., Frémat, Y., Galluccio, L., García-Torres, M., González-Núñez, J., González- Vidal, J. J., Gosset, E., Guy, L. P., Halbwachs, J. L., Hambly, N. C., Harrison, D. L., Hernández, J., Hestroffer, D., Hodgkin, S. T., Hutton, A., Jasniewicz, G., Jean-Antoine- Piccolo, A., Jordan, S., Korn, A. J., Krone- Martins, A., Lanzafame, A. C., Lebzelter, T., Löffler, W., Manteiga, M., Marrese, P. M., Martín-Fleitas, J. M., Moitinho, A., Mora, A., Muinonen, K., Osinde, J., Pancino, E., Pauwels, T., Petit, J. M., Recio-Blanco, A., Richards, P. J., Rimoldini, L., Robin, A. C., Sarro, L. M., Siopis, C., Smith, M., Sozzetti, A., Süveges, M., Torra, J., van Reeven, W., Abbas, U., Abreu Aramburu, A., Accart, S., Aerts, C., Altavilla, G., Álvarez, M. A., Alvarez, R., Alves, J., Anderson, R. I., Andrei, A. H., Anglada Varela, E., Antiche, E., Antoja, T., Arcay, B., Astraatmadja, T. L., Bach, N., Baker, S. G., Balaguer-Núñez, L., Balm, P., Barache, C., Barata, C., Barbato, D., Barblan, F., Barklem, P. S., Barrado, D., Barros, M., Barstow, M. A., Bartholomé Muñoz, S., Bassilana, J. L., Becciani, U., Bellazzini, M., Berihuete, A., Bertone, S., Bianchi, L., Bienaymé, O., Blanco-Cuaresma, S., Boch, T., Boeche, C., Bombrun, A., Borrachero, R., Bossini, D., Bouquillon, S., Bourda, G., Bragaglia, A., Bramante, L., Breddels, M. A., Bressan, A., Brouillet, N., Brüsemeister, T., Brugaletta, E., Bucciarelli, B., Burlacu, A., Busonero, D., Butkevich, A. G., Buzzi, R., Caffau, E., Cancelliere, R., Cannizzaro, G., Cantat-Gaudin, T., Carballo, R., Carlucci, T., Carrasco, J. M., Casamiquela, L., Castellani, M., Castro-Ginard, A., Charlot, P., Chemin, L., Chiavassa, A., Cocozza, G., Costigan, G., Cowell, S., Crifo, F., Crosta, M., Crowley, C., Cuypers, J., Dafonte, C., Damerdji, Y., Dapergolas, A., David, P., David, M., de Laverny, P., De Luise, F., De March, R., de Martino, D., de Souza, R., de Torres, A., Debosscher, J., del Pozo, E., Delbo, M., Delgado, A., Delgado, H. E., Di Matteo, P., Diakite, S., Diener, C., Distefano, E., Dolding, C., Drazinos, P., Durán, J., Edvardsson, B., Enke, H., Eriksson, K., Esquej, P., Eynard Bontemps, G., Fabre, C., Fabrizio, M., Faigler, S., Falcão, A. J., Farràs Casas, M., Federici, L., Fedorets, G., Fernique, P., Figueras, F., Filippi, F., Findeisen, K., Fonti, A., Fraile, E., Fraser, M., Frézouls, B., Gai, M., Galleti, S., Garabato, D., García-Sedano, F., Garofalo, A., Garralda, N., Gavel, A., Gavras, P., Gerssen, J., Geyer, R., Giacobbe, P., Gilmore, G., Girona, S., Giuffrida, G., Glass, F., Gomes, M., Granvik, M., Gueguen, A., Guerrier, A., Guiraud, J., Gutiérrez-Sánchez, R., Haigron, R., Hatzidimitriou, D., Hauser, M., Haywood, M., Heiter, U., Helmi, A., Heu, J., Hilger, T., Hobbs, D., Hofmann, W., Holland, G., Huckle, H. E., Hypki, A., Icardi, V., Janßen, K., Jevardat de Fombelle, G., Jonker, P. G., Juhász, Á. L., Julbe, F., Karampelas, A., Kewley, A., Klar, J., Kochoska, A., Kohley, R., Kolenberg, K., Kontizas, M., Kontizas, E., Koposov, S. E., Kordopatis, G., Kostrzewa-Rutkowska, Z., Koubsky, P., Lambert, S., Lanza, A. F., Lasne, Y., Lavigne, J. B., Le Fustec, Y., Le Poncin-Lafitte, C., Lebreton, Y., Leccia, S., Leclerc, N., Lecoeur-Taibi, I., Lenhardt, H., Leroux, F., Liao, S., Licata, E.,

Lindstrøm, H. E. P., Lister, T. A., Livanou, E., Lobel, A., López, M., Managau, S., Mann, R. G., Mantelet, G., Marchal, O., Marchant, J. M., Marconi, M., Marinoni, S., Marschalkó, G., Marshall, D. J., Martino, M., Marton, G., Mary, N., Massari, D., Matijevič, G., Mazeh, T., McMillan, P. J., Messina, S., Michalik, D., Millar, N. R., Molina, D., Molinaro, R., Molnár, L., Montegriffo, P., Mor, R., Morbidelli, R., Morel, T., Morris, D., Mulone, A. F., Muraveva, T., Musella, I., Nelemans, G., Nicastro, L., Noval, L., O'Mullane, W., Ordénovic, C., Ordóñez-Blanco, D., Osborne, P., Pagani, C., Pagano, I., Pailler, F., Palacin, H., Palaversa, L., Panahi, A., Pawlak, M., Piersimoni, A. M., Pineau, F. X., Plachy, E., Plum, G., Poggio, E., Poujoulet, E., Prša, A., Pulone, L., Racero, E., Ragaini, S., Rambaux, N., Ramos-Lerate, M., Regibo, S., Reylé, C., Riclet, F., Ripepi, V., Riva, A., Rivard, A., Rixon, G., Roegiers, T., Roelens, M., Romero-Gómez, M., Rowell, N., Royer, F., Ruiz-Dern, L., Sadowski, G., Sagristà Sellés, T., Sahlmann, J., Salgado, J., Salguero, E., Sanna, N., Santana- Ros, T., Sarasso, M., Savietto, H., Schultheis, M., Sciacca, E., Segol, M., Segovia, J. C., Ségransan, D., Shih, I. C., Siltala, L., Silva, A. F., Smart, R. L., Smith, K. W., Solano, E., Solitro, F., Sordo, R., Soria Nieto, S., Souchay, J., Spagna, A., Spoto, F., Stampa, U., Steele, I. A., Steidelmüller, H., Stephenson, C. A., Stoev, H., Suess, F. F., Surdej, J., Szabados, L., Szegedi-Elek, E., Tapiador, D., Taris, F., Tauran, G., Taylor, M. B., Teixeira, R., Terrett, D., Teyssandier, P., Thuillot, W., Titarenko, A., Torra Clotet, F., Turon, C., Ulla, A., Utrilla, E., Uzzi, S., Vaillant, M., Valentini, G., Valette, V., van Elteren, A., Van Hemelryck, E., van Leeuwen, M., Vaschetto, M., Vecchiato, A., Veljanoski, J., Viala, Y., Vicente, D., Vogt, S., von Essen, C., Voss, H., Votruba, V., Voutsinas, S., Walmsley, G., Weiler, M., Wertz, O., Wevers, T., Wyrzykowski, Ł., Yoldas, A., Žerjal, M., Ziaeepour, H., Zorec, J., Zschocke, S., Zucker, S., Zurbach, C., and Zwitter, T. (2018b). Gaia Data Release 2. Summary of the contents and survey properties. *Astronomy and Astrophysics*, 616:A1.

Gaia Collaboration, Helmi, A., van Leeuwen, F., McMillan, P. J., Massari, D., Antoja, T., Robin, A. C., Lindegren, L., Bastian, U., Arenou, F., Babusiaux, C., Biermann, M., Breddels, M. A., Hobbs, D., Jordi, C., Pancino, E., Reylé, C., Veljanoski, J., Brown, A. G. A., Vallenari, A., Prusti, T., de Bruijne, J. H. J., Bailer-Jones, C. A. L., Evans, D. W., Eyer, L., Jansen, F., Klioner, S. A., Lammers, U., Luri, X., Mignard, F., Panem, C., Pourbaix, D., Randich, S., Sartoretti, P., Siddiqui, H. I., Soubiran, C., Walton, N. A., Cropper, M., Drimmel, R., Katz, D., Lattanzi, M. G., Bakker, J., Cacciari, C., Castañeda, J., Chaoul, L., Cheek, N., De Angeli, F., Fabricius, C., Guerra, R., Holl, B., Masana, E., Messineo, R., Mowlavi, N., Nienartowicz, K., Panuzzo, P., Portell, J., Riello, M., Seabroke, G. M., Tanga, P., Thévenin, F., Gracia-Abril, G., Comoretto, G., Garcia-Reinaldos, M., Teyssier, D., Altmann, M., Andrae, R., Audard, M., Bellas-Velidis, I., Benson, K., Berthier, J., Blomme, R., Burgess, P., Busso, G., Carry, B., Cellino, A., Clementini, G., Clotet, M., Creevey, O., Davidson, M., De Ridder, J., Delchambre, L., Dell'Oro, A., Ducourant, C., Fernández- Hernández, J., Fouesneau, M., Frémat, Y., Galluccio, L., García-Torres, M., González-Núñez, J., González-Vidal, J. J., Gosset, E., Guy, L. P., Halbwachs, J. L., Hambly, N. C., Harrison, D. L., Hernández, J., Hestroffer, D., Hodgkin, S. T., Hutton, A., Jasniewicz, G., Jean-Antoine-Piccolo, A., Jordan, S., Korn, A. J., Krone-Martins, A., Lanzafame, A. C., Lebzelter, T., Löffler, W., Manteiga, M., Marrese, P. M., Martín-Fleitas, J. M., Moitinho, A., Mora, A., Muinonen, K., Osinde, J., Pauwels, T., Petit, J. M., Recio-Blanco, A., Richards, P. J., Rimoldini, L., Sarro, L. M., Siopis, C., Smith, M., Sozzetti, A., Süveges, M., Torra, J., van Reeven, W., Abbas, U., Abreu Aramburu, A., Accart, S., Aerts, C., Altavilla, G., Álvarez, M. A., Alvarez, R., Alves, J., Anderson,

R. I., Andrei, A. H., Anglada Varela, E., Antiche, E., Arcay, B., Astraatmadja, T. L., Bach, N., Baker, S. G., Balaguer-Núñez, L., Balm, P., Barache, C., Barata, C., Barbato, D., Barblan, F., Barklem, P. S., Barrado, D., Barros, M., Barstow, M. A., Bartholomé Muñoz, S., Bassilana, J. L., Becciani, U., Bellazzini, M., Berihuete, A., Bertone, S., Bianchi, L., Bienaymé, O., Blanco-Cuaresma, S., Boch, T., Boeche, C., Bombrun, A., Borrachero, R., Bossini, D., Bouquillon, S., Bourda, G., Bragaglia, A., Bramante, L., Bressan, A., Brouillet, N., Brüsemeister, T., Brugaletta, E., Bucciarelli, B., Burlacu, A., Busonero, D., Butkevich, A. G., Buzzi, R., Caffau, E., Cancelliere, R., Cannizzaro, G., Cantat-Gaudin, T., Carballo, R., Carlucci, T., Carrasco, J. M., Casamiquela, L., Castellani, M., Castro-Ginard, A., Charlot, P., Chemin, L., Chiavassa, A., Cocozza, G., Costigan, G., Cowell, S., Crifo, F., Crosta, M., Crowley, C., Cuypers, J., Dafonte, C., Damerdji, Y., Dapergolas, A., David, P., David, M., de Laverny, P., De Luise, F., De March, R., de Martino, D., de Souza, R., de Torres, A., Debosscher, J., del Pozo, E., Delbo, M., Delgado, A., Delgado, H. E., Di Matteo, P., Diakite, S., Diener, C., Distefano, E., Dolding, C., Drazinos, P., Durán, J., Edvardsson, B., Enke, H., Eriksson, K., Esquej, P., Eynard Bontemps, G., Fabre, C., Fabrizio, M., Faigler, S., Falcão, A. J., Farràs Casas, M., Federici, L., Fedorets, G., Fernique, P., Figueras, F., Filippi, F., Findeisen, K., Fonti, A., Fraile, E., Fraser, M., Frézouls, B., Gai, M., Galleti, S., Garabato, D., García-Sedano, F., Garofalo, A., Garralda, N., Gavel, A., Gavras, P., Gerssen, J., Geyer, R., Giacobbe, P., Gilmore, G., Girona, S., Giuffrida, G., Glass, F., Gomes, M., Granvik, M., Gueguen, A., Guerrier, A., Guiraud, J., Gutiérrez-Sánchez, R., Hofmann, W., Holland, G., Huckle, H. E., Hypki, A., Icardi, V., Janßen, K., Jevardat de Fombelle, G., Jonker, P. G., Juhász, Á. L., Julbe, F., Karampelas, A., Kewley, A., Klar, J., Kochoska, A., Kohley, R., Kolenberg, K., Kontizas, M., Kontizas, E., Koposov, S. E., Kordopatis, G., Kostrzewa-Rutkowska, Z., Koubsky, P., Lambert, S., Lanza, A. F., Lasne, Y., Lavigne, J. B., Le Fustec, Y., Le Poncin- Lafitte, C., Lebreton, Y., Leccia, S., Leclerc, N., Lecoeur-Taibi, I., Lenhardt, H., Leroux, F., Liao, S., Licata, E., Lindstrøm, H. E. P., Lister, T. A., Livanou, E., Lobel, A., López, M., Managau, S., Mann, R. G., Mantelet, G., Marchal, O., Marchant, J. M., Marconi, M., Marinoni, S., Marschalkó, G., Marshall, D. J., Martino, M., Marton, G., Mary, N., Matijevič, G., Mazeh, T., Messina, S., Michalik, D., Millar, N. R., Molina, D., Molinaro, R., Molnár, L., Montegriffo, P., Mor, R., Morbidelli, R., Morel, T., Morris, D., Mulone, A. F., Muraveva, T., Musella, I., Nelemans, G., Nicastro, L., Noval, L., O'Mullane, W., Ordénovic, C., Ordóñez- Blanco, D., Osborne, P., Pagani, C., Pagano, I., Pailler, F., Palacin, H., Palaversa, L., Panahi, A., Pawlak, M., Piersimoni, A. M., Pineau, F. X., Plachy, E., Plum, G., Poggio, E., Poujoulet, E., Prša, A., Pulone, L., Racero, E., Ragaini, S., Rambaux, N., Ramos-Lerate, M., Regibo, S., Riclet, F., Ripepi, V., Riva, A., Rivard, A., Rixon, G., Roegiers, T., Roelens, M., Romero-Gómez, M., Rowell, N., Royer, F., Ruiz-Dern, L., Sadowski, G., Sagristà Sellés, T., Sahlmann, J., Salgado, J., Salguero, E., Sanna, N., Santana-Ros, T., Sarasso, M., Savietto, H., Schultheis, M., Sciacca, E., Segol, M., Segovia, J. C., Ségransan, D., Shih, I. C., Siltala, L., Silva, A. F., Smart, R. L., Smith, K. W., Solano, E., Solitro, F., Sordo, R., Soria Nieto, S., Souchay, J., Spagna, A., Spoto, F., Stampa, U., Steele, I. A., Steidelmüller, H., Stephenson, C. A., Stoev, H., Suess, F. F., Surdej, J., Szabados, L., Szegedi-Elek, E., Tapiador, D., Taris, F., Tauran, G., Taylor, M. B., Teixeira, R., Terrett, D., Teyssandier, P., Thuillot, W., Titarenko, A., Torra Clotet, F., Turon, C., Ulla, A., Utrilla, E., Uzzi, S., Vaillant, M., Valentini, G., Valette, V., van Elteren, A., Van Hemelryck, E., van Leeuwen, M., Vaschetto, M., Vecchiato, A., Viala, Y., Vicente, D., Vogt, S., von Essen, C., Voss, H., Votruba, V., Voutsinas, S., Walmsley, G., Weiler, M., Wertz, O., Wevems, T., Wyrzykowski, Ł., Yoldas, A., Žerjal, M., Ziaeepour, H., Zorec, J., Zschocke, S., Zucker,

S., Zurbach, C., and Zwitter, T. (2018c). Gaia Data Release 2. Kinematics of globular clusters and dwarf galaxies around the Milky Way. *Astronomy and Astrophysics*, 616:A12.

Gaia Collaboration, Lindegren, L., Hernández, J., Bombrun, A., Klioner, S., Bastian, U., Ramos-Lerate, M., de Torres, A., Steidelmüller, H., Stephenson, C., Hobbs, D., Lammers, U., Biermann, M., Geyer, R., Hilger, T., Michalik, D., Stampa, U., McMillan, P. J., Castañeda, J., Clotet, M., Comoretto, G., Davidson, M., Fabricius, C., Gracia, G., Hambly, N. C., Hutton, A., Mora, A., Portell, J., van Leeuwen, F., Abbas, U., Abreu, A., Altmann, M., Andrei, A., Anglada, E., Balaguer-Núñez, L., Barache, C., Becciani, U., Bertone, S., Bianchi, L., Bouquillon, S., Bourda, G., Brüsemeister, T., Bucciarelli, B., Busonero, D., Buzzi, R., Cancelliere, R., Carlucci, T., Charlot, P., Cheek, N., Crosta, M., Crowley, C., de Bruijne, J., de Felice, F., Drimmel, R., Esquej, P., Fienga, A., Fraile, E., Gai, M., Garralda, N., González-Vidal, J. J., Guerra, R., Hauser, M., Hofmann, W., Holl, B., Jordan, S., Lattanzi, M. G., Lenhardt, H., Liao, S., Licata, E., Lister, T., Löffler, W., Marchant, J., Martin-Fleitas, J.-M., Messineo, R., Mignard, F., Morbidelli, R., Poggio, E., Riva, A., Rowell, N., Salguero, E., Sarasso, M., Sciacca, E., Siddiqui, H., Smart, R. L., Spagna, A., Steele, I., Taris, F., Torra, J., van Elteren, A., van Reeven, W., and Vecchiato, A. (2018d). Gaia Data Release 2. The astrometric solution. *Astronomy and Astrophysics*, 616:A2.

Gaia Collaboration, Prusti, T., de Bruijne, J. H. J., Brown, A. G. A., Vallenari, A., Babusiaux, C., Bailer-Jones, C. A. L., Bastian, U., Biermann, M., Evans, D. W., Eyer, L., Jansen, F., Jordi, C., Klioner, S. A., Lammers, U., Lindegren, L., Luri, X., Mignard, F., Milligan, D. J., Panem, C., Poinsignon, V., Pourbaix, D., Randich, S., Sarri, G., Sartoretti, P., Siddiqui, H. I., Soubiran, C., Valette, V., van Leeuwen, F., Walton, N. A., Aerts, C., Arenou, F., Cropper, M., Drimmel, R., Høg, E., Katz, D., Lattanzi, M. G., O'Mullane, W., Grebel, E. K., Holland, A. D., Huc, C., Passot, X., Bramante, L., Cacciari, C., Castañeda, J., Chaoul, L., Cheek, N., De Angeli, F., Fabricius, C., Guerra, R., Hernández, J., Jean-Antoine-Piccolo, A., Masana, E., Messineo, R., Mowlavi, N., Nienartowicz, K., Ordóñez- Blanco, D., Panuzzo, P., Portell, J., Richards, P. J., Riello, M., Seabroke, G. M., Tanga, P., Thévenin, F., Torra, J., Els, S. G., Gracia- Abril, G., Comoretto, G., Garcia-Reinaldos, M., Lock, T., Mercier, E., Altmann, M., Andrae, R., Astraatmadja, T. L., Bellas-Velidis, I., Benson, K., Berthier, J., Blomme, R., Busso, G., Carry, B., Cellino, A., Clementini, G., Cowell, S., Creevey, O., Cuypers, J., Davidson, M., De Ridder, J., de Torres, A., Delchambre, L., Dell'Oro, A., Ducourant, C., Frémat, Y., García-Torres, M., Gosset, E., Halbwachs, J. L., Hambly, N. C., Harrison, D. L., Hauser, M., Hestroffer, D., Hodgkin, S. T., Huckle, H. E., Hutton, A., Jasniewicz, G., Jordan, S., Kontizas, M., Korn, A. J., Lanzafame, A. C., Manteiga, M., Moitinho, A., Muinonen, K., Osinde, J., Pancino, E., Pauwels, T., Petit, J. M., Recio-Blanco, A., Robin, A. C., Sarro, L. M., Siopis, C., Smith, M., Smith, K. W., Sozzetti, A., Thuillot, W., van Reeven, W., Viala, Y., Abbas, U., Abreu Aramburu, A., Accart, S., Aguado, J. J., Allan, P. M., Allasia, W., Altavilla, G., Álvarez, M. A., Alves, J., Anderson, R. I., Andrei, A. H., Anglada Varela, E., Antiche, E., Antoja, T., Antón, S., Arcay, B., Atzei, A., Ayache, L., Bach, N., Baker, S. G., Balaguer-Núñez, L., Barache, C., Barata, C., Barbier, A., Barblan, F., Baroni, M., Barrado y Navascués, D., Barros, M., Barstow, M. A., Becciani, U., Bellazzini, M., Bellei, G., Bello García, A., Belokurov, V., Bendjoya, P., Berihuete, A., Bianchi, L., Bienaymé, O., Billebaud, F., Blagorodnova, N., Blanco-Cuaresma, S., Boch, T., Bombrun, A., Borrachero, R., Bouquillon, S., Bourda, G., Bouy, H., Bragaglia, A., Breddels, M. A., Brouillet, N., Brüsemeister, T., Bucciarelli, B., Budnik, F., Burgess, P., Burgon, R., Burlacu, A., Busonero, D., Buzzi, R., Caffau, E., Cambras, J., Campbell, H.,

Cancelliere, R., Cantat-Gaudin, T., Carlucci, T., Carrasco, J. M., Castellani, M., Charlot, P., Charnas, J., Charvet, P., Chassat, F., Chiavassa, A., Clotet, M., Cocozza, G., Collins, R. S., Collins, P., Costigan, G., Crifo, F., Cross, N. J. G., Crosta, M., Crowley, C., Dafonte, C., Damerdji, Y., Dapergolas, A., David, P., David, M., De Cat, P., de Felice, F., de Laverny, P., De Luise, F., De March, R., de Martino, D., de Souza, R., Debosscher, J., del Pozo, E., Delbo, M., Delgado, A., Delgado, H. E., di Marco, F., Di Matteo, P., Diakite, S., Distefano, E., Dolding, C., Dos Anjos, S., Drazinos, P., Durán, J., Dzigan, Y., Ecale, E., Edvardsson, B., Enke, H., Erdmann, M., Escolar, D., Espina, M., Evans, N. W., Eynard Bontemps, G., Fabre, C., Fabrizio, M., Faigler, S., Falcão, A. J., Farràs Casas, M., Faye, F., Federici, L., Fedorets, G., Fernández-Hernández, J., Fernique, P., Fienga, A., Figueras, F., Filippi, F., Findeisen, K., Fonti, A., Fouesneau, M., Fraile, E., Fraser, M., Fuchs, J., Furnell, R., Gai, M., Galleti, S., Galluccio, L., Garabato, D., García-Sedano, F., Garé, P., Garofalo, A., Garralda, N., Gavras, P., Gerssen, J., Geyer, R., Gilmore, G., Girona, S., Giuffrida, G., Gomes, M., González-Marcos, A., González-Núñez, J., González-Vidal, J. J., Granvik, M., Guerrier, A., Guillout, P., Guiraud, J., Gúrpide, A., Gutiérrez-Sánchez, R., Guy, L. P., Haigron, R., Hatzidimitriou, D., Haywood, M., Heiter, U., Helmi, A., Hobbs, D., Hofmann, W., Holl, B., Holland, G., Hunt, J. A. S., Hypki, A., Icardi, V., Irwin, M., Jevardat de Fombelle, G., Jofré, P., Jonker, P. G., Jorissen, A., Julbe, F., Karampelas, A., Kochoska, A., Kohley, R., Kolenberg, K., Kontizas, E., Koposov, S. E., Kordopatis, G., Koubsky, P., Kowalczyk, A., Krone-Martins, A., Kudryashova, M., Kull, I., Bachchan, R. K., Lacoste-Seris, F., Lanza, A. F., Lavigne, J. B., Le Poncin-Lafitte, C., Lebreton, Y., Lebzelter, T., Leccia, S., Leclerc, N., Lecoeur-Taibi, I., Lemaitre, V., Lenhardt, H., Leroux, F., Liao, S., Licata, E., Lindstrøm, H. E. P., Lister, T. A., Livanou, E., Lobel, A., Löffler, W., López, M., Lopez-Lozano, A., Lorenz, D., Loureiro, T., MacDonald, I., Magalhães Fernandes, T., Managau, S., Mann, R. G., Mantelet, G., Marchal, O., Marchant, J. M., Marconi, M., Marie, J., Marinoni, S., Marrese, P. M., Marschalkó, G., Marshall, D. J., Martín-Fleitas, J. M., Martino, M., Mary, N., Matijevič, G., Mazeh, T., McMillan, P. J., Messina, S., Mestre, A., Michalik, D., Millar, N. R., Miranda, B. M. H., Molina, D., Molinaro, R., Molinaro, M., Molnár, L., Moniez, M., Montegriffo, P., Monteiro, D., Mor, R., Mora, A., Morbidelli, R., Morel, T., Morgenthaler, S., Morley, T., Morris, D., Mulone, A. F., Muraveva, T., Musella, I., Narbonne, J., Nelemans, G., Nicastro, L., Noval, L., Ordénovic, C., Ordieres-Meré, J., Osborne, P., Pagani, C., Pagano, I., Pailler, F., Palacin, H., Palaversa, L., Parsons, P., Paulsen, T., Pecoraro, M., Pedrosa, R., Pentikäinen, H., Pereira, J., Pichon, B., Piersimoni, A. M., Pineau, F. X., Plachy, E., Plum, G., Poujoulet, E., Prša, A., Pulone, L., Ragaini, S., Rago, S., Rambaux, N., Ramos-Lerate, M., Ranalli, P., Rauw, G., Read, A., Regibo, S., Renk, F., Reylé, C., Ribeiro, R. A., Rimoldini, L., Ripepi, V., Riva, A., Rixon, G., Roelens, M., Romero-Gómez, M., Rowell, N., Royer, F., Rudolph, A., Ruiz-Dern, L., Sadowski, G., Sagristà Sellés, T., Sahlmann, J., Salgado, J., Salguero, E., Sarasso, M., Savietto, H., Schnorhk, A., Schultheis, M., Sciacca, E., Segol, M., Segovia, J. C., Segransan, D., Serpell, E., Shih, I. C., Smareglia, R., Smart, R. L., Smith, C., Solano, E., Solitro, F., Sordo, R., Soria Nieto, S., Souchay, J., Spagna, A., Spoto, F., Stampa, U., Steele, I. A., Steidelmüller, H., Stephenson, C. A., Stoev, H., Suess, F. F., Süveges, M., Surdej, J., Szabados, L., Szegedi-Elek, E., Tapiador, D., Taris, F., Tauran, G., Taylor, M. B., Teixeira, R., Terrett, D., Tingley, B., Trager, S. C., Turon, C., Ulla, A., Utrilla, E., Valentini, G., van Elteren, A., Van Hemelryck, E., van Leeuwen, M., Varadi, M., Vecchiato, A., Veljanoski, J., Via, T., Vicente, D., Vogt, S., Voss, H., Votruba, V., Voutsinas, S., Walmsley, G., Weiler, M., Weingrill, K., Werner, D., Wevers, T., Whitehead, G., Wyrzykowski, Ł., Yoldas, A., Žerjal, M., Zucker, S., Zurbach,

C., Zwitter, T., Alecu, A., Allen, M., Allende Prieto, C., Amorim, A., Anglada-Escudé, G., Arsenijevic, V., Azaz, S., Balm, P., Beck, M., Bernstein, H. H., Bigot, L., Bijaoui, A., Blasco, C., Bonfigli, M., Bono, G., Boudreault, S., Bressan, A., Brown, S., Brunet, P. M., Bunclark, P., Buonanno, R., Butkevich, A. G., Carret, C., Carrion, C., Chemin, L., Chéreau, F., Corcione, L., Darmigny, E., de Boer, K. S., de Teodoro, P., de Zeeuw, P. T., Delle Luche, C., Domingues, C. D., Dubath, P., Fodor, F., Frézouls, B., Fries, A., Fustes, D., Fyfe, D., Gallardo, E., Gallegos, J., Gardiol, D., Gebran, M., Gomboc, A., Gómez, A., Grux, E., Gueguen, A., Heyrovsky, A., Hoar, J., Iannicola, G., Isasi Parache, Y., Janotto, A. M., Joliet, E., Jonckheere, A., Keil, R., Kim, D. W., Klagyivik, P., Klar, J., Knude, J., Kochukhov, O., Kolka, I., Kos, J., Kutka, A., Lainey, V., LeBouquin, D., Liu, C., Loreggia, D., Makarov, V. V., Marseille, M. G., Martayan, C., Martinez-Rubi, O., Massart, B., Meynadier, F., Mignot, S., Munari, U., Nguyen, A. T., Nordlander, T., Ocvirk, P., O'Flaherty, K. S., Olias Sanz, A., Ortiz, P., Osorio, J., Oszkiewicz, D., Ouzounis, A., Palmer, M., Park, P., Pasquato, E., Peltzer, C., Peralta, J., Péturaud, F., Pieniluoma, T., Pigozzi, E., Poels, J., Prat, G., Prod'homme, T., Raison, F., Rebordao, J. M., Risquez, D., Rocca-Volmerange, B., Rosen, S., Ruiz-Fuertes, M. I., Russo, F., Sembay, S., Serraller Vizcaino, I., Short, A., Siebert, A., Silva, H., Sinachopoulos, D., Slezak, E., Soffel, M., Sosnowska, D., Straižys, V., ter Linden, M., Terrell, D., Theil, S., Tiede, C., Troisi, L., Tsalmantza, P., Tur, D., Vaccari, M., Vachier, F., Valles, P., Van Hamme, W., Veltz, L., Virtanen, J., Wallut, J. M., Wichmann, R., Wilkinson, M. I., Ziaeepour, H., and Zschocke, S. (2016). The Gaia mission. *Astronomy and Astrophysics*, 595:A1.

Garrison-Kimmel, S., Boylan-Kolchin, M., Bullock, J. S., and Lee, K. (2014). ELVIS: Exploring the Local Volume in Simulations. *Monthly Notices of the Royal Astronomical Society*, 438:2578–2596.

Garrison-Kimmel, S., Wetzel, A., Bullock, J. S., Hopkins, P. F., Boylan-Kolchin, M., Faucher-Giguère, C.-A., Kereš, D., Quataert, E., Sanderson, R. E., Graus, A. S., and Kelley, T. (2017). Not so lumpy after all: modelling the depletion of dark matter subhaloes by Milky Way-like galaxies. *Monthly Notices of the Royal Astronomical Society*, 471:1709–1727.

Geisler, D., Wallerstein, G., Smith, V., Casetti-Dinescu, and D.I. (2007). Chemical abundances and kinematics in globular clusters and local group dwarf galaxies and their implications for formation theories of the galactic halo. *The Publications of the Astronomical Society of the Pacific*, 119:989–961.

Gibbons, S. L. J., Belokurov, V., and Evans, N. W. (2017). A tail of two populations: chemo-dynamics of the Sagittarius stream and implications for its original mass. *Monthly Notices of the Royal Astronomical Society*, 464:794–809.

Gieles, M. and Zocchi, A. (2015). A family of lowered isothermal models. *Monthly Notices of the Royal Astronomical Society*, 454:576–592.

Gilmore, G. (2018). Gaia: 3-dimensional census of the Milky Way Galaxy. *Contemporary Physics*, 59:155–173.

Gnedin, O. Y., Lee, H. M., and Ostriker, J. P. (1999). Effects of Tidal Shocks on the Evolution of Globular Clusters. *The Astrophysical Journal*, 522:935–949.

Gnedin, O. Y. and Ostriker, J. P. (1997). Destruction of the Galactic Globular Cluster System. *The Astrophysical Journal*, 474:223–255.

Goldstein, H. and Poole, C. (1980). *Classical Mechanics*. Addison-Wesley series in physics. Addison-Wesley Publishing Company.

Gómez, F. A., Helmi, A., Brown, A. G. A., and Li, Y.-S. (2010). On the identification of merger debris in the Gaia era. *Monthly Notices of the Royal Astronomical Society*, 408:935–946.

Gould, A. (2003). An upper limit on the granularity of the local stellar halo. *The Astrophysical Journal*, 592:L63–L66.

Grand, R. J. J., Gómez, F. A., Marinacci, F., Pakmor, R., Springel, V., Campbell, D. J. R., Frenk, C. S., Jenkins, A., and White, S. D. M. (2017). The Auriga Project: the properties and formation mechanisms of disc galaxies across cosmic time. *Monthly Notices of the Royal Astronomical Society*, 467(1):179–207.

Green, G. M., Schlafly, E. F., Finkbeiner, D. P., Rix, H.-W., Martin, N., Burgett, W., Draper, P. W., Flewelling, H., Hodapp, K., Kaiser, N., Kudritzki, R. P., Magnier, E., Metcalfe, N., Price, P., Tonry, J., and Wainscoat, R. (2015). A Three-dimensional Map of Milky Way Dust. *The Astrophysical Journal*, 810:25.

Grillmair, C., Hetherington, L., Carlberg, R., and Willman, B. (2015). An orphan no longer? detection of the southern orphan stream and a candidate progenitor. *The Astrphysical Journal*, 812:L26.

Grillmair, C. J. (2006). Detection of a 60°-long Dwarf Galaxy Debris Stream. *The Astrophysical Journal*, 645:L37–L40.

Grillmair, C. J. (2009). Four New Stellar Debris Streams in the Galactic Halo. *The Astrophysical Journal*, 693:1118–1127.

Grillmair, C. J. and Carlin, J. L. (2016). Stellar Streams and Clouds in the Galactic Halo. In Newberg, H. J. and Carlin, J. L., editors, *Tidal Streams in the Local Group and Beyond*, volume 420, page 87.

Grillmair, C. J. and Dionatos, O. (2006a). A 22° Tidal Tail for Palomar 5. *The Astrophysical Journal*, 641:L37–L39.

Grillmair, C. J. and Dionatos, O. (2006b). Detection of a 63deg Cold Stellar Stream in the Sloan Digital Sky Survey. *The Astrophysical Journal*, 643:L17–L20.

Grillmair, C. J., Freeman, K. C., Irwin, M., and Quinn, P. J. (1995). Globular Clusters with Tidal Tails: Deep Two-Color Star Counts. *The Astronomical Journal*, 109:2553.

Grillmair, C. J. and Johnson, R. (2006). The Detection of a 45° Tidal Stream Associated with the Globular Cluster NGC 5466. *The Astrophysical Journal*, 639:L17–L20.

Harris, W. E. (1996). A Catalog of Parameters for Globular Clusters in the Milky Way. *The Astronomical Journal*, 112:1487.

Hattori, K., Yoshii, Y., Beers, T. C., Carollo, D., and Lee, Y. S. (2013). Very Metal-poor Outer-halo Stars with Round Orbits. *The Astrophysical Journal*, 763:L17.

Hawkins, K., Jofré, P., Masseron, T., and Gilmore, G. (2015). Using chemical tagging to redefine the interface of the Galactic disc and halo. *Monthly Notices of the Royal Astronomical Society*, 453:758–774.

Haywood, M., Di Matteo, P., Lehnert, M. D., Snaith, O., Khoperskov, S., and Gómez, A. (2018). In Disguise or Out of Reach: First Clues about In Situ and Accreted Stars in the Stellar Halo of the Milky Way from Gaia DR2. *The Astrophysical Journal*, 863:113.

Helmi, A. (2008). The stellar halo of the galaxy. *The Astrony and Astrophysics Review*, 15:145–188.

Helmi, A., Babusiaux, C., Koppelman, H. H., Massari, D., Veljanoski, J., and Brown, A. G. A. (2018). The merger that led to the formation of the Milky Way's inner stellar halo and thick disk. *Nature*, 563(7729):85–88.

Helmi, A., Veljanoski, J., Breddels, M. A., Tian, H., and Sales, L. V. (2017). A box full of chocolates: The rich structure of the nearby stellar halo revealed by Gaia and RAVE. *Astronomy and Astrophysics*, 598:A58.

Helmi, A. and White, S. D. M. (1999). Building up the stellar halo of the Galaxy. *Monthly Notices of the Royal Astronomical Society*, 307:495–517.

Helmi, A., White, S. D. M., de Zeeuw, P. T., and Zhao, H. (1999). Debris streams in the solar neighbourhood as relicts from the formation of the Milky Way. *Nature*, 402:53–55.

Hénault-Brunet, V., Gieles, M., Sollima, A., Watkins, L. L., Zocchi, A., Claydon, I., Pancino, E., and Baumgardt, H. (2019). Mass modelling globular clusters in the Gaiaera: a method comparison using mock data from an N-body simulation of M 4. *Monthly Notices of the Royal Astronomical Society*, 483(1):1400–1425.

Hendel, D. and Johnston, K. V. (2015). Tidal debris morphology and the orbits of satellite galaxies. *Monthly Notices of the Royal Astronomical Society*, 454:2472–2485.

Henning, R., Conrad, J., Formaggio, J., Heine, S., Kahn, Y., Minervini, J., Ouellet, J., Perez, K., Radovinsky, A., Safdi, B., Salemi, C., Thaler, J., Winklehner, D., and Winslow, L. (2018). ABRACADABRA, A Search for Low-Mass Axion Dark Matter. In *Henning, Reyco "ABRACADABRA, A Search for Low-Mass Axion Dark Matter" in Proceedings of the 13th "Patras" Workshop on Axions, WIMPs and WISPs, PATRAS 2017 / Maroudas, Marios (eds.), Verlag Deutsches Elektronen-Synchrotron : 2018 ; Patras 2017 : 13th Patras Workshop on Axions, WIMPs and WISPs, 2017-05-15 - 2017-05-19, Thessaloniki*, DESY-PROC, pages 28–31, Hamburg. 13th Patras Workshop on Axions, WIMPs and WISPs, Thessaloniki (Greece), 15 May 2017 - 19 May 2017, Verlag Deutsches Elektronen-Synchrotron.

Hernquist, L. and Quinn, P. J. (1987). Shells and Dark Matter in Elliptical Galaxies. *The Astrophysical Journal*, 312:1.

Høg, E., Fabricius, C., Makarov, V. V., Urban, S., Corbin, T., Wycoff, G., Bastian, U., Schwekendiek, P., and Wicenec, A. (2000). The Tycho-2 catalogue of the 2.5 million brightest stars. *Astronomy and Astrophysics*, 355:L27–L30.

Hudson, M. J., Harris, G. L., and Harris, W. E. (2014). Dark Matter Halos in Galaxies and Globular Cluster Populations. *The Astrophysical Journal*, 787:L5.

Hunt, J. A. S., Bovy, J., Pérez-Villegas, A., Holtzman, J. A., Sobeck, J., Chojnowski, D., Santana, F. A., Palicio, P. A., Wegg, C., Gerhard, O., Almeida, A., Bizyaev, D., Fernandez-Trincado, J. G., Lane, R. R., Longa-Peña, P., Majewski, S. R., Pan, K., and Roman-Lopes, A. (2018). The Hercules stream as seen by APOGEE-2 South. *Monthly Notices of the Royal Astronomical Society*, 474:95–101.

Ibata, R., Irwin, M., Lewis, G. F., and Stolte, A. (2001). Galactic Halo Substructure in the Sloan Digital Sky Survey: The Ancient Tidal Stream from the Sagittarius Dwarf Galaxy. *The Astrophysical Journal*, 547:L133–L136.

Ibata, R., Lewis, G., Irwin, M., and Quinn, T. (2002). Uncovering cold dark matter halo substructure with tidal streams. *Monthly Notice of the Royal Astronomical Society*, 332:915–920.

Ibata, R. A., Bellazzini, M., Malhan, K., Martin, N., and Bianchini, P. (2019). Identification of the long stellar stream of the prototypical massive globular cluster ω Centauri. *Nature Astronomy*, page 258.

Ibata, R. A., Gilmore, G., and Irwin, M. J. (1994). A dwarf satellite galaxy in Sagittarius. *Nature*, 370:194–196.

Iorio, G. and Belokurov, V. (2019). The shape of the Galactic halo with Gaia DR2 RR Lyrae. Anatomy of an ancient major merger. *Monthly Notices of the Royal Astronomical Society*, 482(3):3868–3879.

Iorio, G., Belokurov, V., Erkal, D., Koposov, S. E., Nipoti, C., and Fraternali, F. (2018). The first all-sky view of the Milky Way stellar halo with Gaia+2MASS RR Lyrae. *Monthly Notices of the Royal Astronomical Society*, 474:2142–2166.

Ivezić, Ž., Goldston, J., Finlator, K., Knapp, G. R., Yanny, B., McKay, T. A., Amrose, S., Krisciunas, K., Willman, B., Anderson, S., Schaber, C., Erb, D., Logan, C., Stubbs, C., Chen, B., Neilsen, E., Uomoto, A., Pier, J. R., Fan, X., Gunn, J. E., Lupton, R. H., Rockosi, C. M., Schlegel, D., Strauss, M. A., Annis, J., Brinkmann, J., Csabai, I., Doi, M., Fukugita, M., Hennessy, G. S., Hindsley, R. B., Margon, B., Munn, J. A., Newberg, H. J., Schneider, D. P., Smith, J. A., Szokoly, G. P., Thakar, A. R., Vogeley, M. S., Waddell, P., Yasuda, N., York, D. G., and SDSS Collaboration (2000). Candidate RR Lyrae Stars Found in Sloan Digital Sky Survey Commissioning Data. *The Astronomical Journal*, 120:963–977.

Ivezić, Ž., Sesar, B., Jurić, M., Bond, N., Dalcanton, J., Rockosi, C. M., Yanny, B., Newberg, H. J., Beers, T. C., Allende Prieto, C., Wilhelm, R., Lee, Y. S., Sivarani, T., Norris, J. E., Bailer-Jones, C. A. L., Re Fiorentin, P., Schlegel, D., Uomoto, A., Lupton, R. H., Knapp, G. R., Gunn, J. E., Covey, K. R., Allyn Smith, J., Miknaitis, G., Doi, M., Tanaka, M., Fukugita, M., Kent, S., Finkbeiner, D., Munn, J. A., Pier, J. R., Quinn, T., Hawley, S., Anderson, S., Kiuchi, F., Chen, A., Bushong, J., Sohi, H., Haggard, D., Kimball, A., Barentine, J., Brewington, H., Harvanek, M., Kleinman, S., Krzesinski, J., Long, D., Nitta, A., Snedden, S., Lee, B., Harris, H., Brinkmann, J., Schneider, D. P., and York, D. G. (2008). The Milky Way Tomography with SDSS. II. Stellar Metallicity. *The Astrophysical Journal*, 684:287–325.

Ji, A. P., Frebel, A., Chiti, A., and Simon, J. D. (2016). R-process enrichment from a single event in an ancient dwarf galaxy. *Nature*, 531:610–613.

Johnston, K. (2016). *Origins and Interpretation of Tidal Debris*, volume 420, page 141. Tidal Streams in the Local Group and Beyond, Astrophysics and Space Science Library, Springer International Publishing, Switzerland.

Johnston, K. V. (1998). A Prescription for Building the Milky Way's Halo from Disrupted Satellites. *The Astrophysical Journal*, 495:297–308.

Johnston, K. V., Hernquist, L., and Bolte, M. (1996). Fossil Signatures of Ancient Accretion Events in the Halo. *The Astrophysical Journal*, 465:278.

Johnston, K. V., Zhao, H., Spergel, D. N., and Hernquist, L. (1999). Tidal Streams as Probes of the Galactic Potential. *The Astrophysical Journal*, 512:L109–L112.

Joo, S.-J. and Lee, Y.-W. (2013). Star Formation Histories of Globular Clusters with Multiple Populations. I. ω CEN, M22, and NGC 1851. *The Astrophysical Journal*, 762:36.

Kahn, Y., Safdi, B. R., and Thaler, J. (2016). Broadband and Resonant Approaches to Axion Dark Matter Detection. *Physical Review Letters*, 117:141801.

Kavanagh, B. J. and O'Hare, C. A. J. (2016). Reconstructing the three-dimensional local dark matter velocity distribution. *Physical Review D*, 94:123009.

Keller, S. C., Mackey, D., and Da Costa, G. S. (2012). The Globular Cluster System of the Milky Way: Accretion in a Cosmological Context. *The Astrophysical Journal*, 744:57.

Kepley, A. A., Morrison, H. L., Helmi, A., Kinman, T. D., Van Duyne, J., Martin, J. C., Harding, P., Norris, J. E., and Freeman, K. C. (2007). Halo Star Streams in the Solar Neighborhood. *The Astronomical Journal*, 134:1579–1595.

King, I. (1962). The structure of star clusters. I. an empirical density law. *The Astronomical Journal*, 67:471.

Kirby, E. N., Boylan-Kolchin, M., Cohen, J. G., Geha, M., Bullock, J. S., and Kaplinghat, M. (2013a). Segue 2: The Least Massive Galaxy. *The Astrophysical Journal*, 770:16.

Kirby, E. N., Cohen, J. G., Guhathakurta, P., Cheng, L., Bullock, J. S., and Gallazzi, A. (2013b). The Universal Stellar Mass-Stellar Metallicity Relation for Dwarf Galaxies. *The Astrophysical Journal*, 779:102.

Klement, R. J. (2010). Halo streams in the solar neighborhood. *Astronomy and Astrophysics Review*, 18:567–594.

Knebe, A., Gill, S. P. D., Kawata, D., and Gibson, B. K. (2005). Mapping substructures in dark matter haloes. *Monthly Notices of the Royal Astronomical Society*, 357:L35–L39.

Koposov, S., Belokurov, V., Torrealba, G., and Evans, N. (2015). Beasts of the southern wild: Discovery of nine ultra faint satellites in the vicinity of the magellanic clouds. *The Astrophysical Journal*, 805:130.

Koposov, S., Rix, H.-W., and Hogg, D. (2010). Constraining the milky way potential with a six-dimensional phase-space map of the gd-1 stellar stream. *The Astrophysical Journal*, 712:260–273.

Koposov, S. E., Belokurov, V., Evans, N. W., Gilmore, G., Gieles, M., Irwin, M. J., Lewis, G. F., Niederste-Ostholt, M., Peñarrubia, J., Smith, M. C., Bizyaev, D., Malanushenko, E., Malanushenko, V., Schneider, D. P., and Wyse, R. F. G. (2012). The Sagittarius Streams in the Southern Galactic Hemisphere. *The Astrophysical Journal*, 750:80.

Kordopatis, G., Gilmore, G., Steinmetz, M., Boeche, C., Seabroke, G. M., Siebert, A., Zwitter, T., Binney, J., de Laverny, P., Recio-Blanco, A., Williams, M. E. K., Piffl, T., Enke, H., Roeser, S., Bijaoui, A., Wyse, R. F. G., Freeman, K., Munari, U., Carrillo, I., Anguiano, B., Burton, D., Campbell, R., Cass, C. J. P., Fiegert, K., Hartley, M., Parker, Q. A., Reid, W., Ritter, A., Russell, K. S., Stupar, M., Watson, F. G., Bienaymé, O., Bland-Hawthorn, J., Gerhard, O., Gibson, B. K., Grebel, E. K., Helmi, A., Navarro, J. F., Conrad, C., Famaey, B., Faure, C., Just, A., Kos, J., Matijevič, G., McMillan, P. J., Minchev, I., Scholz, R., Sharma, S., Siviero, A., de Boer, E. W., and Žerjal, M. (2013). The Radial Velocity Experiment (RAVE): Fourth Data Release. *The Astronomical Journal*, 146:134.

Kroupa, P., Theis, C., and Boily, C. M. (2005). The great disk of Milky-Way satellites and cosmological sub-structures. *Astronomy and Astrophysics*, 431:517–521.

Kruijssen, J. M. D., Pfeffer, J. L., Reina-Campos, M., Crain, R. A., and Bastian, N. (2019). The formation and assembly history of the Milky Way revealed by its globular cluster population. *Monthly Notices of the Royal Astronomical Society*, 486(3):3180–3202.

Kunder, A., Kordopatis, G., Steinmetz, M., Zwitter, T., McMillan, P. J., Casagrande, L., Enke, H., Wojno, J., Valentini, M., Chiappini, C., Matijevič, G., Siviero, A., de Laverny, P., Recio- Blanco, A., Bijaoui, A., Wyse, R. F. G., Binney, J., Grebel, E. K., Helmi, A., Jofre, P., Antoja, T., Gilmore, G., Siebert, A., Famaey, B., Bienaymé, O., Gibson, B. K., Freeman, K. C., Navarro, J. F., Munari, U., Seabroke, G., Anguiano, B., Žerjal, M., Minchev, I., Reid, W., Bland-Hawthorn, J., Kos, J., Sharma, S., Watson, F., Parker, Q. A., Scholz, R.-D., Burton, D., Cass, P., Hartley, M., Fiegert, K., Stupar, M., Ritter, A., Hawkins, K., Gerhard, O., Chaplin, W. J., Davies, G. R., Elsworth, Y. P., Lund, M. N., Miglio, A., and Mosser, B. (2017). The Radial Velocity Experiment (RAVE): Fifth Data Release. *The Astronomical Journal*, 153:75.

Küpper, A. H. W., Lane, R. R., and Heggie, D. C. (2012). More on the structure of tidal tails. *Monthly Notices of the Royal Astronomical Society*, 420:2700–2714.

Kuzma, P. B., Da Costa, G. S., Mackey, A. D., and Roderick, T. A. (2016). The outer envelopes of globular clusters - I. NGC 7089 (M2). *Monthly Notices of the Royal Astronomical Society*, 461:3639–3652.

Lancaster, L., Belokurov, V., and Evans, N. W. (2018). Quantifying the Smoothness of the Stellar Halo: A Link to Accretion History. *ArXiv e-prints*, page arXiv:1804.09181.

Lancaster, L., Koposov, S. E., Belokurov, V., Evans, N. W., and Deason, A. J. (2019). The halo's ancient metal-rich progenitor revealed with BHB stars. *Monthly Notices of the Royal Astronomical Society*, 486(1):378–389.

Law, D. and Majewski, S. (2010). The sagittarius dwarf galaxy: A model for evolution in a triaxial milky way halo. *The Astrophysical Journal*, 714:229–254.

Law, D. R. and Majewski, S. R. (2010). Assessing the Milky Way Satellites Associated with the Sagittarius Dwarf Spheroidal Galaxy. *The Astrophysical Journal*, 718:1128–1150.

Lee, S. K. and Peter, A. H. G. (2012). Probing the local velocity distribution of WIMP dark matter with directional detectors. *Journal of Cosmology and Astro-Particle Physics*, 2012:029.

Lee, Y.-W., Joo, J.-M., Sohn, Y.-J., Rey, S.-C., Lee, H.-C., and Walker, A. R. (1999). Multiple stellar populations in the globular cluster ω Centauri as tracers of a merger event. *Nature*, 402:55–57.

Leon, S., Meylan, G., and Combes, F. (2000). Tidal tails around 20 Galactic globular clusters. Observational evidence for gravitational disk/bulge shocking. *Astronomy and Astrophysics*, 359:907–931.

Leung, H. W. and Bovy, J. (2019). Deep learning of multi-element abundances from high-resolution spectroscopic data. *Monthly Notices of the Royal Astronomical Society*, 483(3):3255–3277.

Libralato, M., Bellini, A., Bedin, L. R., Moreno D., E., Fernández-Trincado, J. G., Pichardo, B., van der Marel, R. P., Anderson, J., Apai, D., Burgasser, A. J., Fabiola Marino, A., Milone, A. P., Rees, J. M., and Watkins, L. L. (2018). The HST Large Programme on ω Centauri. III. Absolute Proper Motion. *The Astrophysical Journal*, 854:45.

Lowing, B., Wang, W., Cooper, A., Kennedy, R., Helly, J., Cole, S., and Frenk, C. (2015). Creating mock catalogues of stellar haloes from cosmological simulations. *Monthly Notices of the Royal Astronomical Society*, 446:2274–2290.

Luo, A. L., Zhao, Y.-H., Zhao, G., Deng, L.-C., Liu, X.-W., Jing, Y.-P., Wang, G., Zhang, H.-T., Shi, J.-R., Cui, X.-Q., Chu, Y.-Q., Li, G.-P., Bai, Z.-R., Wu, Y., Cai, Y., Cao, S.-Y., Cao, Z.-H., Carlin, J. L., Chen, H.-Y., Chen, J.-J., Chen, K.-X., Chen, L., Chen, X.-L., Chen, X.-Y., Chen, Y., Christlieb, N., Chu, J.-R., Cui, C.-Z., Dong, Y.-Q., Du, B., Fan, D.-W., Feng, L., Fu, J.-N., Gao, P., Gong, X.-F., Gu, B.-Z., Guo, Y.-X., Han, Z.-W., He, B.-L., Hou, J.-L., Hou, Y.-H., Hou, W., Hu, H.-Z., Hu, N.-S., Hu, Z.-W., Huo, Z.-Y., Jia, L., Jiang, F.-H., Jiang, X., Jiang, Z.-B., Jin, G., Kong, X., Kong, X., Lei, Y.-J., Li, A.-H., Li, C.-H., Li, G.-W., Li, H.-N., Li, J., Li, Q., Li, S., Li, S.-S., Li, X.-N., Li, Y., Li, Y.-B., Li, Y.-P., Liang, Y., Lin, C.-C., Liu, C., Liu, G.-R., Liu, G.-Q., Liu, Z.-G., Lu, W.-Z., Luo, Y., Mao, Y.-D., Newberg, H., Ni, J.-J., Qi, Z.-X., Qi, Y.-J., Shen, S.-Y., Shi, H.-M., Song, J., Song, Y.-H., Su, D.-Q., Su, H.-J., Tang, Z.-H., Tao, Q.-S., Tian, Y., Wang, D., Wang, D.-Q., Wang, F.-F., Wang, G.-M., Wang, H., Wang, H.-C., Wang, J., Wang, J.-N., Wang, J.-L., Wang, J.-P., Wang, J.-X., Wang, L., Wang, M.-X., Wang, S.-G., Wang, S.-Q., Wang, X., Wang, Y.-N., Wang, Y., Wang, Y.-F., Wang, Y.-F., Wei, P., Wei, M.-Z., Wu, H., Wu, K.-F., Wu, X.-B., Wu, Y.-Z., Xing, X.-Z., Xu, L.-Z., Xu, X.-Q., Xu, Y., Yan, T.-S., Yang, D.-H., Yang, H.-F., Yang, H.-Q., Yang, M., Yao, Z.-Q., Yu, Y., Yuan, H., Yuan, H.-B., Yuan, H.-L., Yuan, W.-M., Zhai, C., Zhang, E.-P., Zhang, H.-W., Zhang, J.-N., Zhang, L.-P., Zhang, W., Zhang, Y., Zhang, Y.-X., Zhang, Z.-C., Zhao, M., Zhou, F., Zhou, X., Zhu, J., Zhu, Y.-T., Zou, S.-C., and Zuo, F. (2015). The first data release (DR1) of the LAMOST regular survey. *Research in Astronomy and Astrophysics*, 15:1095.

Luque, E., Pieres, A., Santiago, B., Yanny, B., Vivas, A. K., Queiroz, A., Drlica-Wagner, A., Morganson, E., Balbinot, E., Marshall, J. L., Li, T. S., Neto, A. F., da Costa, L. N., Maia, M. A. G., Bechtol, K., Kim, A. G., Bernstein, G. M., Dodelson, S., Whiteway, L., Diehl, H. T., Finley, D. A., Abbott, T., Abdalla, F. B., Allam, S., Annis, J., Benoit-Lévy, A., Bertin, E., Brooks, D., Burke, D. L., Rosell, A. C., Kind, M. C., Carretero, J., Cunha, C. E., D'Andrea, C. B., Desai, S., Doel, P., Evrard, A. E., Flaugher, B., Fosalba, P., Gerdes, D. W., Goldstein, D. A., Gruen, D., Gruendl, R. A., Gutierrez, G., James, D. J., Kuehn, K., Kuropatkin, N., Lahav, O., Martini, P., Miquel, R., Nord, B., Ogando, R., Plazas, A. A., Romer, A. K., Sanchez, E., Scarpine, V., Schubnell, M., Sevilla-Noarbe, I., Smith, R. C., Soares-Santos, M., Sobreira, F., Suchyta, E., Swanson, M. E. C., Tarle, G., Thomas, D., and Walker, A. R. (2017). The Dark Energy Survey view of the Sagittarius stream: discovery of two faint stellar system candidates. *Monthly Notices of the Royal Astronomical Society*, 468:97–108.

Lux, H., Read, J., Lake, G., and Johnston, K. (2012). Ngc 5466: a unique probe of the galactic halo shape. *Monthly Notices of the Royal Astronomical Society*, 424:L16–L20.

Lynden-Bell, D. (1982). The fornax-leo-sculptor system. *The Observatory*, 102:202–208.

Ma, X., Hopkins, P. F., Faucher-Giguère, C.-A., Zolman, N., Muratov, A. L., Kereš, D., and Quataert, E. (2016). The origin and evolution of the galaxy mass-metallicity relation. *Monthly Notices of the Royal Astronomical Society*, 456:2140–2156.

Mackereth, J. T., Schiavon, R. P., Pfeffer, J., Hayes, C. R., Bovy, J., Anguiano, B., Allende Prieto, C., Hasselquist, S., Holtzman, J., Johnson, J. A., Majewski, S. R., O'Connell, R., Shetrone, M., Tissera, P. B., and Fernández-Trincado, J. G. (2019). The origin of accreted stellar halo populations in the Milky Way using APOGEE, Gaia, and the EAGLE simulations. *Monthly Notices of the Royal Astronomical Society*, 482:3426–3442.

Mackey, A. D. and Gilmore, G. F. (2004). Comparing the properties of local globular cluster systems: implications for the formation of the Galactic halo. *Monthly Notices of the Royal Astronomical Society*, 355:504–534.

Mackey, A. D., Huxor, A. P., Ferguson, A. M. N., Irwin, M. J., Tanvir, N. R., McConnachie, A. W., Ibata, R. A., Chapman, S. C., and Lewis, G. F. (2010). Evidence for an Accretion Origin for the Outer Halo Globular Cluster System of M31. *The Astrophysical Journal*, 717:L11–L16.

Mackey, A. D. and van den Bergh, S. (2005). The properties of Galactic globular cluster subsystems. *Monthly Notices of the Royal Astronomical Society*, 360:631–645.

Majewski, S. R. (1992). A Complete, Multicolor Survey of Absolute Proper Motions to B approximately 22.5: Galactic Structure and Kinematics at the North Galactic Pole. *The Astrophysical Journal Supplement Series*, 78:87.

Majewski, S. R. (2000). The galactic halo: From globular cluster to field stars. In Noels, A., Magain, P., Caro, D., and Jehin, E., editors, *Preceedings of 35th Liege International Astrophysics Colloquium*, page 619.

Majewski, S. R., Nidever, D. L., Smith, V. V., Damke, G. J., Kunkel, W. E., Patterson, R. J., Bizyaev, D., and García Pérez, A. E. (2012). Exploring Halo Substructure with Giant Stars: Substructure in the Local Halo as Seen in the Grid Giant Star Survey Including Extended Tidal Debris from ωCentauri. *The Astrophysical Journal*, 747:L37.

Majewski, S. R., Skrutskie, M. F., Weinberg, M. D., and Ostheimer, J. C. (2003). A Two Micron All Sky Survey View of the Sagittarius Dwarf Galaxy. I. Morphology of the Sagittarius Core and Tidal Arms. *The Astrophysical Journal*, 599:1082–1115.

Malhan, K., Ibata, R. A., Carlberg, R. G., Valluri, M., and Freese, K. (2019). Butterfly in a Cocoon, Understanding the origin and morphology of Globular Cluster Streams: The case of GD-1. *arXiv e-prints*, page arXiv:1903.08141.

Marcolini, A., Sollima, A., D'Ercole, A., Gibson, B. K., and Ferraro, F. R. (2007). Modelling the chemical evolution of ω Centauri using three-dimensional hydrodynamical simulations. *Monthly Notices of the Royal Astronomical Society*, 382:443–454.

Marino, A. F., Milone, A. P., Piotto, G., Cassisi, S., D'Antona, F., Anderson, J., Aparicio, A., Bedin, L. R., Renzini, A., and Villanova, S. (2012). The C+N+O Abundance of ω Centauri Giant Stars: Implications for the Chemical-enrichment Scenario and the Relative Ages of Different Stellar Populations. *The Astrophysical Journal*, 746:14.

Martin, N. F., Ibata, R. A., Rich, R. M., Collins, M. L. M., Fardal, M. A., Irwin, M. J., Lewis, G. F., McConnachie, A. W., Babul, A., Bate, N. F., Chapman, S. C., Conn, A. R., Crnojević, D., Ferguson, A. M. N., Mackey, A. D., Navarro, J. F., Peñarrubia, J., Tanvir, N. T., and Valls-Gabaud, D. (2014). The PAndAS Field of Streams: Stellar Structures in the Milky Way Halo toward Andromeda and Triangulum. *The Astrophysical Journal*, 787:19.

Martínez Delgado, D., Dinescu, D. I., Zinn, R., Tutsoff, A., Côté, P., and Boyarchuck, A. (2004). Mapping Tidal Streams around Galactic Globular Clusters. In Prada, F., Martinez Delgado, D., and Mahoney, T. J., editors, *Satellites and Tidal Streams*, volume 327, page 255.

Mateo, M., Olszewski, E., and Morrison, H. (1998). Tracing the outer structure of the sagittarius dwarf galaxy:detections at angular distances between 10^o and 34^o. *The Astrophysical Journal*, 508:L55–L59.

Matsuno, T., Aoki, W., and Suda, T. (2019). Origin of the Excess of High-energy Retrograde Stars in the Galactic Halo. *The Astrophysical Journal*, 874(2):L35.

Mayet, F., Green, A. M., Battat, J. B. R., Billard, J., Bozorgnia, N., Gelmini, G. B., Gondolo, P., Kavanagh, B. J., Lee, S. K., Loomba, D., Monroe, J., Morgan, B., O'Hare, C. A. J., Peter, A. H. G., Phan, N. S., and Vahsen, S. E. (2016). A review of the discovery reach of directional Dark Matter detection. *Physics Reports*, 627:1–49.

McConnachie, A. W. (2012). The Observed Properties of Dwarf Galaxies in and around the Local Group. *The Astronomical Journal*, 144:4.

McMillan, P. J. (2017). The mass distribution and gravitational potential of the Milky Way. *Monthly Notices of the Royal Astronomical Society*, 465:76–94.

Meylan, G., Mayor, M., Duquennoy, A., and Dubath, P. (1995). Central velocity dispersion in the globular cluster ω Centauri. *Astronomy and Astrophysics*, 303:761.

Meza, A., Navarro, J. F., Abadi, M. G., and Steinmetz, M. (2005). Accretion relics in the solar neighbourhood: debris from ωCen's parent galaxy. *Monthly Notices of the Royal Astronomical Society*, 359:93–103.

Millar, A. J., Raffelt, G. G., Redondo, J., and Steffen, F. D. (2017). Dielectric haloscopes to search for axion dark matter: theoretical foundations. *Journal of Cosmology and Astro-Particle Physics*, 2017:061.

Milone, A. P., Marino, A. F., Bedin, L. R., Anderson, J., Apai, D., Bellini, A., Bergeron, P., Burgasser, A. J., Dotter, A., and Rees, J. M. (2017). The HST large programme on ω Centauri - I. Multiple stellar populations at the bottom of the main sequence probed in NIR-Optical. *Monthly Notices of the Royal Astronomical Society*, 469:800–812.

Mizutani, A., Chiba, M., and Sakamoto, T. (2003). Kinematics of Tidal Debris from ω Centauri's Progenitor Galaxy. *The Astrophysical Journal*, 589:L89–L92.

Morgan, B., Green, A. M., and Spooner, N. J. (2005). Directional statistics for realistic weakly interacting massive particle direct detection experiments. *Physical Review D*, 71:103507.

Morrison, H. L., Helmi, A., Sun, J., Liu, P., Gu, R., Norris, J. E., Harding, P., Kinman, T. D., Kepley, A. A., Freeman, K. C., Williams, M., and Van Duyne, J. (2009). Fashionably Late? Building Up The Milky Way'S Inner Halo. *The Astrophysical Journal*, 694:130–143.

Myeong, G. C., Evans, N. W., Belokurov, V., Amorisco, N. C., and Koposov, S. E. (2018a). Halo substructure in the SDSS-Gaia catalogue: streams and clumps. *Monthly Notices of the Royal Astronomical Society*, 475:1537–1548.

Myeong, G. C., Evans, N. W., Belokurov, V., Koposov, S. E., and Sanders, J. L. (2017a). A halo substructure in Gaia Data Release 1. *Monthly Notices of the Royal Astronomical Society*, 469:L78–L82.

Myeong, G. C., Evans, N. W., Belokurov, V., Sanders, J. L., and Koposov, S. E. (2018b). Discovery of new retrograde substructures: the shards of ω Centauri? *Monthly Notices of the Royal Astronomical Society*, 478:5449–5459.

Myeong, G. C., Evans, N. W., Belokurov, V., Sanders, J. L., and Koposov, S. E. (2018c). The Milky Way Halo in Action Space. *The Astrophysical Journal*, 856:L26.

Myeong, G. C., Evans, N. W., Belokurov, V., Sanders, J. L., and Koposov, S. E. (2018d). The Sausage Globular Clusters. *The Astrophysical Journall*, 863:L28.

Myeong, G. C., Jerjen, H., Mackey, D., and Da Costa, G. S. (2017b). Tidal Tails around the Outer Halo Globular Clusters Eridanus and Palomar 15. *The Astrophysical Journall*, 840:L25.

Myeong, G. C., Vasiliev, E., Iorio, G., Evans, N. W., and Belokurov, V. (2019). Evidence for Two Early Accretion Events That Built the Milky Way Stellar Halo. *arXiv e-prints*, page arXiv:1904.03185.

Navarrete, C., Chanamé, J., Ramírez, I., Meza, A., Anglada-Escudé, G., and Shkolnik, E. (2015). The Kapteyn Moving Group Is Not Tidal Debris From ω Centauri. *The Astrophysical Journal*, 808:103.

Navarro, J. F., Frenk, C. S., and White, S. D. M. (1997). A Universal Density Profile from Hierarchical Clustering. *The Astrophysical Journal*, 490:493–508.

Newberg, H. and Carlin, J. (2016). *Tidal Streams in the Local Group and Beyond*. Astrophysics and Space Science Library, Springer International Publishing, Switzerland.

Newberg, H. J. and Carlin, J. L., editors (2016). *Tidal Streams in the Local Group and Beyond*, volume 420 of *Astrophysics and Space Science Library*.

Newberg, H. J., Willett, B. A., Yanny, B., and Xu, Y. (2010). The Orbit of the Orphan Stream. *The Astrophysical Journal*, 711:32–49.

Newberg, H. J., Yanny, B., Grebel, E. K., Hennessy, G., Ivezić, Ž., Martinez- Delgado, D., Odenkirchen, M., Rix, H.-W., Brinkmann, J., Lamb, D. Q., Schneider, D. P., and York, D. G. (2003). Sagittarius Tidal Debris 90 Kiloparsecs from the Galactic Center. *The Astrophysical Journal*, 596:L191–L194.

Newville, M., Stensitzki, T., Allen, D. B., and Ingargiola, A. (2014). LMFIT: Non-Linear Least-Square Minimization and Curve-Fitting for Python¶.

Ngan, W. H. W. and Carlberg, R. G. (2014). Using Gaps in N-body Tidal Streams to Probe Missing Satellites. *The Astrophysical Journal*, 788:181.

Nichols, M., Colless, J., Colless, M., and Bland-Hawthorn, J. (2011). Accretion of the Magellanic System onto the Galaxy. *The Astrophysical Journal*, 742:110.

Norris, J. E. and Da Costa, G. S. (1995). The Giant Branch of omega Centauri. IV. Abundance Patterns Based on Echelle Spectra of 40 Red Giants. *The Astrophysical Journal*, 447:680.

Norris, J. E., Freeman, K. C., and Mighell, K. J. (1996). The Giant Branch of omega Centauri. V. The Calcium Abundance Distribution. *The Astrophysical Journal*, 462:241.

Norris, J. E. and Ryan, S. G. (1989). Population Studies: Evidence for Accretion of the Galactic Halo. *The Astrophysical Journal*, 336:L17.

Odenkirchen, M., Grebel, E. K., Dehnen, W., Rix, H.-W., Yanny, B., Newberg, H. J., Rockosi, C. M., Martínez-Delgado, D., Brinkmann, J., and Pier, J. R. (2003). The Extended Tails of Palomar 5: A 10° Arc of Globular Cluster Tidal Debris. *The Astronomical Journal*, 126:2385–2407.

Odenkirchen, M., Grebel, E. K., Rockosi, C. M., Dehnen, W., Ibata, R., Rix, H.-W., Stolte, A., Wolf, C., Anderson, John E., J., Bahcall, N. A., Brinkmann, J., Csabai, I., Hennessy, G., Hindsley, R. B., Ivezić, Ž., Lupton, R. H., Munn, J. A., Pier, J. R., Stoughton, C., and York, D. G. (2001). Detection of Massive Tidal Tails around the Globular Cluster Palomar 5 with Sloan Digital Sky Survey Commissioning Data. *The Astrophysical Journal*, 548:L165–L169.

O'Hare, C. A. J. and Green, A. M. (2014). Directional detection of dark matter streams. *Physical Review D*, 90:123511.

O'Hare, C. A. J. and Green, A. M. (2017). Axion astronomy with microwave cavity experiments. *Physical Review D*, 95:063017.

O'Hare, C. A. J., McCabe, C., Evans, N. W., Myeong, G., and Belokurov, V. (2018). A Dark Matter Hurricane: Measuring the S1 Stream with Dark Matter Detectors. *ArXiv e-prints*, page arXiv:1807.09004.

Olszewski, E. W., Saha, A., Knezek, P., Subramaniam, A., de Boer, T., and Seitzer, P. (2009). A 500 Parsec Halo Surrounding the Galactic Globular NGC 1851. *The Astronomical Journal*, 138:1570–1576.

Peñarrubia, J., Martínez-Delgado, D., Rix, H. W., Gómez-Flechoso, M. A., Munn, J., Newberg, H., Bell, E. F., Yanny, B., Zucker, D., and Grebel, E. K. (2005). A Comprehensive Model for the Monoceros Tidal Stream. *The Astrophysical Journal*, 626:128–144.

Peñarrubia, J., Walker, M., and Gilmore, G. (2009). Tidal disruption of globular clusters in dwarf galaxies with triaxial dark matter haloes. *Monthly Notices of the Royal Astronomical Society*, 399:1275–1292.

Pearson, S., Küpper, A., Johnston, K., and Price-Whelan, A. (2015). Tidal stream morphology as an indicator of dark matter halo geometry: The case of palomar 5. *The Astrophysical Journal*, 799:28.

Pedregosa, F., Varoquaux, G., Gramfort, A., Michel, V., Thirion, B., Grisel, O., Blondel, M., Prettenhofer, P., Weiss, R., Dubourg, V., Vanderplas, J., Passos, A., Cournapeau, D., Brucher, M., Perrot, M., and Duchesnay, E. (2011). Scikit-learn: Machine learning in Python. *Journal of Machine Learning Research*, 12:2825–2830.

Pop, A.-R., Pillepich, A., Amorisco, N., and Hernquist, L. (2017). Galaxies with Shells in the Illustris Simulation: Metallicity Signatures. *Galaxies*, 5:34.

Posti, L., Binney, J., Nipoti, C., and Ciotti, L. (2015). Action-based distribution functions for spheroidal galaxy components. *Monthly Notices of the Royal Astronomical Society*, 447:3060–3068.

Posti, L. and Helmi, A. (2018). Mass and shape of the Milky Way's dark matter halo with globular clusters from Gaia and Hubble. *ArXiv e-prints*, page arXiv:1805.01408.

Preston, G., Shectman, S., and Beers, T. (1991). Detection of a galactic color gradient for blue horizontal-branch stars of the halo field and implications for the halo age and density distributions. *The Astrophysical Journal*, 375:121–147.

Price-Whelan, A. M. and Bonaca, A. (2018). Off the Beaten Path: Gaia Reveals GD-1 Stars outside of the Main Stream. *The Astrophysical Journal*, 863(2):L20.

Purcell, C. W., Bullock, J. S., Tollerud, E. J., Rocha, M., and Chakrabarti, S. (2011). The Sagittarius impact as an architect of spirality and outer rings in the Milky Way. *Nature*, 477:301–303.

Purcell, C. W., Zentner, A. R., and Wang, M.-Y. (2012). Dark matter direct search rates in simulations of the Milky Way and Sagittarius stream. *Journal of Cosmology and Astro-Particle Physics*, 2012:027.

Quinn, P. J. and Goodman, J. (1986). Sinking Satellites of Spiral Systems. *The Astrophysical Journal*, 309:472.

Quinn, P. J., Hernquist, L., and Fullagar, D. P. (1993). Heating of Galactic Disks by Mergers. *The Astrophysical Journal*, 403:74.

Renaud, F. (2018). Star clusters in evolving galaxies. *New Astronomy Reviews*, 81:1–38.

Robin, A. C., Luri, X., Reylé, C., Isasi, Y., Grux, E., Blanco-Cuaresma, S., Arenou, F., Babusiaux, C., Belcheva, M., Drimmel, R., Jordi, C., Krone-Martins, A., Masana, E., Mauduit, J. C., Mignard, F., Mowlavi, N., Rocca- Volmerange, B., Sartoretti, P., Slezak, E., and Sozzetti, A. (2012). Gaia Universe model snapshot. A statistical analysis of the expected contents of the Gaia catalogue. *Astronomy and Astrophysics*, 543:A100.

Rocha-Pinto, H. J., Majewski, S. R., Skrutskie, M. F., Crane, J. D., and Patterson, R. J. (2004). Exploring Halo Substructure with Giant Stars: A Diffuse Star Cloud or Tidal Debris around the Milky Way in Triangulum-Andromeda. *The Astrophysical Journal*, 615:732–737.

Rockosi, C. M., Odenkirchen, M., Grebel, E. K., Dehnen, W., Cudworth, K. M., Gunn, J. E., York, D. G., Brinkmann, J., Hennessy, G. S., and Ivezić, Ž. (2002). A Matched-Filter Analysis of the Tidal Tails of the Globular Cluster Palomar 5. *The Astronomical Journal*, 124:349–363.

Roederer, I. U. (2017). The Origin of the Heaviest Metals in Most Ultra-faint Dwarf Galaxies. *The Astrophysical Journal*, 835:23.

Romano, D., Matteucci, F., Tosi, M., Pancino, E., Bellazzini, M., Ferraro, F. R., Limongi, M., and Sollima, A. (2007). The chemical evolution of Omega Centauri's progenitor system. *Monthly Notices of the Royal Astronomical Society*, 376:405–415.

Sanders, J. and Binney, J. (2013). Stream-orbit misalignment - i. the dangers of orbit-fitting. *Monthly Notices of the Royal Astronomical Society*, 433:1813–1825.

Sanders, J. and Binney, J. (2014). Actions, angles and frequencies for numerically integrated orbits. *Monthly Notices of the Royal Astronomical Society*, 441:3284–3295.

Sanders, J. L. and Binney, J. (2016). A review of action estimation methods for galactic dynamics. *Monthly Notices of the Royal Astronomical Society*, 457:2107–2121.

Sanderson, R. E., Helmi, A., and Hogg, D. W. (2015). Action-space Clustering of Tidal Streams to Infer the Galactic Potential. *The Astrophysical Journal*, 801:98.

Savage, C., Freese, K., and Gondolo, P. (2006). Annual modulation of dark matter in the presence of streams. *Physical Review D*, 74:043531.

Sbordone, L., Bonifacio, P., Marconi, G., Buonanno, R., and Zaggia, S. (2005). Family ties: Abundances in terzan 7, a sgr dsph globular cluster. *Astronomy and Astrophysics*, 437:905–910.

Schaerer, D. and Charbonnel, C. (2011). A new perspective on globular clusters, their initial mass function and their contribution to the stellar halo and the cosmic reionization. *Monthly Notices of the Royal Astronomical Society*, 413:2297–2304.

Schaye, J., Crain, R. A., Bower, R. G., Furlong, M., Schaller, M., Theuns, T., Dalla Vecchia, C., Frenk, C. S., McCarthy, I. G., Helly, J. C., Jenkins, A., Rosas-Guevara, Y. M., White, S. D. M., Baes, M., Booth, C. M., Camps, P., Navarro, J. F., Qu, Y., Rahmati, A., Sawala, T., Thomas, P. A., and Trayford, J. (2015). The EAGLE project: simulating the evolution and assembly of galaxies and their environments. *Monthly Notices of the Royal Astronomical Society*, 446:521–554.

Schlafly, E. F. and Finkbeiner, D. P. (2011). Measuring Reddening with Sloan Digital Sky Survey Stellar Spectra and Recalibrating SFD. *The Astrophysical Journal*, 737:103.

Schlafly, E. F., Green, G. M., Lang, D., Daylan, T., Finkbeiner, D. P., Lee, A., Meisner, A. M., Schlegel, D., and Valdes, F. (2018). The DECam Plane Survey: Optical Photometry of Two Billion Objects in the Southern Galactic Plane. *The Astrophysical Journal Supplement Series*, 234(2):39.

Schlegel, D. J., Finkbeiner, D. P., and Davis, M. (1998). Maps of Dust Infrared Emission for Use in Estimation of Reddening and Cosmic Microwave Background Radiation Foregrounds. *The Astrophysical Journal*, 500:525–553.

Schönrich, R., Binney, J., and Asplund, M. (2012). The detection and treatment of distance errors in kinematic analyses of stars. *Monthly Notices of the Royal Astronomical Society*, 420:1281–1293.

Schönrich, R., Binney, J., and Dehnen, W. (2010). Local kinematics and the local standard of rest. *Monthly Notices of the Royal Astronomical Society*, 403:1829–1833.

Searle, L. and Zinn, R. (1978). Composition of halo clusters and the formation of the galactic halo. *The Astrophysical Journal*, 225:357–379.

Sellwood, J. A. (2010). A recent Lindblad resonance in the solar neighbourhood. *Monthly Notices of the Royal Astronomical Society*, 409:145–155.

Shetrone, M. D., Côté, P., and Sargent, W. L. W. (2001). Abundance Patterns in the Draco, Sextans, and Ursa Minor Dwarf Spheroidal Galaxies. *The Astrophysical Journal*, 548:592–608.

Simion, I. T., Belokurov, V., and Koposov, S. E. (2019). Common origin for Hercules-Aquila and Virgo Clouds in Gaia DR2. *Monthly Notices of the Royal Astronomical Society*, 482(1):921–928.

Simpson, J. D. (2019). The very retrograde orbit of the globular cluster FSR1758 revealed with Gaia DR2. *arXiv e-prints*, page arXiv:1902.00447.

Slater, C. T., Bell, E. F., Schlafly, E. F., Morganson, E., Martin, N. F., Rix, H.-W., Peñarrubia, J., Bernard, E. J., Ferguson, A. M. N., Martinez-Delgado, D., Wyse, R. F. G., Burgett, W. S., Chambers, K. C., Draper, P. W., Hodapp, K. W., Kaiser, N., Magnier, E. A., Metcalfe, N., Price, P. A., Tonry, J. L., Wainscoat, R. J., and Waters, C. (2014). The Complex Structure

of Stars in the Outer Galactic Disk as Revealed by Pan-STARRS1. *The Astrophysical Journal*, 791:9.

Smith, M. C. (2016). Kinematically Detected Halo Streams. In Newberg, H. J. and Carlin, J. L., editors, *Tidal Streams in the Local Group and Beyond*, volume 420, page 113.

Smith, M. C., Evans, N. W., Belokurov, V., Hewett, P. C., Bramich, D. M., Gilmore, G., Irwin, M. J., Vidrih, S., and Zucker, D. B. (2009). Kinematics of SDSS subdwarfs: structure and substructure of the Milky Way halo. *Monthly Notices of the Royal Astronomical Society*, 399:1223–1237.

Sohn, S. T., Watkins, L. L., Fardal, M. A., van der Marel, R. P., Deason, A. J., Besla, G., and Bellini, A. (2018). Absolute Hubble Space Telescope Proper Motion (HSTPROMO) of Distant Milky Way Globular Clusters: Galactocentric Space Velocities and the Milky Way Mass. *The Astrophysical Journal*, 862:52.

Sollima, A., Martínez-Delgado, D., Valls-Gabaud, D., and Peñarrubia, J. (2011). Discovery of Tidal Tails Around the Distant Globular Cluster Palomar 14. *The Astrophysical Journal*, 726:47.

Sridhar, S. and Touma, J. (1996). Adiabatic evolution and capture into resonance: vertical heating of a growing stellar disc. *Monthly Notices of the Royal Astronomical Society*, 279:1263.

Stetson, P. B., Bolte, M., Harris, W. E., Hesser, J. E., van den Bergh, S., Vandenberg, D. A., Bell, R. A., Johnson, J. A., Bond, H. E., Fullton, L. K., Fahlman, G. G., and Richer, H. B. (1999). Ages for Globular Clusters in the Outer Galactic Halo: The Second- Parameter Clusters Palomar 3, Palomar 4, and Eridanus. *The Astronomical Journal*, 117:247–263.

Suntzeff, N. B. and Kraft, R. P. (1996). The Abundance Spread Among Giants and Subgiants in the Globular Cluster Omega Centauri. *The Astronomical Journal*, 111:1913.

The MADMAX Working Group, Caldwell, A., Dvali, G., Majorovits, B., Millar, A., Raffelt, G., Redondo, J., Reimann, O., Simon, F., and Steffen, F. (2016). Dielectric Haloscopes: A New Way to Detect Axion Dark Matter. *ArXiv e-prints*, page arXiv:1611.05865.

Tolstoy, E., Hill, V., and Tosi, M. (2009). Star-Formation Histories, Abundances, and Kinematics of Dwarf Galaxies in the Local Group. *Annual Review of Astronomy and Astrophysics*, 47(1):371–425.

Tremaine, S. (1999). The geometry of phase mixing. *Monthly Notices of the Royal Astronomical Society*, 307:877–883.

Tsuchiya, T., Dinescu, D. I., and Korchagin, V. I. (2003). A Capture Scenario for the Globular Cluster ω Centauri. *The Astrophysical Journal*, 589:L29–L32.

Tsuchiya, T., Korchagin, V. I., and Dinescu, D. I. (2004). Disruption of a dwarf galaxy under strong shocking: the origin of ω Centauri. *Monthly Notices of the Royal Astronomical Society*, 350:1141–1151.

Valcarce, A. A. R. and Catelan, M. (2011). Formation of multiple populations in globular clusters: another possible scenario. *Astronomy and Astrophysics*, 533:A120.

Valdes, F., Gruendl, R., and DES Project (2014). The DECam Community Pipeline. In Manset, N. and Forshay, P., editors, *Astronomical Data Analysis Software and Systems XXIII*, volume 485, page 379.

van den Bergh, S. (2000). Updated Information on the Local Group. *The Publications of the Astronomical Society of the Pacific*, 112:529–536.

van den Bosch, F. C., Lewis, G. F., Lake, G., and Stadel, J. (1999). Substructure in Dark Halos: Orbital Eccentricities and Dynamical Friction. *The Astrophysical Journal*, 515:50–68.

Vasiliev, E. (2018). Systematic errors in Gaia DR2 astrometry and their impact on measurements of internal kinematics of star clusters. *arXiv e-prints*, page arXiv:1811.05345.

Vasiliev, E. (2019a). AGAMA: action-based galaxy modelling architecture. *Monthly Notices of the Royal Astronomical Society*, 482(2):1525–1544.

Vasiliev, E. (2019b). Proper motions and dynamics of the Milky Way globular cluster system from Gaia DR2. *Monthly Notices of the Royal Astronomical Society*, 484(2):2832–2850.

Veljanoski, J. and Helmi, A. (2018). Flavours in the box of chocolates: chemical abundances of kinematic substructures in the nearby stellar halo. *ArXiv e-prints*, page arXiv:1804.06365.

Villanova, S., Geisler, D., Gratton, R. G., and Cassisi, S. (2014). The Metallicity Spread and the Age-Metallicity Relation of ω Centauri. *The Astrophysical Journal*, 791:107.

Villanova, S., Piotto, G., King, I. R., Anderson, J., Bedin, L. R., Gratton, R. G., Cassisi, S., Momany, Y., Bellini, A., Cool, A. M., Recio- Blanco, A., and Renzini, A. (2007). The Multiplicity of the Subgiant Branch of ω Centauri: Evidence for Prolonged Star Formation. *The Astrophysical Journal*, 663:296–314.

Vincenzo, F., Spitoni, E., Calura, F., Matteucci, F., Silva Aguirre, V., Miglio, A., and Cescutti, G. (2019). The Fall of a Giant. Chemical evolution of Enceladus, alias the Gaia Sausage. *Monthly Notices of the Royal Astronomical Society*, page L74.

Watkins, L. L., Evans, N. W., Belokurov, V., Smith, M. C., Hewett, P. C., Bramich, D. M., Gilmore, G. F., Irwin, M. J., Vidrih, S., Wyrzykowski, Ł., and Zucker, D. B. (2009). Substructure revealed by RRLyraes in SDSS Stripe 82. *Monthly Notices of the Royal Astronomical Society*, 398:1757–1770.

Webb, J. J. and Bovy, J. (2019). Searching for the GD-1 stream progenitor in Gaia DR2 with direct N-body simulations. *Monthly Notices of the Royal Astronomical Society*, 485(4):5929–5938.

Weinberg, M. D. (1989). Self-gravitating response of a spherical galaxy to sinking satellites. *Monthly Notices of the Royal Astronomical Society*, 239:549–569.

Williams, A. A., Belokurov, V., Casey, A. R., and Evans, N. W. (2017). On the run: mapping the escape speed across the Galaxy with SDSS. *Monthly Notices of the Royal Astronomical Society*, 468:2359–2371.

Williams, A. A. and Evans, N. W. (2015). Made-to-measure dark matter haloes, elliptical galaxies and dwarf galaxies in action coordinates. *Monthly Notices of the Royal Astronomical Society*, 448:1360–1371.

Wylie-de Boer, E., Freeman, K., and Williams, M. (2010). Evidence of Tidal Debris from ω Cen in the Kapteyn Group. *The Astronomical Journal*, 139:636–645.

Yanny, B., Newberg, H. J., Grebel, E. K., Kent, S., Odenkirchen, M., Rockosi, C. M., Schlegel, D., Subbarao, M., Brinkmann, J., Fukugita, M., Ivezic, Ž., Lamb, D. Q., Schneider, D. P., and York, D. G. (2003). A Low-Latitude Halo Stream around the Milky Way. *The Astrophysical Journal*, 588:824–841.

Yanny, B., Newberg, H. J., Kent, S., Laurent- Muehleisen, S. A., Pier, J. R., Richards, G. T., Stoughton, C., Anderson, John E., J., Annis, J., Brinkmann, J., Chen, B., Csabai, I., Doi, M., Fukugita, M., Hennessy, G. S., Ivezić, Ž., Knapp, G. R., Lupton, R., Munn, J. A., Nash, T., Rockosi, C. M., Schneider, D. P., Smith, J. A., and York, D. G. (2000). Identification of A-colored Stars and Structure in the Halo of the Milky Way from Sloan Digital Sky Survey Commissioning Data. *The Astrophysical Journal*, 540:825–841.

Yoon, J., Johnston, K., and Hogg, D. (2011). Clumpy streams from clumpy halos: Detecting missing satellites with cold stellar structures. *The Astrophysical Journal*, 731:58–72.

Zinn, R. (1993). The Galactic Halo Cluster Systems: Evidence for Accretion. In Smith, G. H. and Brodie, J. P., editors, *The Globular Cluster-Galaxy Connection*, volume 48, page 38.

Appendix A

Tidal tails around the outer halo globular clusters Eridanus and Palomar 15

G. C. Myeong[1,2], H. Jerjen[2], D. Mackey[2], and G. S. Da Costa[2]

[1]Institute of Astronomy, University of Cambridge, Madingley Road, Cambridge CB3 0HA, United Kingdom

[2]Research School of Astronomy and Astrophysics, The Australian National University, Canberra, ACT 2611, Australia

Abstract

We report the discovery of tidal tails around the two outer halo globular clusters, Eridanus and Palomar 15, based on *gi*-band images obtained with DECam at the CTIO 4-m Blanco Telescope. The tidal tails are among the most remote stellar streams presently known in the Milky Way halo. Cluster members have been determined from the color-magnitude diagrams and used to establish the radial density profiles, which show, in both cases, a strong departure in the outer regions from the best-fit King profile. Spatial density maps reveal tidal tails stretching out on opposite sides of both clusters, extending over a length of $\sim$760 pc for Eridanus and $\sim$1160 pc for Palomar 15. The great circle projected from the Palomar 15 tidal tails encompasses the Galactic Center, while that for Eridanus passes close to four dwarf satellite galaxies, one of which (Sculptor) is at a comparable distance to that of Eridanus.

[0]Remark: The original project was conceived during my undergraduate study and the early part of the work presented in this Chapter was carried out before I started the current degree. The work presented in this Chapter has been published in Myeong et al. (2017b). I was responsible for the data processing and analysis. Helmut Jerjen and A. Dougal Mackey, made an invaluable contribution by checking the results and improving the first draft into a more logical presentation. Gary S. Da Costa also provided priceless consultation.

A.1 Introduction

It is widely accepted that large galaxies such as the Milky Way formed through accretion and merger of numerous protogalactic fragments (e.g. Blumenthal et al., 1984; Searle and Zinn, 1978). A significant fraction of the Milky Way's globular cluster population is thought to have been acquired by this process, and it is believed that a large portion of the current halo stellar mass may have been donated by their host dwarf galaxies via tidal disruption and mass loss (Forbes and Bridges, 2010; Mackey and Gilmore, 2004).

There are two types of stellar structures that we expect to see around Galactic globular clusters. One can occur around accreted clusters and represents the remnant of the disrupted parent dwarf galaxy (see Olszewski et al. (2009) and Kuzma et al. (2016)). In extreme cases we might see a cluster embedded in an extended stellar stream. This is the case in the halo of M31 (e.g. Mackey et al., 2010) and in our own Galaxy where a number of globular clusters are associated with the disrupting Sagittarius dwarf galaxy (e.g. Law and Majewski, 2010).

The second type consists of narrow stellar streams arising from the dynamical evolution of the cluster itself in the external tidal field of the Milky Way. Many studies have investigated the presence of tidal tails associated with globular clusters (e.g., Grillmair et al., 1995; Leon et al., 2000). It has been found that some globular clusters have stellar distributions that significantly differ from a King profile (King, 1962), extending beyond the nominal tidal radius (Carballo-Bello et al., 2012; Grillmair et al., 1995).

Recently, it has been discovered that the tidal tails of some globular clusters, such as Palomar 5 (Grillmair and Dionatos, 2006a; Odenkirchen et al., 2001) and NGC 5466 (Belokurov et al., 2006a; Grillmair and Johnson, 2006), extend over several hundred parsecs in physical length. In this context it is also interesting to note that many narrow streams, like the Orphan (Belokurov et al., 2006b; Grillmair et al., 2015; Grillmair, 2006) and Phoenix streams (Balbinot et al., 2016) exist in the inner Milky Way halo. These likely originate from completely disrupted globular clusters (Martin et al., 2014; Newberg et al., 2010).

The main point is that the Galactic tidal field, disk and bulge shocks, and two-body relaxation can all affect the outer structures of globular clusters in ways that we do not fully understand. Adding new examples of globular clusters with tidal tails, particularly at large Galactocentric distances, thus gives us additional information about the frequency of this phenomenon and can help to probe the outermost parts of the Galaxy. The properties of such streams can further help to constrain the dark matter distribution in the Galactic halo. For example, the gaps in the tidal tails of Palomar 5 may tell us about the dark matter sub-halos predicted in ΛCDM cosmology (Ngan and Carlberg, 2014).

So far, most studies searching for tidal structures around Milky Way globular clusters have been restricted to relatively nearby targets (e.g., Grillmair and Carlin, 2016) with the

one exception of Palomar 14 (Sollima et al., 2011). In this Chapter we report the discovery of stellar substructures around two distant halo globular clusters, Eridanus ($R_{GC} = 95.0$ kpc) and Palomar 15 (Pal 15; $R_{GC} = 38.4$ kpc).

A.2 Data Analysis

We used the Dark Energy Camera (DECam) at the CTIO 4-m Blanco Telescope to obtain deep imaging around Eridanus and Pal 15. This instrument comprises a 62 CCD mosaic that spans a 3 sqr deg field-of-view and has a pixel scale of 0.27" (Flaugher et al., 2015). For Eridanus, we obtained five dithered 900s g-band images and 11 dithered 600s i-band images on Feb 25-27, 2014 (average seeing $\sim 1.11''$). For Pal 15, we obtained five dithered 360s g-band images and five dithered 360s i-band images on Sept 24-26, 2013 (average seeing $\sim 1.12''$). The nights were part of the observing programs 2014A-0621 for Eridanus and 2013B-0617 for Pal 15 – PI: D. Mackey. The raw images were preprocessed with the DECam Community Pipeline (Valdes et al., 2014), including application of the astrometric solution. We used the resampled images (individual frames) and their corresponding weight maps for our study.

SExtractor (Bertin and Arnouts, 1996) and PSFEx (Bertin, 2011) were employed for source detection and PSF photometry. Star/galaxy separation was performed using the method described in Koposov et al. (2015), which adopts

$$|SPREAD\_MODEL| < SPREADERR\_MODEL + 0.003 \tag{A.1}$$

as the threshold for stars. The instrumental magnitudes were calibrated by crossmatching with the Pan-STARRS1 StackObjectThin catalog (Chambers et al., 2016), and then de-reddened using the Schlegel et al. (1998) dust maps with the extinction coefficients from Schlafly and Finkbeiner (2011). The inferred distances are consistent with those given in Harris (1996).

For a given target we constructed the $((g-i)_0, g_0)$ color-magnitude diagram (CMD) using all stellar objects within $r < 3'$ from the nominal cluster center, and fit a fiducial line representing the locus of cluster members in the CMD. The fiducial line for each cluster was determined empirically. The CMDs for the inner $3'$, which are dominated by cluster members, were subdivided into intervals of g_0 and the 3σ-clipped median $(g-i)_0$ colors determined. A continuous curve through the pairs of mean g_0 and the corresponding median color for each interval then defines the fiducial line for the cluster members. This fiducial line was then used to calculate a weight w for each star detected across the field. The weight quantifies the likelihood of a star being a cluster member based on its distance from the fiducial line along

the color axis. The weight value was calculated using the Gaussian distribution $N(x,\mu,\sigma)$ centred on the fiducial line (normalized to have $w = 1.0$ at the centre), with σ corresponding to the uncertainty in $(g-i)_0$ at the g_0 value, which were taken from the photometric errors generated by SExtractor.

Stars within 2σ range from the fiducial line in color (that is, $w = N((g-i)_{0,*}, (g-i)_{0,fid}, \sigma_{(g-i)_0}) > 0.135$) were considered to have a high probability of being related to the target cluster. We will henceforth call this selection "member stars", although it still contains some contamination from foreground/background objects (henceforth "background") which happen to lie near the cluster population in CMD. To minimise this contamination while maximising the signal due to cluster members, we further restricted our selection to an interval in g_0 defined to cover the region on the CMD with the greatest contrast between "cluster" and "background" stars. In addition, we ensured that the faint end of this interval was 0.5 mag above the 50% photometric completeness limit.

Radial density profiles and spatial density maps were generated to investigate the distribution of the member stars (Figs.A.1 and A.2). For the radial profile (upper left panel), we binned our field-of-view in concentric annuli with logarithmic spacing. Poisson statistics were assumed for calculating the uncertainty in each bin. The best-fitting King profile (King, 1962) was determined by using a python library LIMFIT (Newville et al., 2014) after subtracting the background level. The background level was fixed from the total ($cluster + background$) density profile by determining the median annular density after 3σ-clipping.

Two-dimensional density maps (bottom panels) were constructed by binning the DECam field into cells of size $0.33' \times 0.33'$ for Eridanus and $0.59' \times 0.59'$ for Pal 15, and then smoothing with a Gaussian kernel of width $\sigma = 0.8'$ for Eridanus and $\sigma = 1.47'$ for Pal 15. The bin size and sigma were chosen after testing various combinations to provide the maximum contrast for the tidal features. The median stellar density of the field (=background), beyond 3 tidal radii from the cluster, is 5 star/arcmin^2 ($\sigma = 2.9$ star/arcmin^2) for Eridanus, 7 star/arcmin^2 ($\sigma = 3.1$ star/arcmin^2) for Pal 15 before smoothing. We generated a background map for each cluster in the same manner by using the corresponding subsample of background objects. After this map was normalised to the median 3σ-clipped density of the $w > 0.135$ map determined above, it was subtracted to remove any large-scale gradients or instrumental artefacts across the field. Local RMS values were measured for each of the 62 CCDs. The median was considered to be the background RMS and used to scale the background subtracted spatial density map (bottom left panel).

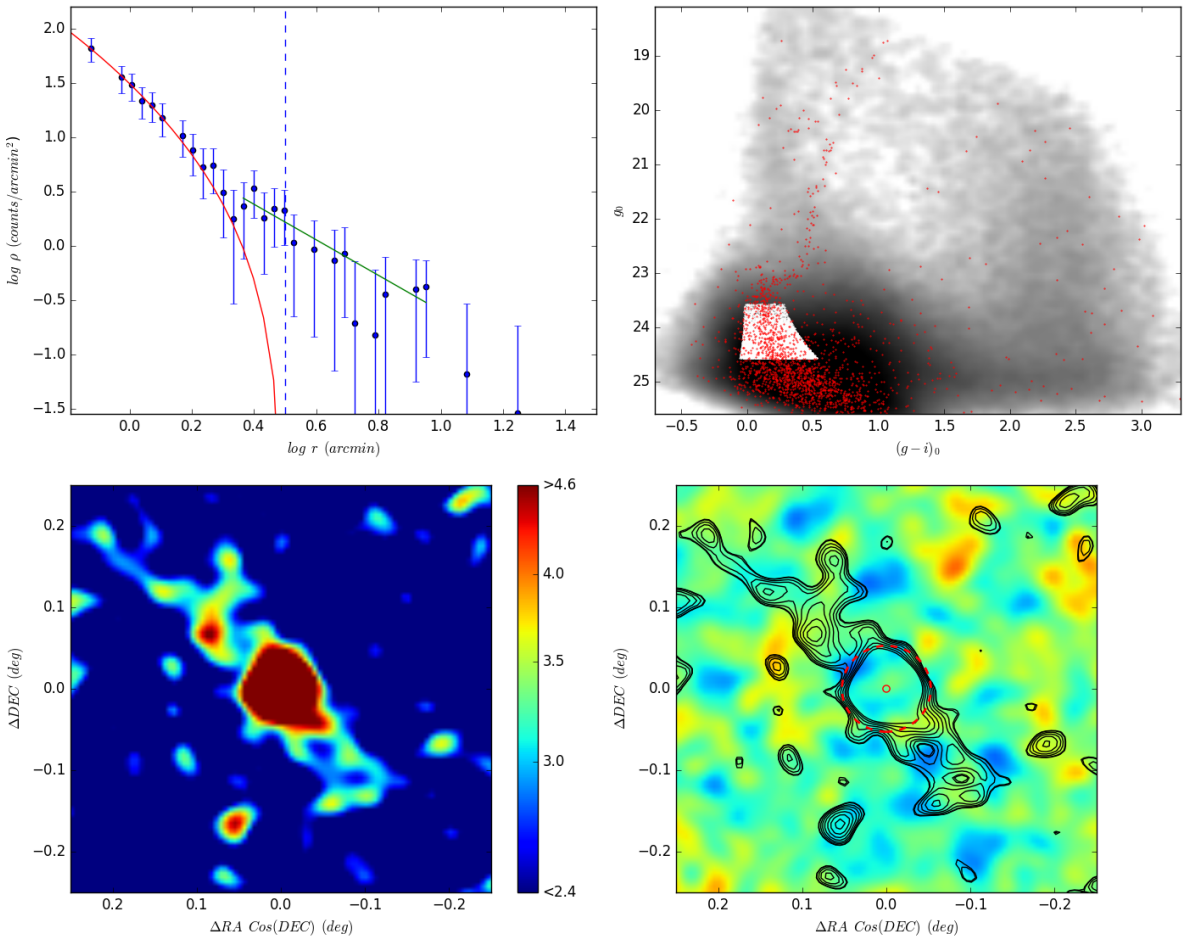

Fig. A.1 Eridanus. Upper Left panel: Background-subtracted radial density profile and the best-fit King profile (red line). The green line is the least-squares fit to the profile after the point where it starts to deviate from the King profile. The blue dashed line indicates the tidal radius from the best-fitting King profile. Upper Right panel: Hess diagram of stellar objects over the DECam field-of-view. Red dots are the stars within $r < 3'$ from the nominal cluster center. The white area highlights the selection box for cluster members. Lower left panel: 2D density map of the Eridanus region after the background subtraction. The field was binned into $0.33' \times 0.33'$ pixels and smoothed with a $\sigma = 0.8'$ Gaussian kernel. Lower right panel: Contour map generated from the lower left panel, superimposed on the background map. Circles are the core radius, $r_c = 0.25'$ (6.6 pc) (solid), and the tidal radius, $r_t = 3.17'$ (83.0 pc) (dashed) from the best-fitting King profile. The scale on the right side of the density map is the signal strength in units of the standard deviation above the background. The contour lines range from $2.7 - 4.75\sigma$ in logarithmic steps.

A.3 Eridanus

Eridanus, at $R_{GC} = 95.0$ kpc (Harris, 1996), is one of the most distant Galactic globular clusters known. It has been classified as a "young" halo cluster, suggesting that it may have originated in an external satellite galaxy and been accreted into the Galactic halo (Mackey and van den Bergh, 2005; Zinn, 1993). Our best-fitting King profile has a core radius $r_c = 0.25' \pm 0.12'$ (6.6 ± 3.1 pc) and a tidal radius $r_t = 3.17' \pm 0.76'$ (83.0 ± 20.0 pc), with the concentration index $c = \log(r_t/r_c) = 1.10 \pm 0.23$. These values agree well with previous measurements ($r_c = 0.25'$ and $r_t = 3.15'$, Harris (1996)). The radial profile exhibits an excess of stars outside $r \sim 1.82'$ ($\log(r) \sim 0.26$), which continues beyond the nominal tidal radius $r > r_t = 3.17'$ and follows a power law with an index of $\gamma = -1.64 \pm 0.16$ (azimuthally averaged).

The spatial density map and the corresponding contour map (lower panels of Figure A.1) reveal two prominent tidal tails extending considerably beyond the tidal radius (dashed circle in the contour map). These structures show no correlation with the background map. Tail 1 extends $\sim 18'$ (~ 480 pc) from the cluster center in North-East direction at a position angle of PA=$40 \pm 5^\circ$. Tail 2 extends $\sim 11'$ (~ 280 pc) in South-West direction (PA=$220 \pm 10^\circ$). The fractional overdensity of cluster stars is 29.4% and 31.6%, respectively, in the distance interval $2.5\,r_t < r < 3\,r_t$. The alignment of the features is close to axisymmetric suggesting that they are likely following the orbit of Eridanus. Given the alignment and the narrow width compared to the size of the cluster, it would seem likely that the features are tidal tails resulting from the dynamical evolution of Eridanus in the tidal field of the Milky Way.

A.4 Palomar 15

Pal 15 is an outer halo globular cluster at $R_{GC} = 38.4$ kpc (Harris, 1996). Although it is classified as an "old" halo cluster, Pal 15 is a good accretion candidate by virtue of its location at a large Galactocentric distance (Mackey and Gilmore, 2004). Our best-fitting King profile has a core radius $r_c = 1.40' \pm 0.15'$ (18.4 ± 2.0 pc) and a tidal radius $r_t = 5.19' \pm 1.12'$ (68.1 ± 14.7 pc), with the concentration index $c = \log(r_t/r_c) = 0.57 \pm 0.11$. This shows good agreement with previous measurements as listed in Harris (1996) ($r_c = 1.20'$, $r_t = 4.77'$). The small concentration index of 0.57, mainly a consequence of the exceptionally large core radius, suggests that Pal 15 has been severely affected by the Galactic tidal field. Both Pal 5 and Pal 14 also have large core radii, and are known to have extensive tidal tails (Odenkirchen et al., 2001; Sollima et al., 2011).

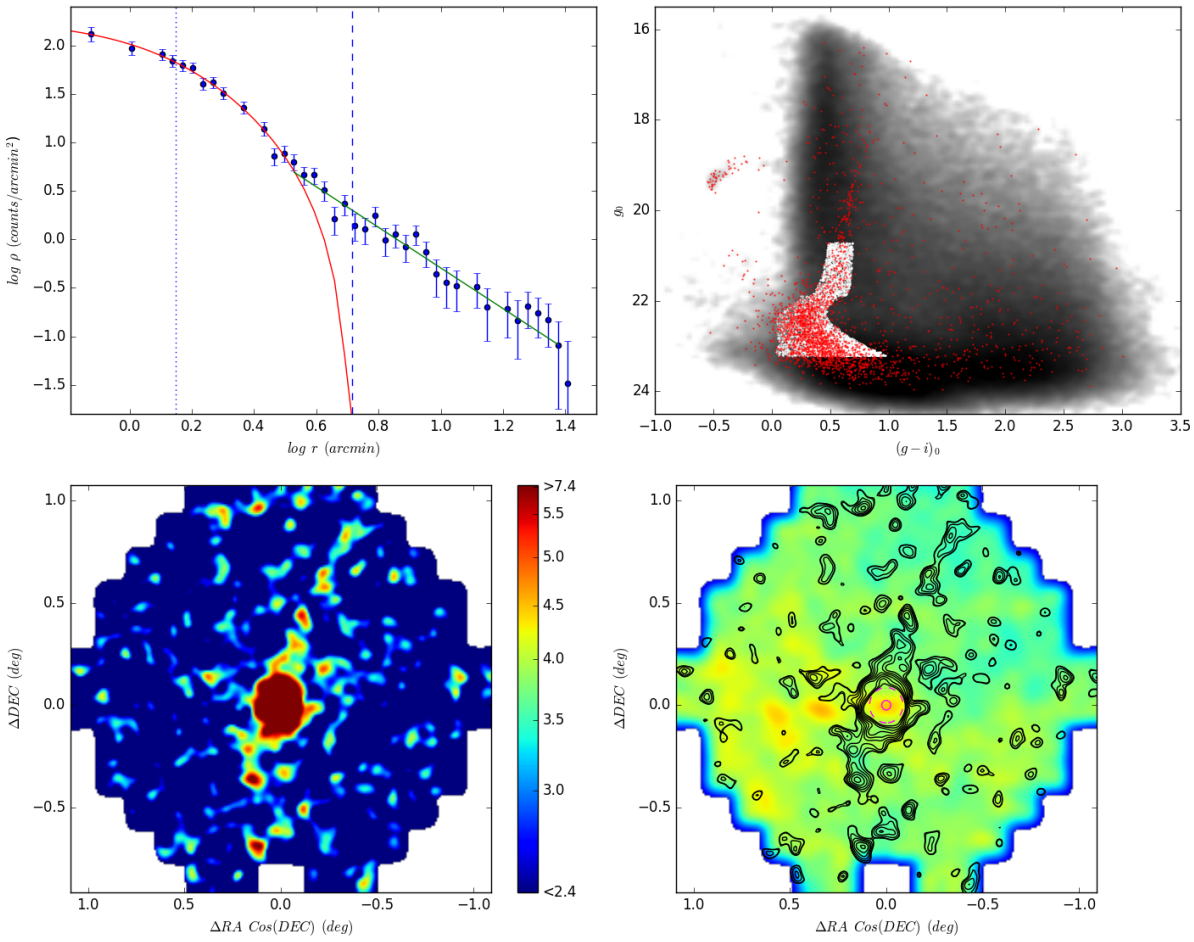

Fig. A.2 The same as Figure A.1 but for Pal 15. Upper Left panel: The dotted line represents the core radius from the best-fitting King profile. Upper Right panel: Hess diagram of stellar objects over the DECam field-of-view. Lower Left panel: The field was binned into $0.59' \times 0.59'$ cells and smoothed with a $\sigma = 1.47'$ Gaussian kernel. Lower Right panel: The two circles are the core radius, $r_c = 1.40'$ (18.4 pc) (solid) and the tidal radius, $r_t = 5.19'$ (68.1 pc) (dashed). The contour lines range from $3.0 - 8.85\sigma$ in logarithmic steps.

The radial profile of Pal 15 follows closely a King profile until the local star density has dropped to $\sim 3\%$ of its central value ($r \sim 3.47'$ or $\log(r) \sim 0.54$), beyond which there is a strong excess of stars that continues past the nominal tidal radius and follows a power law with an index of $\gamma = -2.09 \pm 0.09$ (azimuthally averaged).

The spatial density and contour maps (lower panels in Figure A.2) show clear tidal tail features extending beyond the cluster's tidal radius (dashed circle in the contour map), crossing the field from the North-West to the South. These structures show no correlation with the background trend, nor with the extinction map (Schlafly and Finkbeiner, 2011; Schlegel et al., 1998). Tail 1 extends $\sim 59'$ (~ 780 pc) from the cluster centre in North-West direction at a position angle of PA=$340 \pm 5^\circ$. At the $\sim 3.0\,\sigma$ significance level it consists of two main fragments (see contour map). We tested various combinations of binning sizes and smoothing kernels. The secondary, more distant fragment is visible in every solution. This supports the notion that this continuation of Tail 1 is indeed a real feature. The gap between the two segments may be similar to the gaps seen in the Pal 5 tails, whose origin has been the subject of a number of studies (e.g. Carlberg et al., 2012). Tail 2 extends $\sim 29'$ (~ 380 pc) in South-East direction with a possible kink at half this length. The mean position angle is PA=$150 \pm 10^\circ$. The fractional overdensity of cluster stars is 20.9% and 22.5%, respectively, in the distance interval $2.5\,r_t < r < 3\,r_t$. Both tails have considerable sizes when compared to Pal 15's nominal tidal radius ($r_t = 5.19'$). Although the two tails are different in length, their alignment close to axisymmetric suggests that they are following the orbit of Pal 15. Additionally, both tidal tails are relatively narrow compared to the cluster size, indicating that these stellar streams are, like in the case of Eridanus, the result of the dynamical evolution in the Galactic tidal field.

A.5 Discussion

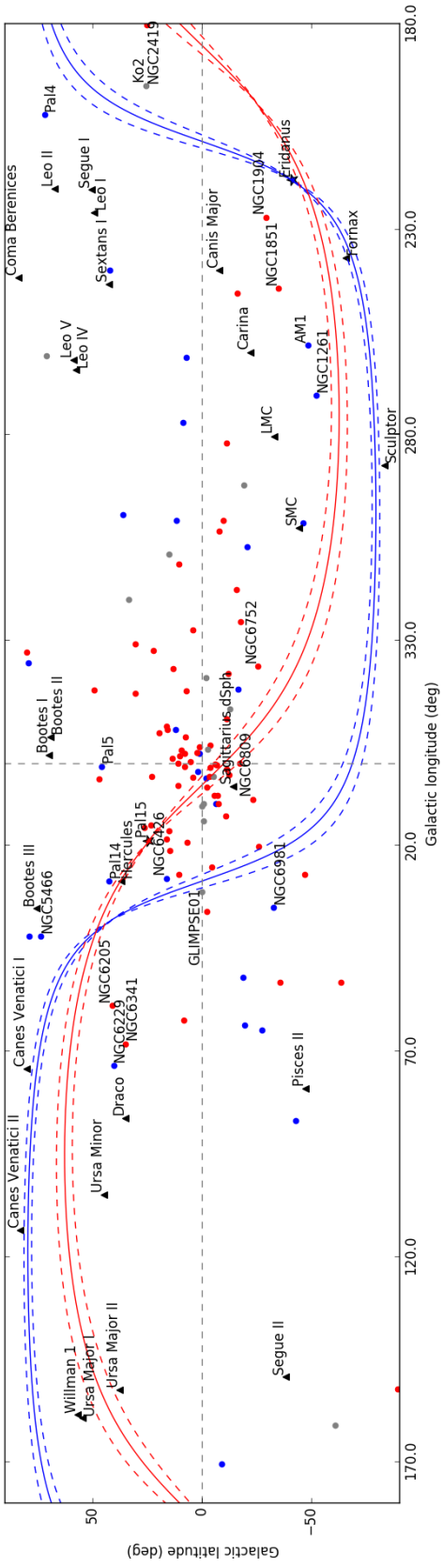

Fig. A.3 Great circle along the direction of the tidal tails of Eridanus (blue line) and Pal 15 (red line). Dashed lines in the same color indicate the corresponding uncertainty range. The two stars are Eridanus (blue) and Pal 15 (red). Milky Way globular clusters listed in Harris (1996) are marked as dots in blue for "young" halo clusters, red for "old" halo clusters, and grey for unclassified (Mackey and van den Bergh, 2005). Major Milky Way dwarf satellite galaxies listed in McConnachie (2012) are marked with black triangles. Vertical and horizontal grey dashed lines indicate 0 deg of Galactic longitude and latitude, respectively.

ID	r_c (pc)	r_t (pc)	c	size_{t1} (pc)	size_{t2} (pc)	$\text{angle}_{\text{inc}}$ (deg)
Eridanus	6.6 ± 3.1	83.0 ± 20.0	1.10 ± 0.23	~ 480	~ 280	~ 180
Pal 15	18.4 ± 2.0	68.1 ± 14.7	0.57 ± 0.11	~ 780	~ 380	~ 170

Table A.1 Basic parameters for the tidal structures of Eridanus and Pal 15. ($_{\text{t1}}$) indicates Tail 1, ($_{\text{t2}}$) indicates Tail 2, and ($\text{angle}_{\text{inc}}$) indicates the angle between two tails.

We have discovered tidal tails extending from the two remote Milky Way globular clusters Eridanus and Pal 15. The narrowness of the tails compared to the cluster size, along with their symmetric orientation on either side of the cluster centres indicates that they are due to the loss of cluster members to the Galactic tidal field, as seen for several other globular clusters such as Pal 5 and NGC 5466, and in numerical simulations (Capuzzo Dolcetta et al., 2005; Combes et al., 1999). Moreover, the power-law slope for each tail region (PA$\pm 10^\circ$) shows $\gamma = -1.20 \pm 0.19$ and $\gamma = -1.25 \pm 0.16$ for Eridanus, $\gamma = -1.24 \pm 0.12$ and $\gamma = -1.26 \pm 0.12$ for Pal 15, which are similar values as in the case of Pal 5 (Odenkirchen et al., 2003) and steeper than constant density.

Table A.1 contains the estimated basic parameters for the tidal tails. Both pairs exhibit significant extent beyond the nominal tidal radius of their respective cluster – the tails of Eridanus span ~ 760 pc in total, while those for Pal 15 trace ~ 1160 pc.

The tails of Pal 15 may well extend beyond the edge of the DECam field-of-view. In this case, our study provides a lower limit on their length, and some additional off-field data will be required to test the true extent of Pal 15's tidal structure. In addition, the tails appear curved, especially if the fragment near the Southern edge of our Pal 15 field is considered to be part of the structure. If confirmed, this could hold information about the underlying Galactic potential or it may be simply related to projection effects (Combes et al., 1999).

For Eridanus, the tidal tails are well confined to the inner part of our DECam field. This suggests that we have effectively found their full extent, unless the star densities in the tails are getting too low relative to the background. This may indicate an eccentric orbit of Eridanus about the Milky Way as we may be seeing its long tails foreshortened.

We generated the great circle along the direction of the tidal tails for each cluster, based on the position angle and its uncertainty estimated for each tail (Figure A.3). We compared its path with the positions of the Milky Way globular clusters listed in Harris (1996) and the Milky Way dwarf satellites in McConnachie (2012). Since the tidal tails are expected to be projected along the orbital path of the cluster (Capuzzo Dolcetta et al., 2005; Combes et al., 1999), this great circle can provide a rough estimate for the cluster's orbit. It is

notable that the potential orbit of Eridanus passes close to the dwarf galaxies Canes Venatici I, Canes Venatici II, Fornax and Sculptor. Sculptor ($R_{GC} = 86$ kpc, McConnachie, 2012) has a comparable distance to that of Eridanus. Since Eridanus is classified as a "young" halo cluster based on its metallicity and horizontal branch morphology (Mackey and van den Bergh, 2005), and indeed exhibits a CMD consistent with an age up to ~ 2 Gyr younger than the oldest Milky Way globular clusters (Stetson et al., 1999), this possible association to Sculptor and/or another of the three satellites might provide additional evidence of Eridanus' extragalactic origin (see also Keller et al. (2012)). Even so, it is striking that despite several indications that both Eridanus and Pal 15 might be accreted, and our data being sensitive enough to detect low surface brightness features at their distances, no clear evidence for stellar debris from parent dwarf galaxies was observed. Carballo-Bello et al. (2015) suggested that Eridanus may be associated with the Monoceros ring based on the modelled orbit of this structure by Peñarrubia et al. (2005); however, the great circle of Eridanus disagrees with this modelled orbit, suggesting no clear association between them.

The great circle defined by the tidal tails of Pal 15 passes close to Ursa Major II which also has a comparable distance of $R_{GC} = 38$ kpc (McConnachie, 2012), suggesting possible association. We further notice that the potential orbits of Eridanus and Pal 15 extend to relatively high Galactic latitudes, indicating that the clusters may be on plunging orbits relative to the Galactic disk. Assuming the orbits are sufficiently eccentric to pass through the inner region of the Milky Way, the clusters could experience periodic disk and/or bulge shocks. Since these processes are known to be destructive (Gnedin et al., 1999; Gnedin and Ostriker, 1997), this could explain why both clusters exhibit tidal tails. A prime example is Pal 5, which suffers this type of tidal shock and is predicted to be destroyed at its next disk crossing (Dehnen et al., 2004).

In the case of Eridanus ($R_{GC} = 95.0$ kpc), we have discovered a new tidal stream in an extremely remote part of the Galaxy which is poorly understood and where no other narrow streams are known. Studying Eridanus and its tails in detail may lead us to a better understanding of the gravitational potential in the extreme outskirts of the Galaxy. A key aspect of this will be understanding whether the tails arise from the action of the tidal field at this large Galactocentric distance, or whether Eridanus is on a very eccentric orbit such that it passes through the inner Milky Way, and the tails are more likely due to the action of the tidal field at smaller radii.